University of Nebraska - Lincoln
DigitalCommons@University of Nebraska - Lincoln

Mechanical (and Materials) Engineering -- Dissertations, Theses, and Student Research

Mechanical & Materials Engineering, Department of

12-2016

Design and Evaluation of Pediatric Gait Rehabilitation Robots

Cale J. Stolle
University of Nebraska-Lincoln, cale.stolle@huskers.unl.edu

Follow this and additional works at: http://digitalcommons.unl.edu/mechengdiss

 Part of the Biomechanical Engineering Commons

Stolle, Cale J., "Design and Evaluation of Pediatric Gait Rehabilitation Robots" (2016). *Mechanical (and Materials) Engineering -- Dissertations, Theses, and Student Research*. 108.
http://digitalcommons.unl.edu/mechengdiss/108

This Article is brought to you for free and open access by the Mechanical & Materials Engineering, Department of at DigitalCommons@University of Nebraska - Lincoln. It has been accepted for inclusion in Mechanical (and Materials) Engineering -- Dissertations, Theses, and Student Research by an authorized administrator of DigitalCommons@University of Nebraska - Lincoln.

DESIGN AND EVALUATION OF SCALABLE PEDIATRIC GAIT REHABILITATION ROBOTS

by

Cale J. Stolle

A DISSERTATION

Presented to the Faculty of

The Graduate College at the University of Nebraska

In Partial Fulfillment of Requirements

For the Degree of Doctor of Philosophy

Major: Engineering

(Biomedical Engineering)

Under the Supervision of Professor Carl A. Nelson

Lincoln, Nebraska

December, 2016

DESIGN AND EVALUATION OF SCALABLE PEDIATRIC GAIT REHABILITATION ROBOTS

Cale Joshua Stolle, Ph.D.

University of Nebraska, 2016

Advisor: Carl A. Nelson

Gait therapy methodologies were studied and analyzed for their potential for pediatric patients. Using data from heel, metatarsal, and toe trajectories, a nominal gait trajectory was determined using Fourier transforms for each foot point. These average trajectories were used as a basis of evaluating each gait therapy mechanism. An existing gait therapy device (called ICARE) previously designed by researchers, including engineers at the University of Nebraska-Lincoln, was redesigned to accommodate pediatric patients. Unlike many existing designs, the pediatric ICARE did not over- or under-constrain the patient's leg, allowing for repeated, comfortable, easily-adjusted gait motions. This design was assessed under clinical testing and deemed to be acceptable.

A gait rehabilitation device was designed to interface with both pediatric and adult patients and more closely replicate the gait-like metatarsal trajectory compared to an elliptical machine. To accomplish this task, the nominal gait path was adjusted to accommodate for rotation about the toe, which generated a new trajectory that was tangent to itself at the midpoint of the stride. Using knowledge of the biomechanics of the foot, the gait path was analyzed for its applicability to the general population.

Several trajectory-replication methods were evaluated, and the crank-slider mechanism was chosen for its superior performance and ability to mimic the gait path

adequately. Adjustments were made to the gait path to further optimize its realization through the crank-slider mechanism.

Two prototypes were constructed according to the slider-crank mechanism to replicate the gait path identified. The first prototype, while more accurately tracing the gait path, showed difficulty in power transmission and excessive cam forces. This prototype was ultimately rejected. The second prototype was significantly more robust. However, it lacked several key aspects of the original design that were important to matching the design goals. Ultimately, the second prototype was recommended for further work in gait-replication research.

DEDICATION

This project was exceptionally difficult to me. My experience lay mostly in transportation safety and in theoretical research and evaluation of structures. This project pushed me into an area where I had not been before, and it was both an eye-opening experience and a challenge. I welcomed it with open arms, but it proved to be difficult.

I'd like to thank my ultimate source of strength and motivation – Jesus Christ. His wisdom guided my patience and my perseverance through innumerable struggles and frustrations during this project, and always helped me to keep my eyes on the future.

I'd also like to thank Dr. Carl Nelson. His guidance and support was integral to both the completion of this project and my efforts in this study. He did not blame me for the shortcomings of my initial project, and was very understanding about my position and effort. I don't think that anyone outside of Dr. Nelson could have pushed me through this project with such grace and kindness. He has helped me in innumerable ways, and I feel he will always be a part of my professional future.

I'd like to thank my coworkers who put up with my gigantic mess. The students working for Dr. Nelson are some of the best coworkers I have ever had, and we shared many laughs and supported each other through our studies. I'd like to especially thank Tao Shen, Mohsen Zahiri, Colin and Devin Elley, Gonzalo Garay-Romero, Baoling Zhao, Kazi Hossain, Saeideh Akbari, and Ross Welch, who stayed with me for most of my tenure, and put up with not only my massive mess, but also my incessant ramblings and my jokes and goofiness.

I'd like to thank Dr. Judy Burnfield and Thad Buster for their assistance with this project, as well as Chase Pfeifer and the rest of the team at the Madonna Rehabilitation

Hospital. Their insight and wisdom provided me with this unique opportunity, and I was very appreciative of their feedback throughout this entire process.

I would like to thank Candice Schoenherr for her support in some of the tough times of this project. Her steady resolve was very helpful when things were stressful for me, and I relied on her strength to finish.

I'd like to thank Ryan Coughlin for his assistance in the construction and design of the first prototype. His help was extensively useful, and he also served as a motivation for me to finish the prototype. I'd also like to thank Nathan Borcyk for his assistance with the final phases of this project including the foot pedals.

I would like to thank my family for their support of me and for always pushing me to achieve my best. I am truly grateful for their presence in my life. They provided me with the foundation of what I believe in and the structures of how I perceive the world and myself. I owe them an eternal debt of gratitude.

Finally, I would like to thank my church family at Cornerstone Christian Church. They are always reliable, supportive, encouraging, and entertaining. I am proud to be a part of that group.

TABLE OF CONTENTS

LIST OF FIGURES

LIST OF TABLES

LIST OF EQUATIONS

CHAPTER 1 – INTRODUCTION

Since the dawn of humanity, walking has been an integral aspect of life. The ability to walk defines the growth of children, the strength of adults, and the decline of health in the elderly. The inability to effectively ambulate comes with a host of physical, psychological, and social implications that are detrimental to the overall well-being of a human. In short, walking is one of the major indicators of human health.

The main purpose of perambulation is mobility. In general, mobility is defined as the capacity to move through physical space, although true mobility spans much farther than this simple definition. Schwanen and Ziegler suggest that mobility, independence, and well-being are all interdependent and complicated mechanisms that complement each other, and can't be undervalued for their importance [1]. According to Schwanen and Ziegler,

> *[F]or those whose embodied capacities have diminished over time mobility, independence and wellbeing can become linked up in a downward spiral (p. 724).*

The impact of mobility on physical and psychological health is profound. Immobility and reduced mobility are linked to a long list of physical health problems spanning across every major organ system [2]. Some of the complications are increased risks for blood clots, indigestion, osteoporosis, changes in hormone balance, bladder infections, pressure ulcers, atrophied muscles, difficulty expanding lungs fully, weakened coughs, and low back pain. Psychologically, immobility can cause depression, anxiety, apathy, mood swings, feelings of helplessness, loss of normal sleep cycles, and delirium.

According to the U.S. Census, 30.6 million American adults and teenagers experience difficulty in perambulation, including walking or climbing stairs [3]. Correspondingly, about 3.6 million people use a wheelchair and 11.6 million people use another form of assistance when walking, such as a cane or walker. The census survey also asked about information on difficulty moving large objects (such as a chair), reaching the top shelf, and standing for long periods of time. The inability to effectively perambulate affects more than simply the ability to move from one location to another.

Gait therapy involves a series of guided tasks facilitated by a therapist in which an individual moves through the motions of walking, often with significant assistance. Gait therapy is useful for many purposes. For one, gait therapy can be used to teach the correct leg movements involved in walking. However, it can also be used with individuals who are unable to walk to provide them with valuable exercise to increase their health. The prevalence of individuals with gait-related disabilities and ambulatory issues adds to the need for reliable, cost-effective gait therapy treatment and exercise.

Gait therapy is especially important for children. According to the U.S. Health and Human Services Advisory Committee, children's muscular, skeletal, and cardiovascular health all show marked improvement with increased physical exercise [4]. Aside from physical benefits, learning how to walk is integral to the development of psychological independence. Between the ages of one and three, children begin to use their newfound walking ability as a way of expressing and exploring their own capability. Erikson [5] theorized that inhibitions in this stage, such as repression of walking capability, would tend to incur self-doubt and self-esteem problems in children that would last for years to come.

Because of this, gait therapy is needed for children. However, many of the gait therapy methods that are used for children right now are either clinician-intensive or expensive. This is an issue when it comes to rural or smaller rehabilitation facilities, hospitals, or home health centers. As such, there exists a need for inexpensive, easy-to-use, effective pediatric gait therapy equipment.

Realistically, there are no gait therapy mechanisms that accurately trace gait trajectories every cycle. However, it is currently unknown what effect gait mechanisms have on therapy as their trajectory becomes more gait-like. One of the goals of this research is to develop a gait-like machine and compare to existing rehabilitation technologies. Using the new machine, it will be possible to determine whether the cyclical, repetitive nature of current gait rehabilitation is the driving force behind gait therapy or if the therapy effectiveness is correlated to trajectory accuracy.

CHAPTER 2 – LITERATURE REVIEW

The goal of pediatric gait therapy is to guide the legs muscles through a gait-like motion for both physical exercise and for teaching muscular movements involved in walking. This is particularly necessary following surgery, illness, accidents, birth defects, and other factors that cause temporary immobility in children. Since walking is the major form of exercise for humans, this therapy is necessary to improve the health and future of children. However, to understand how therapy works, it is necessary to understand the walking motions of children first.

2.1 Pediatric Gait

2.1.1 Development of Gait

Normally, children develop walking skills in a predictable manner, reaching landmark achievements on a fairly rigid timeline. According to Christopher Heffner, "most agree that these abilities are genetically preprogrammed within all infants" [6].

Heffner presented his timeline for when normal gait should occur and the sequential order of learning stages [6]. The learning progression is shown in Table 1.

Table 1 Average Process for Learning Gait [6]

Approximate Age	**Skill Mastery**
2 months	Able to lift head up without assistance
3 months	Able to roll over
4 months	Can sit propped up without falling over
6 months	Able to sit up without support
7 months	Begins to stand while holding onto things for support
9 months	Can begin to walk, still using support
10 months	Is momentarily able to stand without support
11 months	Can stand alone with more confidence
12 months	Begins walking alone without support
14 months	Can walk backward without support
17 months	Can walk up steps with little or no support
18 months	Able to manipulate objects with feet while walking (such as kicking a ball)

The learning progression of how infants come to walk takes many months. During this process, they are increasing their muscle strength, improving their balance, and learning motor control of their limbs for successful gait. Each step (such as learning to crawl and learning to stand with assistance) is developing one of these three areas that are pertinent to the next step.

The factors affecting the development of normal gait vary with each child depending on both their genetic makeup and their environment. Adolph et al. postulated that the three major developmental factors were body dimensions, neural pathways, and walking experience [7]. An experiment conducted by cross-evaluating infants, kindergarteners, and adults showed that there were positive correlations between normality of gait patterns and each of these factors. With body dimensions changing until

the completion of puberty, this infers that gait development is not fully established until adulthood. In order to design for children, it is then important to focus on the similarities and controllable factors, as opposed to the variations existing through natural development.

Early in a child's development, children display the cyclical leg motions where each leg moves identically, phase-shifted by half a cycle [8-9]. Joint flexion and angles are very similar between infant kicking and adult walking, and much of the leg movement timing is dependent on the weight of the child's leg [10-11].

Some researchers have noted that gait maturation continues until after the age of 14 [12-15]. Variations, growth, and strengthening of the musculoskeletal structure is attributed to the variation of stride lengths and timing noted in that maturation process. Even though the stride length and timing matures into puberty, the stochastic timing difference in strides is close to the adult value beginning at age 6 [16].

2.1.2 Comparison of Pediatric and Adult Gait

Comparing the gait trajectories for children and adults shows one major difference: the size of the adult stride length is significantly larger than the pediatric stride length. In order to make a valid comparison between the child and the adult, the gait trajectories must be normalized. Hof suggested that there were several variables available to normalize by using the human body [17]. Specifically related to gait, the normalization factor would be the leg length. Dimensionless data plotted for children ages 1 to 7 shows a strong correlation between the leg length and the stride length, meaning that the stride length could be used as an acceptable normalization factor [18]. Normalization allows for direct comparison regardless of size.

Sutherland noted that the gait of children appeared to “mature” to match the characteristics of adult ambulation [18]. Dimensionless data plotted for children ages 1 to 7 shows a strong correlation between the leg length and stride length. Further analysis shows that there is a maturation of stride length in relation to age. Similar maturation is noted in joint angles, muscular force data, oxygen consumption rate, and pelvic span/ankle spread ratio.

Ganley and Powers tested to see if pediatric gait was statistically different from adult gait motion [19]. A study group of 7-year-olds had a much smaller stride length and higher cadence, but very similar walking velocity. Data also proved that ankle power and ankle moments were significantly smaller in children than in adults. Other gait kinetics mimicked that of adult data. Studies conducted by Chester et al. determined significant difference in ankle plantarflexor moments, sagittal knee moments, sagittal hip moments, frontal hip moments, and hip power [20-21]. Slight angle differences were noted for each of these joints as well, but it was not deemed significant enough to claim that pediatric gait was dissimilar from adult gait.

In one study involving 28 children, knee and ankle flexion and heel strike occurred normally by age 40 months, implying that adult gait patterns may be present earlier in child development than previously thought [22]. Metatarsal trajectory relative to the trunk appears to be similar to adult metatarsal trajectory as early as age 3 [18]. Dimensionless data compared between children ages 5 to 12 showed that there was very little difference in stride parameters throughout the age range [23]. The general consensus, however, is that child gait patterns reliably reach full maturity at or before age 7 [7, 19, 24-29].

2.1.3 Discussion

Immature, unreliable gait trajectories are noted in young children, and continue into adolescence. Thus, measuring gait data of young children is sporadic and does not show significant convergence. However, despite the variation of data, normal pediatric strides have similar shape and body position to adult strides beginning at age 3, and are fully similar by age 7, although stride length and time change. As a result, pediatric gait therapy should aim to reproduce normal adult gait. This will encourage proper foot angles and metatarsal trajectory.

2.2 Phases of Normal Gait

In normal gait, both legs are identical, and neither offers any physical difference from the other. Thus, during normal gait, the motions are both cyclical and symmetric [30]. The limb cycle involves two double-support phases (where both legs are on the ground) and two single-support phases (where one leg is in the air). The body assumes different distinct positions during the gait phase, which can be approximated by the time the time they occur relative to the length of the stride time. A timed gait cycle is shown in Figure 1. Note that this image assumes that the stride starts and ends on initial contact of the shaded leg.

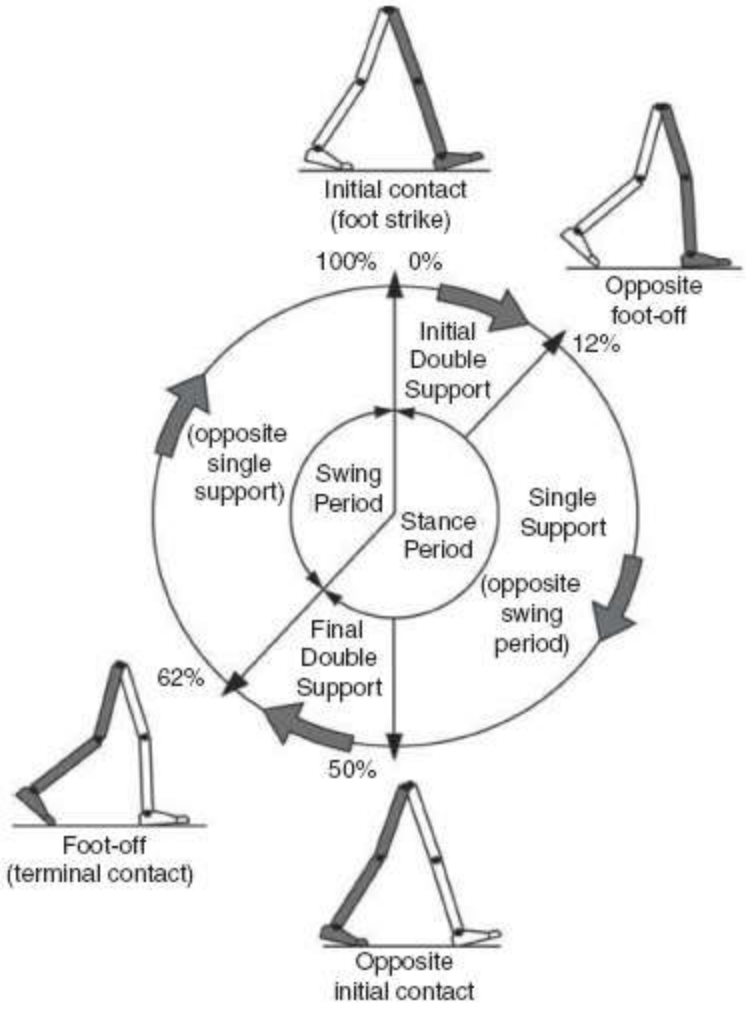

Figure 1. Gait Timing Cycle [30]

Perry separated the gait cycle into 8 distinct phases [31]. Each phase was marked by joint rotation values of interest, as well as active constraints on the foot at the time. The phases are explained in Table 2 and shown graphically in Figure 2.

Table 2. Gait Phases [31]

Phase of Gait	Description
Initial Contact	Moment when the foot first strikes the ground.
Loading Response	Initial double support period when the limb begins to accept weight. At the end of this phase, the opposite limb experiences toe-off.
Mid-Stance	First phase of the single-support when the body advances over the stance limb and weight is transferred from the rear of the foot towards the front of the foot.
Terminal Stance	Last phase of the single-support which ends when the opposite limb experiences first contact.
Pre-Swing	Final double-support period when the knee experiences rapid flexion in preparation for swing and when the weight is shifted to the opposite limb. This phase ends in toe-off.
Initial Swing	The first third of the swing period where the maximum knee flexion occurs. This phase ends when the heel of the swinging foot passes the heel of the opposite limb.
Mid-Swing	Middle third of the swing period where maximum hip flexion occurs. At the end of this phase, the tibia is vertical, perpendicular to the ground surface.
Terminal Swing	Last third of the swing period where the final knee extension achieves maximum step length, and the limb is put in position to accept weight transfer again. This phase ends in initial contact.

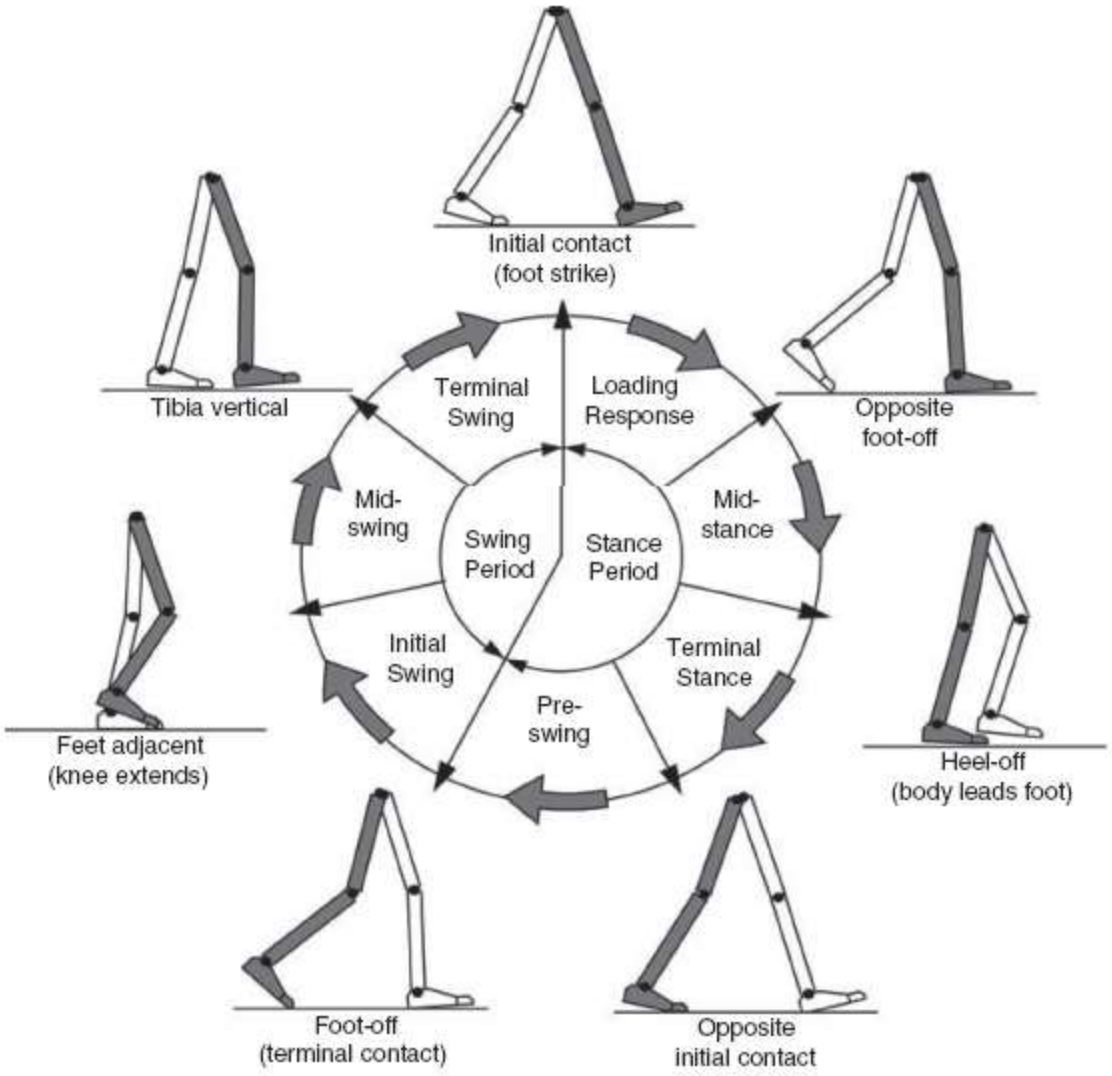

Figure 2. Gait Phases [31]

2.3 Neurogenic Control of Gait

2.3.1 Chaotic Behavior

When the trajectory of each point on the foot is measured and traced, they show similar form with other strides from the same individual. However, they do not share identical cadence and shape, despite the lack of features in the terrain. The variation noted between strides of the same individual has been deemed chaotic due to its random variation of timing and shape.

According to Buzzi et al., the nonlinear dynamics observed during gait exist to assist the body in overcoming obstacles during a normal gait cycle [32]. These seemingly random variances in stride length, timing, and foot path have been attributed to white noise, but show a distinct pattern when each stride is viewed sequentially, indicating that there is a nonlinear pattern affecting the stride variation [33]. This variation displays a fractal pattern, and is intrinsically healthy to the locomotion of an individual [34].

One of the reasons why chaos is important to the gait pattern is that chaotic systems have the ability to adjust to random inputs much more easily [35]. In one perspective, the neuromuscular control of the legs needs to be chaotic in order to seamlessly transition from normal gait to stair climbing to object avoidance, etc. Having a set, established, exact gait path would make slight deviations unnatural and gross deviations challenging, while the chaotic control of gait leads to significantly more fluid and improved gait transitions, adjustments, and initiations [36-37].

2.3.2 Proprioceptive Behavior

Proprioception is clinically defined as “sensory information that contributes to the sense of position of self and movement” [38]. It is a complex, multi-sensor input that involves both afferent and efferent nervous signals and feedback. Proprioception is an integral part of the motor feedback system, and actively contributes to acuity in fine muscular movements.

Proprioceptive training requires continuous motion, and as such, this may explain some of the successes noted by existing gait therapy methods. As stated by Aman et al.,

> *[I]t needs to be considered that proprioception is closely linked to movement. Unlike senses such as audition, where, for example, pitch*

> *perception can be trained in the absence of limb or body movement, proprioception requires movement. Thus, when evaluating the effectiveness of an intervention to improve proprioception, it may be difficult to isolate the sensory from a motor aspect of training. In fact, one can argue that any form of motor learning is associated with proprioceptive processing and thus may train proprioception [39]*

According to Miller, proprioception is best practiced through unbalanced, dynamic movements and teaching the body rapid adjustment to off-center inputs [40]. This is only one type of proprioceptive training, though. Aman et al. classified different types of proprioception, including passive movement training (focusing on the motion of only one joint), somatosensation stimulation (vibration of body segments), somatosensory discrimination (distinguishing of segment rotations and speeds through contact), and combined / multi-system training (involving multiples of these training techniques). While Aman et al. conclude that proprioceptive training is not well-defined, it is noted that there is conclusive evidence that forms of proprioceptive training are effective rehabilitation methods. This infers that there may not be a singular optimal solution to proprioceptive training.

A study was conducted based on a stroke patient where everyday activities were evaluated as therapeutic devices [41]. Results of this study recommend that stroke patients need to focus on proprioceptive-training tasks to rehabilitate above simply moving through motions. This was further evaluated in a study determining the effect of proprioceptors in the gait cycle. Researchers determined that the knee and hip joint angles during gait were strongly tied to a person's perception of their foot's location [42]. Proprioception is integral to protecting the lower limb during gait because the body

naturally attempts to minimize contact forces, choosing a gait path that prevents large impact loading on heel strike. Impact and pressure loading were found to assist in proprioceptive training, and inhibition of joint movement was found to also inhibit proprioceptive learning [43]. This indicates that proprioceptors may have a significant role in determining the gait movements, and also that proprioceptive failure may cause injury and gait abnormalities.

Other studies into therapeutic proprioceptive training have verified that proprioceptive training is beneficial to gait motions, rehabilitations, and overall health [44-47]. It has been noted, however, that proprioceptive training only teaches correct form during walking, but does not improve timing [48].

2.3.3 Discussion

The proprioceptive and chaotic behaviors noted in gait share one commonality: both methods show that the foot is guided through a path to avoid excessive loading of the foot, as is seen in kicking, tripping, or stomping. Also, the biomechanical feedback from normal gait is shown to assist in recurring normal gait paths, as expected in a proprioceptive system [49]. This infers that there may be a correlation between the proprioception of the foot and the chaotic nature of gait. This also implies a success/failure condition in gait, one where premature or unexpected foot contact is deemed unacceptable. During the swing phase of a gait cycle, three points on the foot risk contact with the ground or object: (1) the toe following toe-off, (2) the metatarsal at midswing, and (3) the heel at terminal swing. If contact occurs between the foot and the ground during any of those phases, the stride can be considered a failure.

The success/failure condition imposed by the proprioceptive and chaotic behavior of gait implies that successful therapy must prevent premature foot contact during gait by retraining the proprioception of the body to resume normal, fractal-like chaotic gait patterns. However, other factors are integral to therapy, such as overextension, prevention of muscular damage or excessive joint loading, and timing.

2.4 Gait Therapy Methods

The type of gait therapy available to individuals is dependent on their level of muscular strength. A patient with high muscular strength and control would be able to participate in most types of therapy, whereas patients with little to no muscular strength or control are very limited in their options.

The simplest form of therapy involves physical therapists manually assisting a patient's feet through a gait-like trajectory. Patients often have motive-assisting devices, such as walkers, parallel bars, or a body weight support system. This therapy method has proven effective [50]. However, this method can require specialized training, a multiplicity of therapists, and significant exertion [51].

Body weight-supported treadmill training is less intensive and expensive, assisting clinicians in powering the foot through a gait-like trajectory without requiring the patient to move. Treadmill training has shown to be effective for patients with a minimal amount of strength [52,53], but still requires significant effort from the therapist to guide metatarsal trajectories. One study showed that that the mean difference between treadmill walking and overground walking was very small, beating out both cycling and elliptical therapy methods [54].

Robotic-assisted gait therapy involves the use of automated actuation to assist in propelling the patient's foot through a gait-like trajectory. The idea is that fixing hip, knee, and/or ankle flexion can help teach the foot to track a more gait-like trajectory. A variety of types of robotic orthoses have been developed [55-59], each stating that they have improved joint angles during gait. A study conducted using robotic gait orthoses on pediatric cerebral palsy patients with poor gross motor control showed improvement after robotic gait training [60]. Also, robotic systems have shown to better rehabilitate natural gait motions than some elliptical devices due to their more accurate full-foot angle and trajectory [61]. These devices tend to be expensive, and, as stated earlier, constrain the joint and limit the ability to improve proprioception. This might explain why some research indicates that robotic-assisted gait treatment does not show as much improvement as therapist-assisted gait treatment [62]. However, some newer devices are in development that are both cheaper and simpler [63-66].

Motorized foot-propelling devices, such as elliptical machines, guide the foot through a looping trajectory. Elliptical machines require less effort from the therapist than does treadmill training, making this an easier option for clinics seeing many patients and for people with little muscular strength. Elliptical machines also tend to be easier to operate and cheaper than robotic systems. Kinematic analyses of elliptical devices show that they do assist in effective gait rehabilitation [67-72]. However, as stated earlier, some elliptical devices have shown poorer performance than robotic or treadmill training [60], and their motion does not match normal gait [54].

Gait rehabilitation techniques have been developed by researchers using treadmills with body weight support systems [51] and robot-assisted driven-gait orthoses

[74]. The Lokomat combines robotic gait orthoses with exercise equipment to improve the quality of training while reducing the work load required from the clinician [75-77]. The Lokomat is adjustable to function with both adult and pediatric patients. However, the cost makes the Lokomat infeasible for many small rehabilitation clinics and home health centers [75]. The Lokomat is shown with both adult and pediatric patients in Figure 3.

Figure 3. Lokomat Used with Adult and Pediatric Patients

According to Langhorne et al., following a stroke, physically-intense therapy appears to be the most effective form of treatment, offering the most advantage over a placebo therapy session [79]. Several therapy methods are compared for effectiveness in Figure 4, which offers standard means and deviations (SMD) for objectively-rated therapy methods based on existing literature and data. According to the chart, the most effective forms of therapy involve a cardiovascular element, proper proprioception, and repetition of movements with mechanical assistance. While stroke patients are not fully representative of every patient needing gait therapy, this chart still provides a foundation for understanding effectiveness of individual treatment methods. It should be noted that the treadmill training received positive scores during this study. However, despite its prevalence in rehabilitation, it was not as effective as other, more controlled methods that train proprioception and foot positioning.

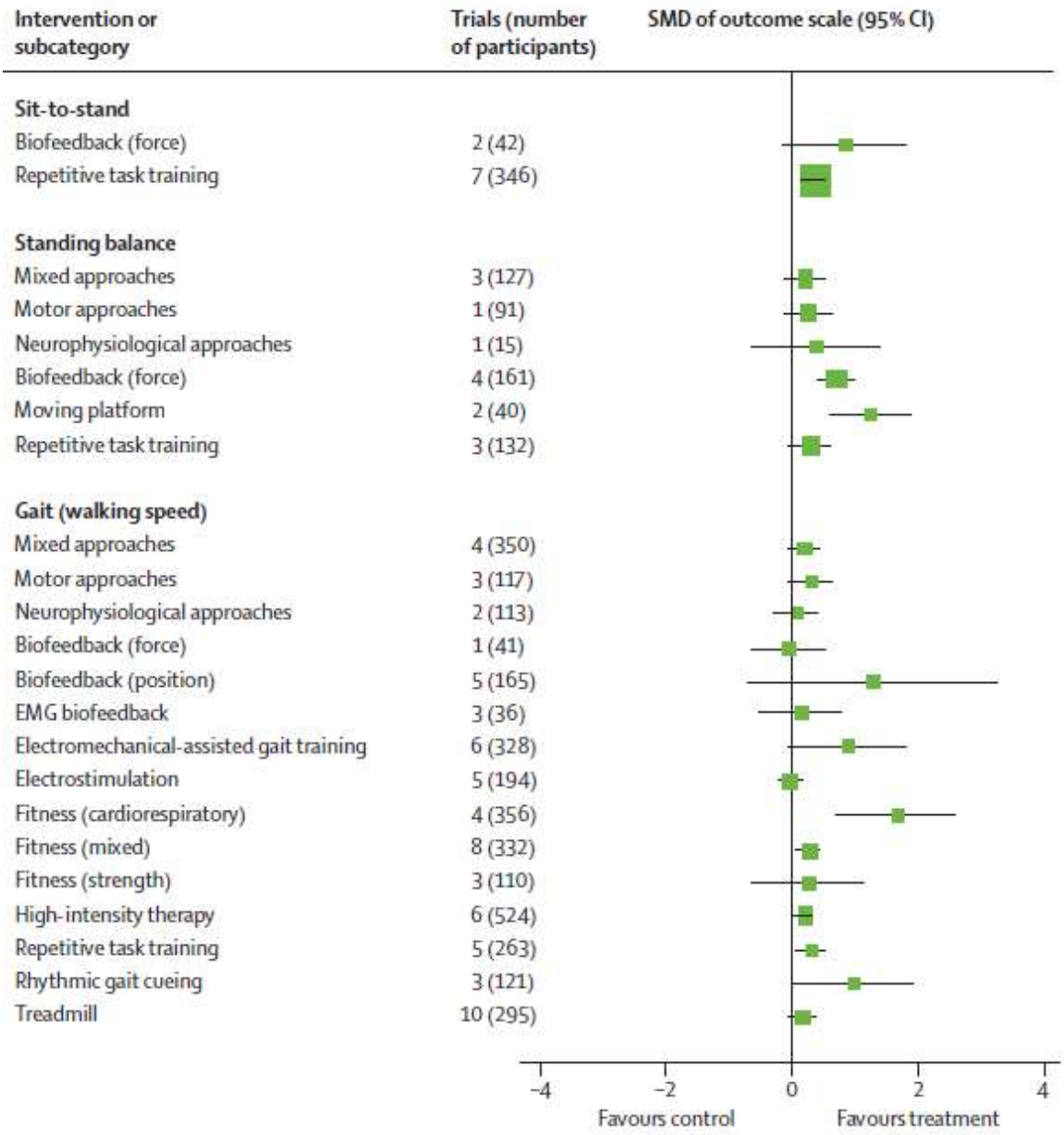

Figure 4. Gait Recovery Effectiveness [79]

One device which addresses some of these concerns is the Intelligently Controlled Assistive Rehabilitation Elliptical (ICARE) system, developed by researchers at Madonna Rehabilitation Hospital and the University of Nebraska [80,81]. The ICARE is a relatively low-cost, ergonomic, effective gait rehabilitation device for adults. The device is a modified, motorized elliptical machine that has been designed to push a

patient's feet through an approximation of gait-like motion. Unlike many other rehabilitation devices, the ICARE was designed so that little muscular strength is required to operate the machine. However, if the patient has sufficient muscular strength, they are able to drive the machine themselves without requiring the motor [82]. Studies have shown that this device effectively meets many of the requirements for gait rehabilitation. While the device emulates the kinematic and EMG demands of adult gait [83], the foot path is elliptical, which is not gait-like in shape or cadence.

The success of the ICARE follows the discussion from Section 2.3.2. While some gait therapy devices have sought to control joint angular motions and specific body postures during gait, the body needs to relearn the proprioceptive positioning needed for the foot to walk, as the ICARE has done. When designing a new gait rehabilitation device, it need not be intensive in its limbic control, but it needs to teach the foot proprioception.

2.5 Conclusions

Designing a device that facilitates rehabilitation for both adults and children, accommodating a broad range of stride lengths, is going to require uniformly scaling the path, which is identical in shape when normalized against the stride length. Initial efforts to construct a pediatric gait therapy machine will begin with the ICARE system. The ICARE has proven to be effective for adult therapy, it is expected to have similar results with pediatric patients. However, a secondary study will be performed to understand the gait path. It is believed that close approximation of the gait path will provide adequate proprioceptive training to better improve gait therapy methods. This will be pursued in a new, novel invention.

CHAPTER 3 – GAIT KINEMATIC ANALYSIS

According to the results noted in Section 2.1.2, it is difficult to capture the full scale of a pediatric stride. While adult data is significantly more consistent, pediatric data shows large variances in trajectory length and timing. Thus, an effort was made to understand both the adult gait and the pediatric gait.

3.1 The Foot

The foot is comprised of 26 different bones – 14 phalangeal bones (comprising the toes), 5 metatarsal bones (comprising the ball of the foot and the forefoot), and 7 tarsal bones (comprising the midfoot and hindfoot). A diagram of the human foot is shown in Figure 5.

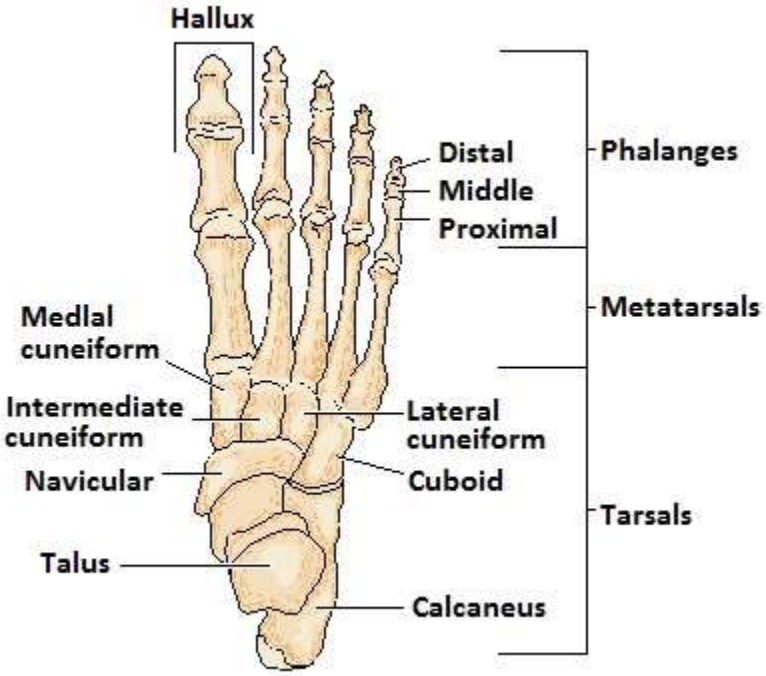

Figure 5. Diagram of the Foot [84]

Each of the joints in the foot fills a specific purpose. Some of those joints (such as the subtalar joint between the talus and the calcaneus) provide vertical support for the

tibia and allow for mild lateral movement for uneven ground [85]. While there is some movement out of the first and second metatarsal, the gross motion of the metatarsals and tarsals are effectively zero, and these are often modeled as being rigid links for simplicity. The metatarsal-phalangeal joint provides a significant rotation of the phalanges, and because of that, many foot models treat the phalanges as another rigid link. The metatarsal-phalangeal joint axis provides the major flexure of the foot during gait.

During gait, the foot traces a path in the sagittal plane. While there is some lateral movement during gait, the movement is relatively insignificant and varies between individuals. Thus, only the sagittal plane is measured when reviewing the each foot point's trajectory in this work. Three distinct points on the foot exist in the sagittal plane, which are helpful in defining the foot position: the heel (posterior location of the foot), the first metatarsal (location of the metatarsal-phalangeal joint axis) and the big toe (anterior location on the foot).

3.2 Stride Trajectory Influences

The gait stride trajectory differs between two individuals for many reasons. Differences in kinematics can occur based on varying force requirements in limbs and proprioceptive learning processes, among other factors. However, the effect of these influences on the trajectory of foot points during gait are not well-understood. Some studies have been conducted on factors like heel heights of females [86-90], but these studies don't focus specifically on gait trajectory.

Influences that may affect the measured foot point trajectories during gait:

- Shoe compliance (Sole material, metatarsal flexure resistance)

- Shoe dimensions (Sole height profile, length of shoe posterior and anterior to the metatarsal)
- Ground compliance (Rigid vs. soft)
- Clothing (Compliance, weight, cover)
- Foot dimensions (Length posterior to metatarsal, length anterior of metatarsal, height of ankle, foot width)
- Leg dimensions (Tibial length, femoral length, distance between hip joints)
- Joint nonlinearities (Knee rotation joint trajectory, hip vertical motion, ankle compression)
- Gender
- Limb Masses (Mass of toe, mass of foot, calf weight profile, thigh weight profile)
- Muscular strength (foot, ankle, calf, thigh, buttock, dorsal)
- Gait hysteresis
- Neurological factors (Perceived obstacles, balance, proprioception)
- Age
- Gait experience (Time since last gait injury, total amount of walking)

Compensating and studying each of these factors would be a monumental task. As such, this research will focus on methods of gathering and comparing data, which will hopefully establish a foundation for future research in these areas and their effect on foot point trajectories during gait.

3.3 Foot Tracking Calculations

When tracking foot data, vectors are collected relative to a fixed coordinate system. Often, the origin is a static location in the room that is arbitrarily chosen. Vectors showing the heel, metatarsal, and toe vectors and points, as well as the segmented model of the foot, are shown in Figure 6.

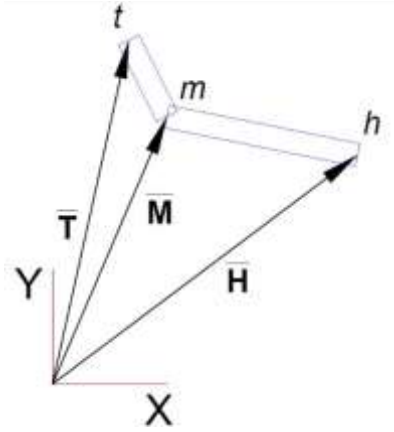

Figure 6. Toe, Metatarsal, and Heel Vectors and Points

Several inaccuracies exist in measuring the foot locations. The heel, metatarsal, and toe vectors (labeled in Figure 6 as $\bar{H}$, $\bar{M}$, and $\bar{T}$, respectively) are vectors measured from the arbitrary origin to the point on the heel, metatarsal, or toe. However, shifting of the skin, movement of the point relative to the body, and an inability to directly measure the bone of the participant prevents these points from precisely representing the skeletal motions.

Ideally, the Y axis of the arbitrary origin is aligned with the direction of gravity. However, a coordinate system rotation may be necessary. For the metatarsal data, the foot travels along a flat trajectory during the stance phase. This provides a good point of reference to create a representative ground line. The angle between the ground line and the X axis is the negative of the coordinate axis rotation angle δ.

In order to obtain the new position vectors in the shifted coordinate system X'-Y', the original vector must be multiplied by the rotation matrix *R* and, if desired, the origin can be shifted to a new location. This shift is represented by Equation 3-1.

$$\bar{V}' = \bar{\bar{R}} * (\bar{V} - \bar{C})$$

Equation 3-1. Origin Coordinate Shift

where $\bar{V}'$ is the rotated position vector (with the foot travelling flat along the X' axis during stance) and $\bar{V}$ is the original position vector of the point. The rotation matrix $R = \begin{bmatrix} \cos\delta & \sin\delta \\ -\sin\delta & \cos\delta \end{bmatrix}$ is used to shift the coordinates. The vector $\bar{C}$ is the vector from the old origin to the new origin using the unrotated coordinate system. It is important to use this shift for the toe, metatarsal, heel, and hip datasets.

Joints in the leg and foot have nearly identical angular paths during repeated normal gait. This means that the foot position traces roughly the same trajectory relative to the hip. Regardless of whether the data was collected from participants on a treadmill or overground walking, the metatarsal, toe, and heel position vectors need to be adjusted by the movement of the hip. The hip rises and falls during each stride due to the rotation of the hip bones about the base of the spine. Compensation for this motion does not provide consistent results. Thus, only the longitudinal travel of the hip is adjusted. The X'-position of the hip is forced to be zero so that the hip only travels along the Y' axis. The metatarsal, heel, and toe values must be adjusted accordingly. This is represented by Equation 3-2.

$$\{\bar{V}'\}_{Adj} = \{\bar{V}'\} - \{Hip_x', 0\}$$

Equation 3-2. Adjustment of Trajectories to Hip Position

where $\{\bar{V}'\}_{Adj}$ is the dataset of all vectors $\bar{V}'$ adjusted for the longitudinal movement of the hip. $\{Hip_x', 0\}$ is the dataset of all hip X positions. This equation can only be true if hip measurements were made simultaneously with the toe, metatarsal, and heel measurements.

After this adjustment, the metatarsal, heel, and toe trajectories show periodic trends, and can generate closed-loop trajectories starting and ending at mid-stance. It should be noted that due to periodic chaotic trends (noted in Section 2.3.1), the trajectory of each point on the foot may not form a closed loop when starting or ending from any other location in stride. Also, there may be some error in the datasets present where the loop is not closed and the two ends do not appear to connect. This error is due to measurement error, often because of the out-of-plane movement of the foot during gait where the footfall of one foot lies lateral to the footfall of the former step. This error is small relative to the height of the trajectories.

Each stride needs to be separated from the dataset so they can be analyzed individually. Each stride has a different path, and does not coincide with the previous path. Thus, the best location to measure the start and end of the stride is when the foot crosses the Y' axis while in stance, marking the midstance phase. The foot is completely flat, and remains flat and in contact with the ground for much of the stance phase. This means that all of the points on the foot undergo only longitudinal travel relative to the hip, making it easier to splice together the ends of the datasets. If any dataset is seen where one of these points is not in contact with the ground or only traveling longitudinally at the midstance location, it must be thrown out as it is not normal gait.

As discussed in Chapter 2, the normalized gait path from a child of at least age 7 is similar to the trajectory of the foot of an adult during normal gait. To normalize the trajectory, the trajectory of each point on the foot must be divided by the length of the hip travel during one stride, and can be determined by measuring the $\{Hip_x', 0\}$ vector along one full stride. A simpler method for normalizing uses the length of the metatarsal travel during one stride, measuring the foremost X' position to the rearmost X' position. Using the approximate stride length, all vectors $\bar{H}$, $\bar{M}$, and $\bar{T}$ are divided by this value. The result of this calculation is the normalized trajectory, as described in Equation 3-3.

$$\{\bar{V}'\}_{Norm} = \frac{\{\bar{V}'\}_{Adj}}{SL}$$

Equation 3-3. Normalized Trajectory Vector

where $\{\bar{V}'\}_{Norm}$ is the full dataset of normalized vectors, and SL is the stride length (either determined from the hip data or from the metatarsal data).

3.4 High-Speed Video Analysis

High-speed video footage was obtained of the author progressing through one stride. Markers were placed on the metatarsal, toe, heel, knee, and hip locations. A sequential image series of the stride phases is shown in Figure 7. Equation 3-1 was applied to the raw heel, toe, and metatarsal data collected from this video, and the corrected data are shown in Figure 8.

Pre-Swing

Initial Swing

Mid-Swing

Terminal Swing

Initial Contact

Loading Response

Mid-Stance

Terminal Stance

Figure 7. Phases of the Author's Gait

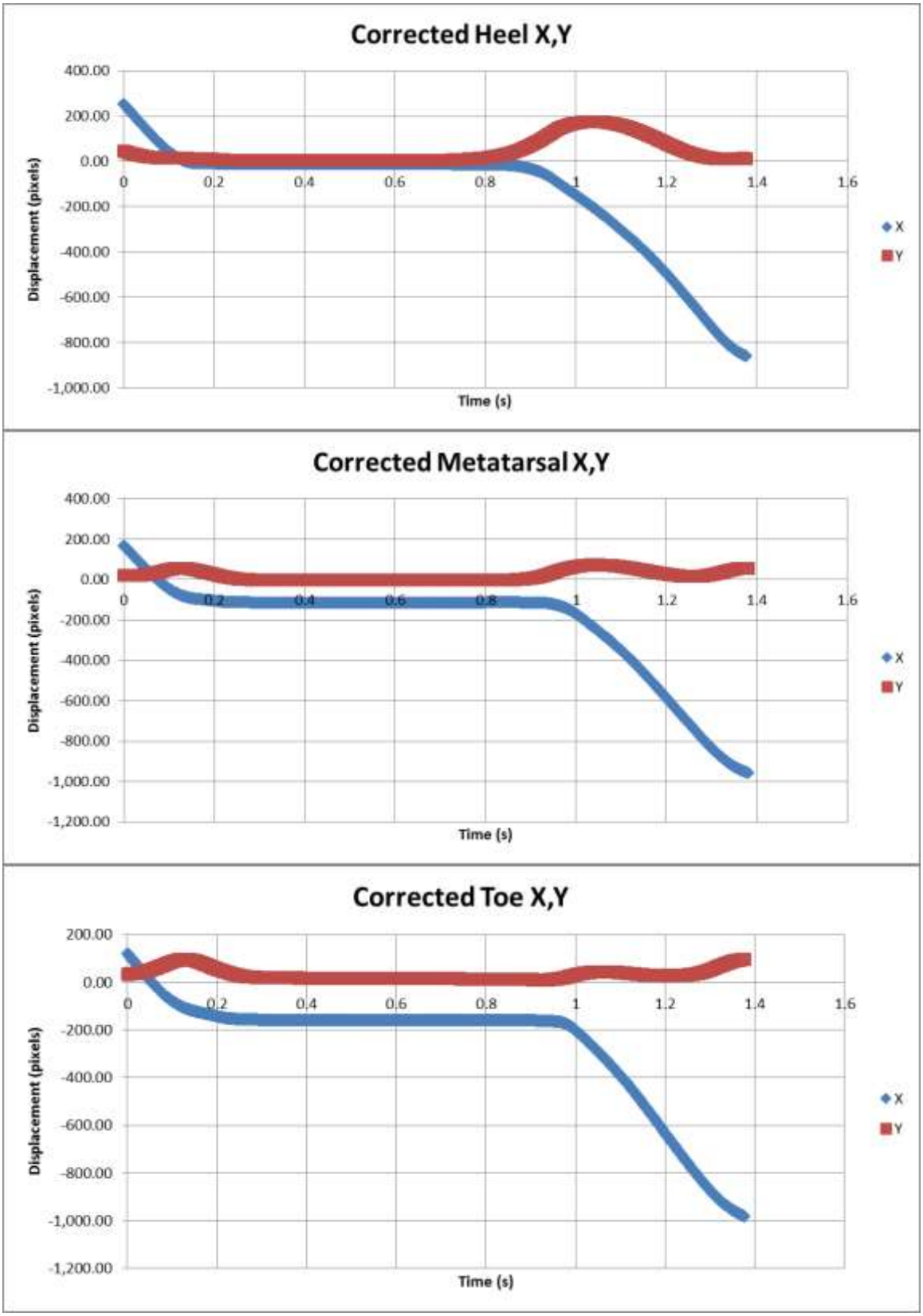

Figure 8. Author's Corrected Cartesian Data for Heel, Metatarsal, and Toe

Since the data obtained were from overground walking, the foot did not return to the same location after each step. The flat part of all of the curves between time 0.3 and 0.85 seconds showed that the foot was fully planted on the ground. Stance phase occurred between 0.1 and 0.95 seconds, while swing phase occurred between 0.0 and 0.1 seconds and 0.95 and 1.4 seconds.

Since this dataset is parametric, we can plot the X' data against the Y' data to see the path traced by the foot during the measurement. These paths are shown in Figure 9. While this plot provides a good representation of the foot path during the swing phase, it does not show the timing of the foot pattern very well. The foot spends most of the gait cycle in the stance phase. However, in Figure 9, the stance phase is represented by only a single point.

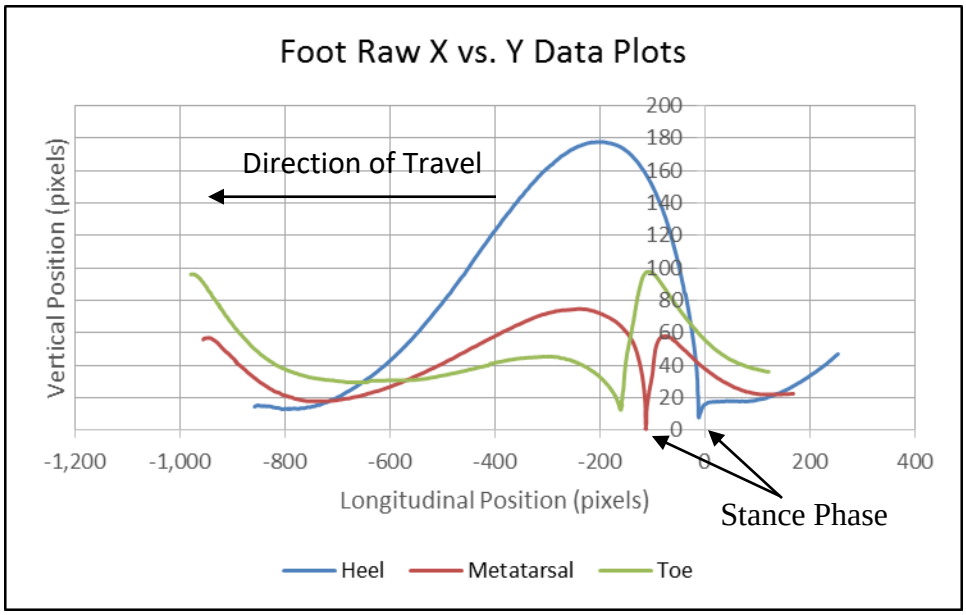

Figure 9. Author's Foot Point Trajectories Relative to Ground

Equations 3-2 and 3-3 were applied to the corrected data shown in Figure 8. The resulting normalized data showed a closed-loop trajectory for all three foot points, as seen in Figure 10. Note that the axes are given in normalized distance values.

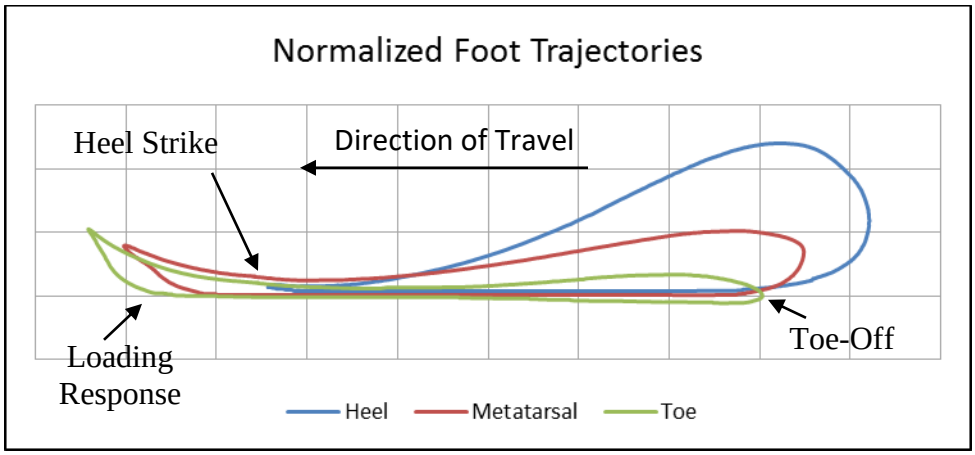

Figure 10. Author's Normalized Full Foot Trajectories

The heel shows the highest lift of all. This occurs when the heel lifts off of the ground during toe-off. The rest of the heel profile tapers off, and is barely above the ground at the forward position. The metatarsal shows a much flatter trajectory, and is characterized by two peaks: one corresponding to the toe-off location of the metatarsal and one corresponding to heel strike.

The toe experiences a relatively low profile, and mostly skims along the ground (with the exception of the heel strike position). However, the toe position dips below the X axis during the stance phase. This is a measurement error. During the loading response phase, the weight shifts from the rear of the foot to the front of the foot. When this happens, a significant amount of load is carried by the metatarsal. As the foot approaches the pre-swing phase, the toe is loaded. Many shoes have a curled up toe portion. During stance, this toe portion bends downward and contacts the ground. While the toe does not actually go below groundline, there is a minute amount of motion out of the toe during stance. The toe loading during flat-shoe stance is shown in Figure 11.

a). Foot during pre-stance b). Foot during terminal stance

Figure 11. Toe Vertical Movement During Stance

3.5 Winter's Data

In 1992, David Winter published a paper about his work in studying the gait trajectory of the foot during different types of gaits including casual walking and brisk walking [91]. Winter tracked points during normal walking across the floor, such as the hip, knee, ankle, heel, and metatarsal. Some of the data taken during this study were provided publicly. Raw X vs. Y data are shown in Figure 12.

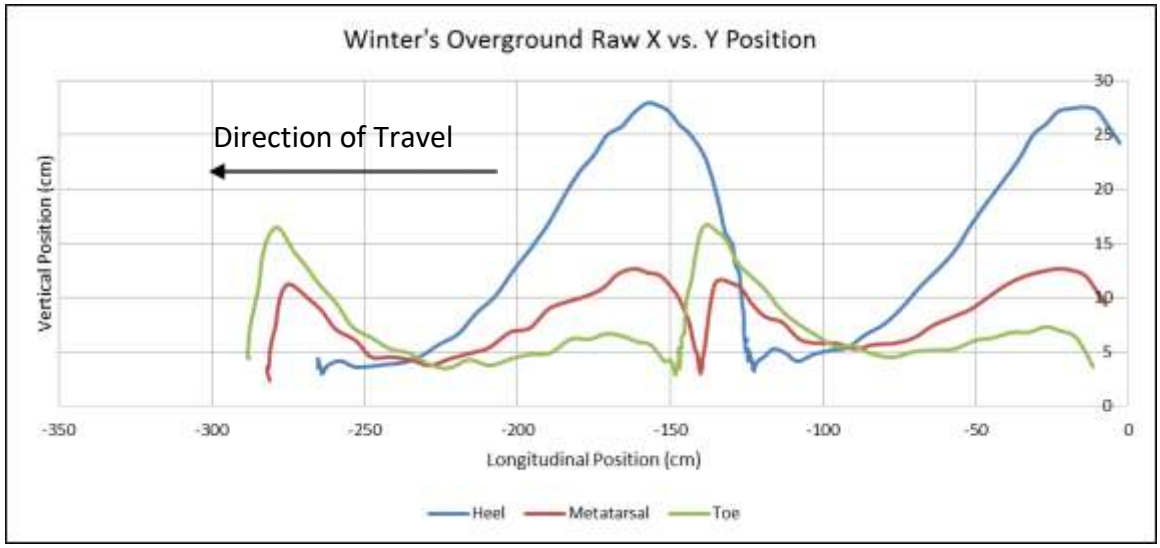

Figure 12. Winter's Raw Foot Point Trajectories

This dataset was not as smooth as the author's dataset, and also tracked fewer points. This explains some of the abnormal shape to the lines in Figure 12. The data were

calculated relative to the hip longitudinal motion and normalized, and the resulting data points are shown in Figure 13.

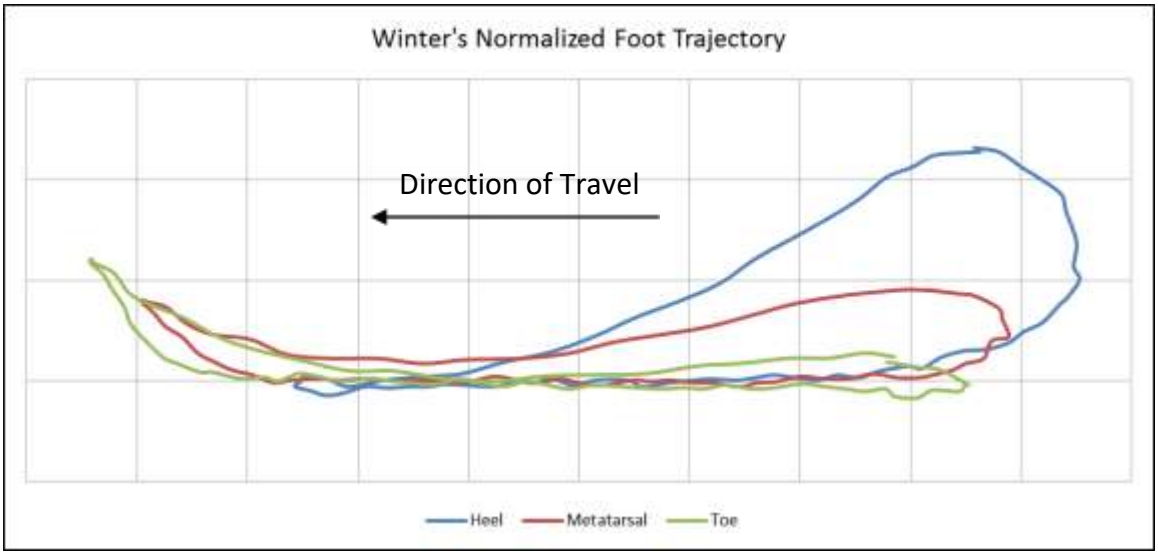

Figure 13. Winter's Normalized Full Foot Trajectories

The normalized full foot trajectories shown in Figure 13 are very similar to the full foot trajectories measured by the author in Figure 10. This implies that the data collection method, individual, and influencing factors were similar between the two cases.

3.6 Madonna Adult Treadmill Walking Data

A data set of 53 strides were collected using the motion sensing software at Madonna Rehabilitation Hospital in Lincoln, Nebraska. These data were collected from a middle-aged male adult at a rapid pace on a treadmill. However, to maintain anonymity, the subject's leg length, height, weight, foot size, and other parameters remain unknown.

When plotted together, the set of 53 strides showed a similar shape, although the size of each differed, and there were minor differences in stride length. However, the consistent shape of each stride showed promising results for analysis. The raw metatarsal,

heel, and toe data are shown in Figure 14. Because of the large number of strides included in this dataset, plotting raw parametric data against time is undesirable.

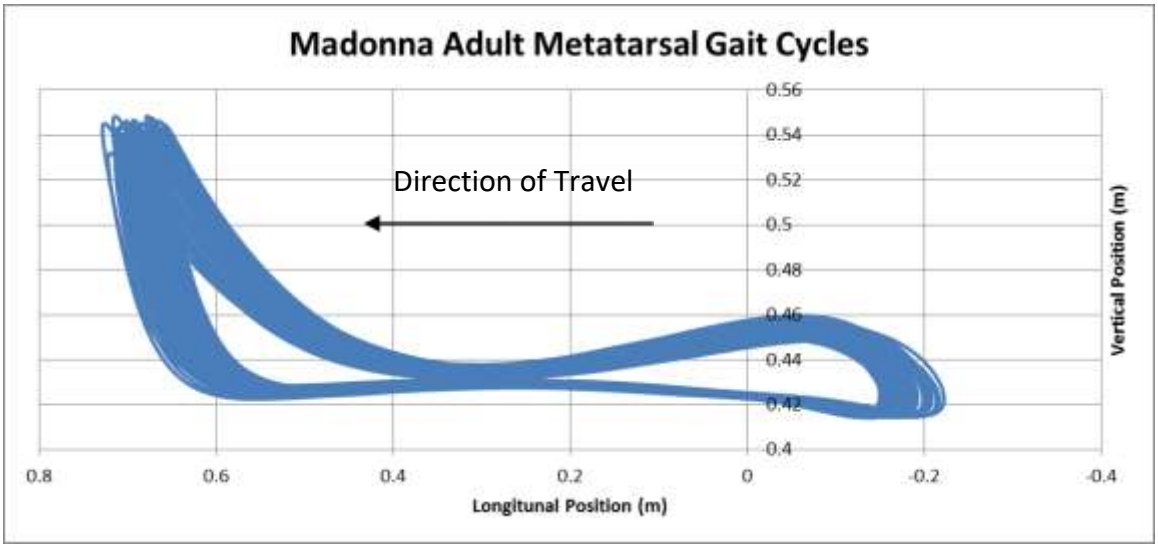

Figure 14. Madonna Adult Raw Treadmill Metatarsal X vs. Y Data

Unlike what was seen in previous datasets, the metatarsal data are not flat during the stance phase. Unfortunately, this makes measurement of the camera skew angle α difficult, and prevents rotating the dataset to the correct orientation due to a lack of a recognizable rotation point.

Analyzing 53 different strides would be time consuming and would not provide valuable feedback. Thus, to better compare each stride to each other and determine the representative stride for this dataset, five distinct points were pulled out of each dataset, as shown in Figure 15.

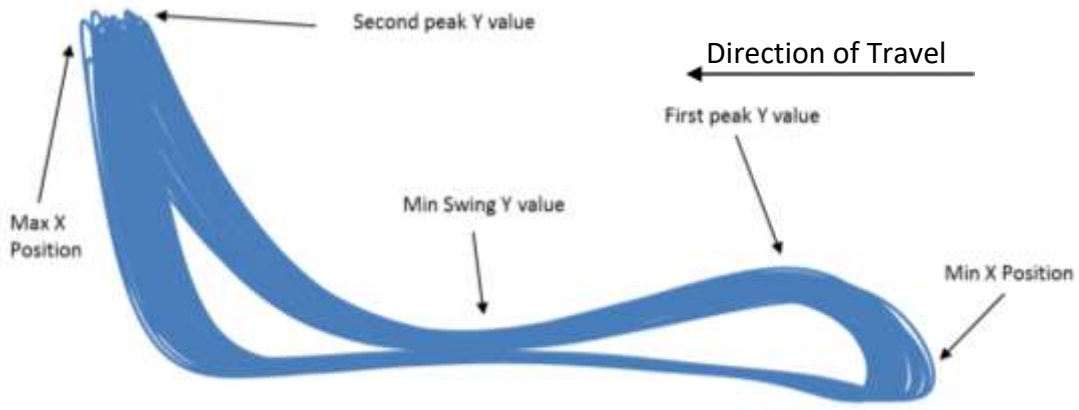

Figure 15. Points of Interest for Madonna Adult Metatarsal Dataset

The X, Y, and time position for each of the five points shown in Figure 15 were measured for the 53 strides. However, it was soon noted that the X values were very similar to each other, so they were removed from further analysis, and only the Y values and time values were considered.

The average vertical displacement and time values were determined from the dataset, along with standard deviations. One stride (#25) showed that it was closest to the average values in nearly every category, and this was chosen as the representative stride as a result. The summary of the analyzed dataset is shown in Table 3.

Table 3. Summary of Madonna Adult Stride Analysis

Stride No.	Average	Standard Dev.	Number within 5% of Average	Stride 25
Stride Length (m)	**0.435**	**0.006**	**53**	0.429
Stride Time (s)	**1.103**	**0.011**	**53**	1.1
Y at Min X (m)	**-0.008**	**0.001**	**16**	-0.00787
1st Peak Y (m)	**0.024**	**0.002**	**23**	0.0257
Min Clearance (m)	**0.005**	**0.002**	**5**	0.00534
2nd Peak Y (m)	**0.113**	**0.004**	**40**	0.113
Y at Max X (m)	**0.110**	**0.005**	**36**	0.110
Min X Time (s)	**0.343**	**0.005**	**53**	0.333
1st Peak Time (s)	**0.434**	**0.006**	**53**	0.425
Clearance Time (s)	**0.553**	**0.008**	**53**	0.550
2nd Peak Time (s)	**0.720**	**0.007**	**53**	0.717
Max X Time (s)	**0.734**	**0.008**	**53**	0.733

All of the peak times for every stride aligned nicely inside the 5% deviation criteria. However, the peak vertical displacement values varied greatly for each peak. This shows a strong cadence, but not necessarily a consistent path. This is consistent with research from Section 2.3.1. The selected path (stride #25) is shown in Figure 16.

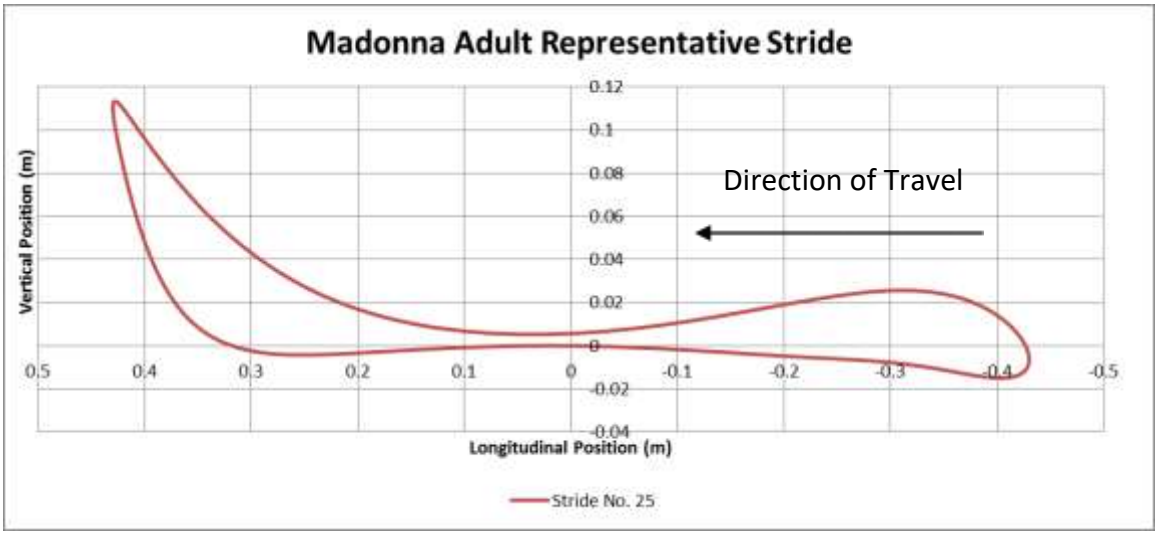

Figure 16. Representative Stride for the Madonna Adult

The stride shown in Figure 16 dips below the zero line, indicating that the metatarsal is dipping below the level line on the treadmill. This could be due to the movement of the track on the treadmill or due to the compression of the metatarsal during the stride. It is unknown whether or not this could be compensated to provide realistic, valuable data for analysis.

3.7 Madonna Child Treadmill Walking Data

A set of 45 pediatric strides were obtained from the Madonna Rehabilitation Hospital. It is unknown what the gender, height, weight, leg length, foot length, or other parameters of the child are due to the anonymity of this data. The strides were collected as a child performed normal gait on a treadmill. Unlike the adult data shown in Figure 14, the child's data showed a large range of stride lengths and times, consistent with research reviewed in Section 2.1.2. The raw Cartesian metatarsal trajectory data obtained from the child are shown in Figure 17.

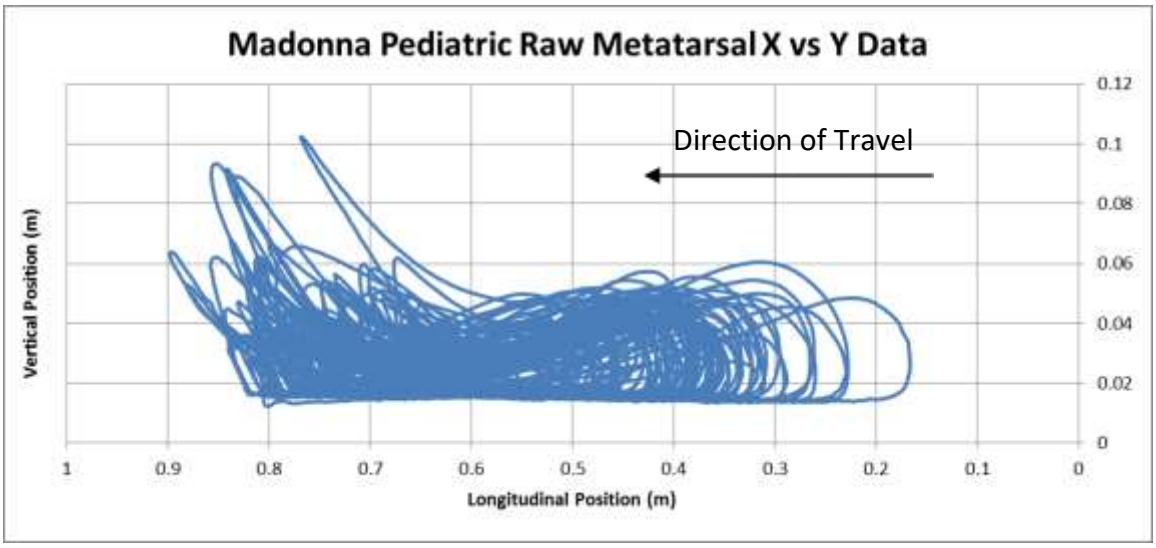

Figure 17. Madonna Pediatric Metatarsal Raw X vs. Y Data

As was done before, to analyze the 45 different strides, the data were separated into individual strides. The vertical position and the time of each stride were calculated. Vertical positions and timings were compared to the average. It was decided that a normalized sum of differences would be the best method of comparing the different datasets. To compute the sum of deviations, the following formula was used:

$$SoD = \sum abs(M_i - M_{ave})/SD_i$$

Equation 3-4. Summation of Deviations

Here, SoD is the sum of deviations, M_i is the dataset value of the particular measurement, M_{ave} is the average value of the particular measurement, and SD_i is the standard deviation of the particular measurement. Looking at the minimum unweighted SoD value showed that stride #44 was significantly closer to the average dataset than other strides. The summary of calculations is shown in Table 4. The pediatric representative stride is shown in Figure 18.

Table 4. Madonna Pediatric Metatarsal Data Summary

Stride No.	Average	Standard Dev.	% Passing	Stride 44
Stride Length (m)	0.1852002	0.033719996	20.00%	0.1825
Stride Time (s)	1.270555556	0.166785942	33.33%	1.3083
Y at Min X (m)	0.008674778	0.003168215	15.56%	0.0076
1st Peak Y (m)	0.026581133	0.006249864	15.56%	0.0273
Min Clearance (m)	0.008272711	0.004966347	6.67%	0.0098
2nd Peak Y (m)	0.028829378	0.014917044	6.67%	0.0230
Y at Max X (m)	0.026646378	0.015096217	6.67%	0.0214
Min X Time (s)	0.459814815	0.079975708	20.00%	0.4583
1st Peak Time (s)	0.537037037	0.089357194	22.22%	0.5500
Clearance Time (s)	0.674074074	0.098988288	26.67%	0.6833
2nd Peak Time (s)	0.809259259	0.120266726	22.22%	0.8250
Max X Time (s)	0.83037037	0.109710874	31.11%	0.8500
Sum of Deviations	9.054206734	5.712954158	NA	2.4043

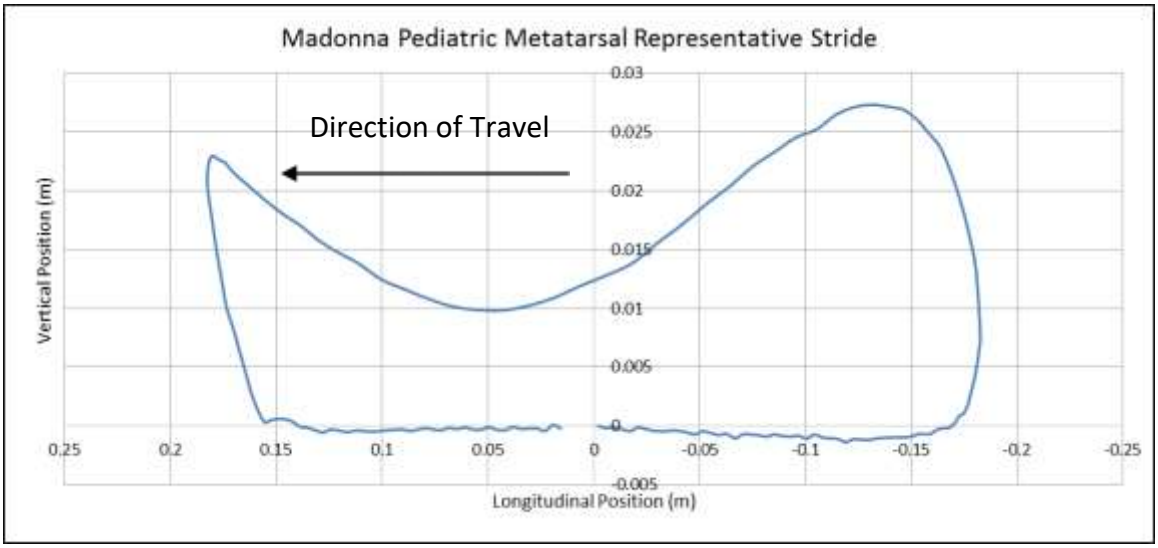

Figure 18. Madonna Pediatric Representative Metatarsal Stride Trajectory

3.8 Data Comparisons

The adult and pediatric data obtained from Madonna were normalized and compared against each other, along with the author's data and Winter's data. The comparison is shown in Figure 19.

s

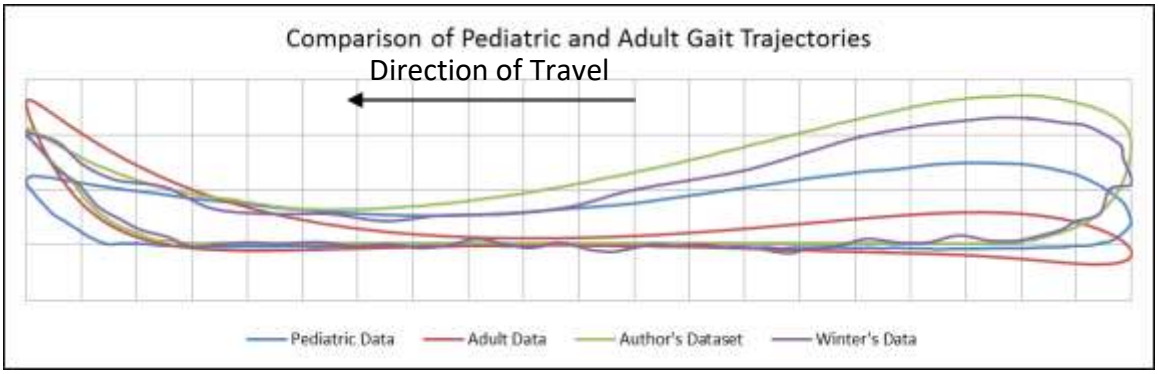

Figure 19. Comparison of Metatarsal Trajectories

The author shows the highest metatarsal trajectory of all of the datasets. This may be due to the size of the toe or shoe. Foot data was not collected during this study, and the purpose of the initial swing phase is to provide enough clearance for the toe to pass over the ground without tripping. The maximum clearance between toe and ground was 0.82 in., as shown in Figure 20.

Figure 20. Height of Toe at First Peak (Initial Swing)

The significance of comparing the two Madonna datasets is that both of them were collected by the same facility, and both used the same methods to collect data.

Unlike the adult dataset, the child's terminal stance does not pass below the groundline. This is because the weight of the child is likely insufficient to deflect the treadmill. Likely, as the foot is lifted off of the treadmill, the groundline returns to normal. This may be one factor to explain why the adult gait path is significantly lower than the child's at the initial swing phase. At the terminal swing phase, the adult's metatarsal trajectory is significantly higher than the gait path of the child. Due to different geometries of the feet, the adult's foot must travel to a higher angle in order to prevent the heel from contacting the ground too soon.

3.9 Selection of a Gait Path

Overground testing data showed significantly higher metatarsal movement than the treadmill data. While this may be attributed to differing positions of the metatarsal target, it may also be a factor of the method of testing, the foot geometries, and whether or not the tested individual was wearing shoes. For the purpose of this project, it is expected that the individual will be wearing shoes.

Selection of a single gait path was not possible using the calculated data from the three datasets. Each dataset was measured differently, using different technology, different foot positions, and different accuracies. A mathematical average of the three trajectories would provide a better gait path for evaluation, although three data points cannot be considered representative of the population. However, by developing a process to model and average gait data, it paves the pathway for future work to be conducted to determine averages based on influencing factors.

In order to obtain an average, each path had to be mathematically modeled. This process is detailed in the following chapter.

CHAPTER 4 – GAIT PATH MATHEMATICAL MODELING

The normalized gait loops from Chapter 3 provided the foundation for the mathematical modeling of the human gait cycle. Ideally, the mathematical model developed to describe the pediatric gait path would be applicable to all stride lengths, and have easily-changeable parameters to control for different stride trajectories. There are two approaches: one involves modeling data that is taken relative to the hip, and another involves modeling data relative to a motionless point on the ground.

4.1 Fourier Series Modeling of Periodic Gait

When the data are measured relative to the hip, the trajectory of each point on the foot forms a closed-loop, such as the trajectory shown in Figure 10. Modeling a closed loop as a parametric function could be performed in either Cartesian or polar coordinates. The Cartesian parametrization of the pediatric metatarsal trajectory is shown in Figure 21. Note that a negative X position value corresponds to having the foot move towards the rear. The Y position is measured relative to the ground.

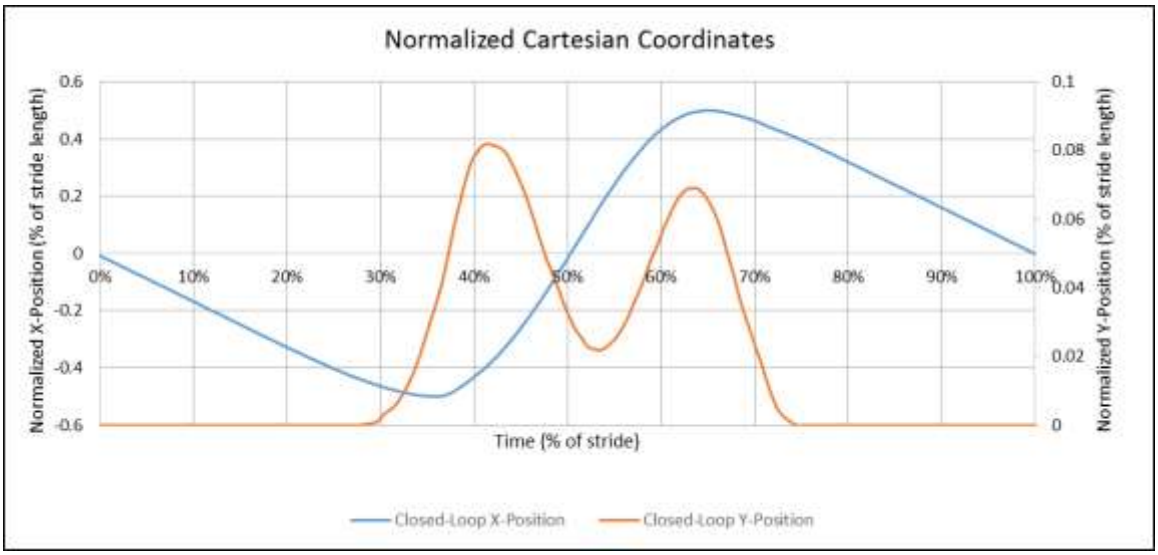

Figure 21. Cartesian Parametrization of Normalized Pediatric Metatarsal Trajectory

The Cartesian parametrization shows a periodic function for the X location that appears to be generally sinusoidal. This is easily modeled as a sum of sinusoids using a Fourier series. If $f(t)$ is the function giving the X coordinate, the Fourier series is given in Equation 4-1.

$$f(t) = \sum_{m=0}^{\infty} a_m \cos\left(\frac{2\pi m t}{T}\right) + \sum_{n=1}^{\infty} b_n \sin\left(\frac{2\pi n t}{T}\right)$$

Equation 4-1. Fourier Series Equation

where *T* is the period, and a_m and b_n are constants determined by the shape of the function. Since this is normalized, we use normalized time units $\tau = t/T$. This changes Equation 4-1 into Equation 4-2.

$$f(t) = \sum_{m=0}^{\infty} a_m \cos(2\pi m \tau) + \sum_{n=1}^{\infty} b_n \sin(2\pi n \tau)$$

Equation 4-2. Normalized Fourier Series Equation

The first term of the infinite series occurs when *m*=0 and is given by a_0. The first term is a constant, and constitutes the average of the equation. The expression for a_0 is given in Equation 4-3.

$$a_0 = \frac{1}{T}\int_0^1 f(\tau) d\tau$$

Equation 4-3. First Term in Fourier Infinite Series

To determine the values of all a_m and b_n to define this function, Equation 4-4 is applied.

$$a_m = \frac{2}{T}\int_0^1 f(\tau)\sin(2\pi m\tau)\,d\tau$$
$$b_n = \frac{2}{T}\int_0^1 f(\tau)\sin(2\pi n\tau)\,d\tau$$

Equation 4-4. Concurrent Terms in Fourier Infinite Series

The terms are normalized through the period. The resulting equation will be scalable by the period to attain the correct stride timing.

The results of Equation 4-4 can be placed into Equation 4-1 to create the full model. The resulting equation for the mathematical model of any foot point trajectory is given by Equation 4-5.

$$X(t) = \frac{L}{T}\sum_{m=0}^{\infty} a_{m,x}\cos(2\pi m\tau) + \sum_{n=1}^{\infty} b_{n,x}\sin(2\pi n\tau)$$
$$Y(t) = \frac{L}{T}\sum_{m=0}^{\infty} a_{m,y}\cos(2\pi m\tau) + \sum_{n=1}^{\infty} b_{n,y}\sin(2\pi n\tau)$$

Equation 4-5. Cartesian Parametrization Using Fourier Series

where τ is the normalized time value equal to the percent of stride time, T is the stride time, and L is the stride length. Note that while perfectly accurate results will be obtained when $m=\infty$ and $n=\infty$, Fourier transforms tend to converge rapidly, and only a few orders of calculation are needed to produce close approximations.

4.2 Metatarsal Trajectory Modeling

4.2.1 Cartesian Pediatric Gait Modeling

The pediatric gait data shown in Figure 21 were put into Equation 4-5, and the constants were determined from Equation 4-4. To determine the goodness of fit, the R^2 value (also known as the Coefficient of Determination) was calculated for each Fourier order. To calculate the R^2 value, the following equation is applied:

$$R^2 = 1 - \frac{\sum_i (y_i - f_i)^2}{\sum_i (y_i - \bar{y})^2}$$

Equation 4-6. R^2 Calculation for Fourier Regression

where y_i is the individual, measured data points, f_i is the Fourier calculated data points corresponding to the times of the measured data points, and $\bar{y}$ is the average of all y_i measured data points. Another way of viewing Equation 4-6 is the sum of squared error measurements divided by the total sum of squares, which is correlated with the overall data variance.

The Cartesian pediatric data series converged quickly, and each parametrized value had an R^2 value that approached 1 with increasing order of the Fourier series. It was noted that the R^2 value was over 99.0% for two orders of the Fourier X series and six orders of the Fourier Y series (o_x=2 and o_y=6), and further orders of X and Y would only improve the fit of the model. The resulting constants are shown in Table 5.

Table 5. Fourier Series Constants for Pediatric Cartesian Parametrization

Pediatric a_m and b_n Constants

	X-Coordinate		R^2		Y-Coordinate		R^2
m,n	a	b			a	b	
0	0.00390				0.01885		
1	-0.00149	0.44097	0.90534		-0.02920	-0.00245	0.61266
2	0.00345	-0.13606	0.99158		0.01023	0.00021	0.68802
3	-0.00359	0.04140	0.99963		0.00597	0.00571	0.73625
4	0.00255	-0.00695	0.99988		-0.01120	-0.00981	0.89382
5	-0.00104	-0.00201	0.99990		0.00750	0.00845	0.98476
6	0.00094	0.00363	0.99997		-0.00211	-0.00345	0.99644
7	-0.00053	-0.00120	0.99998		-0.00040	-0.00069	0.99690
8	0.00069	-0.00027	0.99998		0.00041	0.00173	0.99914

The resulting X and Y coordinates were plotted to determine visual closeness to the original trajectories. The coordinates are plotted against normalized time and against each other in Figures 22 and 23, respectively. The coordinates are plotted with Fourier

series orders o_x=2 and o_y=6. Note: further orders would improve the fit of the equations. However, fewer Fourier series orders were used to show how well the curve was matched at the R^2 = 99.0% value. Full datasets from the pediatric, author, and Winter are shown in Appendix A.

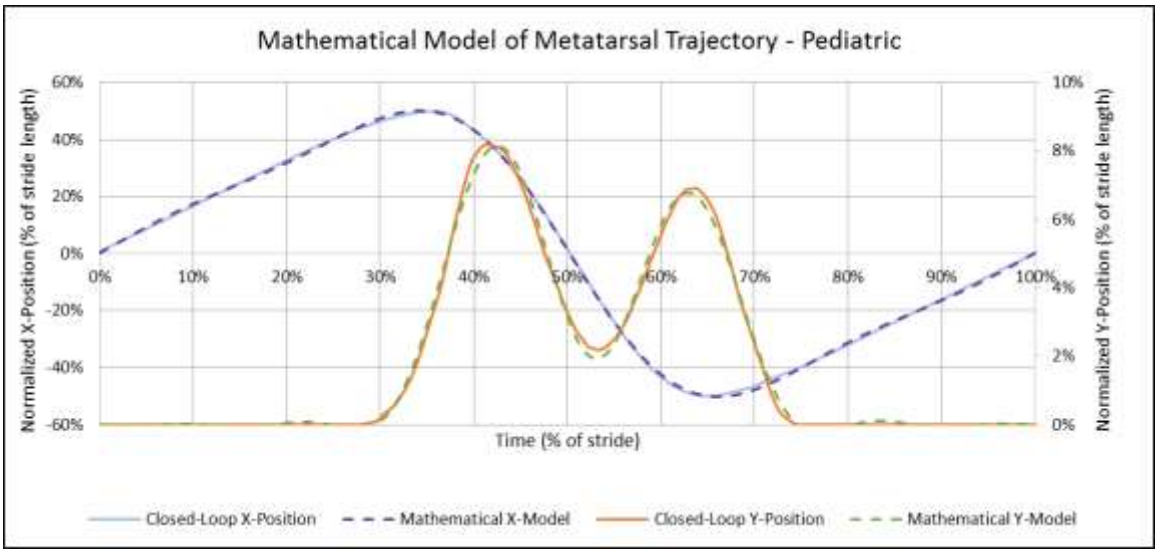

Figure 22. Mathematical Model of Normalized Cartesian Gait Coordinates (o_x=2,o_y=6)

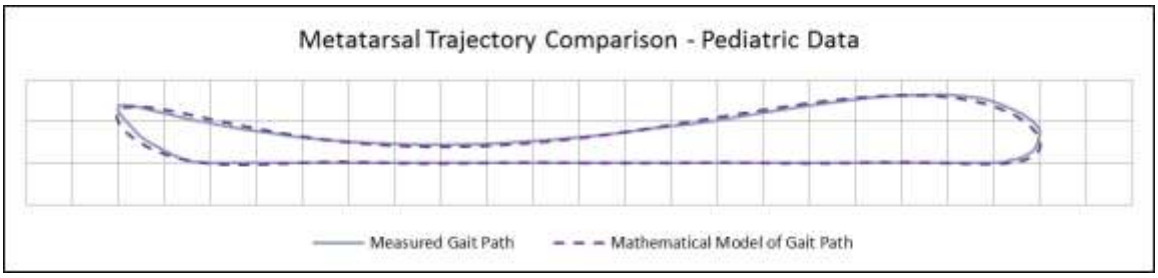

Figure 23. Closed-Loop Trajectory of Cartesian Mathematical Model (o_x=2,o_y=6)

4.2.2 Polar Parametrization of Pediatric Data

The Cartesian coordinate modeling of the pediatric data proved successful, and the convergence was good for lower orders of Fourier series. However, polar parametrization of the gait path was conducted to compare to the Cartesian parametrization.

For the polar parametrization, the location of the origin is very important. Placing the origin changes the distance between the origin and the points on the curve, which can create unique trajectories and profiles. Five points were identified as unique origin locations. These five points are shown in Figure 24. Their coordinates, in units normalized by the stride length, are shown as well.

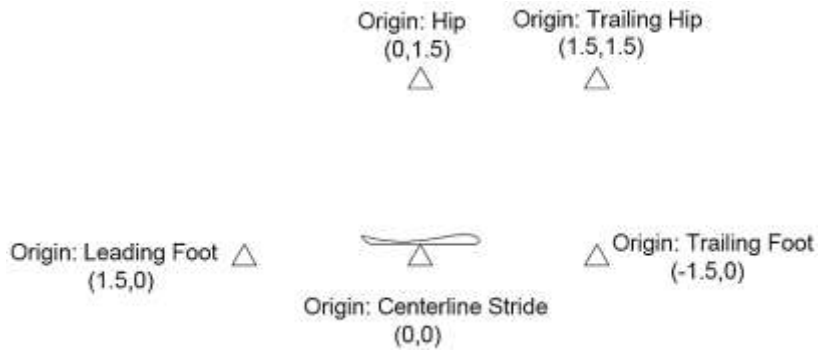

Figure 24. Origin Locations for Analyzing Closed-Loop Polar Parametric Equations

The closed-loop trajectory was used to generate polar parametrizations at each origin location. The resulting plots are shown in Figures 25 through 29.

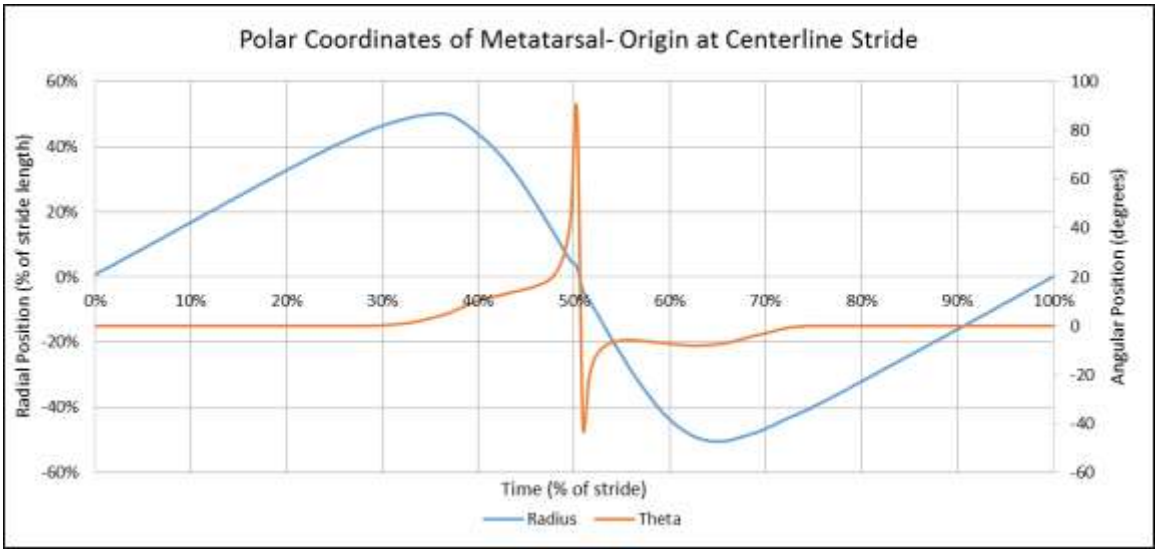

Figure 25. Polar Parametrization of Metatarsal: Origin at Centerline Stride

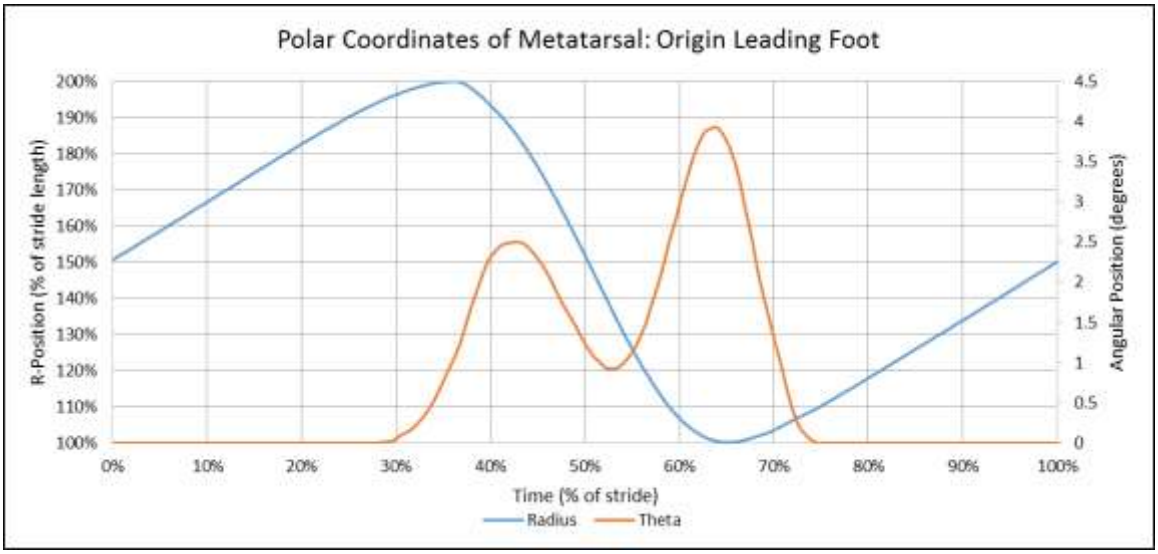

Figure 26. Polar Parametrization of Metatarsal: Origin Leading Foot

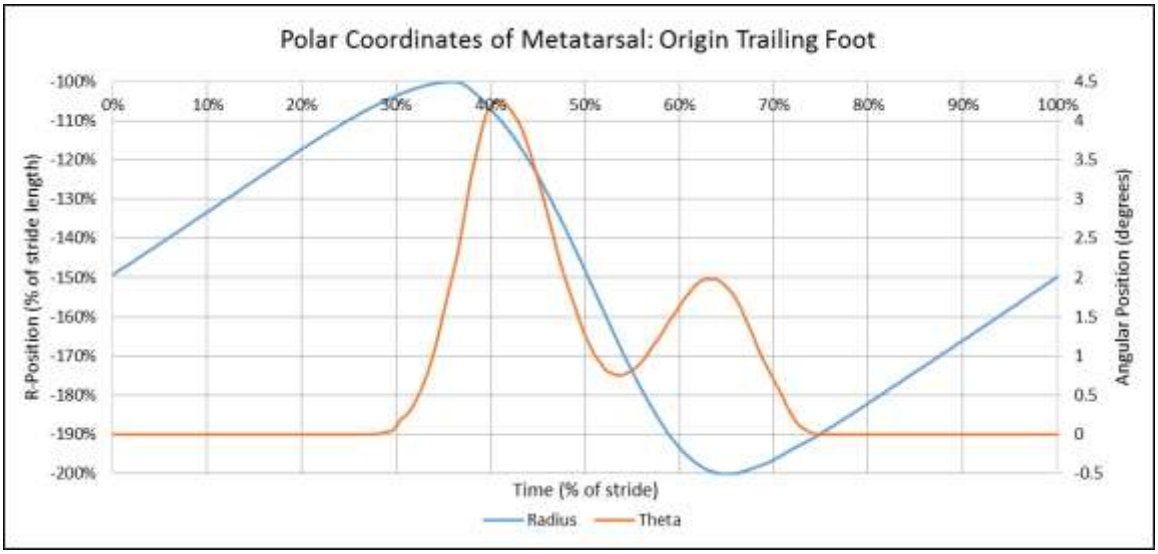

Figure 27. Polar Parametrization of Metatarsal: Origin Trailing Foot

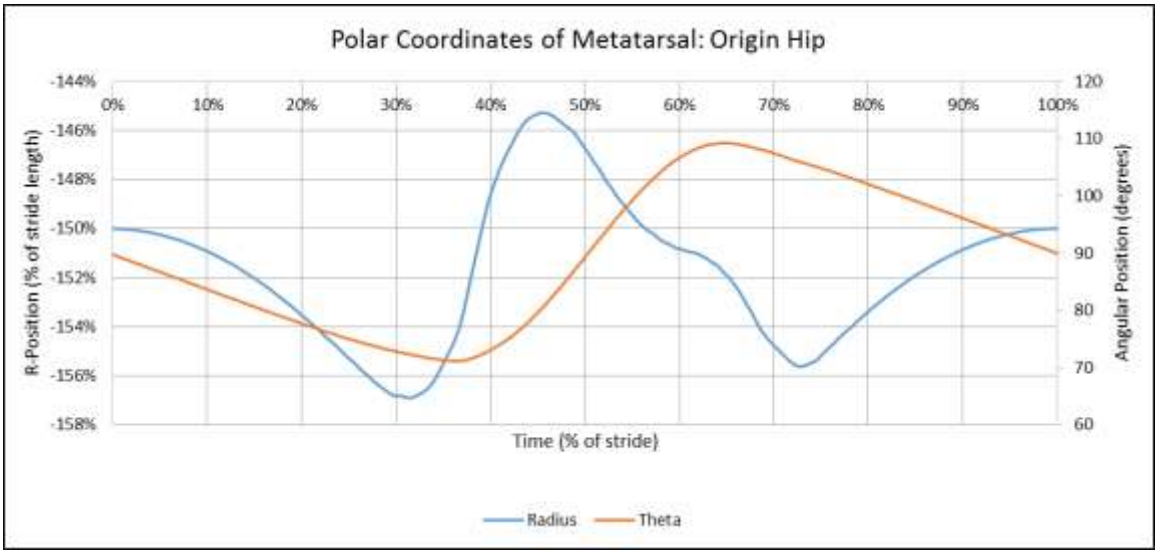

Figure 28. Polar Parametrization of Metatarsal: Origin at Hip

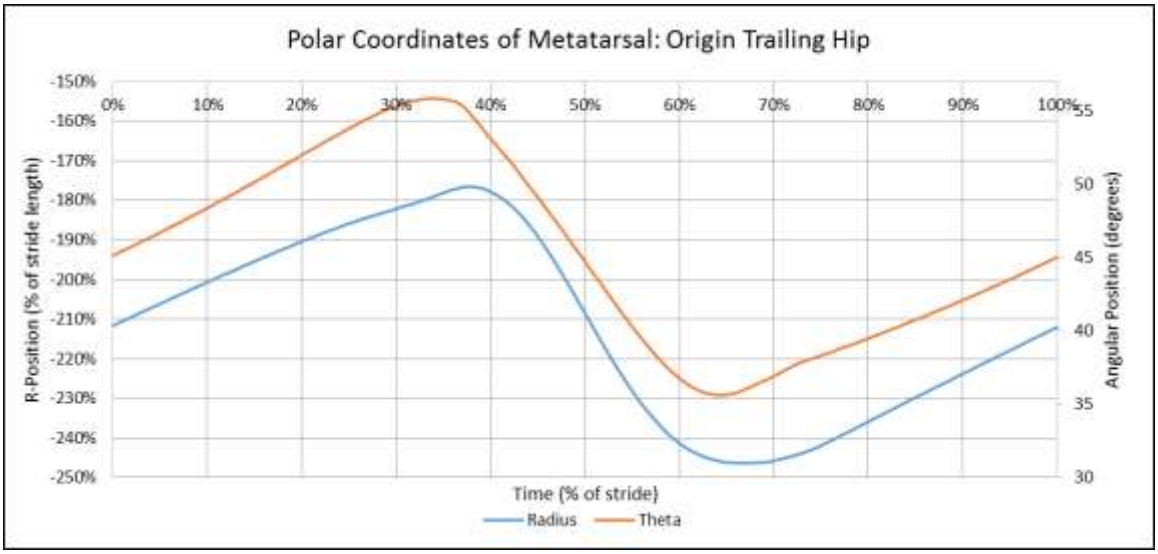

Figure 29. Polar Parametrization of Metatarsal: Origin Trailing Hip

Each of the trajectories shows a different profile curve. When the origin is located at the centerline of the midstance stride (Figure 25), the angular position rapidly travels toward 90 degrees as the profile loops back over the origin. This causes a small shift in the otherwise smooth radial curve. The radial and angular displacements of the metatarsal during stride are very similar when viewed from the leading and trailing foot positions.

The major difference is that the angular position is reversed, and there are small variances in curve shapes.

The movement relative to the hip is more complicated. While the angular displacement is smooth and shows gradual, gentle shift in angular position, the radial position appears to have two distinct peaks with a trough in between. This dataset was not adjusted for the vertical movement of the hip. According to Fang and Hunt, the toe trajectory relative to the hip follows a near-circular path [92]. Fang and Hunt adjusted the toe trajectories according to the vertical movement of the hip during gait. The resulting circular trajectories of the toe are shown in Figure 30.

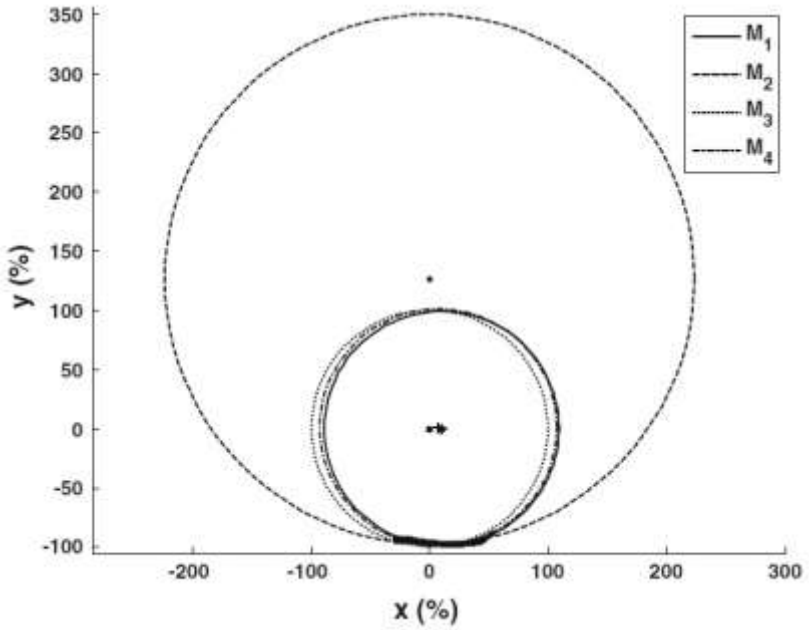

Figure 30. Circular Toe Trajectory Modeling [92]

Fang and Hunt continued the circular toe trajectory modeling with 24 subjects, and showed that the circular model was a simple approximation based on hip height, although the results were fairly diverse [93]. Further results for circular modeling of the toe trajectory relative to the hip are shown in Figure 31. In each case, the dotted, circular-shaped line was generated by the height of the hip.

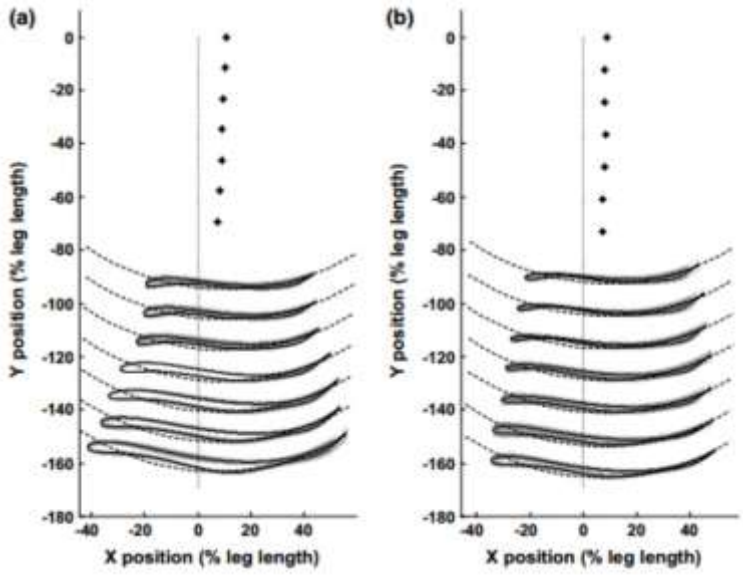

Figure 31. Multi-Subject Circular Toe Trajectory Modeling [93]

While hip data were not provided for the datasets analyzed in this chapter, it is believed based on Figure 30 that adjustment for hip movement would result in a flat path for Figure 28 and only one trough without any ridges. This would make the hip an ideal location for placing the origin and constructing a mathematical model of the heel, metatarsal, and toe trajectories. However, without measuring hip movement, Figure 28 is not smooth.

Figure 29 shows two periodic, smooth functions describing the radial and angular displacement. Unlike the rest of the plots, Figure 29 has only two distinct peaks per line, and both look very easy to model. As a result, Equation 4-5 can be rewritten to account for radial and angular data. Note: The data was normalized using longitudinal stride length, which is an easily-measured variable.

$$R(t) = \frac{L}{T}\sum_{m=0}^{\infty} a_{m,x}\cos(2\pi m\tau) + \sum_{n=1}^{\infty} b_{n,x}\sin(2\pi n\tau)$$
$$\theta(t) = \frac{L}{T}\sum_{m=0}^{\infty} a_{m,y}\cos(2\pi m\tau) + \sum_{n=1}^{\infty} b_{n,y}\sin(2\pi n\tau)$$

Equation 4-7. Radial Parametrization Using Fourier Series

The constants a_m and b_n were calculated for both *R* and θ values. The resulting constants are shown in Table 6. Note that the R^2 values decrease with increasing orders after the third order of both X and Y. While the calculations were extensively checked, the cause of this abnormality was not determined.

Table 6. Fourier Series Constants for Pediatric Polar Parametrization

Pediatric Polar a_m and b_n Constants

	X-Coordinate		R^2		Y-Coordinate		R^2
m,n	a	b			a	b	
0	-2.13136				45.68394		
1	-0.04022	0.30912	0.88457		0.66166	8.57807	0.89497
2	-0.00675	-0.09707	0.96962		-0.07062	-2.66329	0.98286
3	-0.03224	0.03515	0.97445		0.75052	0.68608	0.98487
4	-0.02880	-0.01261	0.96881		0.62797	0.06254	0.98070
5	-0.02260	0.00432	0.96195		0.46719	-0.20970	0.97711
6	-0.02769	0.00060	0.95449		0.60927	0.14438	0.97293
7	-0.02632	-0.00162	0.94692		0.54118	-0.01411	0.96846
8	-0.02589	0.00114	0.93920		0.57838	-0.03921	0.96385

Unlike the Cartesian parametrization and model, the polar parametrization did not produce an acceptable curve. Using o_x=3 and o_y=3 (the closest fit according to R^2 analysis with the Fourier analysis), the radial and angular mathematical positions were calculated. The resulting curves are shown in Figure 32.

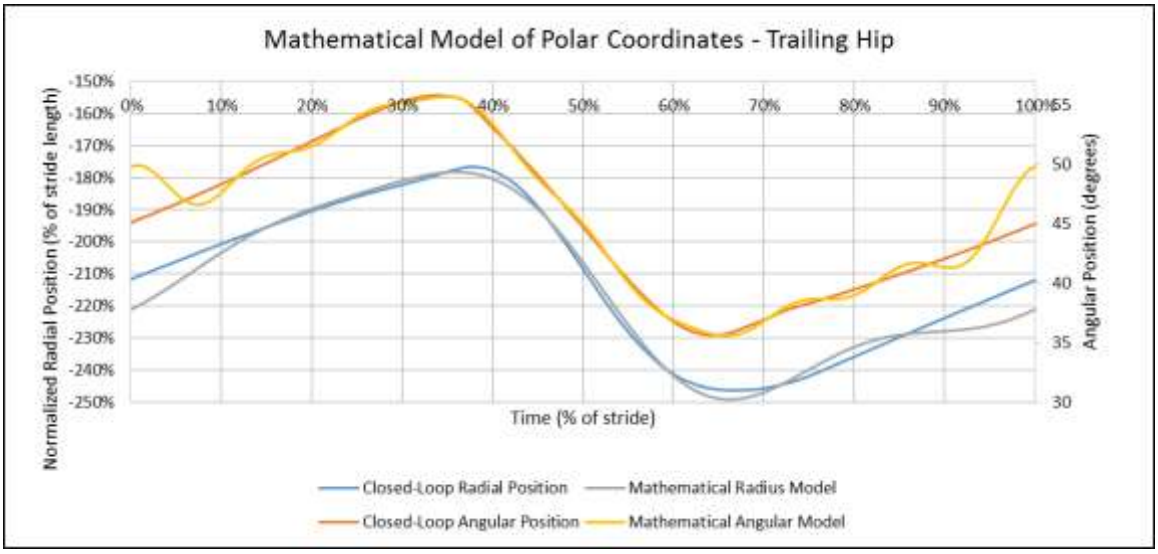

Figure 32. Mathematical Approximation of Polar Parametrization (o_x=2,o_y=6)

The mathematical model of the polar parametrization did not come out properly, despite following the Fourier transform process. While higher-order Fourier series terms usually cause an increase in trajectory accuracy, the R^2 accuracy value dropped with increasing order of Fourier series. One explanation as to why the Fourier series had difficulty modeling this curve is that the actual curve approximates near-straight lines. Fourier series struggle to model straight lines, and require higher order numbers, possibly significantly higher frequency terms. While further work may more closely approximate this curve, it was determined that closed-loop modeling was best conducted using Cartesian coordinates.

4.2.3 Fourier Series Modeling of Author's Data

Equation 4-5 was applied to the Author's data shown in Figure 10. The constants determined from Equation 4-4 are shown in Table 7. Similar to what was seen in the pediatric dataset, the series appeared to converge nicely, and had above a 99.0% R^2 value with o_x=2 and o_y=6. Full Cartesian parametric data is shown in Appendix A.

Table 7. Fourier Series Constants for Cartesian Modeling of Author's Data

Author's a_m and b_n Constants							
	X-Coordinate		R^2		Y-Coordinate		R^2
m,n	a	b			a	b	
0	0.00128				0.03628		
1	-0.00084	0.43503	0.93211		-0.04992	0.00587	0.63050
2	0.00102	-0.11515	0.99742		0.00469	-0.01255	0.67530
3	-0.00414	0.01565	0.99871		0.02245	0.01583	0.86325
4	0.00684	0.00999	0.99943		-0.01789	-0.01199	0.97894
5	-0.00545	-0.00753	0.99986		0.00113	0.00427	0.98382
6	0.00132	0.00134	0.99988		0.00661	0.00076	0.99485
7	0.00190	0.00246	0.99992		-0.00372	-0.00128	0.99872
8	-0.00240	-0.00226	0.99998		-0.00055	0.00037	0.99883

4.2.4 Fourier Series Modeling of Winter's Data

Equation 4-5 was applied to Winter's data shown in Figure 13 [91]. The constants determined from Equation 4-4 are shown in Table 8. Similar to what was seen in the pediatric dataset, the series converged nicely with an R^2 value of 99.0% or higher at o_x=2 and o_y=6. Full Cartesian parametric data are shown in Appendix A.

Table 8. Fourier Series Constants for Cartesian Parametrization of Winter's Data

Winter's a_m and b_n Constants							
	X-Coordinate		R^2		Y-Coordinate		R^2
m,n	a	b			a	b	
0	0.00055				0.03505		
1	-0.00711	0.44439	0.95824		-0.04216	0.00115	0.58105
2	0.00426	-0.09081	0.99836		-0.00722	-0.01001	0.62845
3	-0.00304	0.00772	0.99870		0.02340	0.01643	0.89298
4	0.00425	0.01054	0.99932		-0.01039	-0.01303	0.98326
5	0.00080	-0.00195	0.99935		-0.00266	0.00141	0.98595
6	-0.00015	0.00074	0.99936		0.00366	0.00317	0.99409
7	0.00044	0.00292	0.99940		0.00057	-0.00081	0.99442
8	-0.00233	0.00074	0.99940		-0.00171	-0.00003	0.99524

4.2.5 Comparison of Mathematical Models

The data contained in Tables 5, 7, and 8 were compared to each other. The a_m and b_n constants for both the X and Y coordinates are shown in Figure 33.

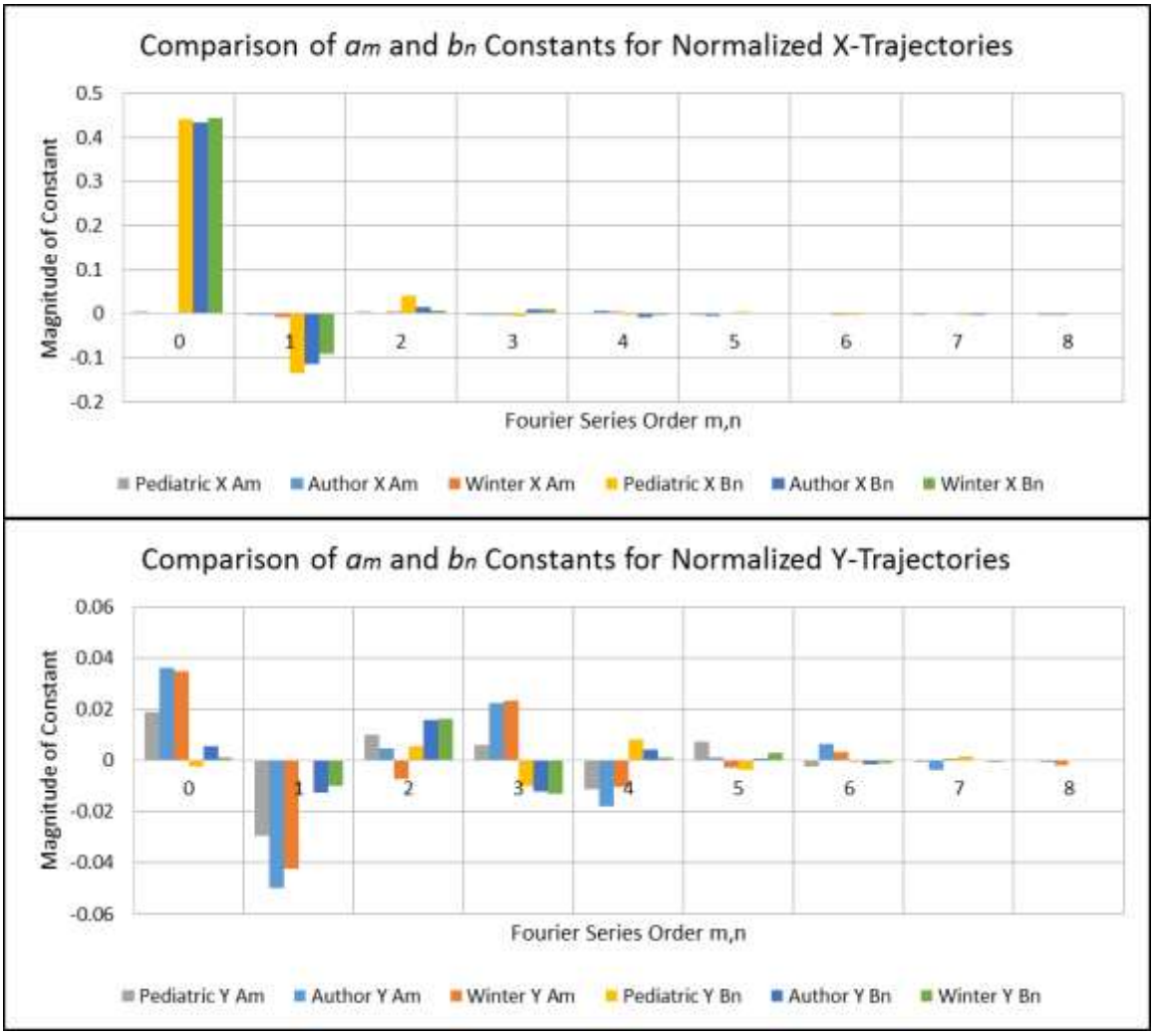

Figure 33. Comparison of Fourier Constants for X and Y Trajectory Coordinates

The a_m and b_n constants showed significant similarity at each Fourier series order, specifically between the author's dataset and Winter's dataset. Peak values at each location indicated not only similarity in gait path timing between the datasets, but also similarity in trajectory shape.

An average was taken of the pediatric, author's and Winter's dataset Fourier series constants. Using these new constants and Equation 4-5, a new trajectory was developed. The Fourier series constants are shown in Table 9. The resulting parametric coordinates are shown in Figure 34, and the resulting traced trajectory is given by Figure 35. Unlike previous Fourier series constants, the error in these was unmeasurable. Thus, order values of o_x=8 and o_y=8 were used to improve smoothness. Full Cartesian parametric data is shown in Appendix A.

Table 9. Fourier Series Average Metatarsal a_m and b_n Constants

Average Metatarsal Am and Bn Constants

	X-Coordinate		Y-Coordinate	
m,n	a	b	a	b
0	0.001952		0.030684	
1	-0.00321	0.449314	-0.04127	0.001555
2	0.002967	-0.11639	0.00262	-0.0076
3	-0.00367	0.022039	0.017633	0.01292
4	0.004643	0.004623	-0.01344	-0.01185
5	-0.00193	-0.00391	0.002033	0.004808
6	0.000715	0.001944	0.002778	0.000164
7	0.000618	0.001426	-0.00121	-0.00095
8	-0.00138	-0.00061	-0.00063	0.000702

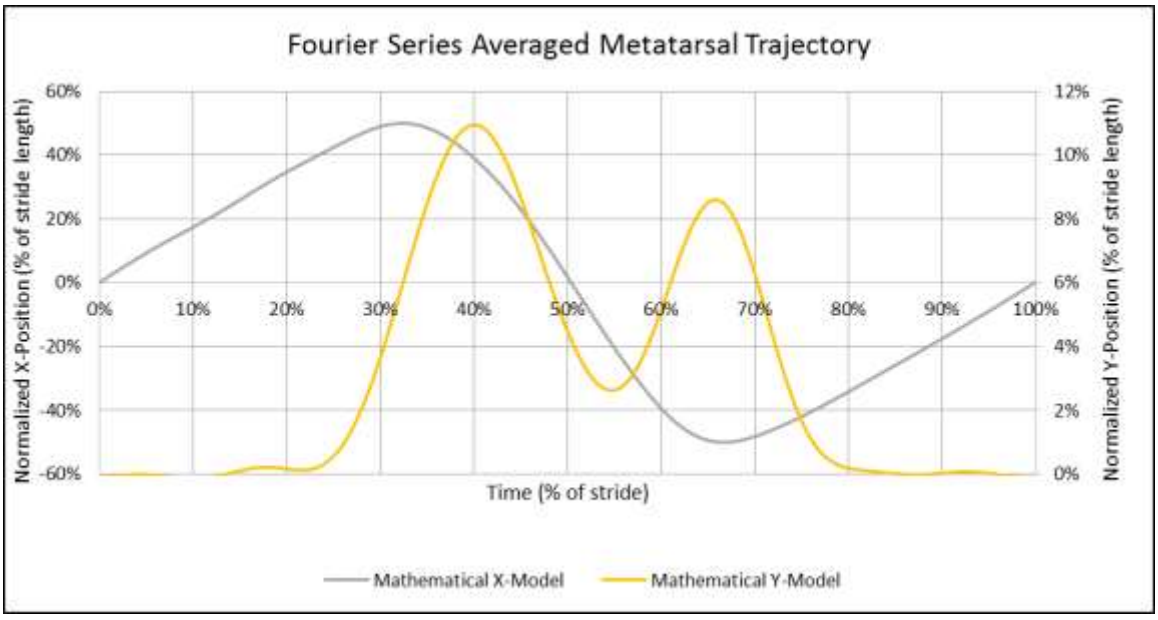

Figure 34. Fourier Series Average Metatarsal Trajectory Parametrization (o_x=8,o_y=8)

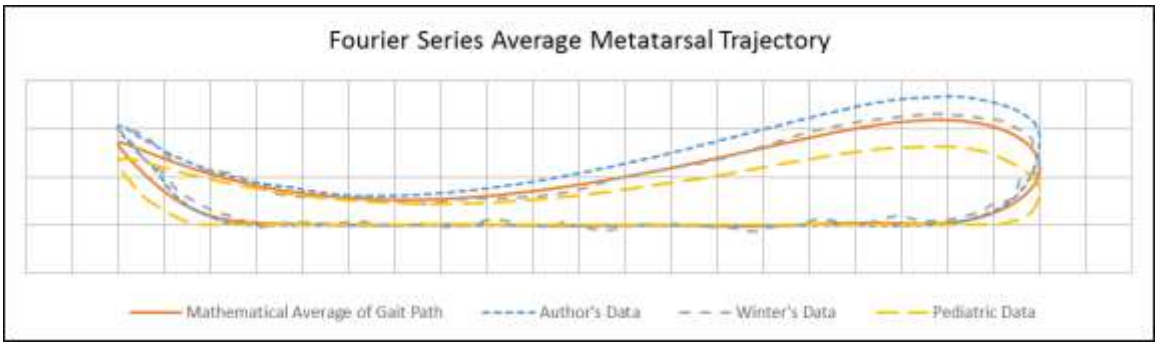

Figure 35. Fourier Series Average Metatarsal Trajectory (o_x=8,o_y=8)

The average curve showed very high similarities with all three curves, and the timing curves showed similarities with all three curves as well. Ideally, more Fourier series terms would be included in the average. However, given the data present, it was decided that this averaged model of the three datasets would be used as the "ideal" metatarsal trajectory path to model for the gait machine.

4.3 Heel Profile

A Fourier analysis was conducted on the heel trajectory of each of the three datasets. Similar to the metatarsal analysis, the heel profiles were calculated to 8 orders of

the Fourier series. For each of these three data sets, it was discovered that the Fourier series converged very quickly, reaching R^2 values of 99.0% or greater within three orders. As such, plots were made of each of the profiles using $o_x=2$ and $o_y=3$ to show convergence. The results of the pediatric, author's dataset, and Winter's dataset Fourier analysis of the heel data are shown in Figures 36 through 38. Note that despite the high convergence, the mathematical model and full heel trajectories were fairly different. Part of this is due to the low order count that was plotted. Part of this is due to the larger data variance. Full Cartesian knee modeling is shown in Appendix A.

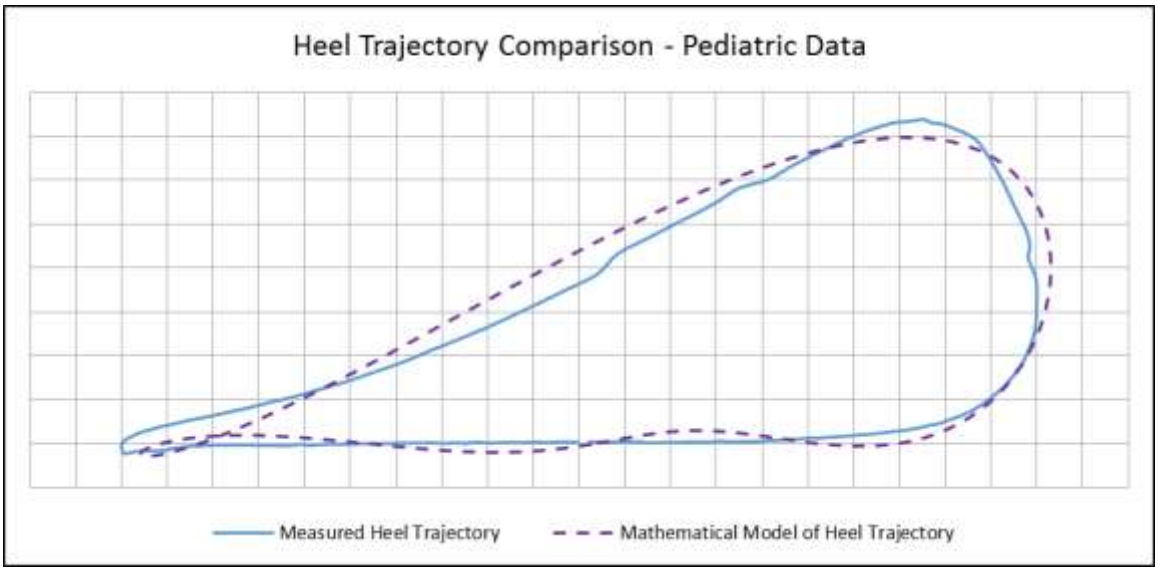

Figure 36. Parametric Modeling of Pediatric Heel Data ($o_x=2$,$o_y=3$)

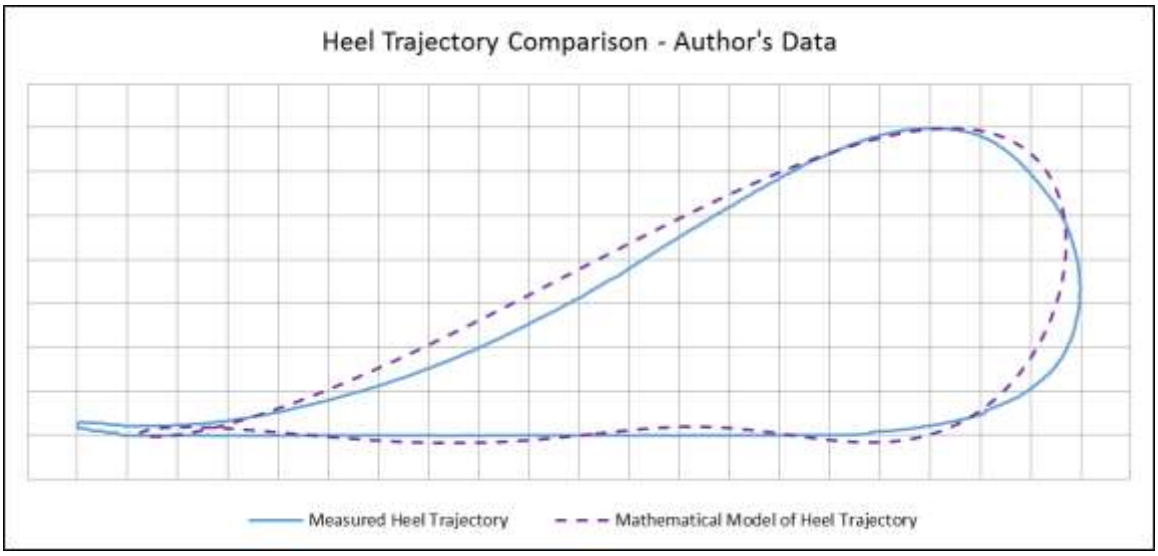

Figure 37. Parametric Modeling of Author's Heel Data (o_x=2,o_y=3)

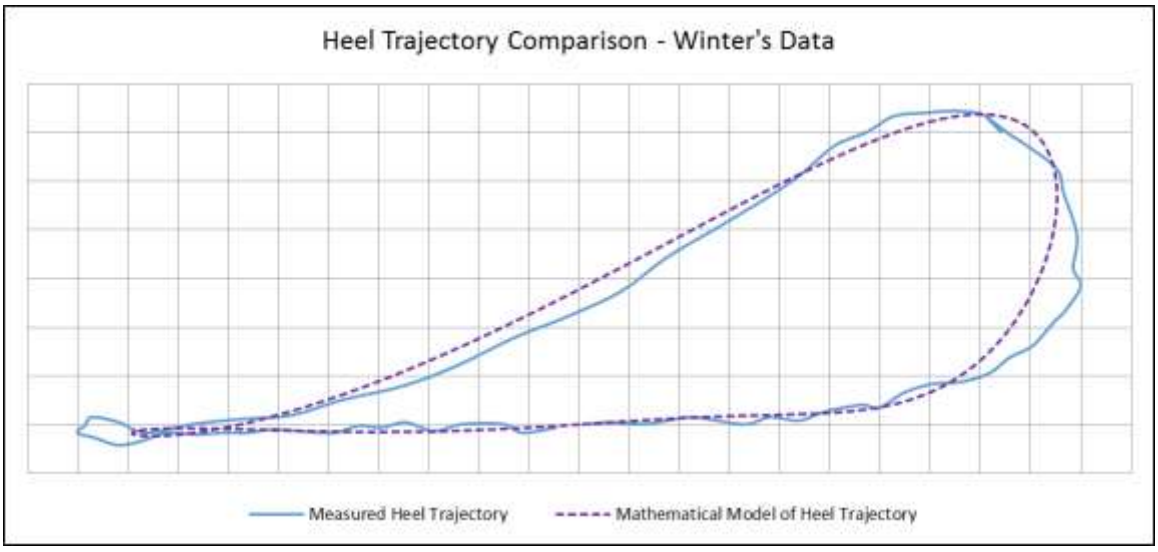

Figure 38. Parametric Modeling of Winter's Heel Data (o_x=2,o_y=3)

Often, the mathematical approximation of the curve proved to be much smoother than the actual dataset. This occurs when real measurements are inaccurate, are recorded with limited accuracy, and require heavy filtering to obtain realistic results. In these cases, highly-accurate curve modeling is undesirable, and a smooth, general curve is preferred.

The a_m and b_n constants were averaged between the author's, Winter's, and pediatric datasets. The resulting 8-order averages are shown in Table 10. The mathematically averaged heel trajectories were plotted parametrically and against each other in Figures 39 and 40.

Table 10. Fourier Series Average Heel a_m and b_n Terms

Average Heel a_m and b_n Constants

	X-Coordinate		Y-Coordinate	
m,n	**a**	**b**	**a**	**b**
0	0.040722		0.084108	
1	-0.0771	0.447013	-0.12761	0.064313
2	0.050769	-0.07244	0.055108	-0.06419
3	-0.02075	-0.01306	-0.01068	0.033135
4	0.003907	0.017561	-0.00143	-0.00955
5	0.002082	-0.00021	0.000826	-0.00077
6	-0.00074	-0.00299	0.000967	0.002664
7	0.000463	0.00262	-0.00094	-0.00054
8	-0.00056	0.00139	0.000245	-0.00074

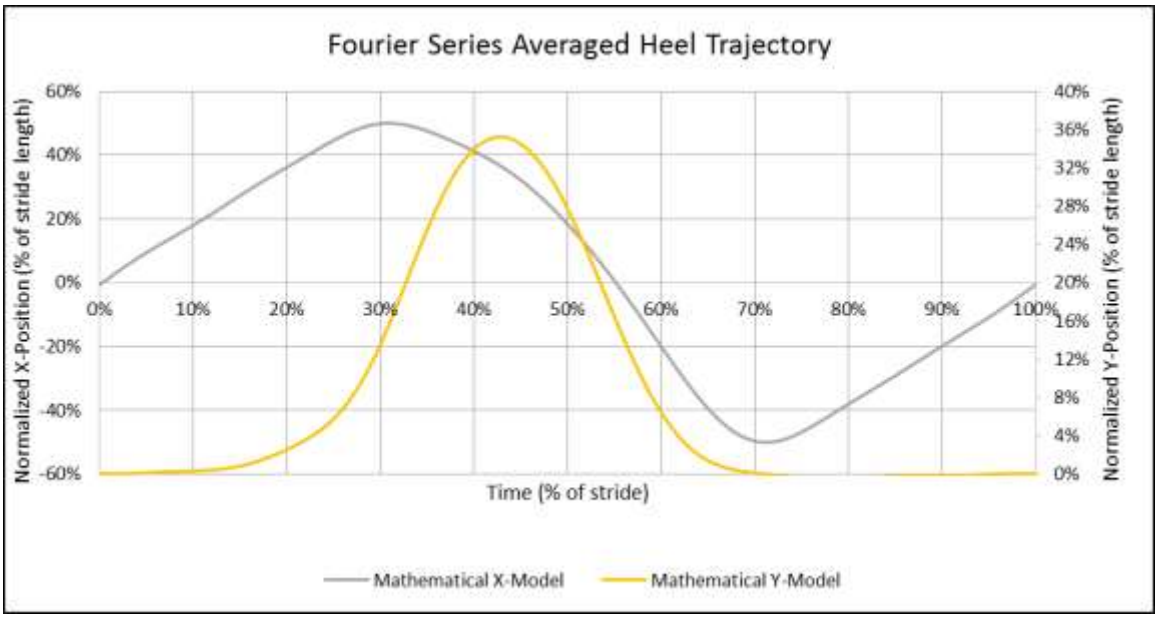

Figure 39. Fourier Series Average Heel Trajectory Parametrization (o_x=8,o_y=8)

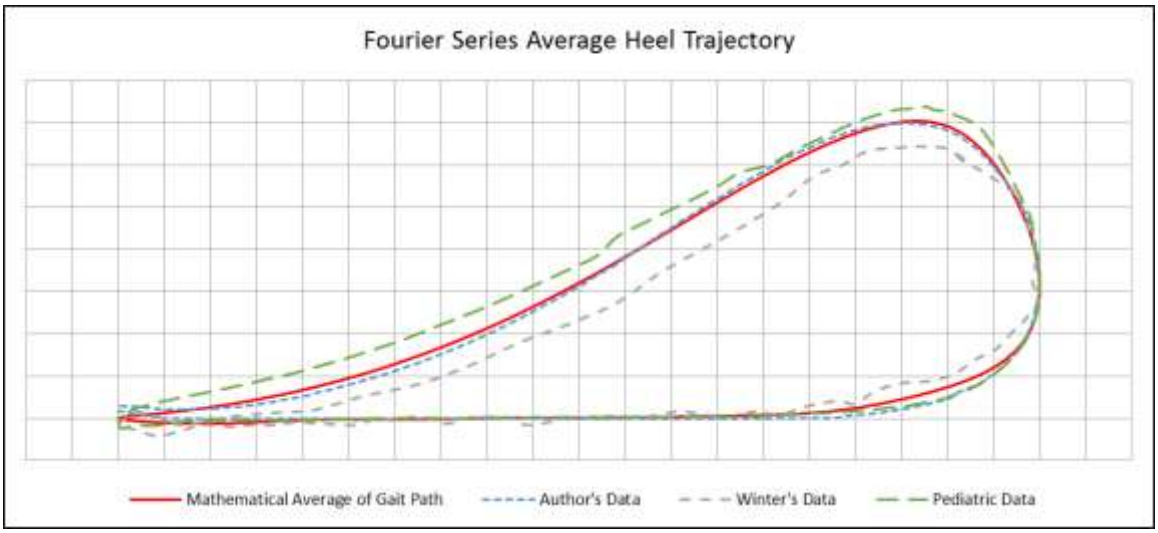

Figure 40. Fourier Series Average Heel Trajectory (o_x=8,o_y=8)

4.4 Foot Angle Modeling

Using the raw metatarsal and heel data from the author's, Winter's, and the pediatric data sets, the foot angle was calculated. The foot angles were zeroed such that the foot was flat during most of stance. The convergence varied between datasets. The pediatric set reached an R^2 value of 99.0% in 3 orders, Winter's dataset convergence in 4 orders, and the author's dataset reached convergence in 5 orders. The mathematical models were compared to the actual data for each of these three datasets in Figures 41 through 43. The full analysis of the foot angle is shown in Appendix A.

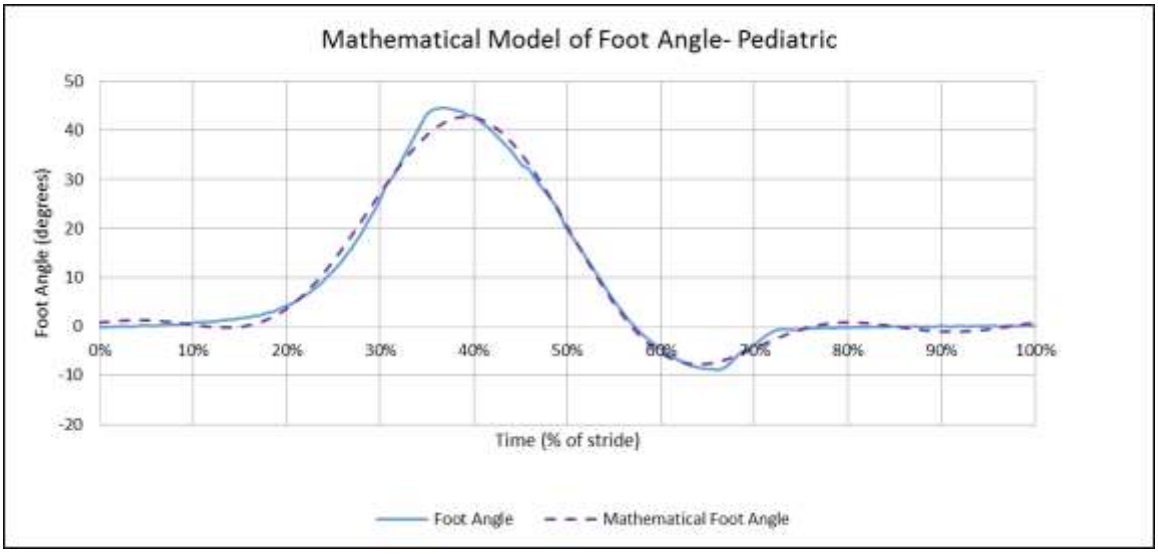

Figure 41. Pediatric Foot Angle Data Mathematical Modeling (o_x=3)

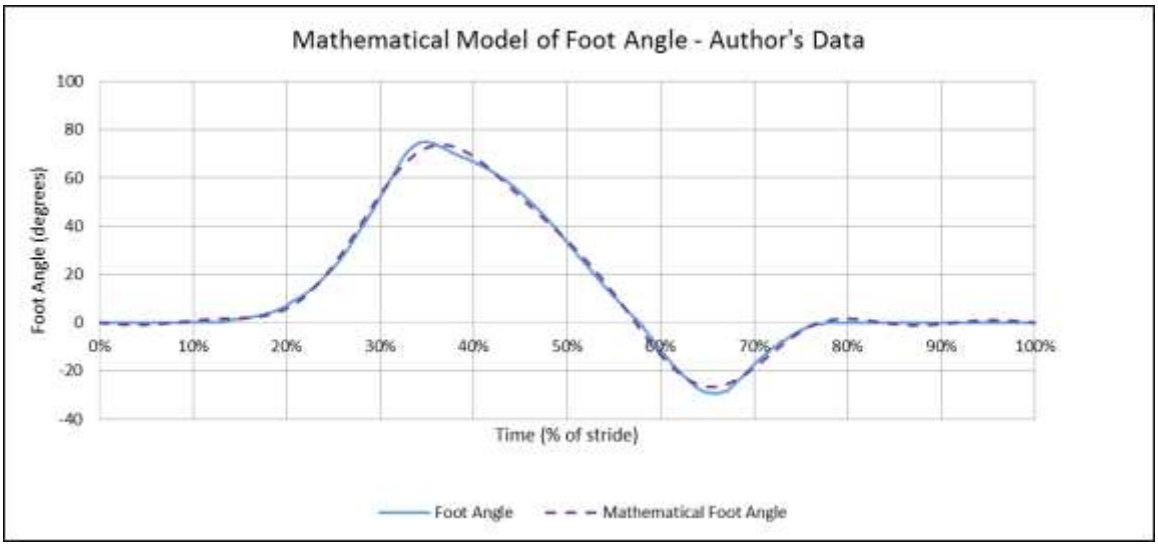

Figure 42. Author's Foot Angle Data Mathematical Modeling (o_x=5)

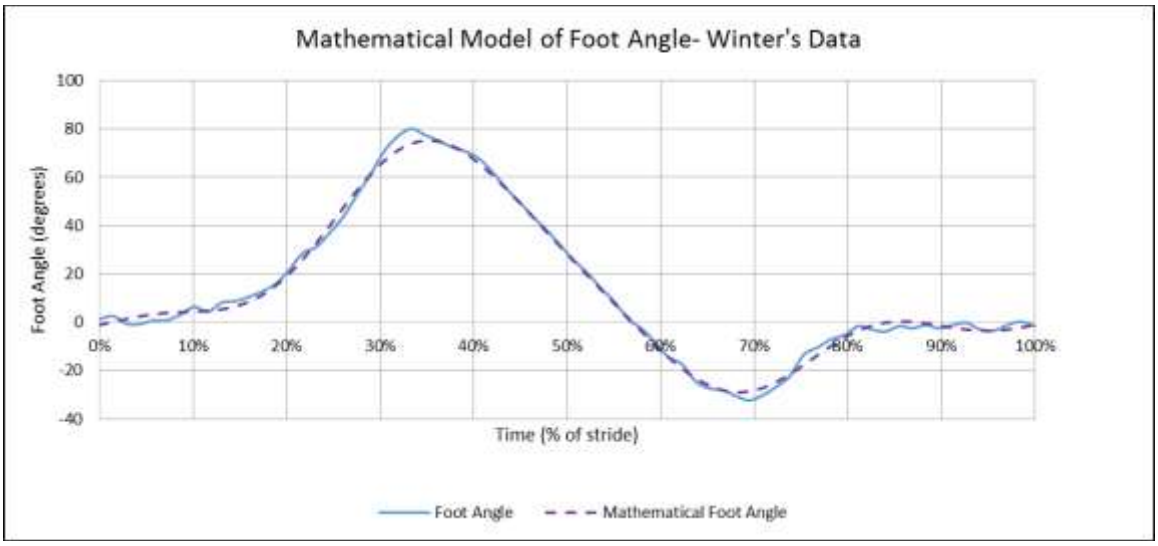

Figure 43. Winter's Foot Angle Data Mathematical Modeling (o_x=4)

The foot angle Fourier series were averaged between the three datasets. The resulting a_m and b_n averages are shown in Table 11. The foot angle traced by the average mathematical approximation is compared to the actual datasets in Figure 44.

Table 11. Average Fourier Series Constants for Foot Angle Modeling

Average Foot Angle a_m and b_n Constants

	X-Coordinate	
m,n	**a**	**b**
0	11.80293	
1	-14.8457	23.02922
2	2.166785	-19.1956
3	1.193393	4.867124
4	-0.49204	2.551773
5	-0.0414	-2.13996
6	0.216997	-0.06041
7	-0.07251	0.79371
8	-0.11119	-0.46419

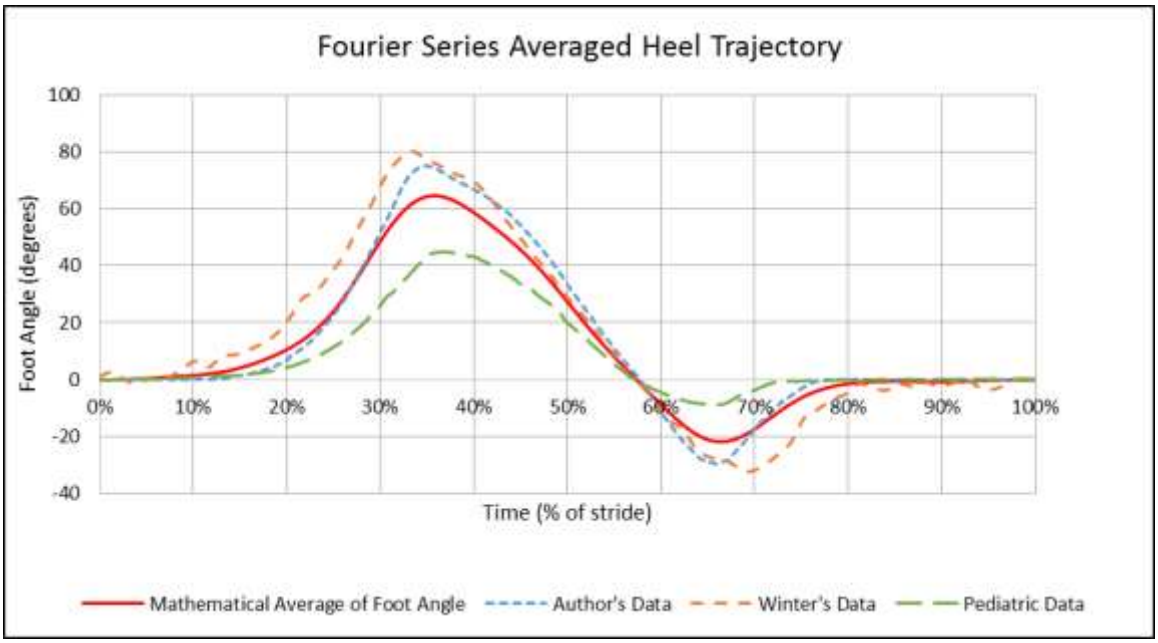

Figure 44. Mathematically-Averaged Fourier Series Foot Angle and Datasets (o_x=8)

4.5 Conclusion

Fourier series mathematical modeling was used to accurately replicate metatarsal, heel, and foot angle data from the research author, Winter's dataset [91], and a pediatric dataset provided by the Madonna Rehabilitation Hospital. While each of these datasets was different, mathematically averaging each of them provided a smooth, differentiable curve that was a good approximation for all three datasets.

In this paper, the three datasets were collected using three different data collection methods by three different sources. It is believed that an accurate trajectory average exists for each foot point, and could be measured given a large number of stride trajectories and a large variety of individuals under standard, repeated, consistent trajectory testing. Until such a Fourier series exists, it is believed that the most accurate, most representative metatarsal, heel, and foot angle trajectories are given by the Fourier series constants described in Tables 9, 10, and 11, respectively. These datasets were used as the representative points modeling the full foot trajectory for the remainder of this study.

CHAPTER 5 – PEDIATRIC INTELLIGENTLY-CONTROLLED ASSISTIVE REHABILITATION ELLIPTICAL

Pediatric models of rehabilitation machines exist (such as treadmills and pediatric ellipticals). However, pediatric rehabilitation machines are not as common as adult machines because of the limited use. Since adult machines can service individuals from around age 12 onward, adult machines have a significantly larger target population. This means that having a designated pediatric machine takes up more space and cost in the facility. Illness, injury, surgery, and other causes of pediatric immobility and gait issues can have long-lasting effects on the individual if not treated as a child, giving a great weight to pediatric rehabilitation.

In order to make a pediatric rehabilitation machine cost-effective, the machine would have to serve both children and adults in their rehabilitation needs. This limits the amount of equipment needed to be purchased and the overall space required for dealing with both patient age groups. As per requests from experts at Madonna Rehabilitation Hospital, the device would have to accommodate stride lengths from 8 inches to 30 inches at least.

5.1 Pediatric Considerations

Modifying an existing system to account for pediatric use requires several considerations. Any pediatric device accommodating the large range of sizes and weights of the varying age group must take into account the normalization factors. According to Hof, each of the gait parameters can be defined in terms of body mass, leg length, cadence, and the gravitational constant [17]. For a retrofitted, existing adult gait therapy mechanism, the mechanism usually has a method of accounting for differing body

weights and cadence. Thus, the major pediatric concern is leg length. Sutherland noted that the leg length and stride length showed strong correlation [18].Thus, the normalization factors can be reduced to only considering stride length, as long as the machine already accounts for varying weights and cadences. Many gait machines already allow a broad range of cadences and are constructed to handle a broad range of patient weights.

There are more physical (anthropometric) considerations that should be made in modifications to an adult gait therapy machine to accommodate pediatric patients. Children differ from adults in the lateral distance between feet when walking. Having foot pedals too far apart would discourage normal gait activity in children. Also, the maximum foot height during the swing phase of gait is significantly smaller for pediatric patients than adults. Any handles or a console that is used for user stability and/or interaction is going to be at differing heights for adults and small children. Adjustments for all three of these distances would be beneficial.

5.2 ICARE System

The Intelligently-Controlled Assistive Rehabilitation Elliptical (ICARE) has proven to effectively rehabilitate adults with little effort from the physical therapist [70,80-83,94-97]. The success of the robotic elliptical machine shows that using a system that constrains the foot motion may be as effective as complicated, expensive systems or therapist-intensive rehabilitation methods. Since walking is the primary form of exercise for the bipedal human, the ICARE provides an opportunity for people with little-to-no walking ability to still engage in physical exercise, making it ideal for children who may require significant assistance in walking.

The full ICARE system involves an elliptical device, a set of ramps and a seat to assist in mounting the device and reaching the pedals, and an overhead body-weight suspension system. The elliptical device and the full system are shown in Figure 45.

Figure 45. ICARE by SportsArt

5.2.1 ICARE Kinematics and Redesign

The ICARE elliptical device consists of a foot pedal riding along a curved bar attached to a crank-rocker four-bar linkage. The foot pedal is mounted to the rocker, whereas the curved, round bar is mounted to the crank. The mounting positions and a dissected view of the coupler and curved bars are shown in Figure 46.

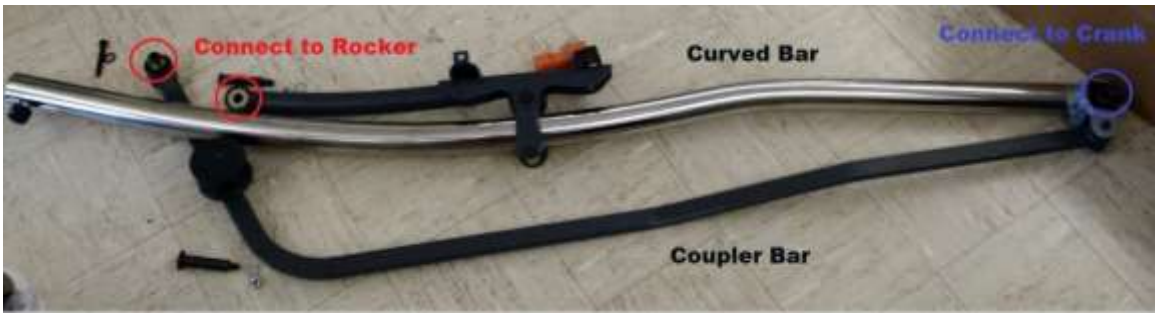

Figure 46. ICARE Coupler and Curved Bars

For the consideration factors listed in Section 5.1, the ICARE stride length is dependent on the height of the connection of the coupler bar to the rocker and the length of the crank. Currently, to adjust for various adult gait lengths, the height of the coupler along the rocker is adjusted while the crank remains fixed. This provides adjustment between 29 in. and 18.5 in. for the stride length in the commercially available version of the ICARE. However, it does not accommodate for stride lengths as small as 8 in., which is the target range of pediatric stride lengths. Thus, to adjust the stride length of the ICARE, modifications will need to be made to the crank.

The foot height during use is highly dependent on the movement of the crank and the profile of the curved bar that the foot pedal rides on. As was previously stated, the crank will be adjusted to modify the stride length. Following adjustments to the crank, the foot path height will be assessed to determine whether further changes are needed to the curved bar.

The lateral distance between foot pedals is a concern. While the foot pedals could be redesigned to slide inward, it was decided that new mounts would allow for the foot pedals to be moved inward. These were designed and installed by Madonna Rehabilitation Hospital staff after the completion of the crank redesign.

5.3 Crank Design

The existing crank is a solid metal piece that is rigidly attached to the axle using a set pin and connects to the end of the coupler bar with a revolute joint. To adjust the length of the crank, the distance between the axle and the revolute joint must be variable.

A three-piece mechanism was designed to replace the crank. The new crank mechanism consists of a mobile axle connection bracket, a screw and collar, and a slotted crank. The screw is connected to the crank through a revolute joint and constrained with the collar. The other end of the screw is threaded into a tapped hole on the axle connection bracket. The axle connection bracket slides along the crank freely, forming a prismatic joint. As the screw turns, it freely rotates in the revolute joint and moves the axle connection bracket vertically relative to the crank. With this design, axial load is transferred from the crank to the axle connection bracket through the screw, while shear and bending loading is transmitted directly from the crank to the connection bracket. The new and old crank designs are compared in Figure 47.

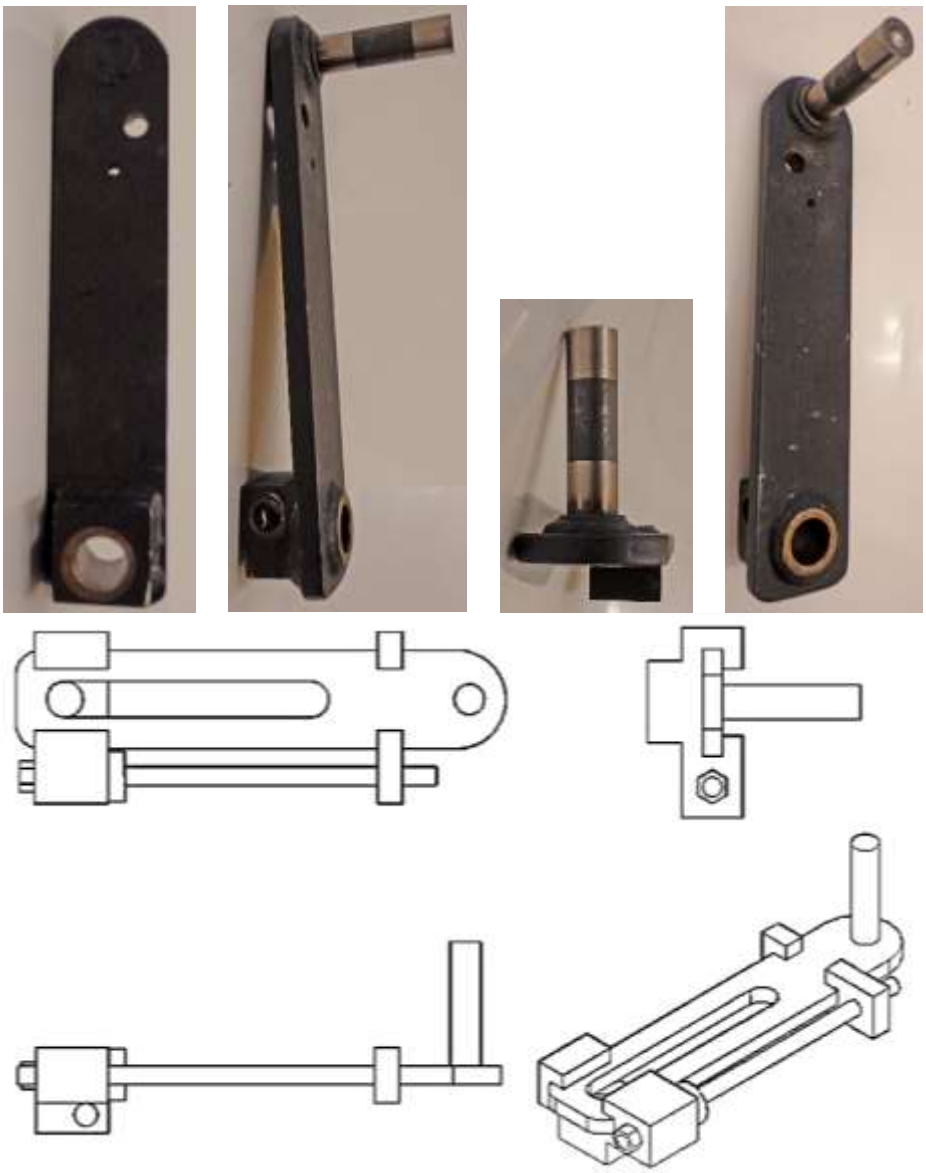

Figure 47. Existing and Proposed ICARE Crank Designs

When designing modifications to an existing system, it is important that the impact of the new pieces be assessed on the existing machine. Ideally, the modified crank would integrate into the system without contacting or disrupting the function of any other component. Due to the presence of the motor overhead and electrical components in the rear of the machine, the crank length could not be extended from the original length. The

screw was located on the side of the axle connection bracket and the crank for this reason.

On the original design, the distance between the center of the axle and the crank revolute joint with the coupler bar was 8.25 in. On the new design, the center-to-center distance could be adjusted from 8.25 in. to 3.25 in.

As the stride length decreased, the height of the foot path also decreased significantly. Foot pedal paths of the modified mechanism are shown in Figure 48. The trajectory of the foot pedal was very similar between the shortest crank length and the largest crank length. After normalizing the trajectories based on the stride length, there were only minor variances in trajectory, as shown in Figure 49. Since normalized child gait data strongly resembled adult gait, similar normalized elliptical paths should be beneficial to pediatric patients. Hence, the new crank mechanism design was determined to successfully reproduce the gait training used in adults for pediatric patients. It should be noted that physical testing is necessary to conclude that this therapy carries the same benefits for children as for adults.

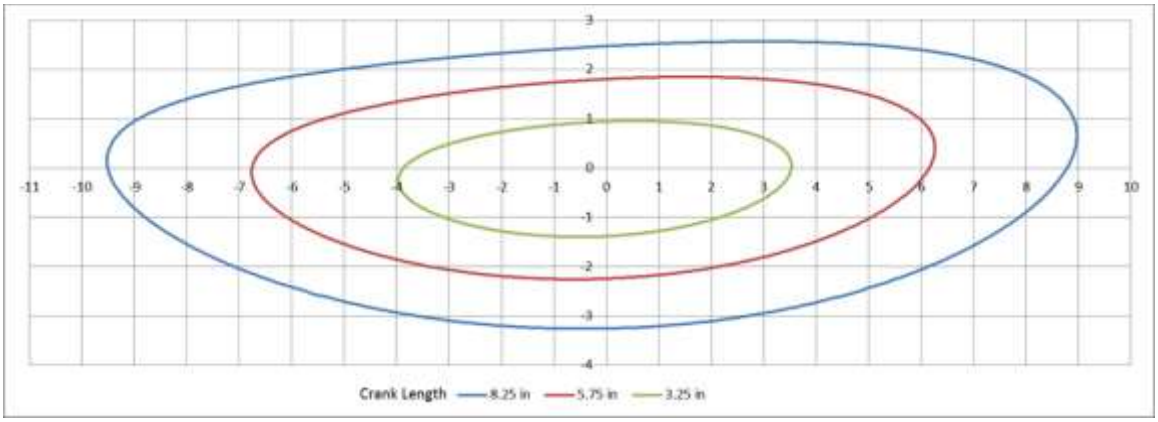

Figure 48. Foot Pedal Paths for Varying Crank Lengths

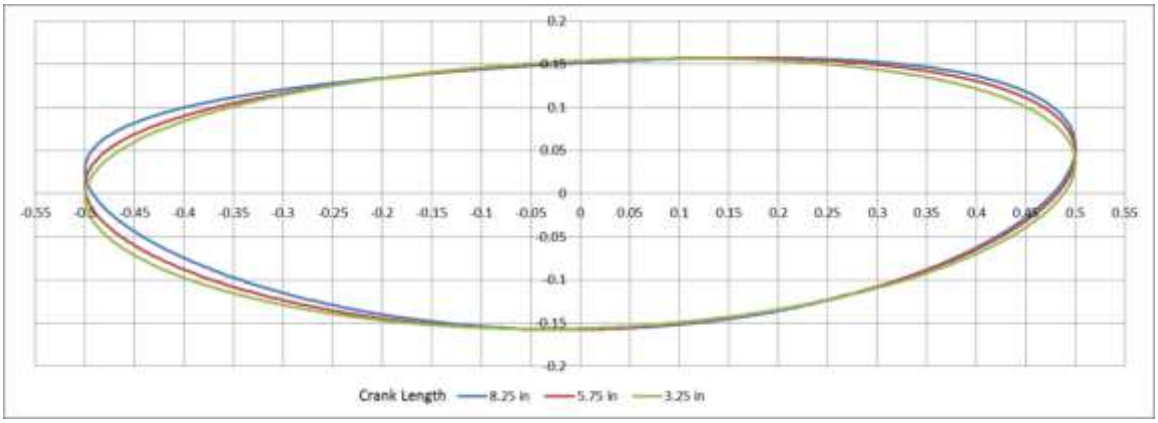

Figure 49. Normalized Foot Pedal Trajectories for Varying Crank Lengths

5.4 Screw Selection

The modified ICARE was designed to have a maximum weight limit of 250 lb. When the body weight support feature is not used, the patient pivots from one foot to the other, applying the full body weight to both pedals in each gait cycle. The proximity of the foot pedals to the rocker mechanism means that much of the patient's weight will be carried by the rocker, limiting the loading on the crank. For safety purposes, the crank mechanism was designed assuming that the entire weight of the patient was placed on the coupler right next to the revolute joint connection with the crank.

5.4.1 Screw Calculations

According to the design, the maximum load imparted on the screw occurs when the screw is in the vertical position. In these positions, the screw resists unscrewing and the threads must not fail. During one cycle, the screw carries all of the weight of the patient and coupler bar in tension and compression. The axial stress in the screw is given by

$$\sigma_a = \frac{F}{A_{eff}} = \frac{4F}{\pi {d_r}^2}$$

Equation 5-1. Screw Axial Stress

where σ_a is the axial stress, F is the axial force, A_{eff} is the effective cross-sectional area of the solid central shaft of the screw, and d_r is the diameter of the solid central shaft of the screw. Here, A_{eff} is used because axial stress is not carried across the open threads.

The most critical loading location on the screw is the thread contact between the screw and the mobile bracket. According to Budynas and Nisbett, experiments with screws have shown that only the first seven engaged threads carry weight, and the first engaged thread carries 38% of the load, with subsequent threads carrying less [98]. Using this loading scenario, the screw hand calculations were performed. A diagram of the simple loading and constraints on the screw is shown in Figure 50.

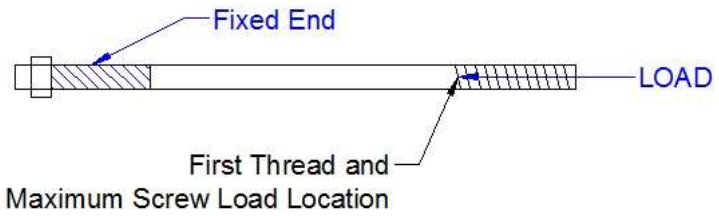

Figure 50. Simple Screw Loading for Screw Selection Calculations

Since the screw contact occurs on the threads, the force occurs on an off-axis incline and lateral and shear forces exist. The force labels on the screw are labeled in Figure 51. The lateral and shear forces are given by

$$\sigma_x = \frac{6F}{\pi d_r n_t p}$$
$$\tau_{yz} = \frac{16T}{\pi {d_r}^3}$$

Equation 5-2. Screw Lateral and Shear Forces [98]

where σ_x is the lateral force, τ_{yz} is the shear force, n_t is the number of threads engaged, p is the pitch, and T is the torque required to turn the screw against the applied force. To

determine maximum stresses at the joint between the screw and the axle connection bracket, substitute 0.38*F* for the force and let n_t be 1 thread [98].

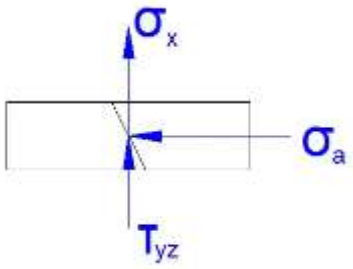

Figure 51. Screw Stress Orientations

The torque *T* is given by

$$T = \frac{F d_m}{2}\left(\frac{l + \pi f d_m \sec\alpha}{\pi d_m - f l \sec\alpha}\right) + \frac{F f_c d_c}{2}$$

Equation 5-3. Torque Required To Turn Screw Against Applied Load [98]

where d_m is the pitch diameter, f is the coefficient of static friction between the bracket and the screw, l is the screw lead, α is the thread angle, f_c is the coefficient of friction between the bracket and the collar, and d_c is the mean collar diameter.

Designing and implementing a new screw is difficult and costly. Thus, these calculations were performed on existing commercially available screws. To determine the constants for the calculations, different diameters and pitches of ACME screws were compared to each other.

A fatigue analysis was conducted so that the screw would survive an infinite number of cycles. Different fatigue models exist, but one of the more stringent models was developed by Soderburg [99]. According to the Soderburg model of fatigue,

$$SF = \frac{\sigma_\infty}{\sigma_a}\left[1 - \left(\frac{\sigma_m}{\sigma_y}\right)\right]$$

Equation 5-4. Fatigue Safety Factor Determination

where

- *SF* is the safety factor
- σ_a is the amplitude of stress variation away from σ_m
- σ_∞ is the maximum material strength at infinite stress cycles
- σ_m is the mean cyclic stress applied to the material
- σ_y is the yield stress of the material

5.4.2 Selected Screw Description

A 3/8-12 ACME threaded screw was selected. The calculation parameters for the screw are shown in Table 12.

Table 12. 3/8-12 ACME Threaded Screw Parameters

Variable	Description	Value
d_n	Nominal screw diameter	0.3750 in.
d_r	Minor diameter of screw	0.2917 in.
d_m	Pitch diameter	0.3333 in.
p	Pitch	0.08333 in.
l	Lead	0.2708 in.
α	Thread angle	14.5 deg
f	Static friction coefficient between screw and bracket	0.08
f_c	Friction coefficient between collar and bracket	0.08
d_c	Mean collar diameter	0.5 in.

Using F = 270 lb, the maximum torque, axial, lateral, and shear forces are

$$T = 21.09\ lb - in$$
$$\sigma_a = 4{,}040.18\ psi$$
$$\sigma_x = 8{,}061.12\ psi$$

$$\tau_{yz} = 4{,}327.53\ psi$$

The Von Mises stress is given by

$$\sigma_{vm} = \left[\frac{(\sigma_1 - \sigma_2)^2 + (\sigma_2 - \sigma_3)^2 + (\sigma_3 - \sigma_1)^2}{2}\right]$$

Equation 5-5. Von Mises Stress Calculation [98]

where σ_1, σ_2, and σ_3 are the principle stresses of the system, which can be determined by reducing the stress matrix into row echelon form. Using this formula, the Von Mises stress was 14,485 psi, and the maximum shear stress is 5,408 psi. Assuming that the threaded rod material is tempered steel with a minimum tensile strength of 97,300 psi, using the Von Mises method, the factor of safety for a 270-lb axial load on a 3/8–12 ACME threaded rod would be 6.7173. For fatigue loading, σ_m=0 psi and σ_a is the Von Mises maximum stress of 14,485 psi. According to Budynas and Nesbit, the infinite stress σ_∞ for tempered steel is 49,300 psi. Using Equation 5-4, the axial loading and unloading of the threaded rod would result in a fatigue safety factor of 3.4035.

Some bending would occur in the threaded rod based on the loading configuration. The effects of the bending load are important to consider, and should be evaluated for their effect on the system.

5.5 Simulation Model and Method

The crank, axle connection bracket, and screw were modeled using the LS-DYNA explicit, nonlinear, finite-element simulation software from Livermore Software Technology Corporation [100].

Each component was modeled as A36 steel under elastic loading. Components were constructed of 5 mm long cubic solid elements. Load was applied uniformly at the revolute joint between the crank and the coupler. The axle was simulated as a rigid

cylinder passing through the crank mechanism. The axle connection bracket was rigidly attached to the axle, while the crank was allowed to rotate about the axle. The 3/8–12 screw was simplified as a 0.2917-in. diameter tube rigidly attached to the crank and the axle connection bracket. The component names and loading locations for the simulation are shown in Figure 52. The simulation model is shown in Figure 53. Note that the circle on the left represents the rigid axle connection to the mobile bracket and the circle on the right represents the simulated coupler connection, which was used as a site to apply an average pressure summing to 270 lb on the lever arm.

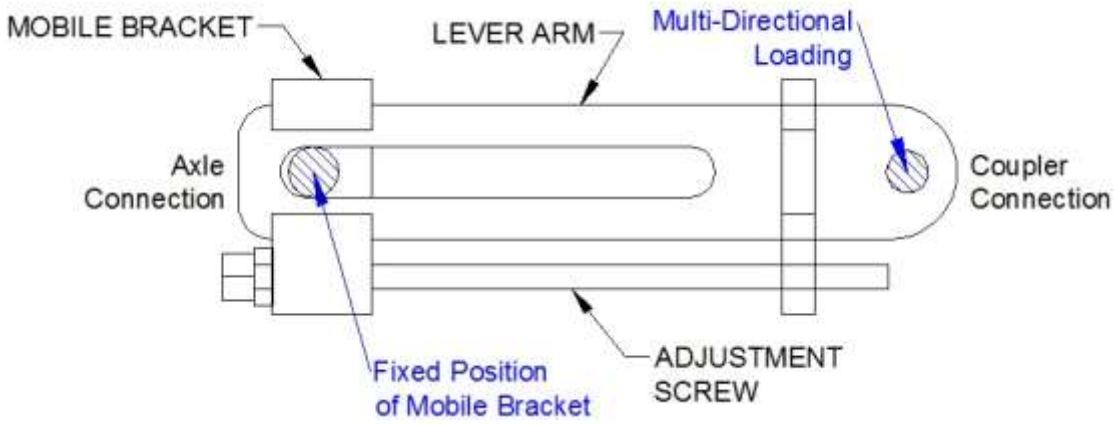

Figure 52. Component Labels and Loading Locations

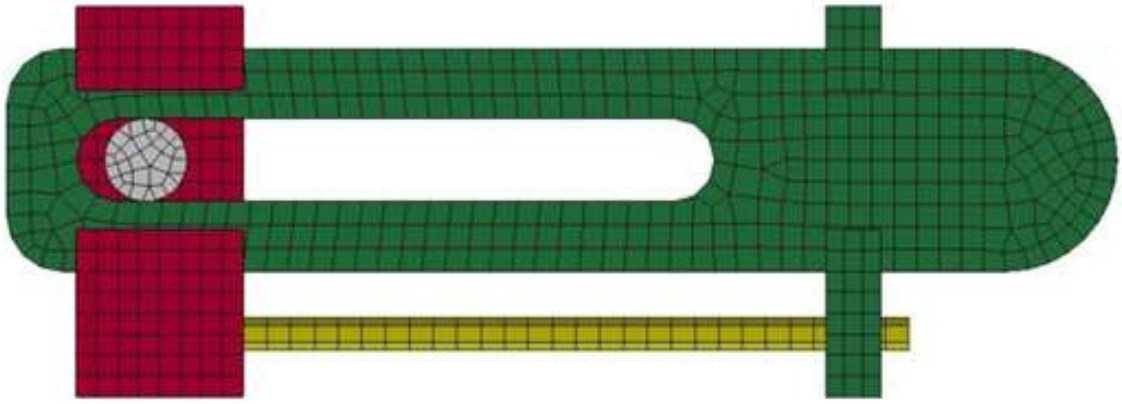

Figure 53. Simulated Crank, Bracket, and Screw

Initial simulations showed that the position of the axle (represented by the rigid blue circle in Figures 52 and 53) affected the stresses on the crank and the maximum stress seen in the system. After several adjustments, it was noticed that the maximum stress in the system was observed when the axle was located 0.25 in. away from the inner edge of the slot. Also, it was observed that beginning the simulation with the axle only in contact with the bracket (not the crank itself) would increase the maximum stress as well. This case could be seen in manufacturing if the tolerances for the axle and the slot are insufficient. This configuration was used for all testing.

In physical testing, surface finish, material type, presence of particulates, and many other factors contribute to the friction between two surfaces. Friction due to penalty-based contact in finite element simulations can be difficult to calculate. To gather a full picture of the effects of friction on a system, the coefficient of friction between the components must be analyzed. Based on the results of the friction study, the friction coefficient is chosen to maximize the stresses in the system. This method tends to produce conservative estimates of contact forces. During the course of the simulations, it was discovered that the friction between the axle connection bracket and the crank showed a significant effect on the maximum stress. The friction coefficient was decreased and the results were observed.

In penalty-based contact, contact forces are dependent on the mesh of the component. Coarser meshes tend to produce higher contact forces and stresses, while finer meshes tend to be “softer” and mitigate some of the hard points. The original, 5-mm long mesh was refined to 1.6-mm long cubic solid elements for comparison.

A static analysis of the crank assembly was conducted. Weight was applied to the crank mechanism in four directions corresponding to axial and transverse loading. The maximum stresses in the crank and screw were noted for each simulation.

The crank assembly was also modeled dynamically. A rotational speed was imparted on the crank mechanism, simulating the axle spinning. The crank rotated at a rate of 1 rev/s while experiencing a constant downward load of 270 lb.

5.6 Simulation Results

During the static simulations, the maximum stresses were located around the bottom of the slot of the crank, occurring along shear planes that extended from the contact with the axle connection bracket. For the screw, the maximum stresses occurred at the connection between the screw and the axle connection bracket.

It was found that reducing the friction between the crank and the axle connection bracket increased the contact stresses in the crank, but decreased overall maximum stresses in the system. Very low friction values are not expected in the real assembly, however, and utilizing a higher-than-expected friction coefficient in the simulation yields maximum stress values that are conservative.

For each simulation, removing the contact between the crank and the axle caused higher stresses in the crank. Since the maximum stresses were observed around the slot in each simulation, the axle contact was serving to strengthen the slot. Thus, the simulations predict that if the tolerance between the crank and the axle is loose, the crank will experience larger stress values.

The maximum observed Von Mises stress values for the statically-loaded, coarse-mesh simulation models are shown in Table 13. In the vertical direction, loading the

crank and screw in tension resulted in the lowest observed maximum stresses. When loaded in compression, the stresses were larger, partly because mild deflection of the screw showed some column buckling. However, the stresses observed during axial loading were acceptable, and the crank performed well under axial loads.

Table 13. Maximum Observed Von Mises Stresses in Simulated Crank – Original Mesh

Loading Direction	**Max Observed Stress in Crank**	**Max Observed Stress in Screw**
Axially Up	1,085 psi	366 psi
Axially Down	6,270 psi	5,868 psi
Laterally Toward Non-Screw Side	29,370 psi	17,842 psi
Laterally Toward Screw Side	30,472 psi	16,820 psi

In the lateral direction, the stresses were significantly larger. Contact forces between the corner of the axle connection bracket and the crank created high-stress shear planes that extended from the outside contact surface to the slot. The shear planes are shown in Figure 54.

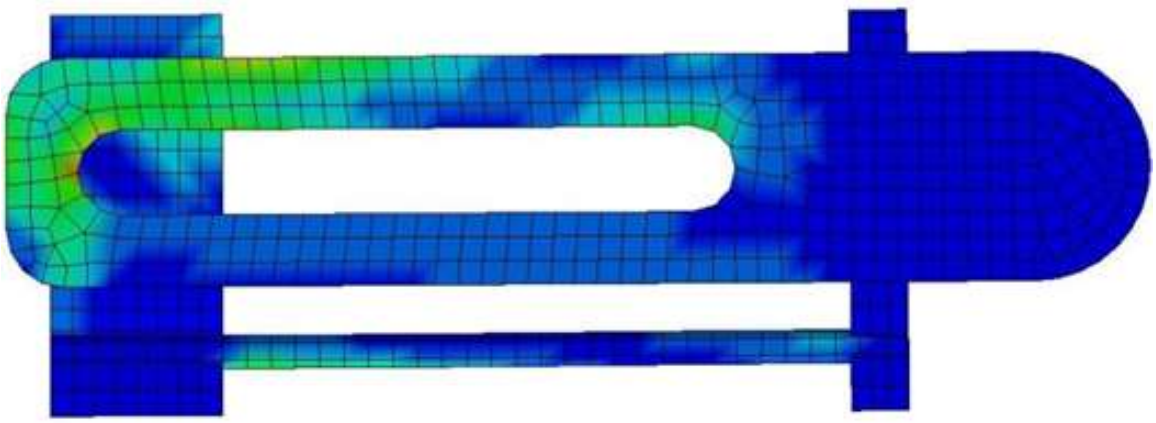

Figure 54. Shear Planes on Simulated Crank in Lateral Loading Configuration

The mesh was refined, and a smaller mesh was used to simulate the lateral loading of the crank mechanism. The finer mesh was approximately one third the length of the coarse mesh. The crank mechanism showed similar stress distribution through the crank between the coarse mesh and fine mesh models, but the fine mesh model experienced significantly reduced stresses. Stress values are noted in Table 14.

Table 14. Maximum Observed Von Mises Stresses in Simulated Crank – Reduced Mesh

Loading Direction	**Max Observed Stress in Crank**	**Max Observed Stress in Screw**
Laterally Toward Non-Screw Side	18,948 psi	12,590 psi
Laterally Toward Screw Side	17,827 psi	13,992 psi

The crank mechanism was rotated at 1 rev/s with a constant downward load applied. The axle contact was included in this simulation, but it was determined that the axle contact was the least critical case, and in further simulations, this contact was ignored.

The loading on the lever arms caused vibration, and the stress did not vary smoothly with time. Lower overall loads were observed during this simulation. The maximum stress in the rotating bracketed lever arm was 16,244 psi and occurred in the side of the crank above the axle connection bracket opposite the screw. The lever arm was nearly vertical, and the slight angle caused bending moments to concentrate in the side of the crank. However, this stress is lower than the stresses observed in static loading of the bracketed lever arm design. Contact stresses were observed to be significantly lower also. The maximum stress state of the rotating lever arm is shown in Figure 55.

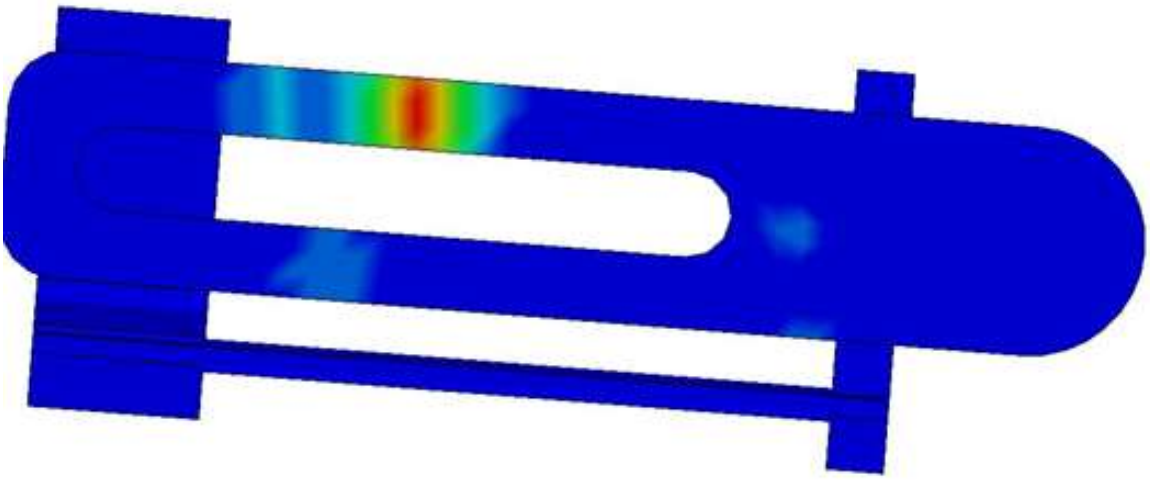

Figure 55. Maximum Stress State During Dynamic Testing

5.7 Discussion

Simulation analysis showed that the new crank mechanism could experience peak stress values of up to 30,500 psi in the crank and 17,800 psi in the screw. Low-grade, hot-rolled steel has a yield strength of at least 33,000 psi. Thus, the crank mechanism would not be able to be constructed from inexpensive steel.

It was decided that the crank mechanism should be constructed from cold-rolled steel with a minimum yield strength of 60,000 psi. While this increases the cost significantly, the safety factor of at least 1.97, combined with the conservative stress estimates and loading conditions, means that the mechanism is unlikely to fail.

The simulation measured high bending stresses in the screw near the connection to the axle connection bracket. As calculated earlier, the screw experiences significant stresses under axial loading. Using Equation 5-4, the fatigue safety factor for the threaded rod was determined to be 2.77. It should be noted that the simulation treated the connection between the screw and the axle connection bracket as a fixed cantilever beam. There was no ability to rotate, bend, or compress at the connection site. While this

doesn’t perfectly model the connection, it provides a conservative estimate of the stresses experienced by the screw at that location as long as the other simulation constraints hold to be true.

Simulation results showed that the design would not experience stresses above 35 kpsi. To be able to handle this load, it is recommended that the crank be constructed from cold-rolled steel or other higher-strength steels.

5.8 Design Issues

The pediatric ICARE machine has been tested using children at Madonna Rehabilitation Hospital. Several conference abstracts are available at the time of this writing [101-103]. Following discussion with the researchers at Madonna Rehabilitation Hospital, the pediatric ICARE appears to be functioning properly. After the results of this testing period have been analyzed, the design will be re-assessed, and potential design improvements will be suggested.

One problem was noted with the completion of this study. As stated earlier, simulation results showed that the stress concentration in the crank increased when the axle was not in contact with the slot of the crank. This led the crank to be designed with minimal tolerance for the axle shaft in the slot. However, it was found that dust, debris, and other foreign objects can cause the adjustment process to seize when amalgamated around the axle in the crank slot. This caused the collar to slide down the length of the screw when adjustments were made, creating contact problems and disabling the machine. Using an ACME threaded nut welded to the shaft as a replacement for the collar would prevent this slippage. This was found to be strong enough to overcome the dust in the slot.

The tolerances on the moving bracket allowed the bracket to twist while sliding along the crank, causing an irritating clanking noise during one stride cycle. Also, it was discovered that the threads on the ACME threaded rod were grinding and producing particulates, and this was making it difficult to turn and causing issues with adjustment. To solve these issues, the tolerance on the inside of the bracket was decreased, and the threaded rod diameter was increased from 0.375 in. to 0.5 in. The final design, installed on the ICARE system, is shown in Figure 56. Drawings of the final pediatric ICARE crank parts are shown in Appendix B.

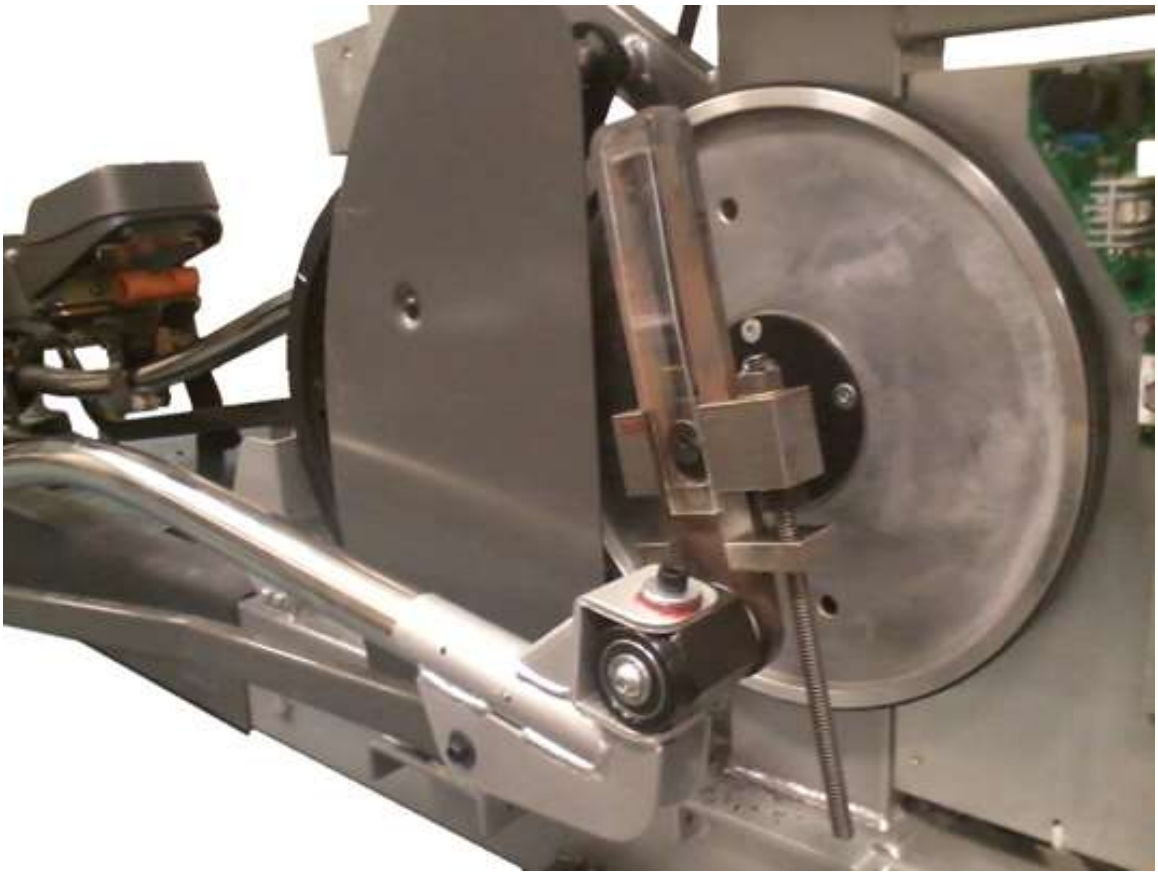

Figure 56. Pediatric ICARE Final Design

5.9 Conclusions

The adult ICARE elliptical system was evaluated and modified to accommodate pediatric patients as well as adult patients. The machine was developed by designing an

adjustable crank that allows for stride reduction from the claimed maximum of 30 in. down to 7.5 in. Adjustment produces a nearly linear scaling of the adult elliptical stride path for the foot.

The pediatric ICARE machine has been tested using children at Madonna Rehabilitation Hospital. Several conference abstracts are available at the time of this writing [101-103]. Following discussion with the researchers at Madonna Rehabilitation Hospital, the pediatric ICARE appears to be functioning properly. After the results of this testing period have been analyzed, the design will be re-assessed, and potential design improvements will be suggested.

CHAPTER 6 – DETERMINATION OF GAIT REPLICATION METHOD

At the beginning of this project, researchers had two overarching design goals: (1) to design a gait therapy machine that could accommodate pediatric and adult patients to limit the number of therapy machines needed for a facility, and (2) to develop a machine that more accurately mimics the trajectory of the foot during gait. Following the successful development of the pediatric ICARE unit, it was noted that the gait profiles from the new crank, shown in Figure 49, still show a very large gait height change per stride, which is significantly different from the average gait profile shown in Figure 35.

Thus, a brand-new rehabilitation machine was developed.

6.1 Design Goals

A rehabilitation mechanism for use in a healthcare, rehabilitation, or home-health setting would need to accommodate the setting so it doesn't discomfort or endanger other individuals around it. As such, a set of design goals were established. The primary design goals for the project were:

- **Gait-Like Trajectory:** The mechanism must constrain the feet to a trajectory similar to normal gait motion, as shown in Figures 35 and 40.
- **Scalable:** The mechanism must accommodate for individuals with a stride length between 6 and 40 in. while producing an easily-scaled full foot trajectory (including accurate foot angles) such that the size of the trajectory is scalable, but the shape remains constant. Ideally, the scaling would be linear, as this is the easiest form of scaling to understand. This would make sure that therapists using the device can easily read and adjust the scale of the gait path to fit the user. Also,

the scaling process should be performed by one motive element, eliminating the possibility of accidental misalignment or inaccurate mechanism trajectory.

- **Practical for Small Facilities:** The mechanism will be designed specifically so that small, lower-budget rehabilitation facilities are able to use this technology. This means that it cannot be clinician-intensive, require extensive training, or be difficult to operate.

In order to be considered a successful rehabilitation machine, the primary design goals must be accomplished. If the primary design goals are not achieved, the rehabilitation device cannot be considered an advancement over existing technology. While secondary goals exist that are important to address, any issues arising with the secondary design goals could be fixed after the prototyping phase. The secondary design goals for the rehabilitation robot were:

- **Adjustable:** The mechanism should be able to accommodate for specific impairments, such as different stride lengths for each foot or reduced step heights.
- **Cost-Effective:** The mechanism must be affordable so that smaller rehabilitation centers and in-home users could afford to purchase the device.
- **Small Footprint:** The mechanism must not require excessive space to store or operate.
- **Motorized:** The mechanism must utilize a motor that propels the patient's foot through a gait-like trajectory. The motor component is critical to assist patients with low muscular strength.

- **Backdrivable:** The mechanism must be able to be manually driven without requiring significant effort, which would make it usable as a workout device for individuals with capable motor function.
- **Ergonomic:** The mechanism must not impair the normal gait motion of the user in any way, and must avoid uncomfortable interferences that may prevent effective rehabilitation. The device must feel stable, easy to mount, and not cause significant vibrations or sound while in use.

To satisfy the first design goal, the mechanism must be able to guide the foot through a gait-like trajectory. There are two ways of achieving this goal: (1) by directly tracing the path, and (2) by parametrizing the path and independently controlling movement. Each design option has its benefits and drawbacks. For example, by directly controlling the path, the machine requires one motor and has minimal power transmission losses due to changing axles, and more easily fulfills the backdrivability design goal. On the other hand, by parametrizing the path, individual tweaks can be made to either the toe height or the stride length without requiring a full disassembly of the machine, and power transmission can be optimized.

The first method of tracing the gait path is direct gait replication. This could be achievable through one of several traditional path-tracing methods, such as the four-bar linkage or the pantograph. The second method of tracing the gait path involves parametrization. Here, the trajectory is separated into independent vector components as functions of time.

Initial efforts to model the foot involved only modeling the metatarsal trajectory, and determining an effective method of controlling foot angle beyond that. Thus, all

further discussion about gait trajectory replication in this chapter pertains to metatarsal trajectory.

6.2 Four-Bar Linkage – Direct Gait Replication

The coupler bar on a four-bar linkage traces a variety of different paths based on the linkage lengths of the four-bar. As seen in the ICARE system evaluated in Chapter 5, many elliptical machines operate using a four-bar linkage. The traditional four-bar linkage consists of four planar bodies connected by four one-degree-of-freedom joints (revolute axis oriented normal to the plane of motion, or prismatic axis in the plane of motion) with an input and an output. The output can either consist of the trajectory of a link (such as the coupler), the angular position of a link (such as a rocker), or the linear position of a link (such as a slider). Using the four-bar linkage as a path-tracing mechanism involves measuring the trajectory of the coupler link.

There are different types of four-bar linkages, shown in Figure 57. Each mechanism has distinct uses and advantages.

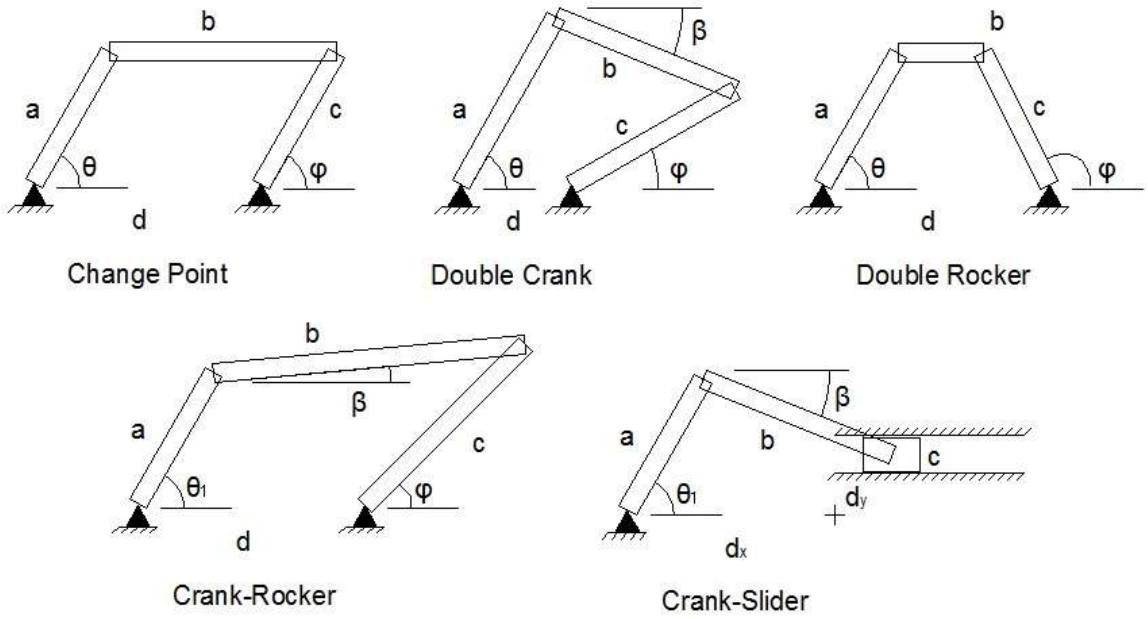

Figure 57. Four-Bar Mechanical Isomers

The Grashof existence conditions help determine what linkages are possible given set link lengths [104-105]. The Grashof conditions use trigonometry to determine what the link lengths must be to form a mechanism. For these equations, link L refers to the longest link, link S refers to the shortest link, and links P and Q refer to the intermediate links. The Grashof existence conditions are shown in Table 15. Note that the existence condition for the crank-slider mechanism was also included in Table 15.

Table 15. Grashof Existence Condition for Four-Bar Linkages

Existence Condition	Shortest Link (S)	Mechanism Constructed
$L + S < P + Q$	Ground	Double-Crank
$L + S < P + Q$	Crank	Rocker-Crank
$L + S < P + Q$	Coupler	Double-Rocker
$L + S = P + Q$	Any	Change Point
$L + S > P + Q$	Any	Double Rocker
$b - a \geq d_y$	Crank	Crank-Slider

One four-bar configuration is the double-crank (also known as the drag-link mechanism). This design consists of two links connected to the ground through revolute joints, both of which complete full rotations. Given uniform, constant angular velocity from one of the cranks, the mechanism can output non-uniform angular velocity. A trajectory traced by the output crank will always be a circle. For this reason, it was excluded from consideration.

A specialized case of the double-crank is the change point configuration. A change point mechanism is capable of fully rotating to a point where all four links become collinear. As stated earlier, none of the double crank mechanisms were considered for gait replication, so the change point configuration was discarded.

Another four-bar configuration is the double-rocker. This mechanism is characterized by two links connected to the ground through revolute joints, both of which oscillate between fixed angular positions as the coupler makes full rotations between them. Without directly powering the coupler, this mechanism would be difficult to control, and was excluded from consideration.

Another realization of a four-bar linkage is the crank-slider. In this, the mechanism converts between linear, translational motion and angular, rotational motion. The slider follows a predictable, oscillating trajectory based on the length of the crank and the ground link vertical offset (labeled $L_{4,x}$ in Figure 57). Each point on the coupler traces a closed, convex, non-circular path. Since the goal of this new mechanism is to produce a gait-like trajectory that improves on the existing elliptical trajectories, this mechanism was ruled out as a viable candidate.

The crank-rocker four-bar linkage converts the full, circular rotation of the crank into an oscillating, finite angular movement of the rocker. Similar to the crank-slider, the rocker arm experiences periodic, predictable oscillations. The coupler on the four-bar linkage traces a variety of paths, such as the ones generated in Figure 58. Each coupler trajectory forms a closed loop, but they vary between convex curves, self-intersecting curves, and many other shapes. For this reason, it is much easier to consult an atlas of four-bar linkages, such as the one produced by Hrones and Nelson [106]. After consulting this atlas, none of the reviewed curves closely resembled the path presented in Figure 35. If a sixth-order curve could be fit to the metatarsal trajectory path, then the four-bar likely could be synthesized.

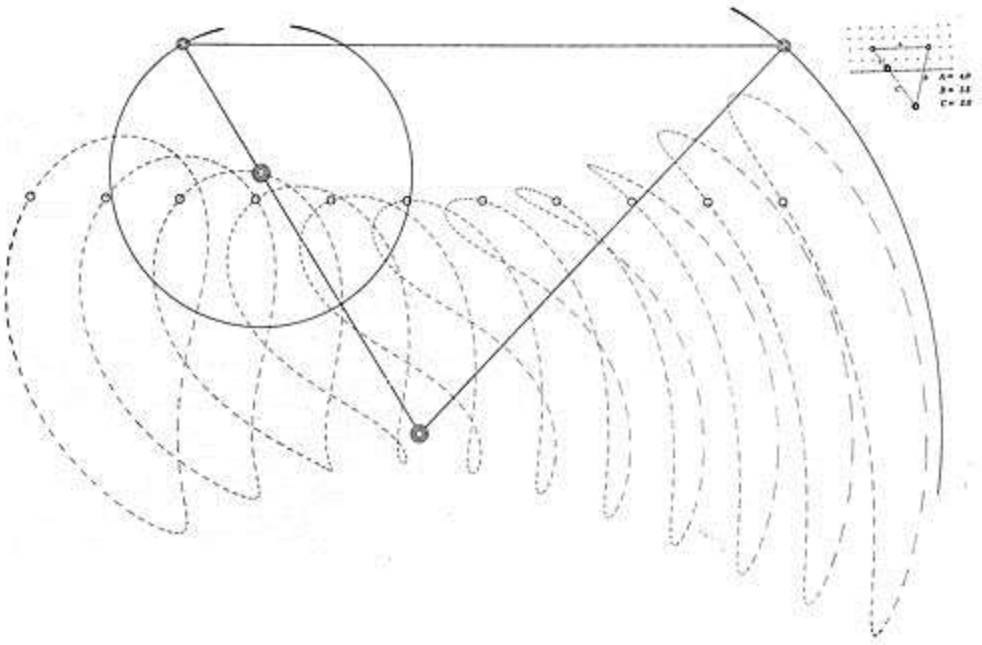

Figure 58. Sample Coupler Trajectories [106]

6.2.1 Development of Four-Bar Linkage Mathematical Model

The rocker-crank mechanism shown in Figure 57 is a one degree-of-freedom mechanism. Each link can be represented by a vector. Since the four-bar linkage forms a closed object, all of the vectors must sum to zero. From this knowledge, each vector was broken into X and Y Cartesian components using the link length and the rotation angle. The resulting summation is given by

$$a\cos\theta + b\cos\alpha - c\cos\varphi - d = 0$$
$$a\sin\theta + b\sin\alpha - c\sin\varphi = 0$$

Equation 6-1. Parametric Equations of Four-Bar Linkage Positions

where

- a is the length of the crank,
- b is the length of the coupler,
- c is the length of the rocker arm,

- d is the length of the ground link, which is the distance between the fixed pivot on the crank and the fixed pivot on the rocker
- θ is the angle between the crank and the ground link
- α is the angle between the coupler and the ground link
- φ is the angle between the rocker arm and the ground link

Note that all angles are measured counterclockwise from the ground link (which is assumed to be horizontal for simplicity. Ground rotation can be easily adjusted at a later time using a rotation of coordinate axes). From Equation 6-1, it is possible to derive Freudenstein's equation [107], which is given by

$$R_1 \cos(\theta) - R_2 \cos(\varphi) + R_3 = \cos(\theta - \varphi)$$

Equation 6-2. Freudenstein's Equation [107]

where

$$R_1 = \frac{d}{c}$$

$$R_2 = \frac{d}{a}$$

$$R_3 = \frac{a^2 + c^2 + d^2 - b^2}{2ac}$$

Freudenstein's equation can be used to determine the relationship between the crank rotation angle and the rocker angle. Knowing the positions of both the crank and rocker, the coupler position can be determined.

There are several methods available to optimize mechanism paths. The Burmester method utilizes five points to calculate the trajectory of a coupler curve of a four-bar configuration that passes through each point [108]. Initial efforts in using this method indicated a substantially large mechanism would be generated, forming a curve that extended far beyond the desired extents of the metatarsal curve.

Often, genetic algorithms and evolutionary methods are used to solve four-bar linkage problems due to the complexity of the calculations involved in determining the coupler position with respect to time [109-111]. Other algorithms have been implemented through use of specialized MATLAB optimization functions [111-114].

6.2.2 Conclusions

The four-bar linkage as a method of fully replicating the gait path was not pursued for this project. The gait path is a parametric function that involves both timing and position. Seeking a four-bar linkage to approximate the path of the foot during gait would require precise and variable control of the rotation of the machine to compensate for the timing and position control.

Also, according to the second design goal, the mechanism must be adjustable. To have perfect adjustment would require precise adjustment of each link to form a scaled mechanism producing a scaled coupler output. Independent adjustments of four linkages would be cumbersome and difficult, and may be prone to scaling error. In some configurations of the four-bar linkage, it is possible to have minimal changes in trajectory shape by scaling only one component, as seen in the crank redesign of Chapter 5. However, the goal of this project was to develop a non-elliptical gait-like trajectory, and utilizing a configuration similar to the one seen on the ICARE would not provide significant benefits. Thus, the four-bar linkage as a method of fully replicating the foot's motion was not pursued.

6.3 Pantograph – Direct Gait Replication

Pantographs rely on geometrical constraints of similar triangles or parallelograms to produce similar motions at different points on a linkage. One frame of a pantograph is

shown in Figure 59. The pantograph is fixed at point A, the lateral input movement occurs at point O, and the output motion occurs at point C.

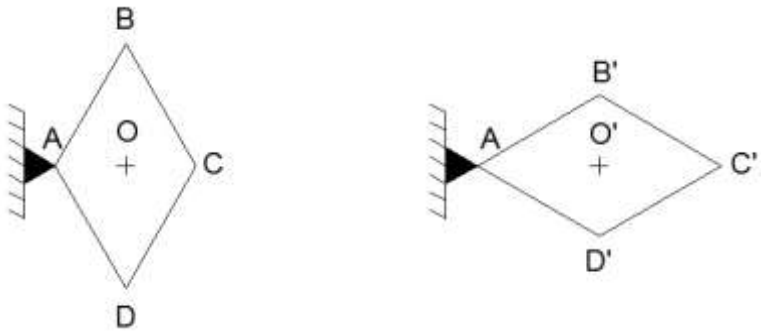

Figure 59. Single Pantograph Frame

Links AB, BC, CD, and DA all have the same length, forming a rhombus. Isosceles triangle ABC and ADC each pass through motor point O. When the pantograph frame is stretched from ABCD to AB'C'D', the distance AO' changes. By similarity of triangles, lengths AO' and O'C' both expand at the same rate. This allows fixed movements of point O or C to produce scaled movement across the pane. Since pantographs rely on similarity of shape for all of the panes, this produces greatly scaled motion based on the input motion. Two separate pantograph mechanisms were considered for replicating gait motion.

6.3.1 Pantograph Realization #1

In one design, two long beams connect with two shorter beams to create a scaling mechanism, as shown in Figure 60. Triangles ABC and ADF are similar triangles. Point A is rigidly attached to the ground, and point F is attached to a foot pedal. Point C is attached to a pin that would follow the reference gait path. A mechanism would be constructed to power a pin through a gait-like trajectory. Through this motion, the pin's rigid connection with point C would control the shape of the pantograph trajectory.

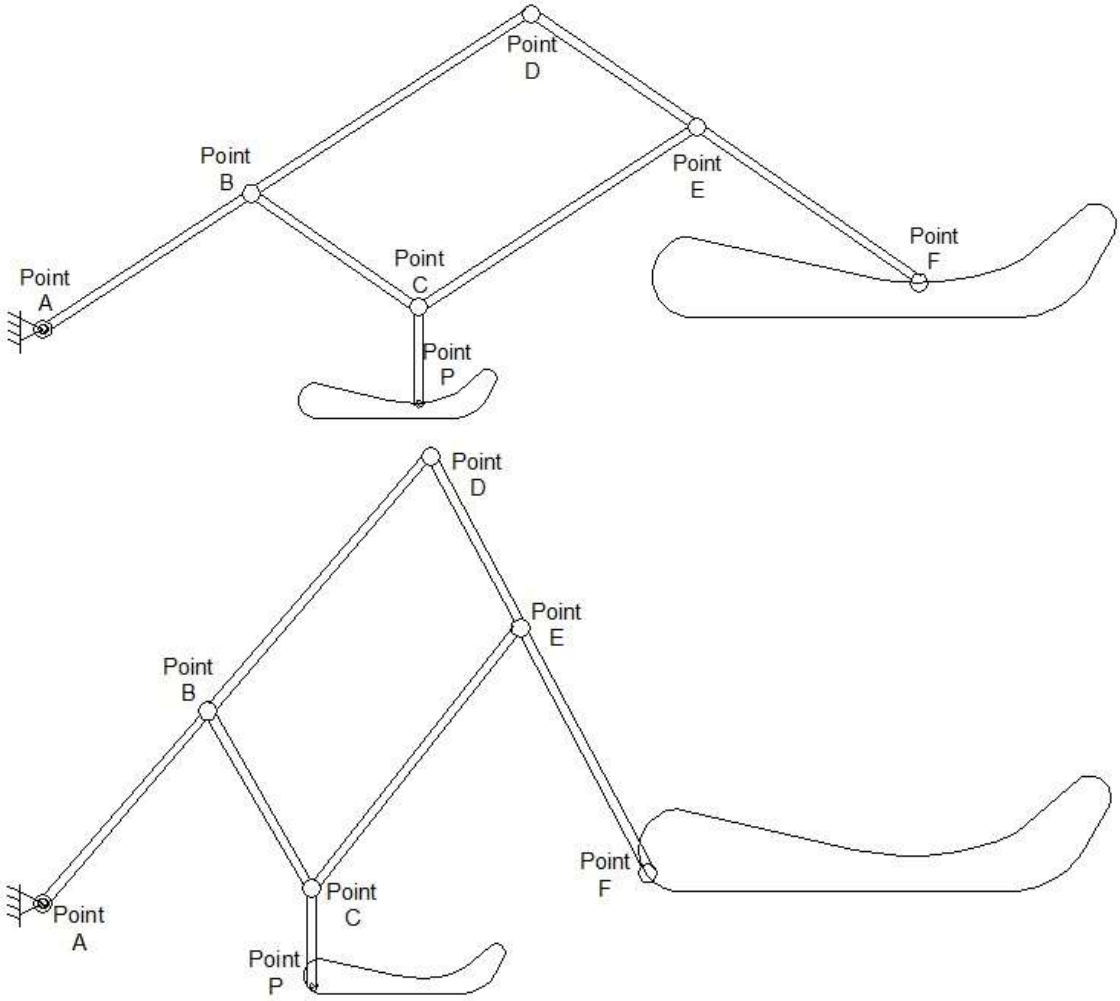

Figure 60. Pantograph Path-Tracing Mechanism: Design 1

While this mechanism would be a simplistic method of accurately tracing the gait trajectory, scaling would be difficult. In order to have exact path scaling, the triangular symmetry must be maintained. To do this, points A, C, and F must lie along a straight line. A motor would have to change link lengths so that the geometric similarities of the triangles ABC and CEF remained. Also, the size of triangle ADF would be fairly cumbersome in order to achieve a scaling between 8 and 40 in. This would make using and mounting the machine difficult.

6.3.2 Pantograph Realization #2

A telescoping pantograph would extend outward, as shown in Figure 61. Again, point A would be rigidly attached to the ground, and point C would trace the gait path similar to the design shown in Figure 60. The foot pedal would be located at point C. In order to scale, point C would be constrained to a different location along the axis of the pantograph.

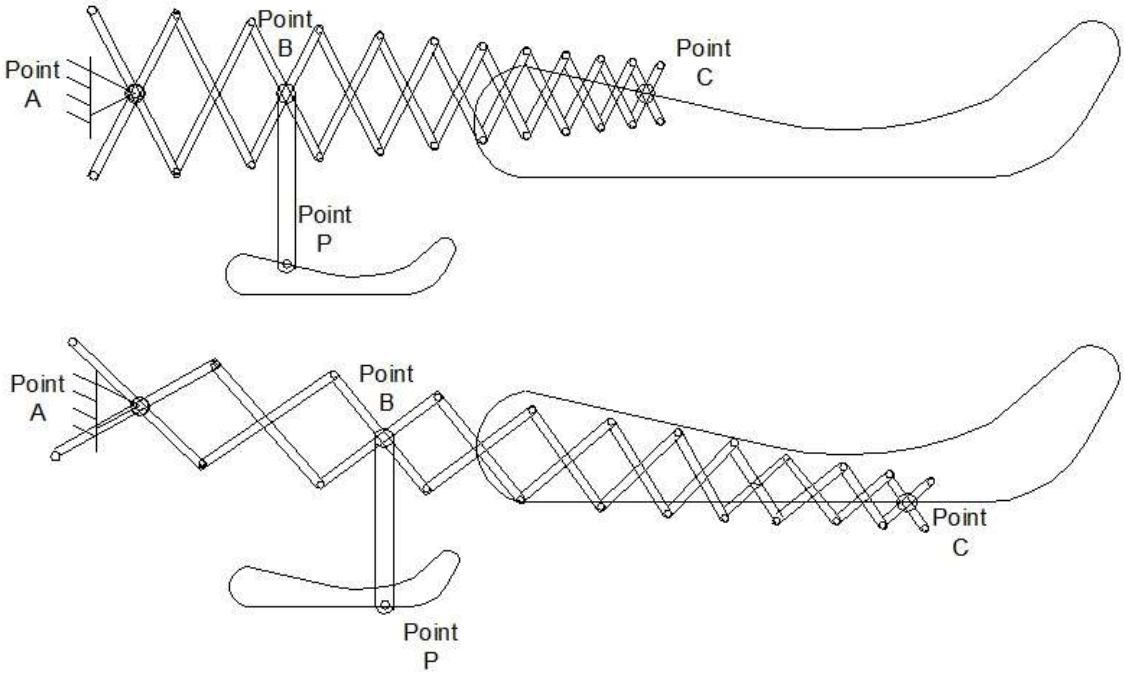

Figure 61. Pantograph Path-Tracing Mechanism: Design 2

This mechanism is significantly more compact than the one shown in Figure 60. Also, scaling on this mechanism simply requires moving along the pantograph's central axis. Constraining point C to a position on the axis would be difficult, however. In order to have accurate scaling, point C must move laterally with the position of the point directly above and below it on the pantograph. One solution would be to pin C to different hinge joints of the pantograph, but this leaves for sparse, discrete scaling points.

Another issue with the scissoring joints of this mechanism is that it poses a potential pinch risk. For a device intended to be used with children, having dangerous, pinching joints would cause serious concern for users of the device and could damage the machine. This would require shielding, and would produce a rather bulky enclosure.

This pantograph machine is constrained only to move along one plane. With large loads transmitted through the system from point C to point B, this likely would cause some twisting of the pantograph rods. This would need to be minimized to prevent damage to the system.

6.3.3 Assessment of Pantograph Feasibility

The pantograph mechanism has been proven to be a potent mechanism, and has implications in art [115], with extendable arms [116], minimally-invasive surgical robots [117], and other applications. Each of these applications, however, involved low-load situations, and the extension of the pantograph was much slower than would be needed for a gait therapy robot.

Because of the loading conditions required on a gait machine during operation, the difficulty in scaling, the safety concerns of using this for pediatric patients, and concerns over the machine jamming or damaging itself during operation, the pantograph device was not pursued.

6.4 Foundations of Parametric Gait Modeling

In direct path modeling, the trajectory of the metatarsal from Figure 35 was recreated using known mechanisms. For parametric gait modeling, the gait path is broken up into separate, independent coordinate pairs based on the time, similar to the parametric mathematical modeling that was performed in Section 4.2.2.

Parametrization in Cartesian coordinates is difficult to scale. Independent mechanisms controlling the X and Y positions of the foot pedal are required, and each mechanism must be scaled about a defined point. This requires two adjustable, scalable inputs for the system.

As an alternative to Cartesian parametrization, polar parametrization only requires one scalable, radial input and one fixed, angular input. Due to the dimensionless nature of the angle, no scaling is necessary. However, the origin of the polar parametrization is important to controlling the trajectory of the foot, as shown by the vastly different curves presented in Section 4.2.2.

6.4.1 Leading Foot Parametric Solution

To match the design goals presented in Section 6.1, the mechanism must not be too difficult to scale, or become excessively large when scaled. For example, consider a crank-slider system with an origin consistent with the parametric origin located 1.5 stride lengths in front or back of the foot, as shown in Figure 62. Note that a metatarsal trajectory curve is plotted on top of the sliding foot plate in this figure.

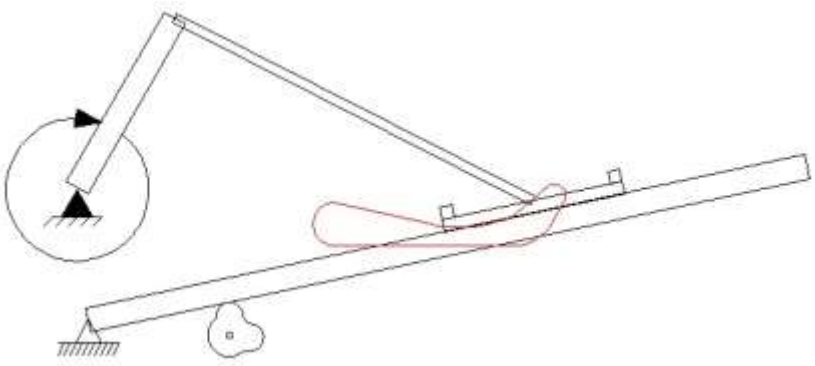

Figure 62. Sample Radial Parametrization of Metatarsal Trajectory

This system would require the radial and angular positions seen in Figure 26 or 27, which generates very smooth, easily replicable trajectories. However, if a 40-in. long

stride length were to be obtained by this mechanism, the scaling for those particular curves would require at least 80 in. of space between the origin of the rotating bar and the rear of the metatarsal trajectory according to these design parameters. Note that the distance between the rotating bar and the rear of the trajectory does not account for the length of the foot pedal behind the metatarsal. This distance was undesirable, and creates an excessive mechanism footprint. Moving the origin point closer to the metatarsal trajectory does decrease the required distance, but the change in angle of the bar during one cycle increases.

6.4.2 Hip Origin Parametric Solution

As discussed in Section 4.2.2 and references 92 and 93, the toe trajectory has been modeled as tracing an arc trajectory about the hip. Using the toe trajectory in Figure 30, a device could be designed to mimic the toe trajectory while rotating about the hip. For example, one realization involves attaching a foot pedal to an actuated, adjustable linkage that lifts the foot during stride and lowers during gait (similar to Figure 30). The cadence of this motion could be controlled with a four-bar linkage. This idea is shown in Figure 63.

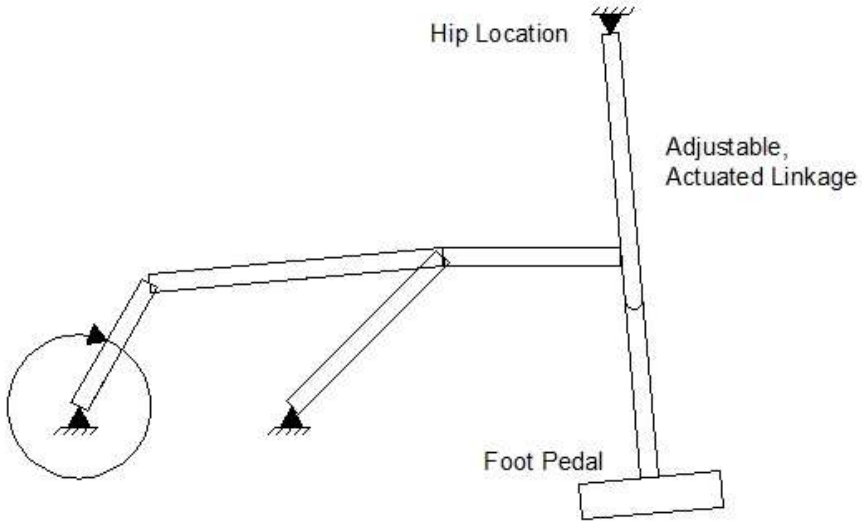

Figure 63. Scalable Device with Polar Origin at Hip

While this idea is feasible, it would require novel design to make the stride adjustment between 8 and 40 in. This design shows some promise, as it is accessible from the rear for body weight support mechanisms. This device would be wider than traditional gait therapy mechanisms, and may not fit through doorways. Due to time restrictions, this idea was not pursued.

6.4.3 Parametrization to a Point on the Gait Path

A mechanism with the origin located on the gait path would be conceptually simple. This would minimize the footprint of the mechanism because the length of the system utilized by the user would be determined by two factors: the maximum stride length and the length of the foot pedal. Having an origin located on the gait path would also make placement of the handle bars easier. However, tracing the metatarsal trajectory with polar coordinates results in radial-angular curves like the ones seen in Figure 25. The discontinuity in the angular data is associated with high angular accelerations, which are unrealistic.

Using the mathematical-average metatarsal and foot angular data from Chapter 4, it is possible to construct an equation that describes the gait trajectory at each location along the foot. This equation is given by

$$\overrightarrow{V_p} = \overrightarrow{V_m} + L_{p-m} * \langle \sin(A_f), \cos(A_f) \rangle$$

Equation 6-3. Foot Point Gait Path Determination

where $\overrightarrow{V_p}$ is the set of X,Y vector coordinates defining the gait path of the chosen location of the foot, $\overrightarrow{V_m}$ is the set of X,Y vector coordinates defining the metatarsal gait path, L_{p-m} is the distance from the metatarsal to the chosen foot location (normalized by the stride length), and A_f is the angle defining the foot angle during gait.

Equation 6-4 can be used to cause the swing and stance trajectories to be tangent at 0, resulting in the angular and radial position parametrizations shown in Figures 64 and 65. With this new trajectory, a radial parametric equation to be established at the center point of the stride. It was determined that when $L_{p-m} = -0.1$ (at a point in front of the foot located 0.1 stride lengths ahead of the metatarsal), the gait path resembled that of Figure 64.

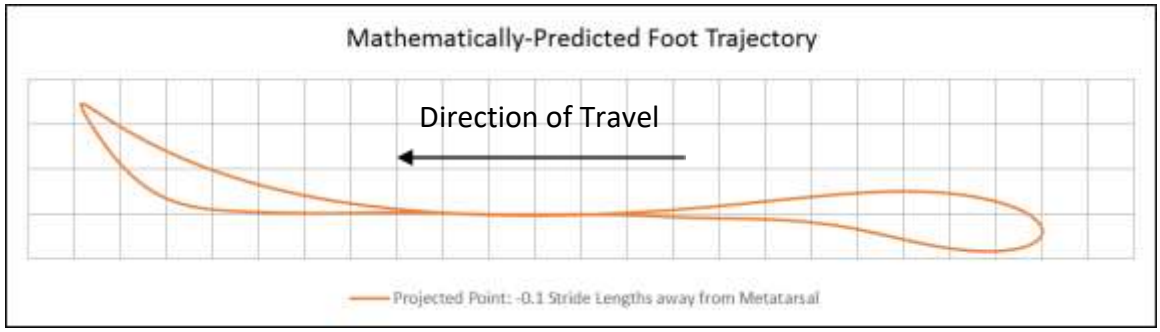

Figure 64. Projected Foot Path with Minimized Trajectory Height at Center Stride

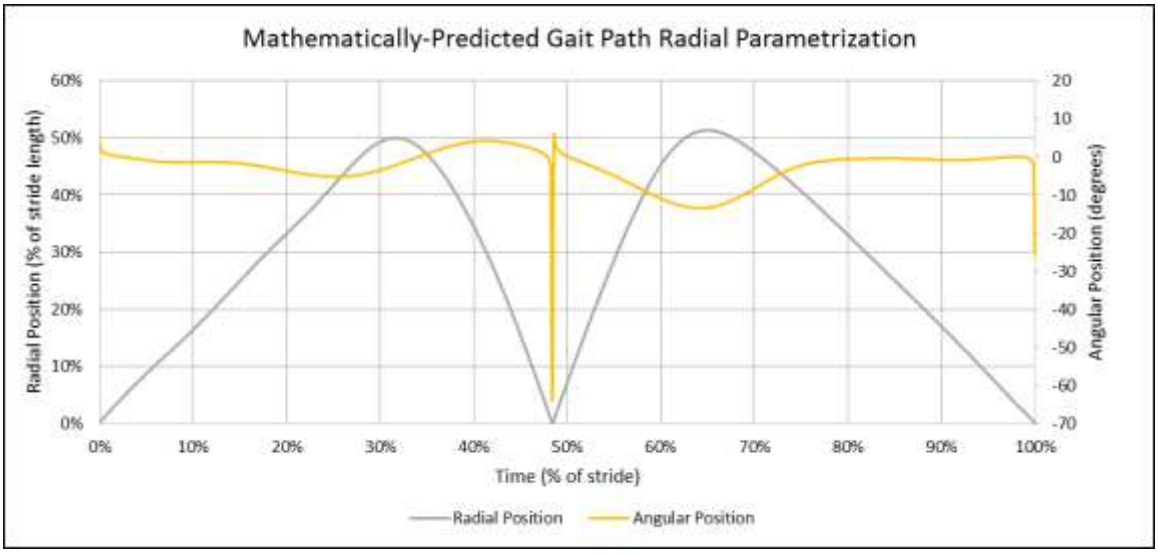

Figure 65. Raw Radial and Angular Traces of Mathematically Predicted Point

Both the angular and radial position of Figure 65 show discontinuity at the start and end of the stride, and the midstride also experiences a discontinuity. To compensate for both of these, the radial position was allowed to become negative for half of the cycle, and the angular position was forced to be zero directly at and around the discontinuities. The resulting parametrization is shown in Figure 66.

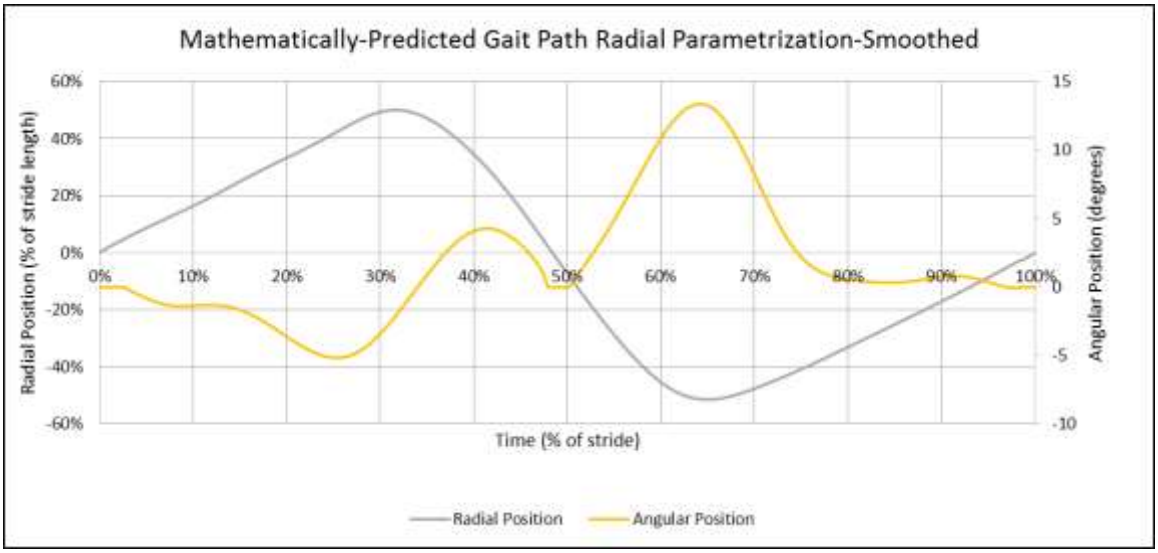

Figure 66. Smoothed Mathematically-Predicted Gait Path Radial Parametrization

As shown above, it was possible to find a point on the foot that follows a trajectory that tangentially intersects itself at the stride midpoint. However, the foot does not pivot about this point. Modeling the stride about this point requires a forced lift of the heel to operate, or the person would have to lift their foot off of the ground and assume normal heel trajectory. While this would make the gait replication process more difficult, it was considered to be the best method for reproducing gait trajectories.

6.5 Scotch Yoke-Cam – Parametrized Gait Replication

The gait path shown in Figure 64 is promising when considered for parametric modeling. One realization of this mechanism is a sliding foot carriage operating on a rotating beam propelled by a Scotch yoke mechanism (double-slider). The beam angular movement could be controlled by a crank rotating at a constant speed. This design is shown in Figure 67. The rotation of Link B drives the forward and backward movement of the foot pedal, Link D. Adjustment to Link B changes the stride length. Rotation of Link E causes Link A to pivot. In order to center the stride over the pivot point on Link A, the length of Link C would have to be adjusted.

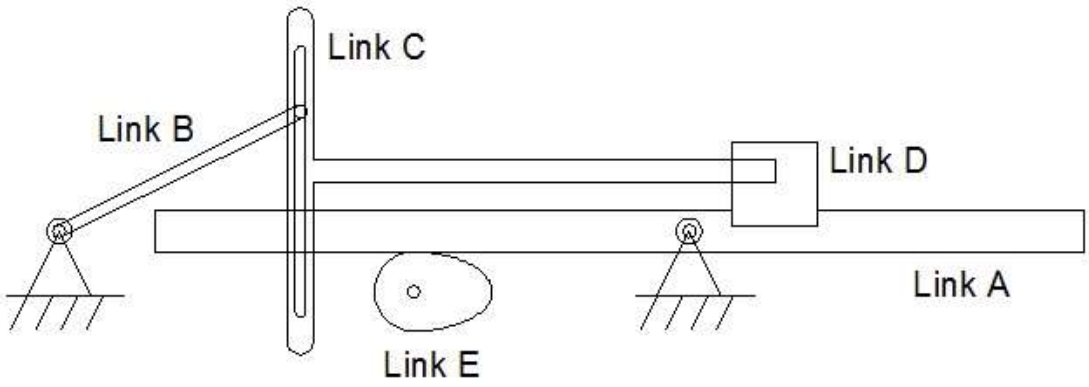

Figure 67. Scotch Yoke Realization of Parametric Modeling

This design showed potential as a solution. The sliding Link C along the rail would pose some frictional issues, and would not be as efficient as possible in that regard. Also, the motor would require a special control to attempt to mimic the timing of the radial curve, which is not perfectly sinusoidal.

6.6 Rocker-Cam – Parametric Gait Replication

Building on the idea of the Scotch yoke mechanism described in Figure 67, a rocker-crank mechanism was proposed to propel the foot through the movements. The rocker would be connected to the forward-backward movement of the foot pedal, and this would be scaled by increasing and decreasing the height of the connection to the rocker, which scales the output distance linearly. The benefit of using a rocker-crank mechanism include (1) fine-tuned design of the four-bar linkage would allow for a rocker movement more consistent with the foot pedal motion, (2) easier scaling, (3) more efficient transfer of load, and (4) more stable application of load than using a pin-in-slot configuration.

Using a crank-rocker to power the foot pedal requires more linkages than a Scotch yoke mechanism. The proposed rocker-cam mechanism is shown in Figure 68. The revolution of the crank (Link A) causes the rocker (Link C) to pivot, which (in turn) slides the foot pedal (Link E) along the rail (Link F). The rotation of the cam (Link G) is in phase with the rotation of the crank, and drives the pivoting motion of the rail.

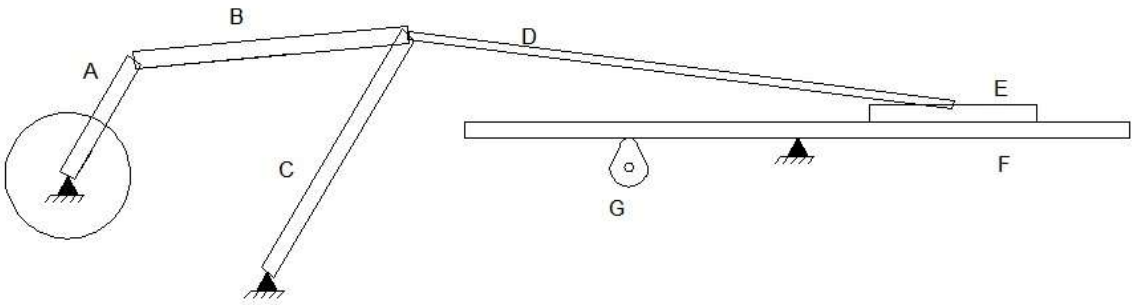

Figure 68. Rocker-Cam Parametric Gait Replication

One problem with the rocker-cam configuration shown in Figure 68 is that the scaling is not linear. Since the connection between the rocker and the foot pedal (Link D) is rigid, moving Link D along the rocker will actually cause the foot pedal position to move slightly. This would have to be compensated for in the final design.

Another issue with the proposed rocker-cam configuration is that the mechanism is difficult to power under the user's will. At the forward and backward positions, the mechanism is difficult to self-power. The machine may require some assistance in moving the feet through this locking position. A flywheel or attached motor would help.

6.7 Conclusions and Chosen Mechanism

While several viable options were considered for realizing the planar gait path replication problem, one option stood out the most as fulfilling the design goal requirements shown in Section 6.1. Direct gait path replication methods showed a strong ability to accurately replicate the trajectory, but did not show acceptable timing control, maximum forces, and mechanism footprint. On the other hand, parametric gait path replication methods showed an ability to precisely control timing and mechanism footprint, but were significantly more complicated and risked de-coupling the radial and angular motions of the foot. It was decided that the rocker-cam design shown in Section 6.6 would be pursued for gait path replication.

CHAPTER 7 – ITERATION I

The rocker-cam mechanism described in Section 6.6 was chosen to replicate the trajectory of a foot point located 0.1 stride lengths in front of the metatarsal. The mechanism was refined, and efforts were made to ensure linear scaling, proper timing, and accuracy of trajectory. A method of integrating heel lift was incorporated into the design in order to facilitate the foot angle changes. It should be noted that due to time restrictions, a full system simulation was not conducted.

7.1 Overall Design

Three separate systems are needed to fully replicate the foot motion:

- The four-bar linkage driving the foot forward-backward motion along the rail
- The cam rotation driving the rail angular position
- The mechanism for heel lift to replicate foot angle during gait

The sliding mechanism attached to the rocker to determine path scaling will be subject to slight vertical motions during the movement of the rocker. One method of compensating for this nonlinearity is to constrain a bar to only move longitudinally. This bar would have a sliding connection with the rocker, and the height of this bar off of the ground determines the overall scaling. Movement of this bar would cause a pinion to rotate, generating a rotational motion. Converting the motion into rotational distance allows for gearing to occur, which minimizes the required size of the four-bar linkage. The rotational motion is converted back into translation along the rail at the central hub.

The mechanism for heel lift must be constant along the length of the rail, remaining unchanged with varying stride lengths. One method of lifting the heel involves

a secondary rail that lifts up the rear of the foot carriage. This could be accomplished through the use of cams and a rail. The proposed concept of the full system is shown in Figure 69.

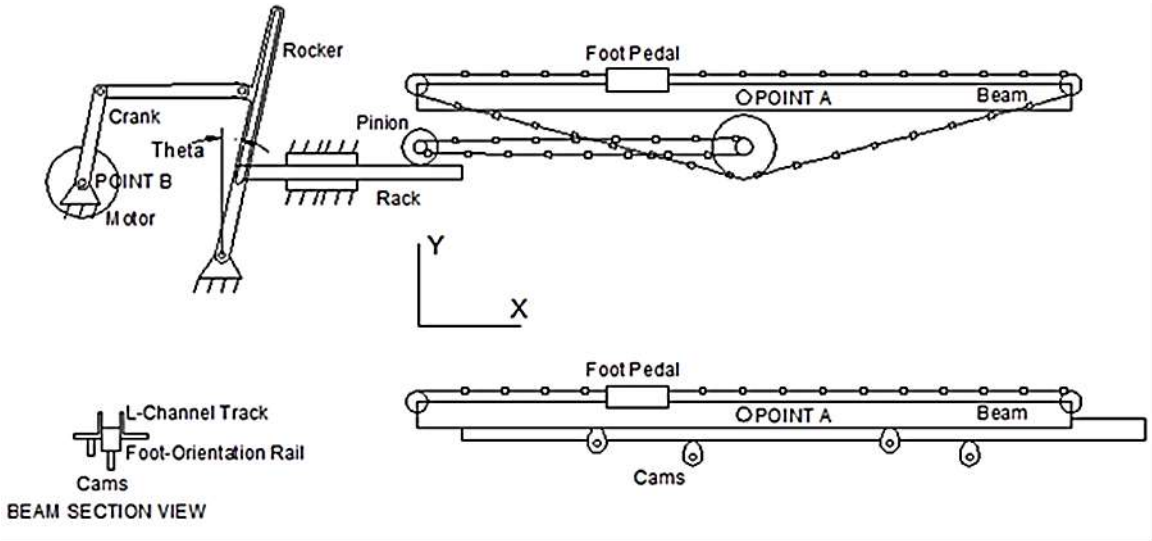

Figure 69. Proposed Mechanism Control Systems

7.2 Rocker Optimization

The four-bar linkage needs to be designed so that the rotation of the rocker matches the timing of the foot longitudinal motion seen in Figure 66. Several considerations go into the design of a four-bar linkage:

- The transmission angle (the angle between the coupler and the rocker) is integral to determining the mechanism efficiency. Transmission angles near 90 degrees minimize power losses.
- The coupler and rocker bar cannot encounter any toggle positions (points where the coupler and rocker are parallel); this may cause the mechanism to experience unpredictable movements and/or catastrophic failure due to shock loading.

- The four-bar linkages must not contact anything during their rotations or else this could cause catastrophic failure or seizure of the machine.
- The four-bar link lengths must abide by the rocker-crank Grashof condition given by Table 15.

Special conditions are applied to this mechanism to match the design goals in Section 6.1:

- The mechanism must not have a large footprint.

A simple four-bar mechanism was chosen as a starting point for the design. A crank length of 8 in. was selected. The transmission angle was chosen to vary a total of 60 degrees, deviating 30 degrees from perpendicular in either direction. From these parameters, the rocker length was chosen to be 16 in., and the coupler length was chosen to be 14 in. The resulting configuration is shown in Figure 70.

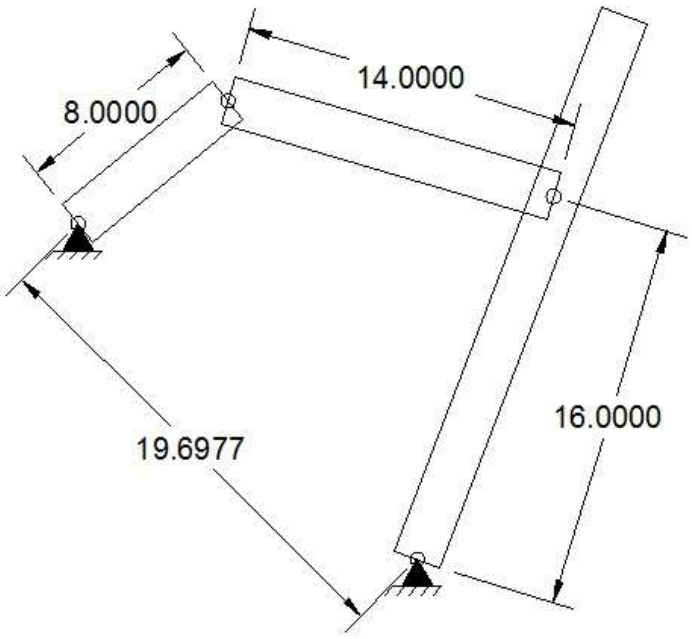

Figure 70. Initial Four-Bar Linkage Configuration for Analysis

An iterative MATLAB program was written to perform a nonlinear optimization on the design of the four-bar linkage. From Freudenstein's equation (Equation 6-2), it is possible to derive an equation for the rocker angle:

$$\varphi = \frac{\cos^{-1}(R_1 \cos\theta + R_3)}{A_3} - \psi$$

Equation 7-1. Rocker Angle (Derived from Freudenstein's Equation)

where each of the dimensionless simplification variables are explained below:

$$A_3 = \sqrt{(\cos\theta + R_2)^2 + \sin^2\theta}$$

$$\psi = \tan^{-1}\left(\frac{-\sin\theta}{\cos\theta + R_2}\right)$$

$$R_1 = \frac{d}{c}$$

$$R_2 = \frac{d}{a}$$

$$R_3 = \frac{a^2 + c^2 + d^2 - b^2}{2ac}$$

Each of the mechanism parameters is explained below:

- *a* is the length of the crank,
- *b* is the length of the coupler,
- *c* is the length of the rocker arm,
- *d* is the length of the ground link, which is the distance between the fixed pivot on the crank and the fixed pivot on the rocker
- θ is the angle between the crank and the ground link
- φ is the angle between the rocker arm and the ground link

To determine the optimal four-bar configuration to match the rocker angle equation from Equation 7-1, a nonlinear optimization method was used. In random stochastic optimization methods (such as genetic algorithms or information search

methods), random variable changes are assessed to determine a minimizing vector direction [118]. For gradient based methods (such as steepest descent or Newton's method), the direction of descent is determined and iteratively utilized to directly find a minimum [119]. By nature, gradient-based methods converge significantly faster than stochastic optimization methods when the search space is "well behaved."

With this problem, the four-bar linkage is limited by the Grashof existence condition for the crank-rocker mechanism provided in Table 15. This also means that the crank must be the smallest link in the mechanism. These constraints can be easily implemented into the gradient-based solution, and thus, the steepest descent method was chosen for optimization.

First of all, a time-dependent least-squares optimization was implemented that summed the squares of the errors between the produced rocker angle and the ideal rocker angle. The optimized function was given by

$$f(\vec{x}) = \sum_{i=0}^{N} (R(\vec{x})_i - FS_i)^2$$

Equation 7-2. Optimization Function (Least-Squares Error)

where *N* is total number of points considered for the optimization; $R(\vec{x})_i$ is the rocker angle given by a particular time in the cycle *i*; $\vec{x}$ is the vector containing the lengths of the crank, coupler, rocker, and ground linkages, respectively; and FS_i is the Fourier series average function value at that time in the cycle. Here, $R(\vec{x})_i$ is given by Equation 7-1 based on the timing of the crank.

The equation for each iteration of a gradient-based optimization method is given by [120-121]

$$\overrightarrow{x_{i+1}} = \overrightarrow{x_i} - \alpha \overrightarrow{P_i}$$

Equation 7-3. Iterative Equation for Optimization Problem

where $\overrightarrow{x_{i+1}}$ is the vector set of the lengths of the four linkages in the next iteration, $\overrightarrow{x_i}$ is the vector set of current linkages, $\overrightarrow{P_i}$ is the vector defining the minimizing direction for this iteration, and α is the scalar applied to the equation to define the magnitude of the minimizing direction to ensure adequate minimization. For the steepest descent method, the minimization direction is given by

$$\overrightarrow{P_i} = \Delta R(\overrightarrow{x_i}) = \mathbf{J}^{\mathrm{T}} * (R(\vec{x})_i - FS_i)$$

Equation 7-4. Minimizing Direction Vector for Steepest Descent

where $\mathbf{J}^{\mathrm{T}}$ is the transpose of the Jacobian matrix of Equation 7-1 with respect to the linkage lengths, $\vec{x}$. Using the steepest descent method of nonlinear optimization, the initial conditions were input and the program was run to completion twice, obtaining two separate four-bar linkage designs. The initial conditions and the result of both program iterations are compared to the desired rocker trajectory in Figure 71. The full MATLAB program code is found in Appendix C. The optimized four-bar linkage configurations are shown in Figures 72 and 73.

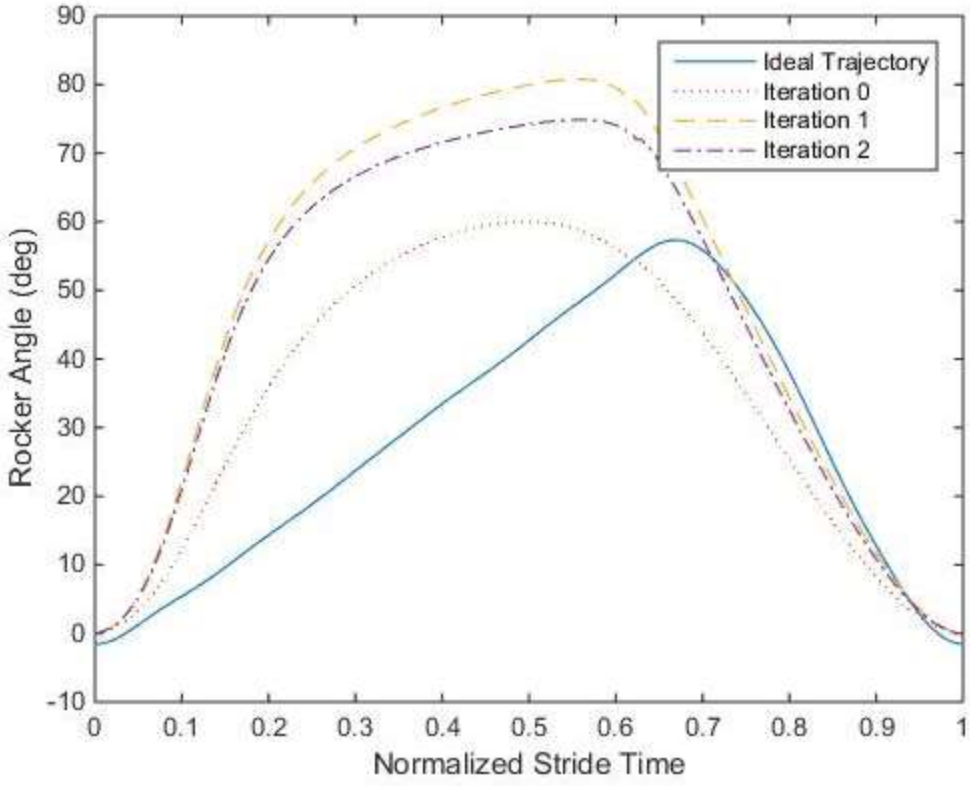

Figure 71. Nonlinear Optimization Comparison of Four-Bar Rocker Angles

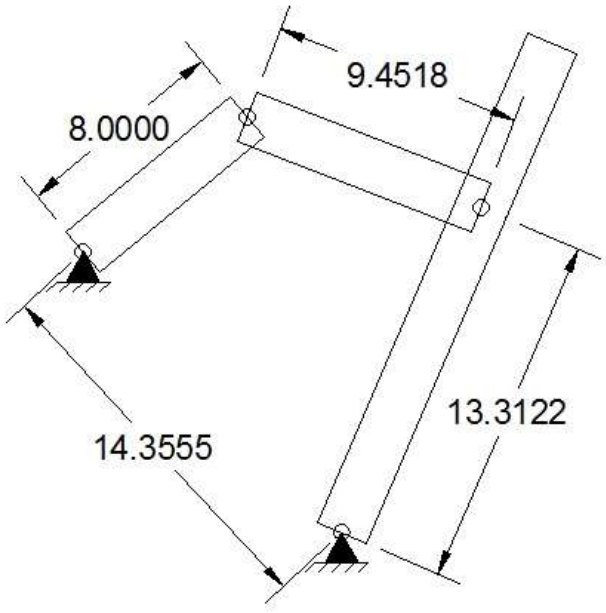

Figure 72. Nonlinear Optimization Configuration I

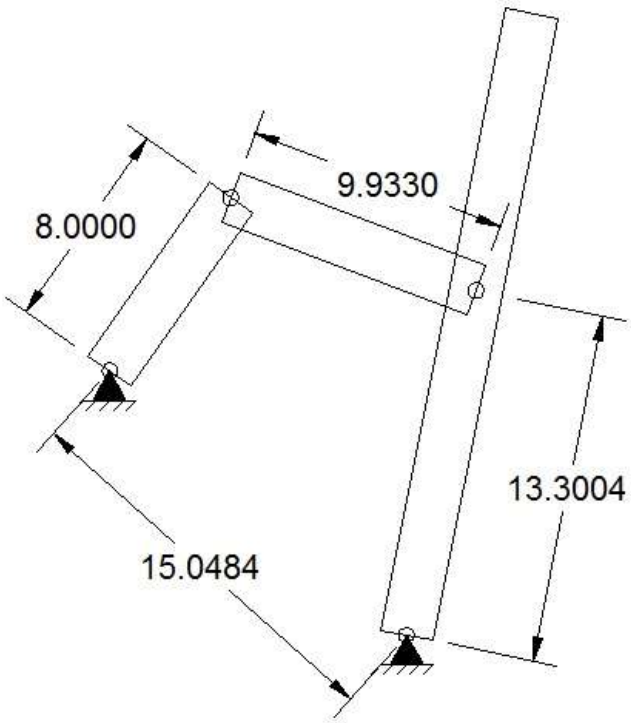

Figure 73. Nonlinear Optimization Configuration II

7.2.1 Discussion and Four-Bar Selection

Comparing the rocker angles given in Figure 71, the original, non-optimized rocker angle curve generated by the mechanism in Figure 70 appears to approximate the ideal curve well. Using a least-squares method of determining error, the 200-point curve had an error value of 5.49, as compared to the optimized curve's error value of 1.72. A least-squares curve does not fully explain the closeness of fit, however. While it does mathematically show that the curve better follows the shape of the ideal rocker angle, the optimized curve does not show that it is a better fit for driving human foot motion. The non-optimized rocker appears to be smoother and does not have as sharp of a transition between forward and backward motion, which would reduce the stresses imparted on the system by minimizing the accelerations. Efforts to force smoothness on the optimization code would result in four-bar configurations that are less accurate than the initial

configuration. For these reasons, the non-optimized four-bar linkage from Figure 70 was selected for use with the gait therapy device.

7.3 Cam Design

A trajectory can be explicitly written as a parametrized set of coordinates that are functions of time. Implicitly, each coordinate is dependent on the other coordinate. Small changes in the timing of one coordinate can drastically affect the overall trajectory, producing a highly erroneous shape. From Section 7.2, the chosen four-bar linkage results in a rocker angle profile that differs from the desired rocker motion. In order to have a working parametrization, the crank angle (and the position of the cam, which is integrally linked to the crank angle) must be adjusted. Using a lookup algorithm to determine when the corresponding time is for each crank rotation position, the difference between the actual time and the required crank position can be measured. This timing lag is shown in Figure 74. This can be used to adjust the rail angle for the new design.

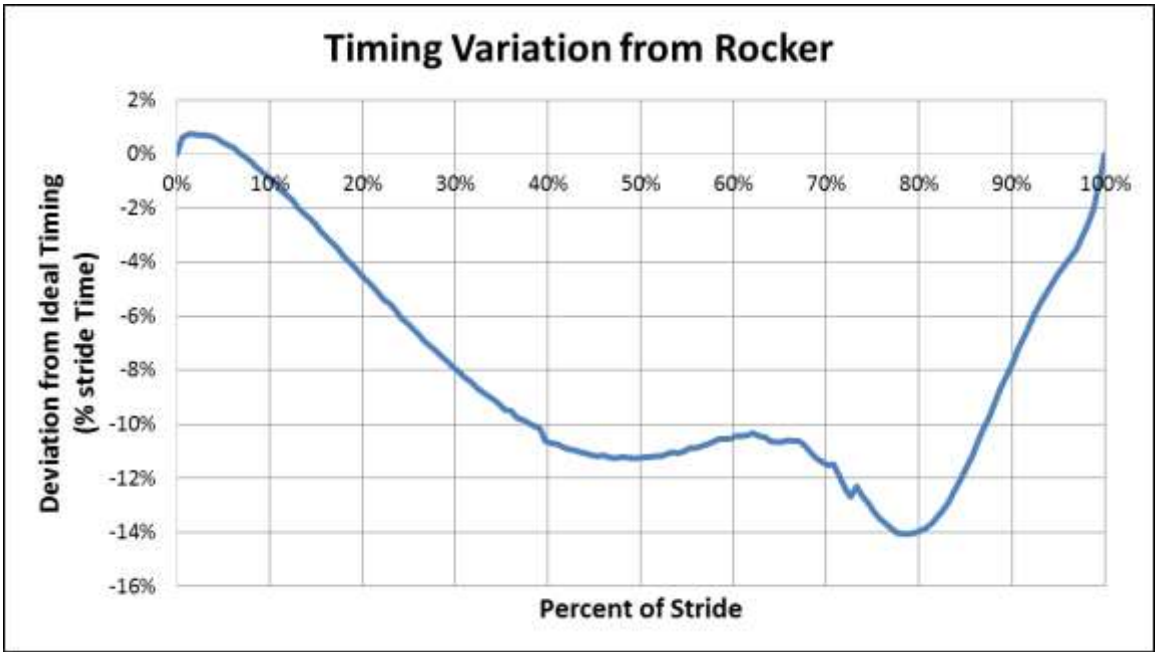

Figure 74. Timing Lag for Chosen Four-Bar Linkage

Cam placement along the rail affects the cam acceleration, cam displacement, and cam loading. Two issues arise when considering cam placement. (1) The farther away from the pivot point the cam is, the larger the cam height variability, higher necessary velocities, and larger accelerations by conversion of radial to Cartesian coordinates. This equates to higher forces transmitted through the cam. (2) The closer to the pivot point the cam is, the longer the cantilever when the foot pedal is at its maximum stride length. Longer cantilevers mean that the rail is subject to more instability, as the user feels more movement in the system further from the pivot point.

Since the maximum stride length was ideally chosen to be 40 in., the cam position was picked to be half of that – 10 in. away from the pivot point in either direction. Having dual cams allows for the rail to be supported fully as the foot travels through the trajectory. Using the cam placement and the timing lag determined from Figure 74, the cam vertical profile was generated. The cam vertical profile is shown in Figure 75.

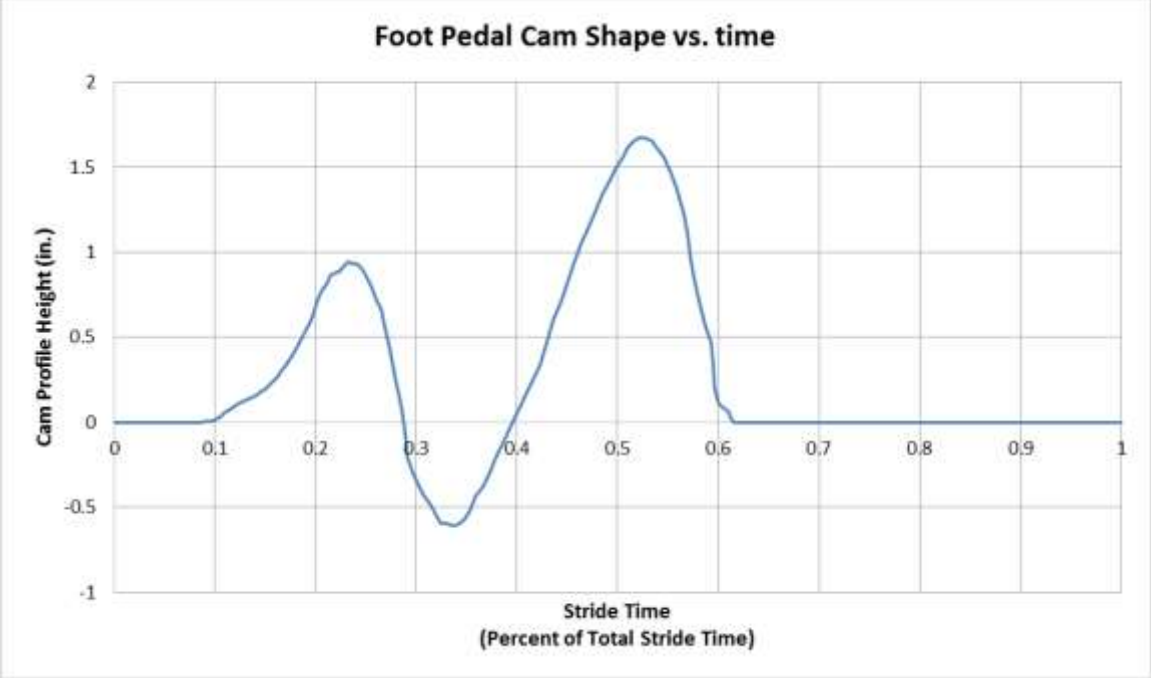

Figure 75. Time-Adjusted Cam Height Profile

Ideally, the cam would rotate at approximately 1 rev/s (2π rad/s). The cam acceleration was determined using trapezoidal numerical integration. Unfortunately, placing the cam at 10 in. away from the pivot line meant that the cam experienced extremely high accelerations at this rotation speed. It was decided that accelerations should be limited to approximately the gravitational constant, which is recommended to maintain sufficient contact between the cam and the follower [122]. A 330 in./s^2 maximum acceleration was manually applied to the profile. Both the ideal and acceleration-limited profiles are shown in Figure 76. Note that the accelerations were zero outside of the bounds of this graph. Using the second derivative of the cam height position from Figure 75, the acceleration-limited cam displacement was compared to the ideal cam displacement. The resulting profile is shown in Figure 77.

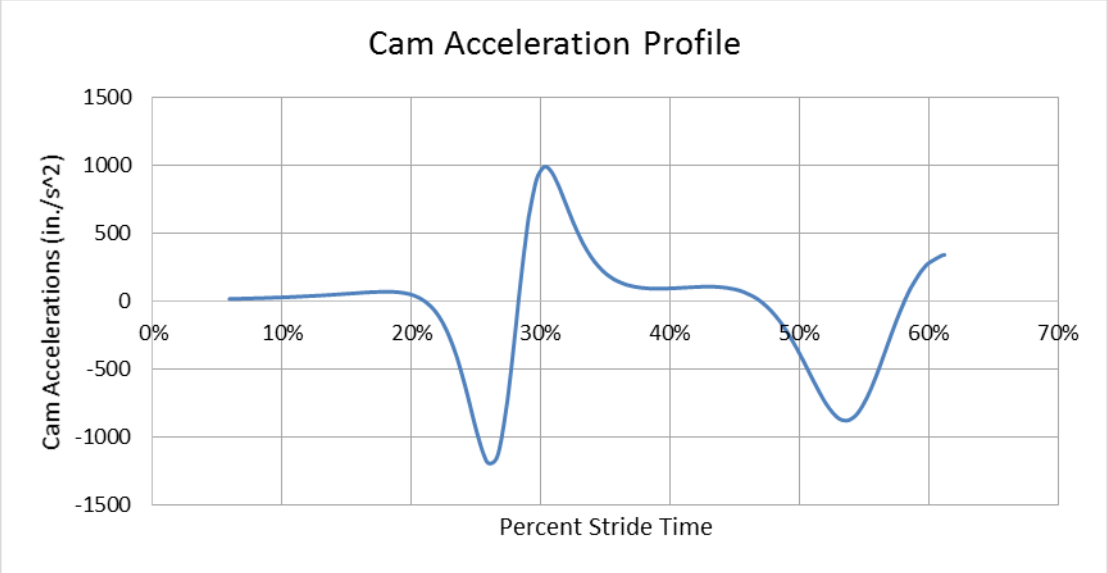

Figure 76. Cam Acceleration Profile

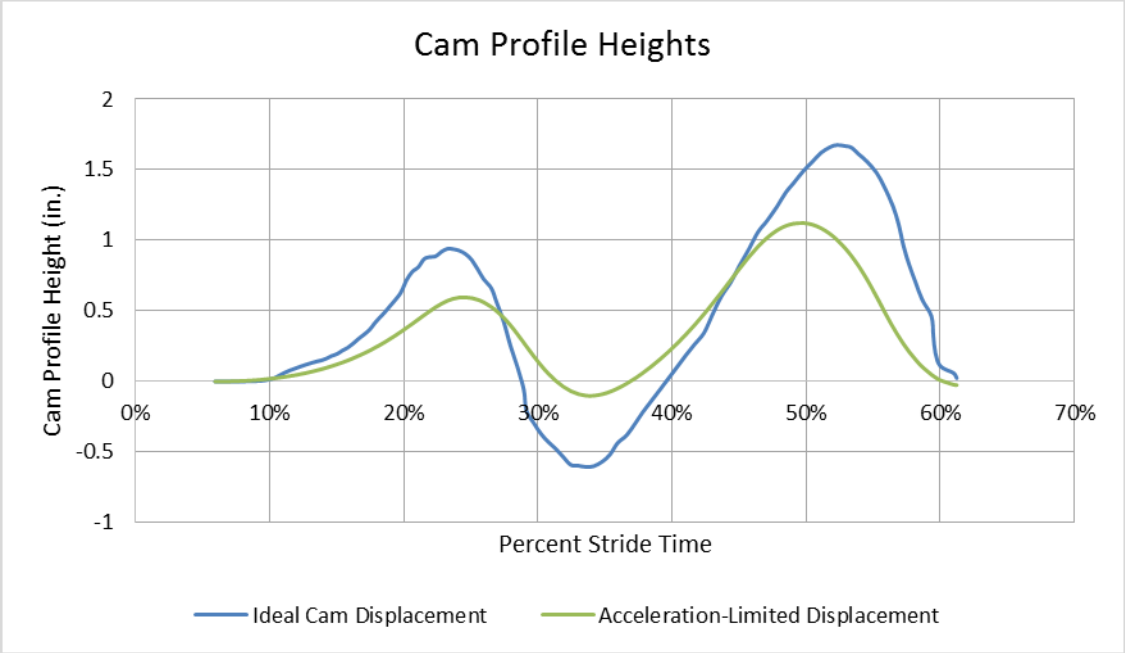

Figure 77. Cam Displacement Profile

While the acceleration-limited cam displacement did not result in the desired angular displacements, it was enough to register a significant rail movement. Using the acceleration-limited cam displacement profile, a cam was generated. The full cam shape is shown in Figure 78. The projected foot path generated by using the four-bar linkage from Figure 70 paired with the cam shape from Figure 78 is shown in Figure 79. Note that the two trajectories are similar, though the mechanical trajectory shows obvious narrowing.

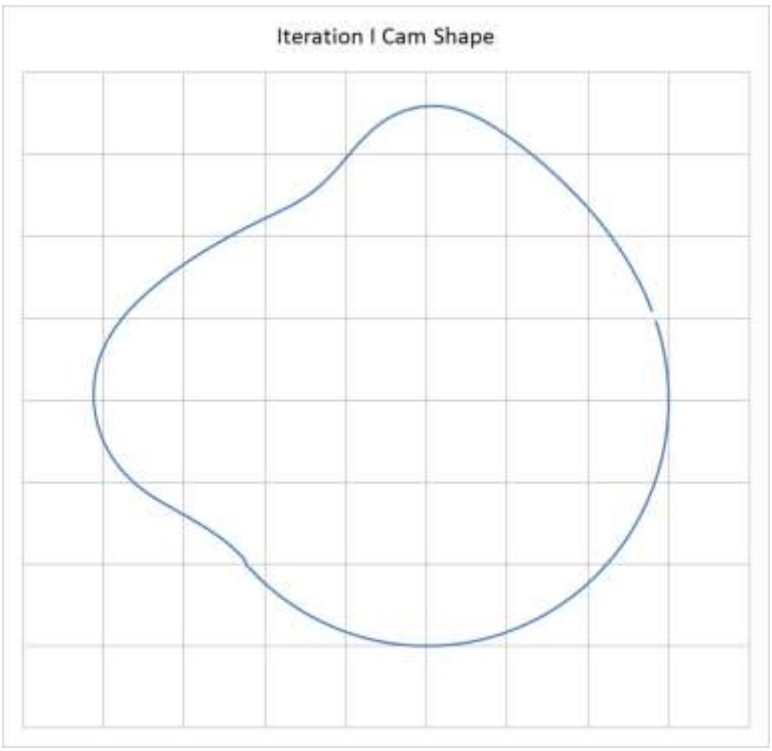

Figure 78. Iteration I Cam Shape

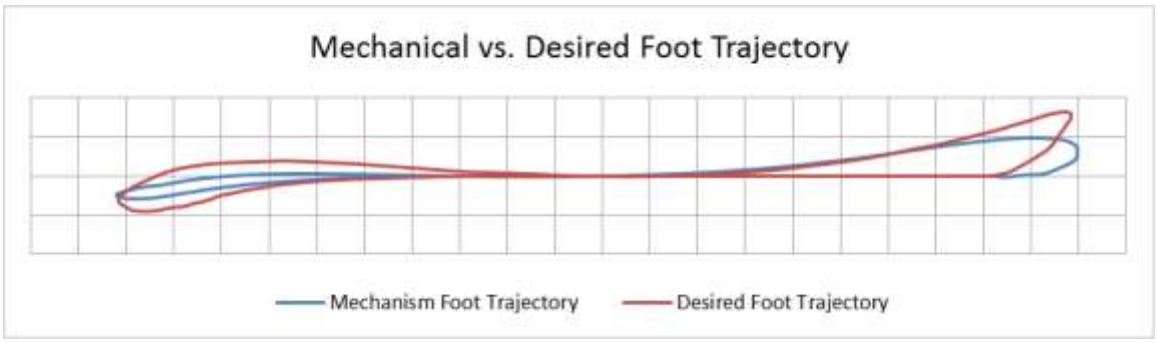

Figure 79. Mechanical vs. Desired Gait Trajectories

The purpose of powering the toe through a gait-like trajectory is to attempt to simulate walking. While the mechanical gait-like trajectory was a reduced form of the desired trajectory, it would still displace the foot from the ground, which may be enough to trigger a gait-like motion. Testing will determine the effectiveness.

7.4 Foot Angle

The foot angle was decided to be fixed by lifting the rear of the foot carriage. To accomplish this, a rail underneath the foot carriage rose and engaged a wheel on the underside of the foot carriage, causing the carriage to rotate upward. The distance needed for this lift depended on the placement of the wheel relative to the pivot point. The farther away from the pivot point that the wheel was mounted, the larger the distance to lift the foot. At the same time, the closer to the pivot point, the more difficult to constrain the foot pedal lateral and rotational movements.

A 5-in. diameter wheel was mounted to the bottom of the foot pedal 6 in. away from the pivot point, resulting in the geometry shown in Figure 80.

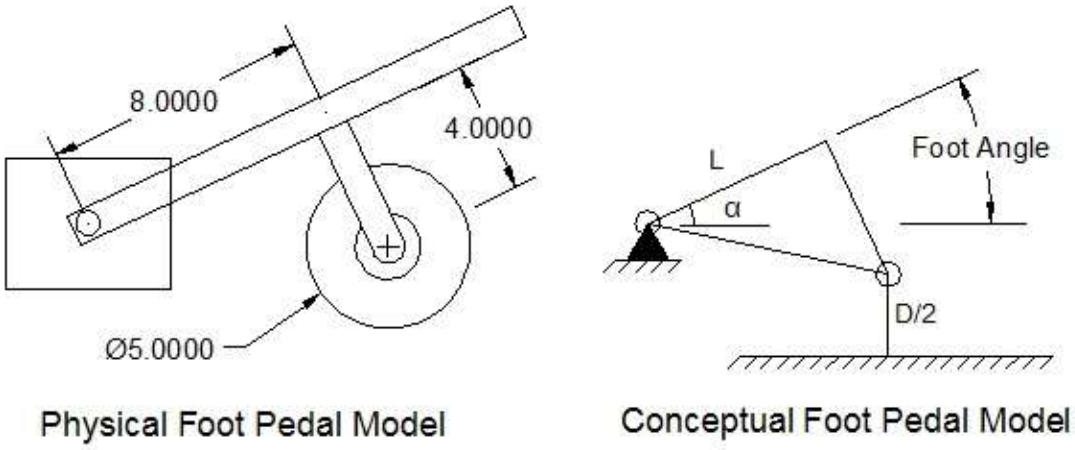

Figure 80. Foot Pedal Model

Based on the foot pedal geometry, the foot angle correlated with the rail lift according to the equation:

$$b = L \tan \alpha$$

Equation 7-5. Foot Angle Relationship with Rail Lift

where *b* is the height of the heel lift. Applying this correction to the foot angle, the profile for the heel cam was generated. This was adjusted according to the time correction shown in Figure 74, and the resulting heel cam profile is shown in Figure 81.

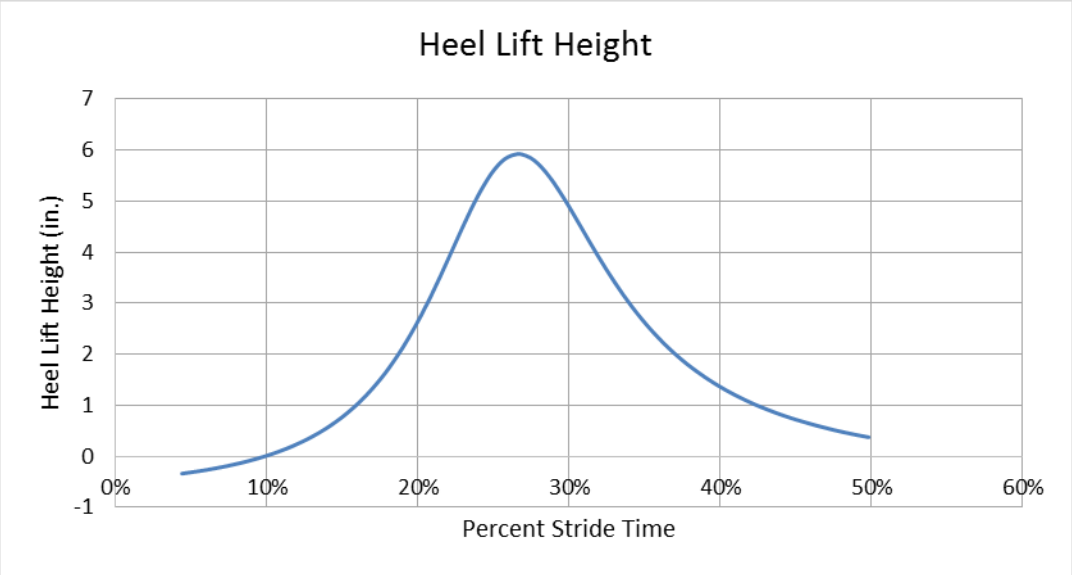

Figure 81. Ideal Heel Lift Height Profile

Acceleration was determined using the displacement profile from. The accelerations of this cam were fairly large for the chosen profile. Using the same maximum acceleration limit set for the rail angle cams (330 in./s^2), a new acceleration profile was generated. The two acceleration profiles are compared in Figure 82. Note that the acceleration is considered zero outside of the bounds of this figure. The acceleration-limited profile was manually generated, and had to attempt to match the ideal acceleration curve. At the same time, double integration of the acceleration curve has to result in a net zero displacement so that the cycle is maintained. The resulting lift acceleration and displacement curves are shown in Figures 82and 83, respectively.

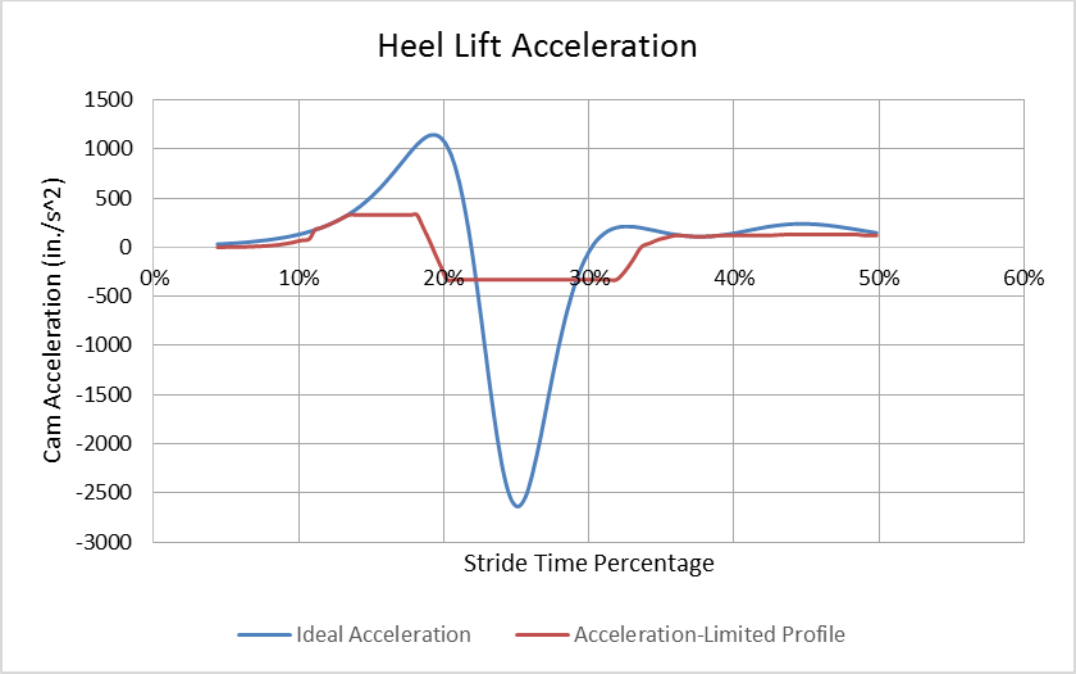

Figure 82. Acceleration Comparison between Ideal and Acceleration-Limited Profiles

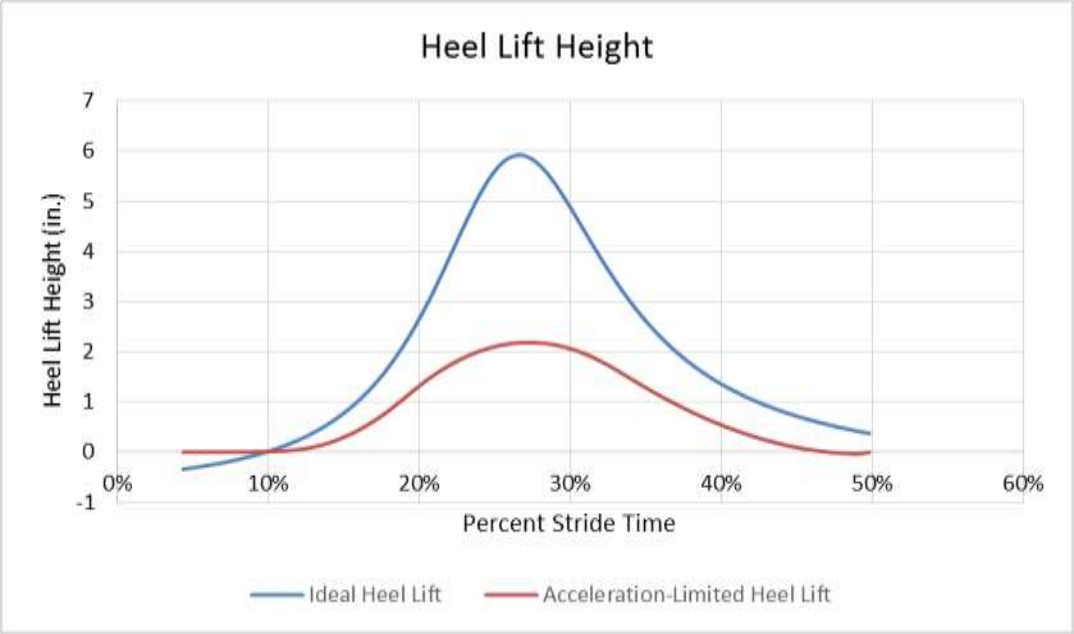

Figure 83. Heel Lift Displacement Comparison

The heel lift for the acceleration-limited displacement profile was significantly lower than the target heel lift displacement profile. The cam profile generated by the heel lift curve is shown in Figure 84. The disparity in heel heights in Figure 83 causes a

deficiency in the foot angle, as shown in Figure 85. While the foot angle was significantly less severe for the acceleration-limited cam profile, it was hoped that minimal pressure on the heel during toe-off would assist the users in manually passing through the full foot motion.

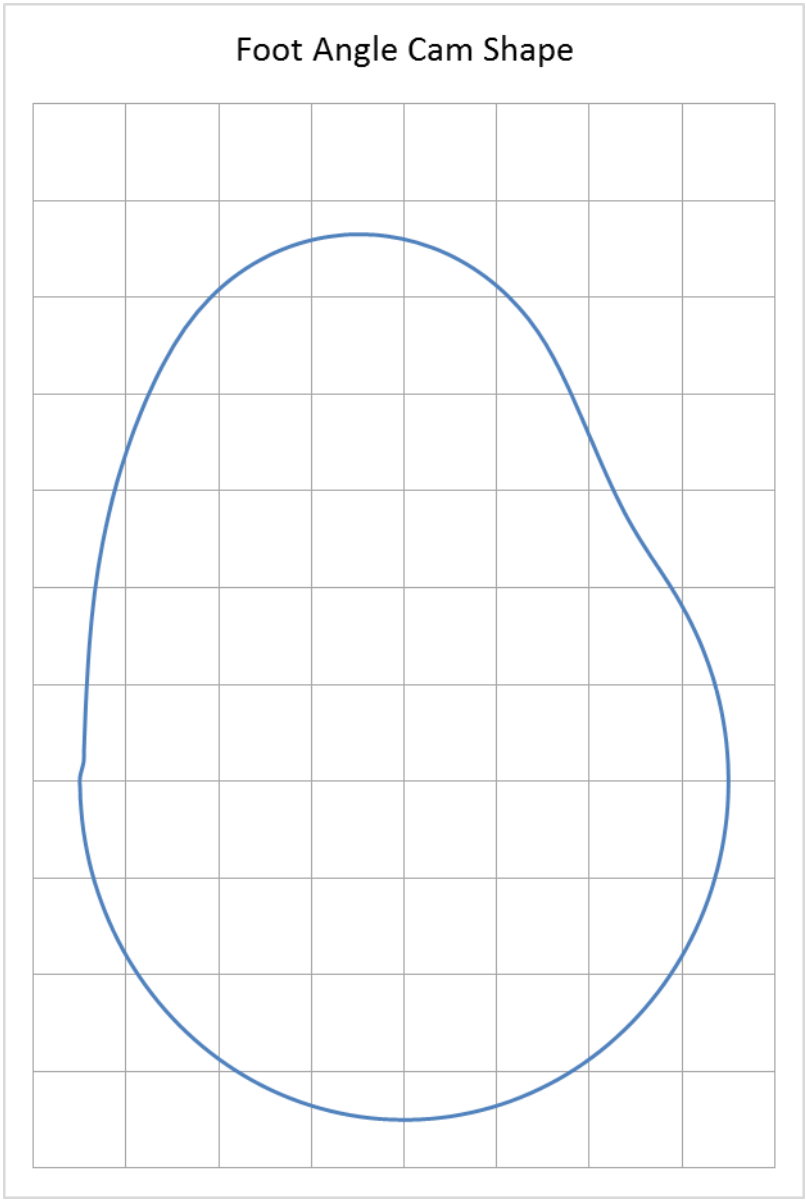

Figure 84. Foot Angle Cam Shape

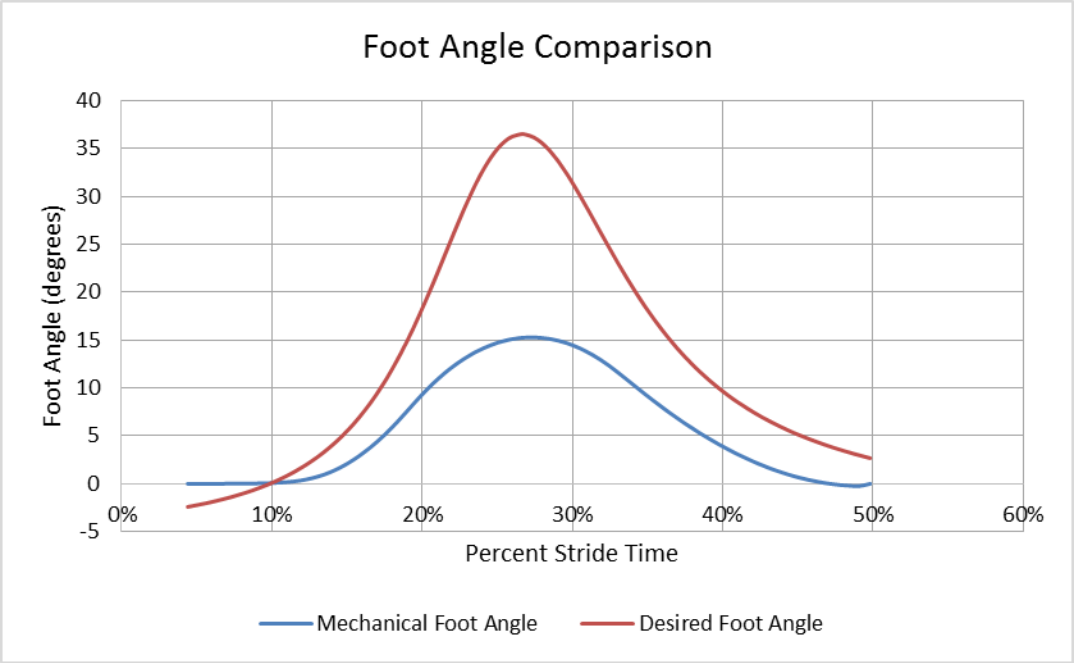

Figure 85. Mechanical vs. Desired Foot Angle Comparison

7.5 Full Construction of Iteration I

The design presented in Figure 69 was constructed using the refined four-bar linkage and cam profiles. The full design is shown in Figures 86 through 89.

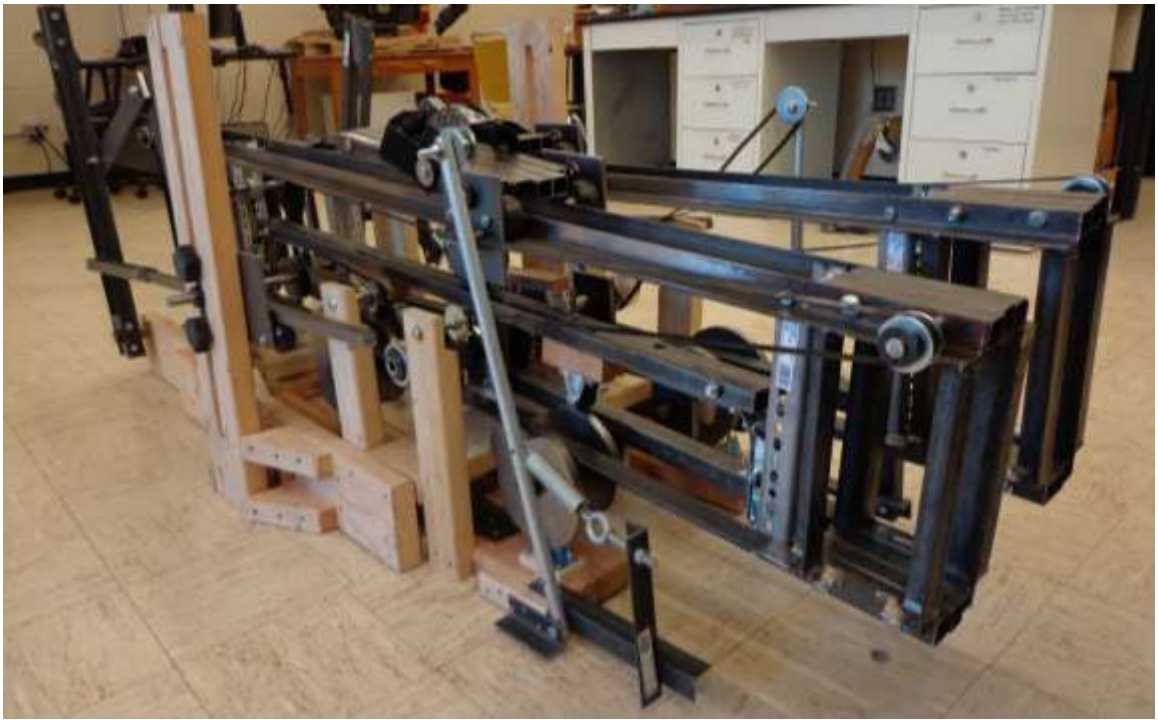

Figure 86. Iteration I Design: Front Right View

Figure 87. Iteration I Design: Front Left View

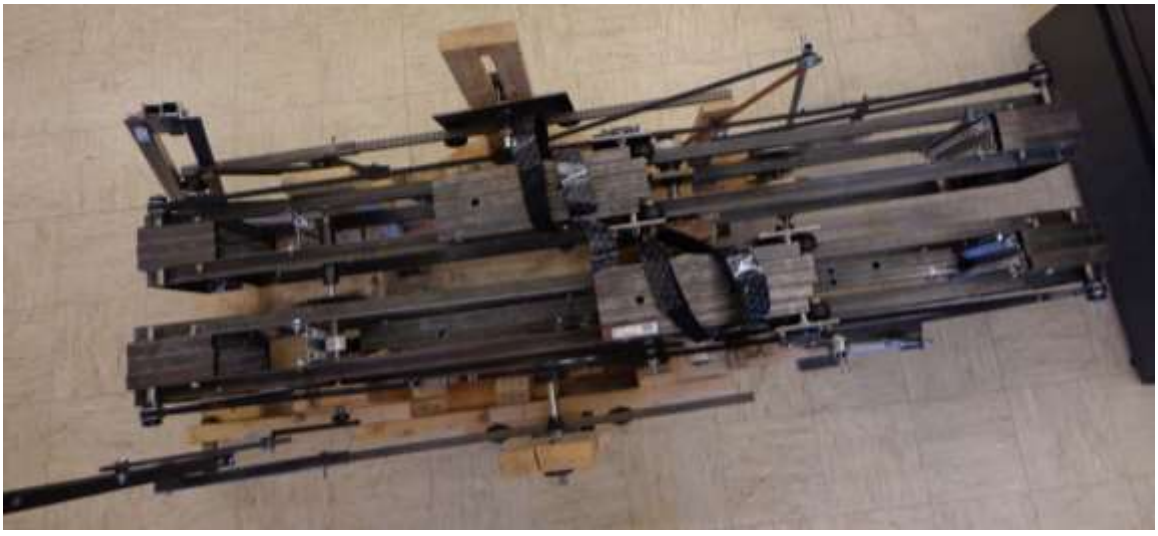

Figure 88. Iteration I Design: Top View

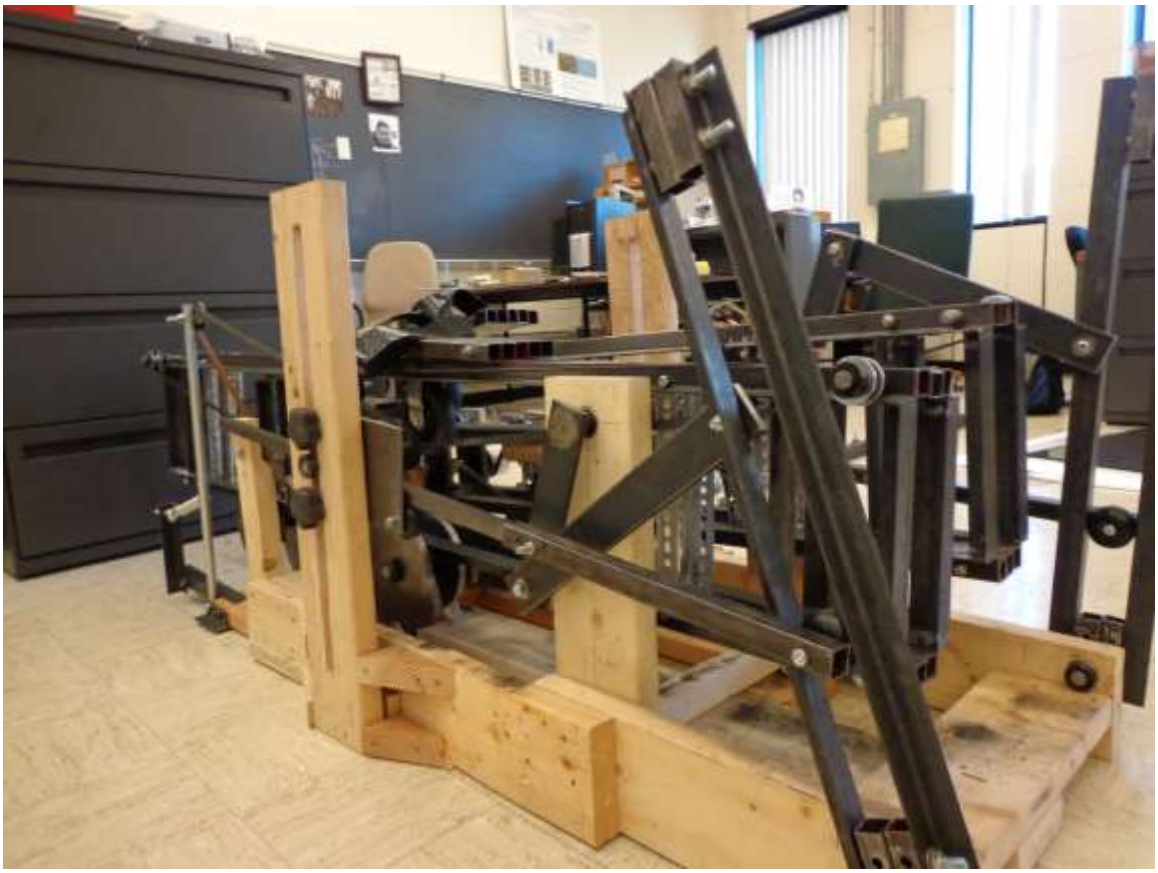

Figure 89. Iteration I Design: Rear Left View

7.6 Iteration I Performance

The mechanism, as constructed, was unable to move under human input. As constructed, the resistances in the system were too great to overcome. When individual systems were powered by hand, they showed marked resistance and movement was choppy.

The inability of the machine to operate naturally means that the foot angle control system was not tested. To minimize the power requirements of the system, analysis on the mechanism was conducted without the foot angle control system in place.

The rail angle control system was overconstrained due to the presence of dual cams and the rail pivoting point. In order for the cams to rotate, the rail had to flex. Applying some clearance between the mechanism and one of the cams alleviated this

constraint. However, the sharp accelerations of the cams made rotation very difficult, and the rail would shake with each rotation.

The foot pedal longitudinal control system was inefficient. As designed in Figure 69, the belt that carried the longitudinal load around the rail had to have tensioners attached to it to maintain contact with the bottom, rotating gear. This caused significant friction in the system, and made the forward and backward motion of the foot difficult. The vertically-constrained bar attached to the rocker experienced large moments, and this caused the mechanism constraining the bar to crack during use. Also, the rack and pinion had difficulties with jamming due to the poor constraints, and made a considerable amount of noise during operation.

Overall, the system was arrested and could not operate under motorized assistance, let alone purely human control. Motion was choppy and loud. The rail was not convenient to use, as it was shaky and tall. The arrested behavior was blamed on poor tolerancing, misaligned shafts, heavy components, rail weight, and large cam accelerations. The performance of Iteration I, compared to the mechanism design goals outlined in Section 6.1, is summarized in Table 16.

Table 16. Iteration I Performance vs. Design Goals

Design Goal	Description	Iteration I Performance
Gait-Like Trajectory	Traced path must resemble average gait curve	Traced path was similar to gait path, including foot angle
Scalable	Must accommodate pediatric and adult patients	Mechanism was scalable for stride lengths, but scaling control fractured
Practical	Usable in small facilities	One motor controlled all functions, easy to manage.
Adjustable	Accommodate specific impairments	Adjustable for varying stride lengths, adjustment was simple
Cost-Effective	- -	Comparably priced due to cheap components
Small Footprint	- -	Heavy, but small enough to be functional in a rehabilitation setting
Motorized	Able to be motorized	Mechanism was arrested, could not be powered at all
Backdrivable	Able to be driven by human power	Impossible to backdrive
Ergonomic	Easy and comfortable to mount and operate	Not comfortable, sturdy, quiet, or easily mounted

CHAPTER 8 – ITERATION II

Design Iteration I was considered a failure. Despite aiming to satisfy all the design conditions of Section 6.1, the inability of the mechanism to move overshadowed its design. As such, a new design was considered and created to replace Iteration I. It should be noted that, similar to Iteration I, time restrictions prevented the construction and evaluation through a full-system simulation.

8.1 Design Goals Revisited

The original design goals for this project were to design a machine that replicated a gait-like trajectory with a scalable output. Ideally, the mechanism would also have a small footprint, be cost-effective, adjustable, backdrivable, motorized, and ergonomic. Iteration I attempted to tackle all of the design goals.

The gait-like trajectory for Iteration I was acceptable. However, the scaling mechanism for Iteration I was overly complicated and caused the mechanism to break. The constraints for the scaling mechanism would need to be adjusted on the new design.

Iteration I had an acceptable footprint. To improve the design, the height of the foot pedals in the new design would need to be decreased to make mounting the machine easier. Ideally, that would also equate with a significant weight decrease.

Iteration I was fairly cost-effective, proving that the design did not need to be expensive in order to be constructed. More leniency on cost would be allotted to the next design to utilize better components and improve the machining quality.

It was not possible to backdrive Iteration I. Further iterations utilizing similar rocker-cam mechanisms to Iteration I would not be backdrivable either, and as such, that design goal was omitted from consideration.

The rail would need to be significantly sturdier in the next design. For Iteration I, the rail was large and cumbersome, and tended to sway noticeably when mounted. Also, to decrease the operating noise, the cam shapes would need to be adjusted to lower the acceleration limits.

Finally, in order to make it functional, methods to reduce the number of tensioners needed and axles needed to operate the machine need to be implemented. For Iteration I, there were four separate cam axles, one central axle, one crank axle, and numerous tensioners to maintain tightness in the long stretches of belt and chain.

8.2 Complete Design

The full design for Iteration II is shown in Figures 90 and 91. This design implemented many of the design changes needed as mentioned above. Overall, the system showed improved power transmission, ergonomics, weight reduction, and manufacturing difficulty, while showing slight increases in nonlinear scaling, reduction of the accuracy of the full trajectory of the foot, and removal of the foot angle control system. Individual changes to components and systems are discussed in the following sections.

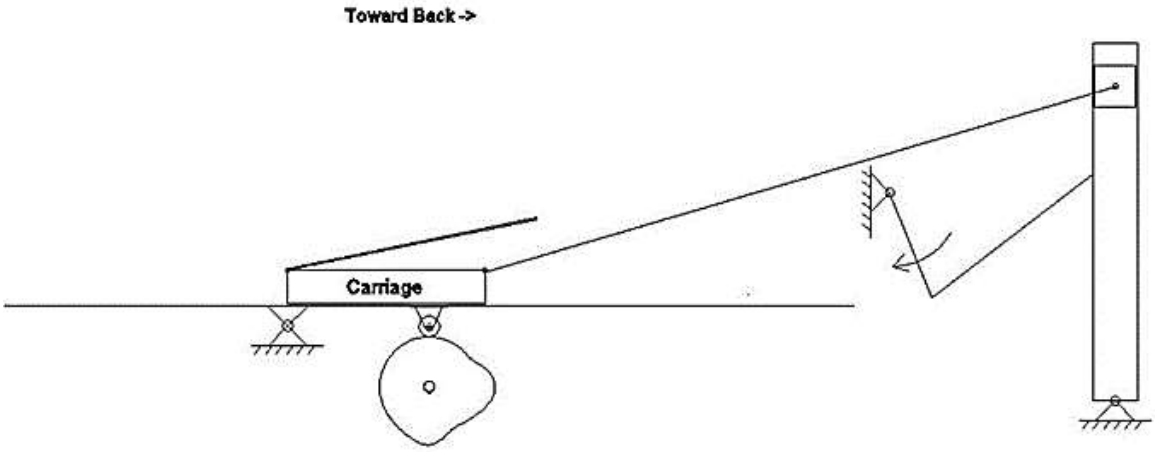

Figure 90. Conceptual Design of Iteration II

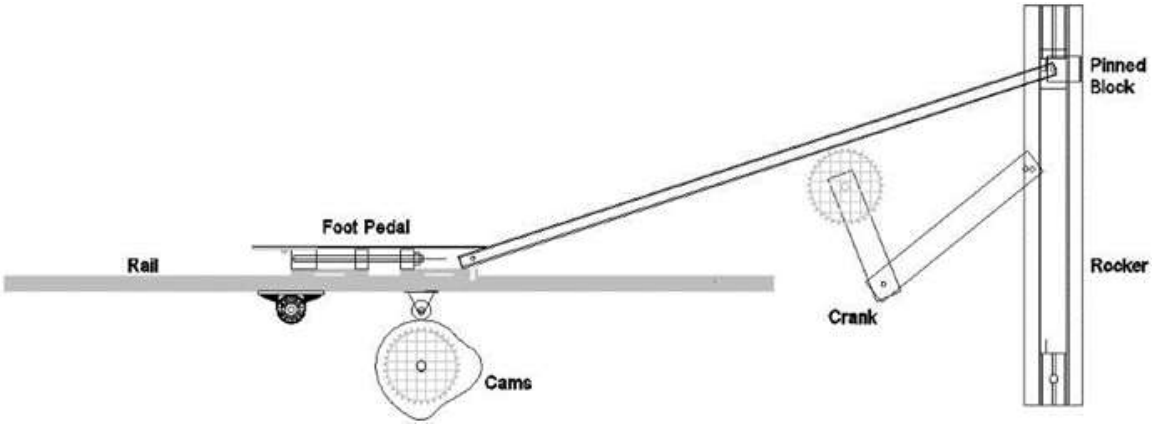

Figure 91. Component Model of Iteration II

8.3 Improved Scaling Mechanism

For Iteration I, the scaling mechanism consisted of a rack that was constrained to slide forward and backward along a horizontal path with oscillation of the rocker. The forces passing through the rocker loaded the machine past its stress limit, causing cracking of the adjustable scaling component.

A simpler method of connecting the scaling bar to the rocker is through a sliding block that is able to move up and down along the length of the rocker. To fix this block in place, a pin was placed through one of many holes vertically spaced along the rocker and into the block. While this did discretize the scaling, it also allowed for repeatable, precise stride adjustments.

Rather than using a convoluted myriad of tensioners, pinions, and axles to connect the rocker to the food pedal, it was decided to directly connect the two. A bar extended from the pinned block down to the foot pedal, where it connected to the foot pedal with a revolute joint. This significantly simplified the connection and minimized potential losses due to power transmission. One issue with this setup is that the distance between the carriage and the block changes depending on how high the connection is above the rail.

Also, the originally horizontal rocking motion created by the rocker now experienced some vertical deflection which increased with increasing stride length. This introduced nonlinearity into the scaling.

8.4 Redesigned Rail and Carriage

The rail design for Iteration I of the gait mechanism device utilized a tall, welded rectangle with a homemade carriage riding along it. The rectangle provided space for the foot angle-controlling rail to translate inside of it. While this option was inexpensive and robust, it was wobbly in out-of-plane motions, tall, and cumbersome. The rail was replaced with an off-the-shelf rail and linear motion carriage, as shown in Figure 92. This configuration, while significantly more expensive than the rail and carriage used in Iteration I, would provide more stability, less frictional losses, and weigh significantly less. Also, the height of the rail was reduced from 12.44 in. to 1.18 in.

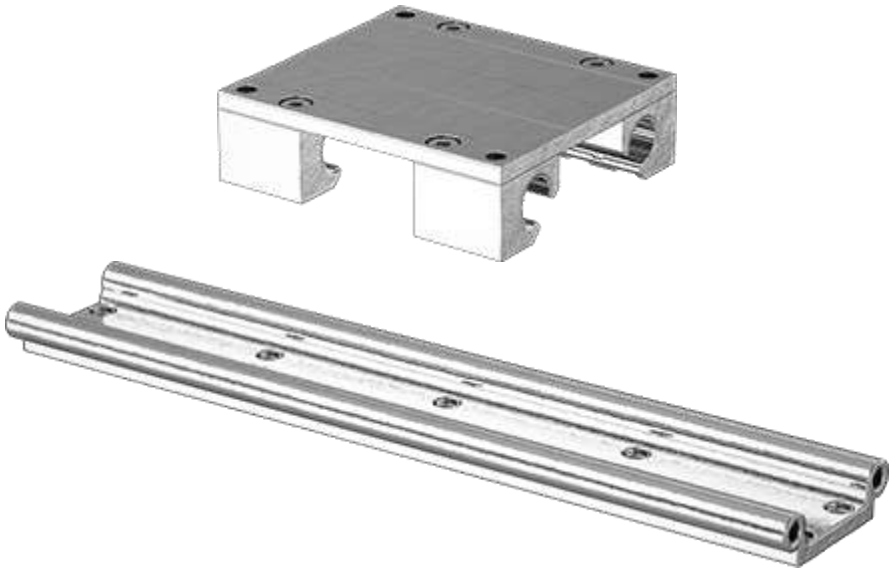

Figure 92. Off-The-Shelf Rail and Linear Motion Carriage

As stated in Section 8.3, the new scaling mechanism caused a change in distance between the rocker and the carriage as the stride length was adjusted. To compensate for that, the scaling mechanism was connected to a secondary carriage riding along the rail.

That carriage was connected to the foot pedal carriage through an adjustable link (screw). The idea behind the adjustable link was that it would allow researchers to fine-tune the location of the carriage to the correct position. This is important since the full foot trajectory is scaled about the center point of the stride at the pivot point of the rail.

8.5 Cam Acceleration Limitations

The cam profile from Iteration I proved to be too severe. It was decided that the profile would be further limited in acceleration to approximately 60% of the gravitational acceleration, or 220 in./s^2. The decision to use 60% of the original accelerations was arbitrary, and due to the time constraints of the design, further optimization analysis was impossible (but could still be done in the future). The resulting cam acceleration curve for the Iteration II cam is compared to the Iteration I cam and the desired rail acceleration in Figure 93. The resulting rail angular displacement is compared to Iteration I and the desired displacement in Figure 94.

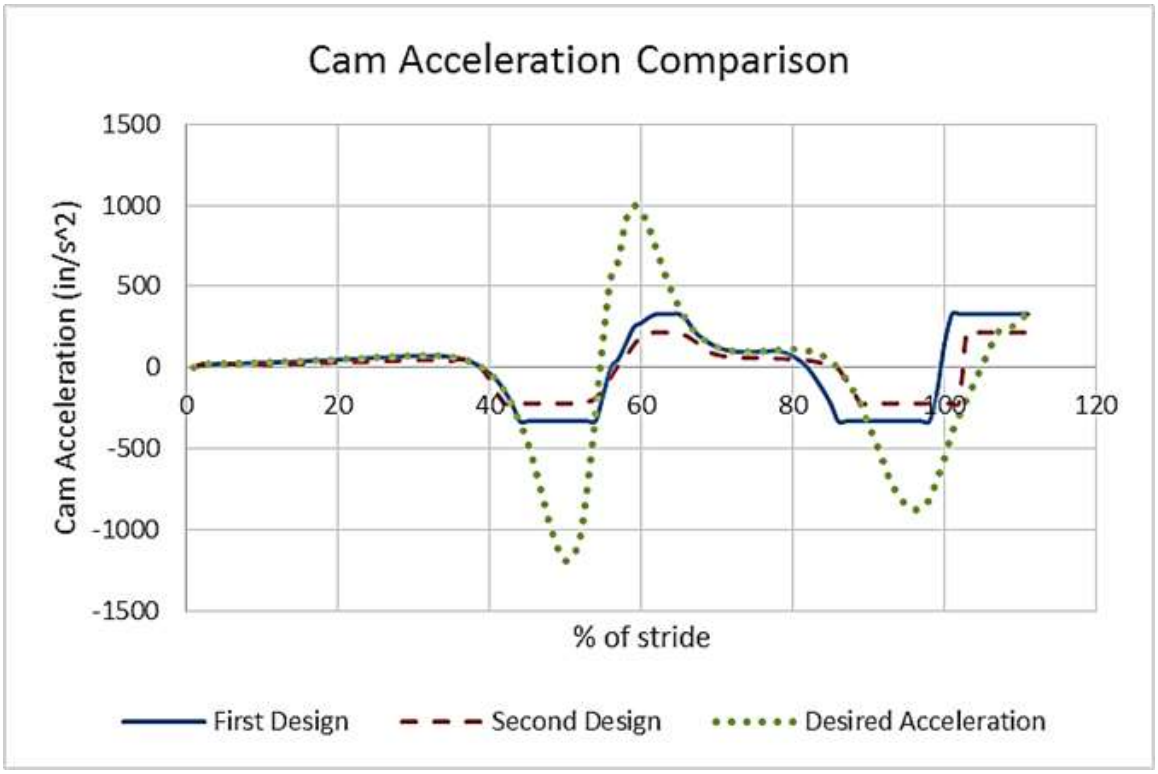

Figure 93. Cam Acceleration Comparison

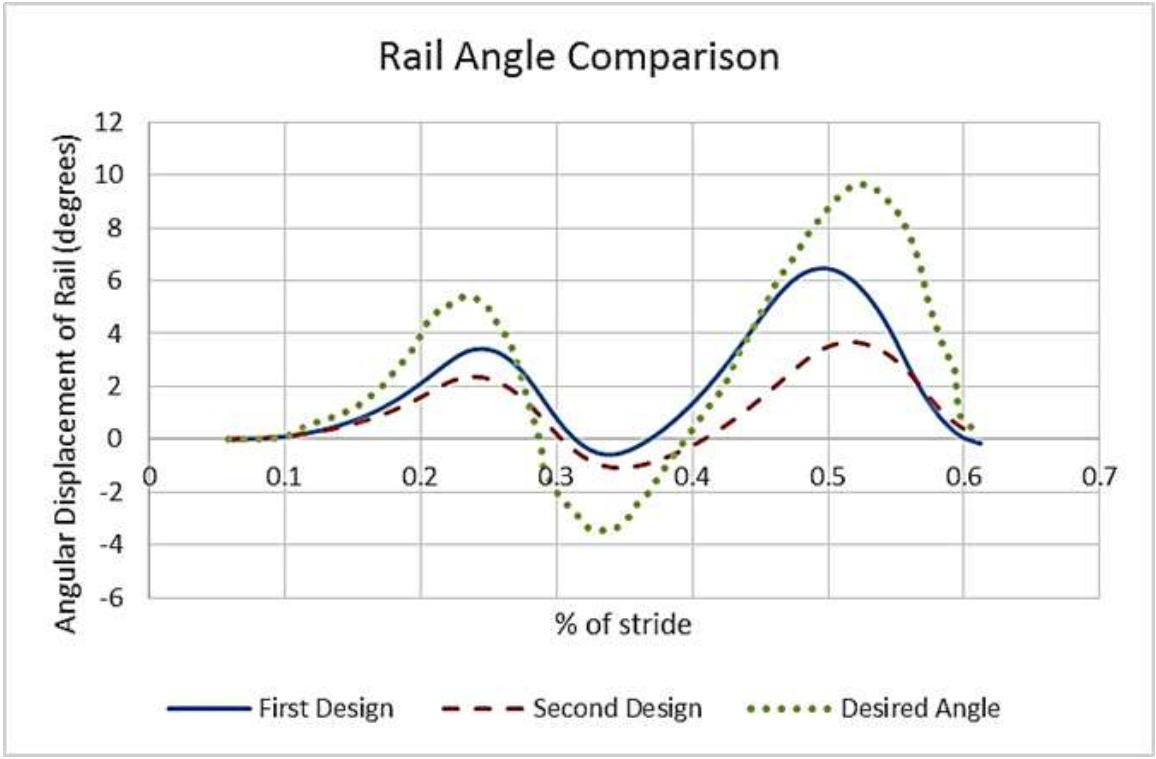

Figure 94. Rail Angular Displacement Comparison

The limited-acceleration cam profile for Iteration II resulted in significantly reduced rail angles. With peak rail angles of approximately 3.5 degrees, the user may feel the force transmitted through the cam, but likely will not feel a significant change in rail angle. There is a possibility this will trigger natural foot movements. Normal foot movements may occur if the user lifts the heel during toe-off and lifts the toe during heel strike.

8.6 Removal of Foot Angle Rail

In Iteration I, a mobile rail actuated with the bottom of the foot pedal to change the foot pedal angle, causing the foot pedal to rotate. After review, it was the belief of the Madonna researchers that this was unnecessary. During normal gait, the tendon connecting the heel to the calf muscle pulls on the heel, causing the heel to rise during toe-off. The foot then rotates about the knee joint, and at heel strike, the toe is oriented at an incline to the horizontal. The rotation of the knee is the primary cause of the foot angle following toe-off. Between the knee rotation and the natural heel lift, the foot may trace a natural trajectory during gait without the extra assistance. Thus, it was advised that the foot angle rail should be removed.

8.7 Motorization

Because the system is not backdrivable, the machine required a motor to operate. Specifically, the motor was needed for assistance in overcoming the toggle points of the four-bar linkage. Unlike Iteration I, which had six separate axles and multiple tensioners, this design only had two axles. The simplest form of connecting them involved using a single chain wrapped around the cam axle and the crank axle.

A motor was utilized to propel the foot and turn the cams to dictate foot angle. The unloaded motor speed was 1,750 RPM, with a maximum voltage of 80 Volts. The stall torque was 27 N-m, and the stall current was 7.6 Amps. To maximize the torque output of the motor, the motor needed to run near 1,750 RPM when the machine was at maximum speed. As stated earlier, the ideal speed for the machine was 1 rev/sec (or 60 RPM). Assuming the max speed occurs at 80% of the ideal stride time, the max RPM of the machine would be expected to be 75 RPM. In order to get this scaling up near the motor speed, the motor had to be scaled down by a factor of 23.33.

The smallest ANSI-40 steel sprocket sold by McMaster-Carr is a 9-tooth, 5/8-in. bore sprocket. This sprocket was mounted onto the motor axle, and it interfaced with a 45-tooth, ANSI-40 sprocket on the power transmission axle. A 9-tooth, ANSI-40 sprocket on the power transmission axle interfaced with 35-tooth, ANSI-40 sprockets on the cam axle and the crank axle. Overall, the gear ratio for this machine was 19.44. While that was less than the desired gear ratio, a higher gear ratio would only be possible with a third power transmission axle or larger sprockets on the cam and crank axles. The resulting chain diagram for the machine is shown in Figure 95.

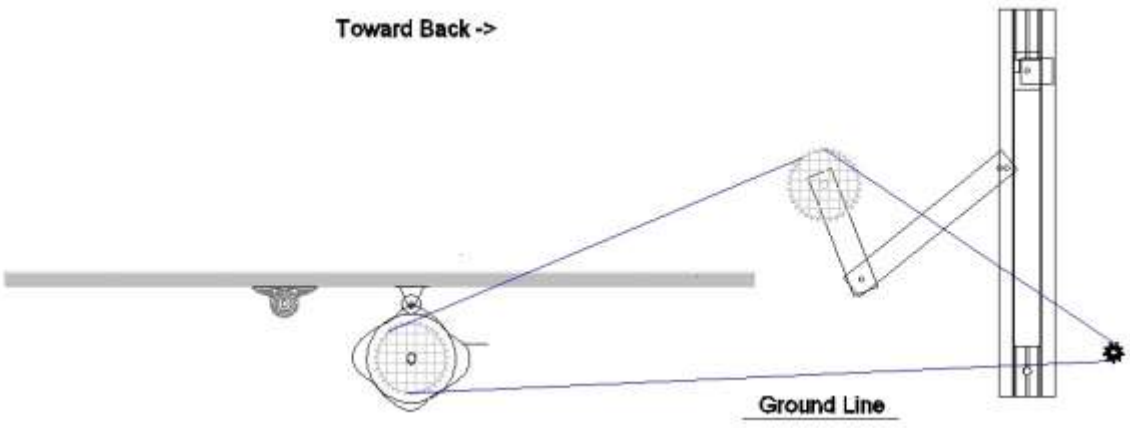

Figure 95. Initial Power Transmission Configuration

The contact angle is defined as the angle (measured from the center of a sprocket) that the chain is in contact with the sprocket. Ideally, this angle would be at least 120 degrees, although it is possible to have lower contact angles at larger tooth numbers on a sprocket [123,124]. Also, it was noticed during operation that the 9-tooth power transmission sprocket was slipping against the chain, causing the system to jump over that sprocket and not engage. To improve the contact angles of these sprockets and tighten the chain into the sprockets, it was suggested that idler sprockets be mounted. Two idler sprockets were attached to the system, and they helped to route the chain. One idler sprocket was mounted on a fixed shaft that passed through the system laterally. The other idler sprocket was mounted to a bolt so that the chain tension could be manually adjusted. The resulting power transmission diagram is shown in Figure 96.

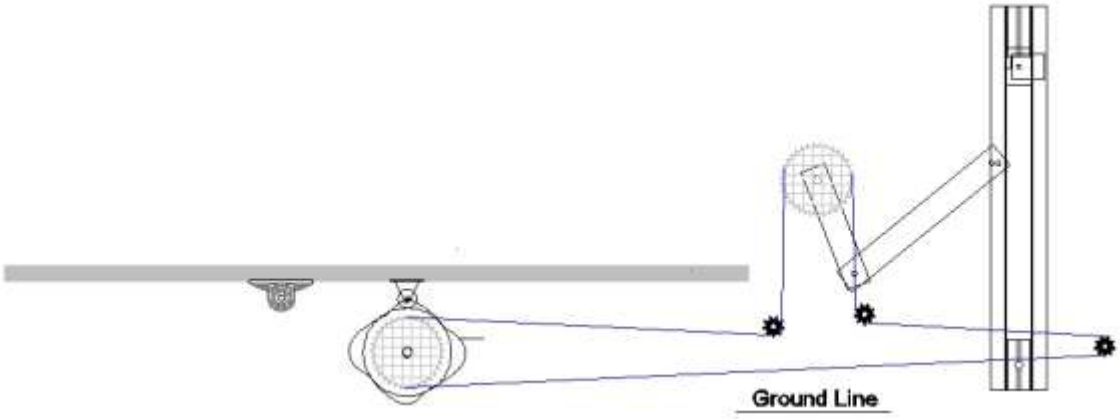

Figure 96. Chain-Tensioned Power Transmission Diagram

It was noted that the structure supporting the crank axle was deflecting significantly during operation using the configuration shown in Figure 96. This was attributed to the large forces transmitted through the chain during several peak locations of the cam's rotation. In order to prevent failure in the support structure for the crank axle, the power transmission to the crank axle and to the cam axle must be separated.

Two 9-tooth, ANSI-40 sprockets were placed on the power transmission axle, and the cam and crank engaged different sprockets. This decreased the force transmitted through each chain. The resulting configuration is shown in Figure 97.

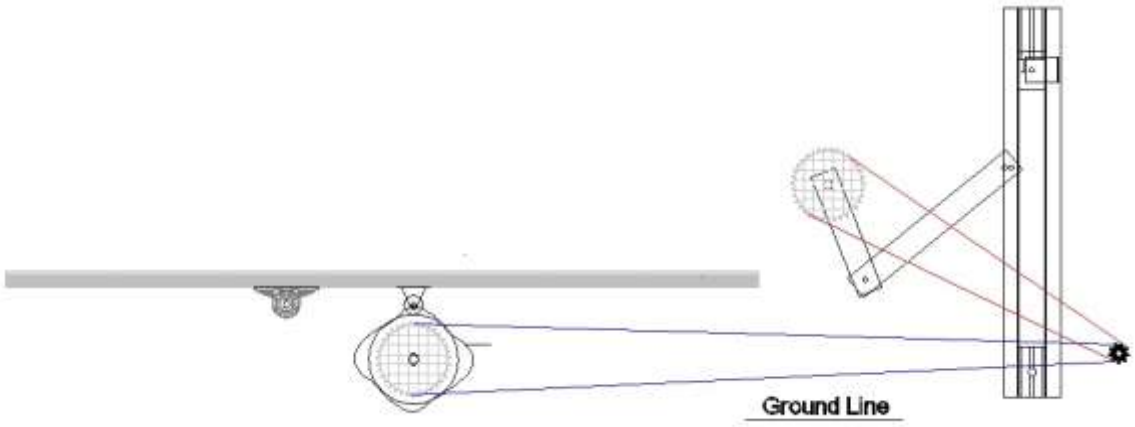

Figure 97. Dual-Chain Power Transmission System

8.8 Iteration II Construction

Iteration II was constructed, and the full mechanism was proven to be operational. Initial testing showed that the machine was capable of handling 250-lb individuals and propelling the feet without significant issues. The constructed Iteration II, as designed, is shown in Figure 98. The constructed Iteration II with a new foot pedal is shown in Figure 99.

Figure 98. As-Designed Iteration II Assembly

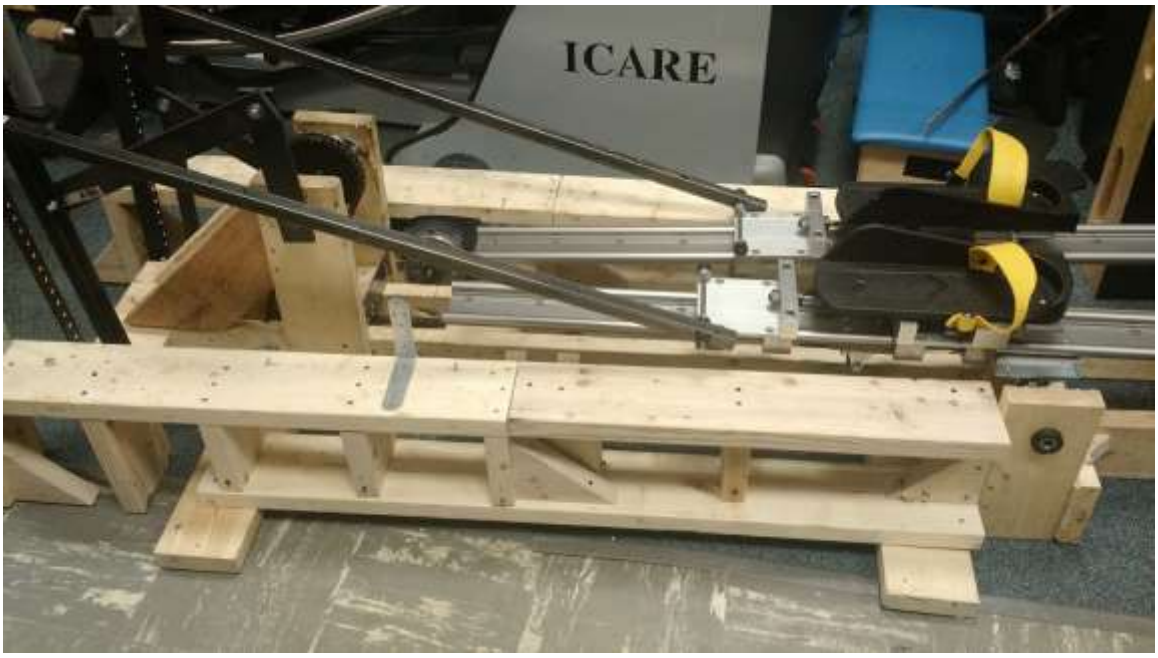

Figure 99. Assembled Iteration II with New Foot Pedal

One major design change was implemented by the Madonna staff. While the device had been designed to model the trajectory of a point on the foot just in front of the toe (see Section 6.4), researchers at Madonna showed concern about the user being able to lift the foot pedal naturally. As such, they requested that the pivot point be shifted from the toe to a point near the metatarsal. No redesign work to the cam or four-bar linkage was done, and the new foot pedal (shown in Figure 99) replaced the existing foot pedal along with the change.

8.9 Preliminary Performance Evaluation

Early results from the testing of the Iteration II design show that the device did not encourage a gait-like trajectory. Rather, the device appeared to operate more like a set of skis, where the stance and swing phase followed nearly the same trajectory. On use of the machine, it was noted that the device did not encourage the user to bend the knee or flex the ankle joint anywhere near the proper positions. The foot angle was very flat for most of the trajectory.

As per the opinion of the author after use, the timing of the stride did feel very comfortable, and the anterior and posterior motions of the legs felt natural. This can be accredited to the four-bar linkage selection.

While these are preliminary results, they warrant future work. More effort needs to be spent determining how to encourage the proper foot angles to be achieved during gait. It is believed that this will assist in producing a gait-like trajectory.

8.10 Conclusions

A second iteration of the scalable pediatric gait therapy device was designed and constructed. With a new rail, carriage, connection between the rocker and the carriage,

and cam shape, the second iteration showed dramatic changes. While offering significant improvements in efficiency, power transmission, simplicity, weight, and size, preliminary testing confirmed the design concerns that these improvements would come at the cost of a less-accurate gait path. Further work will be needed to assess this machine and potential improvements for a third iteration. The performance of the machine was compared to the design goals from Section 6.1 in Table 17.

Table 17. Iteration II Performance vs. Design Goals

Design Goal	Description	Iteration II Performance
Gait-Like Trajectory	Traced path must resemble average gait curve	Traced path was fairly similar to gait path, although the foot angles were incorrect
Scalable	Must accommodate pediatric and adult patients	Mechanism was scalable for stride lengths, although nonlinearity was introduced
Practical	Usable in small facilities	Easily managed, one motor controls all movements
Adjustable	Accommodate specific impairments	Adjustable for varying stride lengths
Cost-Effective	- -	Comparably priced. Uses more expensive components, but less machining and fewer parts
Small Footprint	- -	Smaller footprint than Iteration I
Motorized	Able to be motorized	Mechanism was fully operable with a motor
Backdrivable	Able to be driven by human power	Impossible to backdrive
Ergonomic	Easy and comfortable to mount and operate	Some noise, comfortable movement, some mounting difficulty. Overall, fairly ergonomic

CHAPTER 9 – FULL-STUDY DISCUSSION AND CONCLUSIONS

Gait therapy is a complex process. It may require intensive therapist involvement, expensive equipment, or carefully-designed equipment, but it is rarely cheap. Aside from the difficulties of normal, adult gait therapy, pediatric gait therapy is not standard, and is difficult to perform because of the intensity required out of the therapists. Specialized equipment or intensive therapist involvement are usually required to assist pediatric patients. To combat both of these needs, several scalable, low-cost gait therapy devices were developed and are presented in this document.

9.1 Summary of Research

Before the therapy device could be designed, researchers utilized gait trajectory data to increase knowledge of the foot point trajectories during gait. These data were also mathematically modeled using a Fourier series, and the Fourier series average was compared to each dataset. The resulting trajectory proved to be an average of the three normalized curves.

A pediatric gait therapy device was proposed and constructed as a modification to an existing, proven system. The Intelligently-Controlled Assistive Rehabilitation Elliptical (ICARE) was modified using a variable-length crank to adjust for different stride lengths down to 8 in. Initial testing results of this device show sufficient efficacy as a pediatric rehabilitation device, and further studies are underway.

Another pediatric gait therapy device was designed and constructed from scratch to attempt to more accurately trace the trajectory of the foot during gait. While complications arose in designing these machines, the end design utilized polar parametric modeling of the foot path. The full prototype to accommodate is still undergoing testing.

9.2 Comparison of Pediatric ICARE and Iteration II Designs

Both the pediatric ICARE and the Iteration II gait therapy device were invented to assist children through adults in rehabilitation and exercise. While the two devices are significantly different, each offers a different set of benefits. As such, the two devices were compared against the initial design goals presented in Section 6.1. The comparison is shown in Table 18.

Table 18. Design Goal Comparison Between Pediatric ICARE and Iteration II

Design Goal	Pedi ICARE	Iteration II
Gait-Like Trajectory	Traced path was dissimilar to gait path, but foot angles were acceptable	Traced path was fairly similar to gait path, although the foot angles were incorrect
Scalable	Mechanism was scalable for multiple stride lengths	Mechanism was scalable for multiple stride lengths, although nonlinearity was introduced
Practical	Easily managed, one motor controls all movements	Easily managed, one motor controls all movements
Adjustable	Adjustable for varying sizes of individuals	Adjustable for varying sizes of individuals
Cost-Effective	Comparably priced	Comparably priced. Expected to be in the range of the ICARE's cost
Small Footprint	Reasonable footprint	Larger footprint than the pediatric ICARE
Motorized	Propels feet through a full cycle	Propels feet through a full cycle
Backdrivable	Able to be driven by human power	Impossible to backdrive
Ergonomic	Easy and comfortable to mount and operate. Decently ergonomic	Some noise, comfortable movement, some mounting difficulty. Overall ergonomic

Overall, the primary design goals were tentatively achieved by Iteration II, while the gait-like trajectory was not achieved by the pediatric ICARE. The cadence and overall trajectory was more gait-like for Iteration II. The trunk, hip, and pelvic motions were more accurate for Iteration II, but the foot, knee, and ankle angles for the pediatric ICARE were more consistent with normal gait.

For the secondary design goals, each design showed minor improvements over the other. One notable difference was that Iteration II was not backdrivable. Also, Iteration II produced noises and did not have the full system to assist in mounting the device that the pediatric ICARE has. Iteration II was approximately 24 in. longer than the pediatric ICARE. At the conclusion of this study, neither design fully accomplished all design goals.

9.3 Adult and Purchasing Recommendations

The pediatric ICARE is expected to be more expensive than the normal ICARE due to adjustments and redesigned parts that will be more expensive. As such, a normal-sized adult purchasing the ICARE system for personal exercise or rehabilitation use would not want to purchase the pediatric ICARE version despite its ability to account for adult usage. However, small rehabilitation facilities and exercise facilities likely would want to purchase the pediatric version as it is able to accommodate a far broader population without requiring multiple machines. The pediatric ICARE is a tentative name, and is designed to accommodate both a pediatric and a full-size, 250-lb adult equally.

Iteration II is a unique machine that has the capability to adjust for both adult and pediatric patients. Users seeking exercise likely would prefer a machine that does not

require motorized assistance, and thus probably would not choose Iteration II. However, for rehabilitative purposes, this design would be desirable due to its gait-like cadence and upper-body motions.

9.4 Scientific Contributions of this Study

A Fourier series model of three gait paths and an average gait path are provided in Appendix A. Plots of the minimum Fourier series order satisfying $R^2 > 0.99$ are also shown, along with eighth-order Fourier series approximations. Each of these could be used as individual datasets for researchers seeking gait data. Also, the gait path analysis and averaging method from Chapters 3 and 4 can be used to process and identify future average gait paths.

The pediatric ICARE system developed in Chapter 5 has a pending patent application no. US 2016-023788 issued September 29, 2016 [125]. It is expected that this project will be manufactured. The Iteration II and several foot pedal designs (discussed in Chapter 10) were included in a patent application that is currently in progress. If clinical testing goes well, it is expected that this design will be manufactured.

Three publications were produced as a result of this work through international journals, with one pending journal publication [126-128].

CHAPTER 10 – FUTURE WORK

This research project occurred over the course of three years. However, the results of this study warranted further work. At the beginning of this study, it was noted that elliptical machines did not encourage a gait-like trajectory, but through their proprioceptive training, they still were proved effective. Following the design of the gait machine, new research avenues open up to allow for comparison of gait-like proprioceptive training to existing non-gait like machines, such as the pediatric ICARE. Also, this provides opportunity to assess whether proprioceptive training methods, such as the Iteration II prototype, show improvement over joint-restrictive therapy types, such as robotic exoskeletons.

Further work was also recommended in each research area from this study.

10.1 Improved Gait Trajectory Mathematical Model

The mathematical model obtained as an average of three gait trajectories used three different data sets from different sources. This means that the points may not have been consistently measured or marked. Despite the smoothness of the average curve, this curve may not be perfectly representative of a gait trajectory path.

Further work is needed to collect standardized toe, metatarsal, and heel trajectory data from multiple individuals. It is believed that more datasets will help determine an overall average gait trajectory that can be used as a model for comparison to gait abnormalities.

One specific note was that gait capture trajectories were different between treadmill and overground walking. While studies have been performed to compare the

joint motions for each, gait trajectory has not been compared for each, and benefits and drawbacks exist for each collection method.

Several gait path affecting factors were discussed in Section 3.2. Individual corrections for foot size, gender, femoral and tibial lengths, etc. could be performed to improve the accuracy of the foot model based on the person being modeled. A cohesive, comprehensive study could determine the effect of each influencing factor, which would give insight into how humans perambulate and potential improvements in the fields of prosthetics, gait rehabilitation, sports training, and disease treatment.

Aside from a more accurate walking trajectory model, other standard gait exercises could be modeled and averaged similar to how the gait trajectory was modeled in Chapter 4. Proposed full foot trajectory models could be created for stair stepping, object avoidance, jumping, and running. This could also serve as a tool for analysis and improvement of sports performance.

10.2 Pediatric ICARE Improvements

The pediatric ICARE described in Chapter 5 showed positive preliminary results. However, some mechanical issues were noted with the crank after some time and use. First of all, a collar was used to restrict movement of the crank relative to the axle. When excessively loaded, the collar would slip along the threaded rod, causing the crank to jolt during operation. This connection needs to be evaluated and redesigned to prevent this from happening (e.g. changing the collar to a nut or welding it in place). Also, it was discovered that debris, dirt, dust, or other material present in the slot of the crank would cause the crank adjustment motion to seize. While this may be related to the collar slip issue, it may also be addressed by other means.

The foot plate on the pediatric ICARE was rigidly mounted to the four-bar coupler of the machine. This was not conducive to changing foot angles during gait as the foot remains relatively flat during the stride. Efforts will be undertaken to redesign the foot plate to promote more natural foot angles during stride.

10.3 Pediatric Gait Therapy Device

The mobile, rotating rail used in Iteration II from Chapter 8 showed mixed results in preliminary clinical testing. Two biomechanical flaws were noted with this motion: (1) the foot was not reaching an adequate foot angle at toe-off and (2) the foot was not reaching an adequate foot angle at heel strike. Both of these features were credited with causing a drastic deficiency in knee flexure during operation. Explanations for this are that the foot constraints were too stringent and that the pivoting action of the rail (inhibited through continued acceleration reduction) proved ineffective.

One proposed method of dealing with the foot angle problem is direct enforcement of foot plate angle. Using an actuator to drive the vertical motion of the foot can result in precise, exact angles that directly influence the foot position. While this method may theoretically produce the desired results, there are some complications. As discussed in Section 2.3.1, chaotic neurogenic control of foot position, angle, and trajectory are healthy for mobile individuals. Removing the body's natural desire to vary strides may limit the effectiveness of training. However, further testing is needed to determine the effect of allowing chaotic foot control during propelled gait therapy.

Throughout the testing of Iteration I and II, the rail angle control posed issues to the power consumption, gait replication, and stability of the machine. As new foot pedals for the machine are designed, a new mechanism was proposed as an alternative to

evaluate the foot pedals. The base configuration of the new design is shown in Figure 100. Instead of a mobile, pivoting rail, the rail consisted of an immobile beam (F) that the carriage (E) traveled on. The carriage motion was dictated by a four-bar linkage (A-B-C). A sliding linkage (D) on the rocker (C) scaled the carriage longitudinal movement.

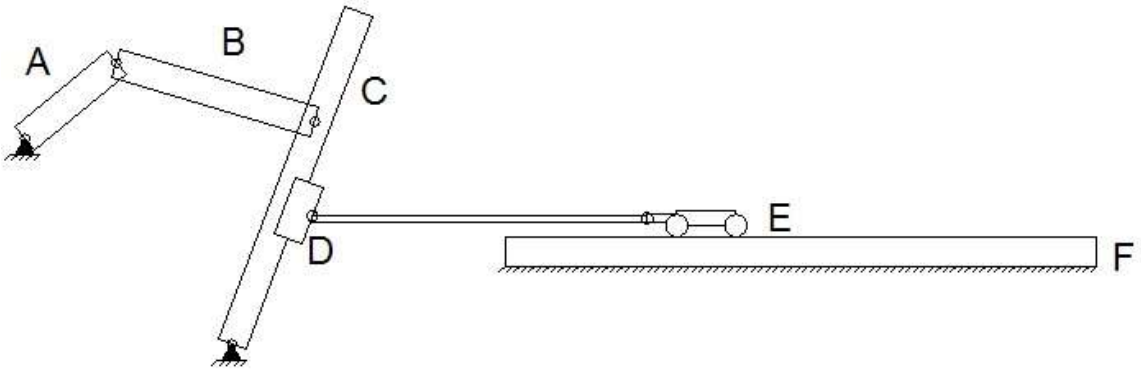

Figure 100. Base Configuration for Proposed Iteration III Gait Mechanism

The benefits of utilizing the new machine are significant. First, without any under-rail support system, the rail is able to be placed as close to the ground as possible, minimizing the mechanism mounting height. Second, without the rail angle controls, the support structure need not be as bulky, and the overall mechanism weight can be reduced. Third, the mechanism power requirements will drop without the need for the cam. The high-power elliptical motor used in Iteration II could be replaced with a cheaper, less powerful motor with the sole purpose of assisting the user in propelling the foot forward and backward. Finally, as long as the foot pedal design isn't too expensive, this design should be the cheapest design proposed. This would satisfy nearly all of the design goals set forth in Section 6.1.

There are a few drawbacks to the basic design of the new machine. While the gait trajectory accuracy may show improvement over Iteration II, there is no guarantee that the resulting trajectory will be gait-like. Also, if the foot pedal requires actuation, an

onboard actuator will require either a hydraulic hose or electrical cord. Extending and retracting these cords so that they do not interfere with the carriage motion on the rail will prove challenging, and preventing damage to the cord or hose involved will also be necessary.

As further work on the new machine design shown in Figure 100 and as potential additions to Iteration II, three pedal designs were proposed, and are discussed below.

10.3.1 Double-Axis Pedal Design

For the first foot pedal design, the foot pedal (G) consisted of two links serially connected to the carriage through revolute joints. The second revolute joint was configured such that it could move along the foot pedal. The distance between these two revolute joints was adjusted to be consistent with the distance between the heel and the metatarsal of the patient. The carriage design is shown in Figure 101.

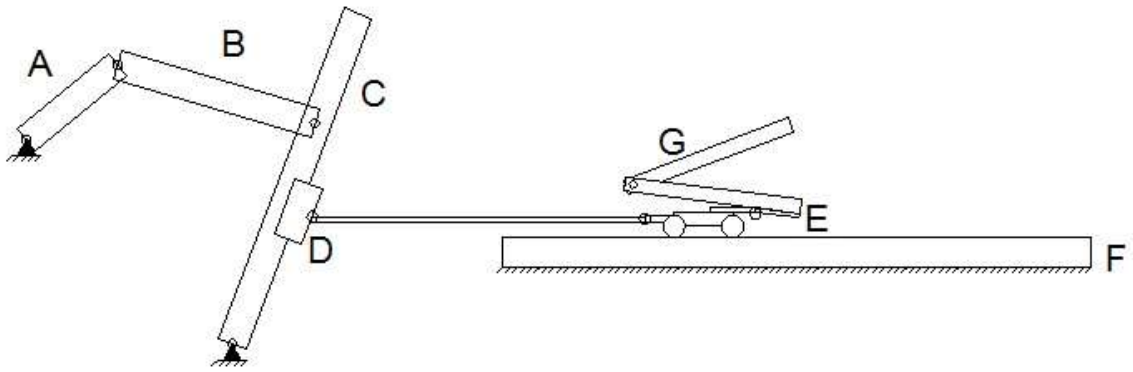

Figure 101. Dual-Axis Pivoting Foot Pedal Design

This design does not require outside actuation. The foot pedal weight can be counterbalanced by spring-loading the joints. This would minimize the resistance to foot rotation in the mechanism. However, similar to the foot pedal design from Iteration II, there is no guarantee that the user will lift either the toe or heel during each stride. Using

stronger, more powerful spring loading likely would assist in encouraging a gait-like trajectory, but is not as easily scalable and will not affect small children and adults equally.

10.3.2 Pivoting Plate Pedal

For the second foot pedal design, the foot pedal (G) consisted of a pivoting plate with wheels attached to the bottom, as shown in Figure 102. Actuators below the pivoting plate locked the rotation of the pivoting plate by pushing plates into the wheels. During the swing phase, these actuators would deactivate, and the pedal would be allowed to freely pivot about the center point to the desired foot angle during heel strike and the desired foot angle during toe-off.

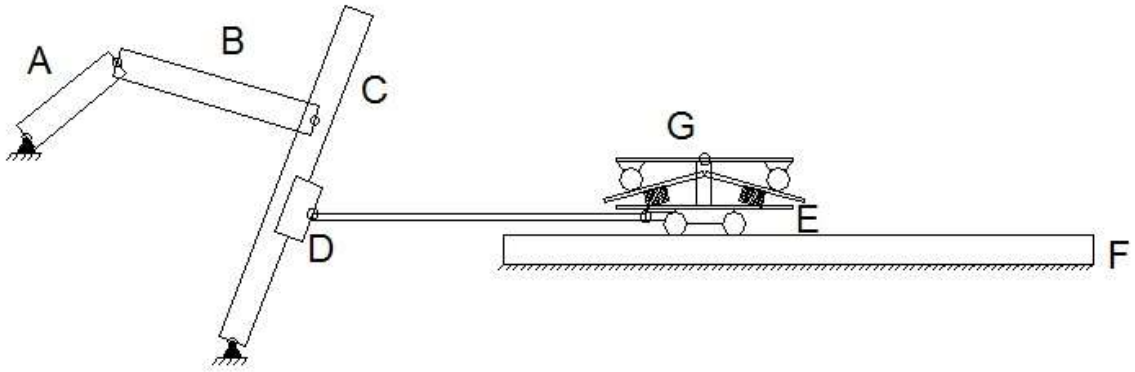

Figure 102. Pivoting and Locking Foot Pedal Design

This design shows potential for allowing the user to dictate the foot angle rotation based on their comfort level. Using stops at the maximum allowed foot angle (using rigid plates that prevent further rotation of the platform), the maximum and minimum foot angle could be precisely controlled.

10.3.3 Rotating Pedal

The third proposed foot pedal design was a foot plate with u-groove wheels attached to it, as shown in Figure 103. A locking actuator engaged the bottom of the foot pedal, disallowing it from moving. The mechanism would unlock during the swing phase and lock while the foot is in stance. The foot plate was designed such that the heel and metatarsal would be located equidistant from each of the wheel on the foot plate. This means that the center of the curved arc rail occurred at a position very near to the ankle. When unlocked, pressure on the metatarsal (as is seen during toe-off) causes the rear of the foot to rise. Pressure on the heel (as is seen during heel strike) causes the toe of the foot to rise. Ideally, the rotation about the ankle would feel natural when the foot angle changes during heel strike and toe-off.

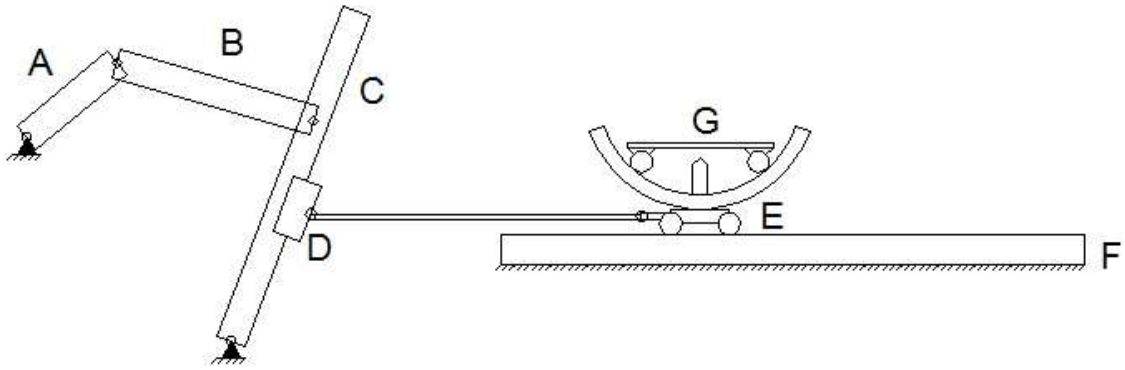

Figure 103. Rotating Foot Pedal Design

This design is the most complicated of the three proposed designs. The locking mechanism used to prevent foot pedal movement during the stance phase is not well realized. Also, in order to mount the machine safety, both pedals must be in the locked position when off. This means that the actuation action causes the foot pedal to unlock. Despite its complicated nature, this design is intended to encourage rotation about the ankle, which may produce more comfortable foot rotations during gait.

10.4 Other Gait Rehabilitation Devices

As outlined in Chapter 6, several viable gait replication methods were presented. However, due to time restraints of this project, some of these ideas were not given adequate analysis and design. For example, the hip-origin device shown in Figure 63, the offset polar parametrized device shown in Figure 62, the pantograph device shown in Figure 60, and the Scotch yoke mechanism in Figure 67 could be optimized to eliminate the concerns. Future work may develop designs from these ideas.

10.5 Discussion

Overall, comparisons between the results of the pedi-ICARE machine and the Iteration II design will show whether more gait-like motion helps to improve gait therapy. To determine an average gait trajectory, more data needs to be collected and the method employed in Chapter 4 should be performed to determine group sample average trajectories. For the pediatric ICARE in Chapter 5, minor adjustments to the crank constraints and future automated adjustments of the screw will improve the design. Also, efforts will be undertaken to improve the foot plate design on the machine to better promote natural foot angles. For the pediatric gait therapy mechanism in Chapter 8, initial results indicate that the knee flexion and foot angles are insufficient. However, it is uncertain whether these are correlated or not. New foot plates will need to be assessed to promote more natural foot angles, and the effect on the knee flexion will need to be assessed. This may involve the construction of a new device along the lines of some of the devices that were presented in Chapter 6.

CHAPTER 11 – REFERENCES

1. Schwanen, T., and Ziegler, F., "Wellbeing, Independence and Mobility: An Introduction", *Ageing and Society*, v. 31:5, July 2011, 719-733.
2. HC Pro, "Complications from Immobility by Body System", November 27, 2012, < http://www.hcpro.com/LTC-286850-10704/Complications-from-immobility-by-body-system.html>.
3. Brault, M.W., "Americans with Disabilities: 2010", *Current Population Reports*, U.S. Census Bureau, July 2012.
4. U.S. Department of Health and Human Services, *Physical Activity Guidelines Advisory Committee Report*, Washington D.C., 2008.
5. Erikson, E.H., *Childhood and Society*, Norton, New York, 1950.
6. Heffner, C.L., "Motor and Cognitive Development", *Psychology 101*, 2016, <allpsych.com>.
7. Adolph, K.E., Vereijken, B., and Shrout, P.E., "What Changes in Infant Walking and Why", *Child Development*, v. 74:2, March 2003, 475-497.
8. McGraw, M.B., *Growth: A Study of Johnny and Jimmy*, Apple-Century Co., New York, 1935.
9. McGraw, M.B., *The Neuromuscular Maturation of the Human Infant*, Columbia University Press, New York, 1945.
10. Thelen, E., and Fisher, D.M., "Newborn Stepping: An Explanation for a 'Disappearing Reflex'", *Developmental Psychology*, v. 18, 1982, 760-775.
11. Adolph, K.E., "Babies' Steps Make Giant Strides Toward a Science of Development", *Infant Behavior & Development*, v. 25, 2002, 89-90.
12. Wu, Y., Zhong, Z., Lu, M., and He, J., "Statistical Analysis of Gait Maturation in Children Based on Probability Density Functions", 33rd Annual International Conference of the IEEE, Boston, MA, June 9, 2011.
13. Norlin, R., Odenrich, P, and Sandlund, B., "Development of Gait in the Normal Child", *Journal of Pediatric Orthopedics*, v. 1:3, 1981, 261-266.
14. Hausdorff, J.M., Zemany, L., Peng., C.K., and Goldberger, A.L., "Maturation of Gait Dynamics: Stride-to-Stride Variability and its Temporal Organization in Children", *Journal of Applied Physiology*, v. 86:3, March 1999, 1040-1047.
15. Wu, M., Liao, L., Luo, X., Ye, X., Yao, Y., Chen, P., Shi, L., Huang, H, and Wu, Y., "Analysis and Classification of Stride Patterns Associated with Children Development Using Gait Signal Dynamics Parameters and Ensemble Learning Algorithms", *Biomedical Research International*, v. 2016, article I.D. 9246280, February 2016, 1-8.
16. Ashkenazy, Y., Hausdorff, J.M., Ivanov, P.C., Goldberger, A.L., and Stanley, H.E., "A Stochastic Model of Human Gait Dynamics", *Physica A: Statistical Mechanics and its Applications*, v. 316:2, December 2002, 662-670.
17. Hof, A.L., "Scaling Gait Data to Body Size", *Gait & Posture*, v. 4, 222-223.
18. Sutherland, D.H., Olshen, R., Cooper, L., and Woo, S., "The Development of Mature Gait", *Journal of Bone and Joint Surgery*, v. 62, 1980, 336-353.

19. Ganley, K.J., and Powers, C.M., 2005, "Gait Kinematics and Kinetics of 7-Year-Old Children: A Comparison to Adults Using Age-Specific Anthropometric Data," *Gait & Posture*, v. 21:2, 141-145.
20. Chester, V.L., Tingley, M., and Biden, E.N., 2006, "A Comparison of Kinetic Gait Parameters for 3-13 Year Olds," *Clinical Biomechanics*, v. 21:7, 726-732.
21. Chester, V.L., and Wrigley, A.T., 2008, "The Identification of Age-Related Differences in Kinetic Gait Parameters Using Principal Component Analysis," *Clinical Biomechanics*, v. 23:2, 212-220.
22. Burnett, C.N., and Johnson, E.W., "Development of Gait in Childhood: Part II", *Developmental Medicine & Child Neurology*, v. 13:2, April 1971, 207-215.
23. Stansfield, B.W., Hillman, S.J., Hazlewood, M.E., Lawson, A.M., Mann, A.M., Loudon, I.R., and Robb, J.E., "Normalisation of Gait Data in Children", *Gait & Posture*, v. 17:1, 2003, 81-87.
24. Bernstein, N., *The Coordination and Regulation of Movements*, Pergamon Press, Oxford, England, 1967.
25. Breniere, Y., and Bril, B., "Development of Postural Control of Gravity Forces in Children During the First 5 Years of Walking", *Experimental Brain Research*, v. 121, 1998, 255-262.
26. Bril, B., and Ledebt, A., "Head Coordination as a Means to Assist Sensory Integration in Learning to Walk", *Neuroscience and Behavioral Reviews*, v. 22, 1998, 555-563.
27. Keen, M., "Early Development and Attainment of Normal Mature Gait", *Journal of Pediatric Orthopedics*, v. 5:2, 1993, 35-38.
28. Dusing, S.C., and Thorpe, D.E., "A Normative Sample of Temporal and Spatial Gait Parameters in Children Using the GAITRite Electronic Walkway", Gait & Posture, v. 25:1, 2007, 135-139.
29. Stansfield, B.W., Hillman, S.J., Hazlewood, M.E., and Robb, J.E., "Regression Analysis of Gait Parameters with Speed in Normal Children Walking at Self-Selected Speeds", Gait & Posture, v. 23:3, 2006, 288-294.
30. Murphy, K.P., Matthews, D.J., and Alexander, M.A., *Pediatric Rehabilitation: Principles and Practice*, Ed. 5, New York: Demos Medical, 2015.
31. Perry, J., *Gait Analysis: Normal and Pathological Function*, Thorofare, NJ: Slack Inc, 1992.
32. Buzzi, U.H., Stergiou, N., Kurz, M.J., Hageman, P.A., and Heidel, J., "Nonlinear Dynamics Indicates Aging Affects Variability During Gait", *Clinical Biomechanics*, v. 18:5, 2003, 435-443.
33. Hausdorff, J.M., Peng, C.K., Ladin, Z., Wei, J.Y., and Goldberger, A.L., "Is Walking a Random Walk? Evidence for Long-Range Correlations in Stride Interval of Human Gait", *Journal of Applied Physiology*, v. 78:1, January 1995, 349-358.
34. Hausdorff, J.M., Mitchell, S.L., Firtion, R., Peng, C.K., Cudkowicz, M.E., Wei, J.Y., and Goldberger, A.L., "Altered Fractal Dynamics of Gait: Reduced Stride-

Interval Correlations with Aging and Huntington's Disease", *Journal of Applied Physiology*, v. 82:1, January 1997, 262-269.
35. Baker, G.L., and Gollub, J.P., *Chaotic Dynamics*, Cambridge University Press, New York, 1996.
36. Abarbanel, H.D.I., *Analysis of Observed Chaotic Data*, Springer, New York, 1996.
37. Kurz, M.J., *Chaos in Gait*, Dissertation presented to the Graduate College at the University of Nebraska, Omaha, Nebraska, 2006.
38. Johnson, E.O., and Soucacos, P.N., "Proprioception", *International Encyclopedia of Rehabilitation*, Center for International Rehabilitation Research Information and Exchange, 2016. < http://cirrie.buffalo.edu/encyclopedia/en/article/337/>.
39. Aman, J.E., Elangovan, N., Yeh, I.L., and Konczak, J., "The Effectiveness of Proprioceptive Training for Improving Motor Function: A Systematic Review", *Frontiers in Human Neuroscience*, v. 8, Article 1075, January 2015, 1-18.
40. Miller, J., "Proprioception & Balance Exercises", Physioworks, Accessed October 14, 2016, < http://physioworks.com.au/treatments-1/proprioception-balance-exercises>.
41. Carr, J.H., and Shepherd, R.B., *A Motor Relearning Programme for Stroke*, 2nd Ed., Aspen Publishers, Rockville, MD, 1987.
42. Riskowski, J.L., Mikesky, A.E., Bahamonde, R.E., Alvey III, T.V., and Burr, D.B., "Proprioception, Gait Kinematics, and Rate of Loading During Walking: Are They Related?", *Journal of Musculoskeletal and Neuronal Interactions*, v. 5:4, 2005, 379-387.
43. Kosak, M.C., and Reding, M.J., "Comparison of Partial Body Weight-Supported Treadmill Gait Training Versus Aggressive Bracing Assisted Walking Post Stroke", *Neurorehabilitation and Neural Repair*, v. 14:1, March 2000, 13-19.
44. Wang, R.Y., "Effect of Proprioceptive Neuromuscular Facilitation on the Gait of Patients with Hemiplegia of Long and Short Duration", *Physical Therapy*, v. 74:12, December 1994, 1108-1115.
45. Zouita, A.B.M., Bousselmi, M., Darragi, M., Ferchichi, H., Dziri, C., and Ben Salah, F.Z., "Proprioception Rehabilitation and Gait Parameters in Athletes after Ankle Sprain", *Annals of Sports Medicine and Research*, v. 3:5, 2016, 1077-1081.
46. LeMoyne, R., Coroian, C., Mastroianni, T., Opalinski, P., Cozza, M., and Grundfest, W., "The Merits of Artificial Proprioception, With Applications in Biofeedback Gait Rehabilitation Concepts and Movement Disorder Characterization", *Biomedical Engineering*, de Mello, C.A.B. (ed.), InTech, Croatia, 2009, 165-198.
47. Lewek, M.D., Feasel, J., Wentz, E., Brooks Jr, F.P., and Whitton, M.C., "Use of Visual and Proprioceptive Feedback to Improve Gait Speed and Spatiotemporal Symmetry Following a Chronic Stroke: A Case Series", *Physical Therapy*, v. 92:5, May 2012, 748-756.
48. Mirek, E., Chwala, W., Longawa, K., Rudzinska, M., Adamkiewicz, P., and Szczudlik, A., "Proprioceptive Neuromuscular Facilitation Method of Therapeutic

Rehabilitation in the Treatment of Patients with Parkinson Disease", *Neurologia i Neurochirurgia Polska*, v. 37 Supplement 5, 2003, 89-102.

49. Kuo, A.D., and Donelan, J.M., "Dynamic Principles of Gait and their Clinical Implications", *Physical Therapy*, v. 90:2, February 2010, 157-176.
50. Eng, J.J., Tang, and Tang, P.F., "Gait Training Strategies to Optimize Walking Ability in People with Stroke: A Synthesis of the Evidence", *Expert Review of Neurotherapeutics*, v. 7:10, 2007, 1417-1436.
51. Corbridge, L.M., Goldman, A.J., Shu, Y., Buster, T.W., and Burnfield, J.M., "Clinician's Muscle Effort during Partial Body Weight Support Treadmill Training: Is it Hard Work?", Online Proceedings, *American Physical Therapy Association's 2009 Annual Conference and Exposition*, 2009, <http://apps.apta.org/Custom/abstracts/pt2009/abstractsPt.cfm?m_id=19675>.
52. Visintin, M., Barbeau, H., Korner-Bitensky, N., and Mayo, N.E., "A New Approach to Retrain Gait in Stroke Patients through Body Weight Support and Treadmill Stimulation", *Stroke*, v. 29, 1998, 1122-1128.
53. Kosak, M.C., and Reding, M.J., "Comparison of Partial Body Weight-Supported Treadmill Gait Training Versus Aggressive Bracing Assisted Walking Post Stroke", *Neurorehabilitation and Neural Repair*, v. 14:1, March 2000, 13-19.
54. Damiano, D.L., Norman, T., Stanley, C.J., and Park, H.S., "Comparison of Elliptical Training, Stationary Cycling, Treadmill Walking and Overground Walking", *Gait & Posture*, v. 34:2, June 2011, 260-264.
55. Banala, S.K., Kim, S.H., Agrawal, S.K., and Scholz, J.P., "Robot Asissted Gait Training with Active Leg Exoskeleton (ALEX)", *IEEE Transactions on Neural Systems and Rehabilitation Engineering*, v. 17:1, February 2009, 2-8.
56. Olson, J., "Hospitals Have New Tool to Help Paralyzed Patients: Robotics", *Star Tribune*, May 31, 2016, <http://www.startribune.com/hospitals-have-new-tool-to-help-paralyzed-patients-robotics/381213281/>.
57. Veneman, J.F., Kruidhof, R., Hekman, E.E.G., Ekklenkamp, R., Van Asseldonk, E.H.F., and van der Kooij, H., "Design and Evaluation of the LOPES Exoskeleton Robot for Interactive Gait Rehabilitation", *IEEE Transactions on Neural Systems and Rehabilitation Engineering*, v. 15:3, September 2007, 379-386.
58. Sale, P., Franceschini, M., Waldner, A., and Hesse, S., "Use of the Robot Assisted Gait Therapy in Rehabilitation of Patients with Stroke and Spinal Cord Injury", *European Journal of Physical and Rehabilitation Medicine*, v. 48:1, 2012, 111-121.
59. Peshkin, M., Brown, D.A., Santos-Munne, J.J., Makhlin, A., Lewis, E., Colgate, J.E., Patton, J., and Schwandt, D., "KineAssist: A Robotic Overground Gait and Balance Training Device", *9th International Conference on Rehabilitation Robotics*, 2005.
60. Meyer-Heim, A., Ammann-Reiffer, C., Schmartz, A., Schafer, J., Sennhauser, F.H., Heinen, F., Knecht, B., Dabrowski, E., and Borggraefe, I., "Improvement of Walking Abilities after Robotic-Assisted Locomotion Training in Children with Cerebral Palsy", *Archives of Disease in Childhood*, v. 94, 2009, 615-620.

61. Hornby, G.T., Kinnaird, C.R., Holleran, C.L., Rafferty, M.R., Rodriguez, K.S., and Cain, J.B., "Kinematic, Muscular, and Metabolic Responses During Exoskeletal-, Elliptical-, or Therapist-Assisted Stepping in People with Incomplete Spinal Cord Injury", Physical *Therapy*, v. 92:10, October 2012, 1278-1291.
62. Hornby, T.G., Campbell, D.D., Kahn, J.H., Demott, T., Moore, J.L., and Roth, H.R., "Enhanced Gait-Related Improvements after Therapist – Versus Robotic-assisted Locomotor Training in Subjects with Chronic Stroke", *Stroke*, v. 39, 2008, 1786-1792.
63. Ha, K.H., Murray, S.A., and Goldfarb, M., "An Approach for the Cooperative Control of FES with a Powered Exoskeleton During Level Walking for Persons with Paraplegia", *IEEE Transactions on Neural Systems and Rehabilitation Engineering*, v. 24:4, 2016, 455-466.
64. Farris, R.J., Quintero, H.A., and Goldfarb, M., "Preliminary Evaluation of a Powered Lower Limb Orthosis to Aid Walking in Paraplegic Individuals", *IEEE Transactions on Neural Systems and Rehabilitation Engineering*, v. 19:6, 2011, 652-659.
65. Goldfarb, M., Lawson, B.E., and Shultz, A.H., "Realizing the Promise of Robotic Leg Prostheses", *Science Translational Medicine*, v. 5:210, 2013, 210.15.
66. Goldfarb, M., Farris, R.J., and Quintero, H.A., *Movement Assistance Device*, US Patent Application No. 2014-049494, October 9, 2013.
67. Yeseta, M.C., Taylor, A.P., Buster, T.W., Shu, Y., and Burnfield, J.M., "Exercise Endurance and Functional Mobility Improve for Individuals with Physical Disabilities After Training on a Motorized Elliptical", *Rehabilitation Engineering and Assistive Technology Conference*, 2012.
68. Bradford, J.C., and Pidcoe, P.E., "Development of a Low-Cost Robotic Gait Trainer", Conference Proceedings of the Annual Meeting of the American Society of Biomechanics, 2009, 1-2.
69. Tom-Wigfield, D., Haynes, E., and Martin, R., "Activity-Based Restorative Therapy Steps into Robotic Gait Training for Innovative Approaches for Patients with Chronic Spinal Cord Injuries", *Rehab Management*, June 7, 2016.
70. Burnfield, J. M., Shu, Y., Buster. T. W., and Taylor. A., "Similarity of Joint Kinematics and Muscle Demands between Elliptical Training and Walking: Implications for Practice", *Physical Therapy*, v. 90:2, 2010, 289-305.
71. Shyu, J. H., Chen, C. K., and Luo, Y. J., "Research and Development of an Adjustable Elliptical Exerciser", *13th World Congress in Mechanism and Machine Science*, Guanajuato, México, 19-25 June 2011.
72. Lin, M.P., Chang, Y.J., and Yu, M.D., "Phase-Dependent Modulation of Soleus H-Reflex and Post-Activation Depression during Elliptical Trainer and Treadmill Walking in Humans," *Physiotherapy*, v. 101 Supplement 1, 3881.
73. Sawicki, G.S., Gordon, K.E., and Ferris, D.P., "Powered Lower Limb Orthoses: Applications in Motor Adaptation and Rehabilitation", *Rehabilitation Robotics*, 2005.

74. Meyer-Heim, A., Borggraefe, I., Ammann-Reiffer, C., Berweck, S., Sennhauser, F. H., Colombo, G., Knecht, B. and Heinen, F., "Feasibility of Robotic-Assisted Locomotor Training in Children with Central Gait Impairment", *Developmental Medicine & Child Neurology*, v. 49, 2007, 900-906.
75. Morrison, S., "Financial Feasibility of Robotics in Neurorehabilitation", *Spinal Cord Injury Rehabilitation*, v. 17:1, 2011, 77-81.
76. Mehrholz, J., Elsner, B., Werner, C., Kugler, J., and Pohl, M., "Electromechanical-Assisted Training for Walking After Stroke", *Cochrane Database of Systematic Reviews*, v. 7, 2013, Article CD006185, Wiley, <http://onlinelibrary.wiley.com/doi/10.1002/14651858.CD006185.pub3/epdf>.
77. Dundar, U., Toktas, H., Solak, O., Ulasli, A.M., and Eroglu, S., "A Comparative Study of Conventional Physiotherapy Versus Robotic Training Combined with Physiotherapy in Patients with Stroke", *Topics in Stroke Rehabilitation*, v. 21:6, 2014, 453-461.
78. Fasoli, S. E., Ladenheim, B., Mast, J., and Krebs, H. I., "New Horizons for Robot-Assisted Therapy in Pediatrics", *American Journal of Physical Medicine & Rehabilitation*, v. 91:11, November 2012, S280–S289.
79. Langhorne, P., Coupar, F., and Pollock, A., "Motor Recovery After Stroke: A Systematic Review", *The Lancet Neurology*, v8:8, August 2009, 741-754.
80. Nelson, C.A., Burnfield, J.M., Shu, Y., Buster, T.W., Taylor, A.P., and Graham, A., "Modified Elliptical Machine Motor-Drive Design for Assistive Gait Rehabilitation," *Journal of Medical Devices*, v. 5:2, 2011.
81. Burnfield, J.M., Shu, Y., Buster, T.W., Taylor, A., and Nelson, C.A., "Impact of Elliptical Trainer Ergonomic Modifications on Perceptions of Safety, Comfort, Workout and Usability by Individuals with Physical Disabilities and Chronic Conditions", *Physical Therapy*, v. 91:11, 2011, 1604-1617.
82. Burnfield, J.M., Irons, S.L., Buster, T.W., Taylor, A.P., Hildner, G.A., and Shu, Y., "Comparative Analysis of Speed's Impact on Muscle Demands During Partial Body Weight Support Motor-Assisted Elliptical Training", *Gait and Posture*, v. 39:1, 2014, 314-320.
83. Burnfield, J.M., Shu, Y., Buster, T.W., and Taylor, A.P., "Similarity of Joint Kinematics and Muscle Demands Between Elliptical Training and Walking: Implications for Practice", *Physical Therapy*, v. 90:2, 2010, 289-305.
84. "Introduction", NRAS, July 18, 2016, <http://www.nras.org.uk/introduction>.
85. Pinney, S., Ed., "Bones and Joints of the Foot and Ankle Overview", *Foot Education*, October 17, 2015, <http://www.footeducation.com>.
86. Cronin, N.J., "The Effects of High Heeled Shoes on Female Gait: A Review", *Journal of Electromyography and Kinesiology*, v. 24:2, April 2014, 258-263.
87. Nadége, K.F.E, Jean-Marie, F., Mansourou, L.M., Polycarpe, G., Gabriel, A.Y., and Sophia, L., "Wearing High Heel Shoes During Gait: Kinematics Impact and Determination of Comfort Height", *American Journal of Life Sciences*, v. 3:2, 2015, 56-61.

88. Nwankwo, M.J., Egwuonwu, A.V., Ezeukwu, A.O., and Nwafulume, C.K., "Effects of Different Heel Heights on Selected Gait Parameters of Young Undergraduate Females", *Journal of Paramedical Sciences*, v. 3:3, 2012, 9-14.
89. Esenyel, M., Walsh, K., Walden, J.G., and Gitter, A., "Kinetics of High-Heeled Gait", *Journal of the American Podiatric Medical Association*, v. 93:1, January 2003, 27-32.
90. Barkema, D., *The Effect of Heel Height on Frontal Plane Joint Moments, Impact Acceleration, and Shock Attenuation During Walking*, A Thesis, Iowa State University, 2010.
91. Winter, D.A., "Foot Trajectory in Human Gait: A Precise and Multifactorial Motor Control Task", *Phys Ther.*, Issue 72, January 1992, 45-53.
92. Fang, J., and Hunt, K.J., "Foot Trajectory Approximation Using the Pendulum Model of Walking", *Medical and Biological Engineering and Computation*, 52nd ed., 2014, 45-52.
93. Fang, J., Hunt, K.J., Xie, L., and Yang, G.Y., "Modelling of the Toe Trajectory During Normal Gait using Circle-Fit Approximation*", Medical and Biological Engineering and Computation*, v. 54, 2016, 1481-1489.
94. Burnfield, J.M., Taylor, A.P., Buster, T.W., Shu, Y., Goldman, A.J., and Nelson, C.A., Use of Intelligently Controlled Assistive Rehabilitation Elliptical Trainer to Improve Walking and Fitness during Acute Stroke Rehabilitation", *Stroke*, v. 42:3, 2011, e326.
95. Buster, T.W., Burnfield, J.M., Taylor, A.P., and Stergiou, N., "Lower Extremity Kinematics During Walking and Elliptical Training in Individuals With and Without Traumatic Brain Injury", *Journal of Neurologic Physical Therapy*, 37:4, 2013, 176-186.
96. Irons, S.L., Brusola, G.A., Buster, T.W., and Burnfield, J.M., "Novel ICARE Intervention Improves Six-Minute Walk Test and Oxygen Cost for an Individual with Progressive Supranuclear Palsy", *Cardiopulmonary Physical Therapy Journal*, v. 26:2, 2015, 36-41.
97. Irons, S.L., Burnfield, J.M., Buster, T.W., Karkowski-Schelar, E., and Johns, E., Individuals with Multiple Sclerosis Improved Walking Endurance and Decreased Fatigue Following Motor-Assisted Elliptical Training Intervention", Accepted, *2016 American Congress of Rehabilitation Medicine (ACRM)*, 93rd Annual Conference: Progress in Rehabilitation Research. Chicago, IL, November 3, 2016.
98. Budynas, R.G., and Nisbett, K.J., *Shigley's Mechanical Engineering Design*, 8th ed., McGraw Hill, New York, 2008.
99. ASM International, "Fatigue", *Elements of Metallurgy and Engineering Alloys*, 2008, 243-264.
100. Hallquist, J.O., *LS-DYNA Keyword User's Manual*, Livermore Software Technology Corporation, Livermore, CA, 2001.
101. Burnfield, J.M., Buster, T.W., Irons, S.L., Cesar, G.M., Nelson, C.A., Rech, N.R., and Nichols, E.M., "Pediatric Walking vs. Training on Prototype Motor-Assisted Elliptical: Kinematic comparison at self-selected comfortable speed.

Accepted, *2016 American Congress of Rehabilitation Medicine (ACRM) 93rd Annual Conference: Progress in Rehabilitation Research*, Chicago, IL, November 3, 2016.

102. Burnfield, J.M., Buster, T.W., Irons, S.L., Rech, N., Cesar, G.M., Pfeifer, C.M., and Nelson, C.A., "Pediatric Intelligently Controlled Assistive Rehabilitation Elliptical for Walking and Fitness: Prototype Development and Biomedical Analysis", Presented at RESNA/NCART (Rehabilitation Engineering Society of North America/National Coalition for Assistive and Rehab Technology) 2016 annual convention, July 10-14, Arlington, VA.
103. Buster, T.W., Burnfield, J.M., Irons, S.L., Nelson, C.A., Trejo, L.H., and Leutzinger, T.J., "Pediatric Walking vs. Training on a Prototype Motor-Assisted Elliptical: Kinematic and EMG Comparisons at Self-Selected Fast Speeds", Conference proceedings, *2016 Annual Meeting Gait and Clinical Movement Analysis Society*, Memphis, TN, May 17-20, 2016.
104. Zhang, Y., Finger, S., and Behrens, S., "Planar Linkages", *Introduction to Mechanisms*, Carnegie Mellon University, Pittsburgh, PA, 2010, <https://www.cs.cmu.edu/~rapidproto/mechanisms/chpt5.html>.
105. "Kinematic Inversions of Four Bar Chain, Slider Crank and Double Slider Crank Mechanism", *Engineering Tutorials*, March 14, 2013, <http://engineering.myindialist.com/2013/kinematic-inversions-of-four-bar-chain-slider-crank-and-double-slider-crank-mechanism/#.WAsGc-ArK00>.
106. Hrones, J.A., and Nelson, G.L., *Analysis of the Four-Bar Linkage*, Massachusetts Institute of Technology, New York, 1951.
107. Freudenstein, F., "An Analytical Approach to the Design of Four-Link Mechanisms", *American Society of Mechanical Engineers*, v. 76:3, April 1954, 483–492.
108. Murray ,A.P., and McCarthy, J.M., "Determining Burmester Points from the Analysis of a Planar Platform", *Journal of Mechanical Design*, v. 117, June 1995, 303-307.
109. Kunjur, A., and Krishnamurty, S., "Genetic Algorithms in Mechanism Synthesis." University of Massachussetts, Accessed May 4, 2014, <http://www.ecs.umass.edu/mie/labs/mda/mechanism/papers/genetic.html>.
110. Roston, G.P., and Sturges, R.H., "Genetic Algorithm Synthesis of Four-Bar Mechanisms", Pennsylvania State University, Accessed May 4, 2014, <http://citeseerx.ist.psu.edu/viewdoc/download?doi=10.1.1.119.9140&rep=rep1&type=pdf>.
111. Dulger, L.C., Erdogan, H., and Kutuk, M.E., "Matlab's GA and Optimization Toolbox: A Fourbar Mechanism Application", *International Journal of Intelligent Systems and Application in Engineering*, Vol. 2, Ed. 1, 10-15.
112. Li, J,. "The Optimization Design of the Four-Bar Linkage Based on MATLAB", *International Conference on Intelligent Systems Research and Mechatronics Engineering*, 2015, 788-791.

113. Vilas, C.P., and Ghosal, A., "Optimal Synthesis of Adjustable Planar Four-Bar Crank-Rocker Type Mechanisms for Approximate Multi-Path Generation", Indian Institute of Science Department of Mechanical Engineering, Accessed October 22, 2016, 1-29, <http://www.mecheng.iisc.ernet.in/~asitava/chanekar-1.pdf>.
114. Lanni, C., and Ceccarelli, M., "An Optimization Problem Algorithm for Kinematic Design of Mechanisms for Two-Finger Grippers", *The Open Mechanical Engineering Journal, v. 3*, 2009, 49-62.
115. "How to Make a Pantograph", 1920-20.com, 2012, <http://www.1920-30.com/toys/things-to-make/pantograph.html>.
116. Goldstein, R., and Veloso, M., "Extendable Pantograph Arms", Association for the Advancement of Artificial Intelligence, 2016, <https://www.aaai.org/ocs/index.php/SSS/SSS16/paper/download/12727/11931>.
117. Long, H., Yang, Y., Jingjing, X., and Peng, S., "Type Synthesis of 1R1T Remote Center of Motion Mechanisms Based on Pantograph Mechanisms", Journal of Mechanical Design, v. 138, January 2016, 014501-1-5.
118. Rojas, R., "Genetic Algorithms", *Neural Networks*, Springer-Verlag, Berlin, 1996, 429-450.
119. Bertsekas, D.P., *Constrained Optimization and Lagrange Multiplier Methods*, Massachusetts Institute of Technology, 1996.
120. "Gradient Projection Methods", NEOS Optimization Guide, University of Wisconsin-Madison, <http://www.neos-guide.org/content/gradient-projection-methods>.
121. Dolan, E., *The NEOS Server 4.0 Administrative Guide*, Technical Memorandum ANL/MCS-TM-250, Mathematics and Computer Science Division, Argonne National Laboratory, 2001.
122. Zhang, Y., Finger, S., and Behrens, S., "Cams", *Introduction to Mechanisms*, Carnegie Mellon University, Pittsburgh, PA, 2010,
123. Johns, W.E., "Notes on Sprockets and Chains", *Gizmology.net*, 2003, <http://www.gizmology.net/sprockets.htm>.
124. Ryabov, G.K., and Serzhantova, L.P., *Minimum Possible Contact Angle of Chain Transmission Sprockets*, January 1985.
125. Nelson, C.A., Stolle, C.J., Burnfield, J.M., Buster, T.W., and McCrory, B.J., *Assistive Rehabilitation Elliptical System*, US Patent Application No. US 2016-023788, September 29, 2016.
126. Nelson, C.A., Stolle, C.J., Burnfield, J.M., and Buster, T.W., "Modification of the ICARE System for Pediatric Therapy", *Journal of Medical Devices*, V. 9 (4), Published online August 6, 2015.
127. Nelson, C.A., Stolle, C.J., Burnfield, J.M., and Buster, T.W., "Synthesis of a Rehabilitation Mechanism Replicating Normal Gait", *14th IFToMM World Congress Proceedings*, OS1-016, October 25, 2015.

128. Stolle, C.J., Nelson, C.A., Burnfield, J.M., and Buster, T.W., “Improved Design of a Gait Rehabilitation Robot”, *Proceedings of the 5th International Workshop on Medical and Service Robots*, Graz, Austria, July 4-6, 2016.

APPENDIX A – FOURIER SERIES MODELING OF FOOT GAIT PATHS

Pediatric Metatarsal Data

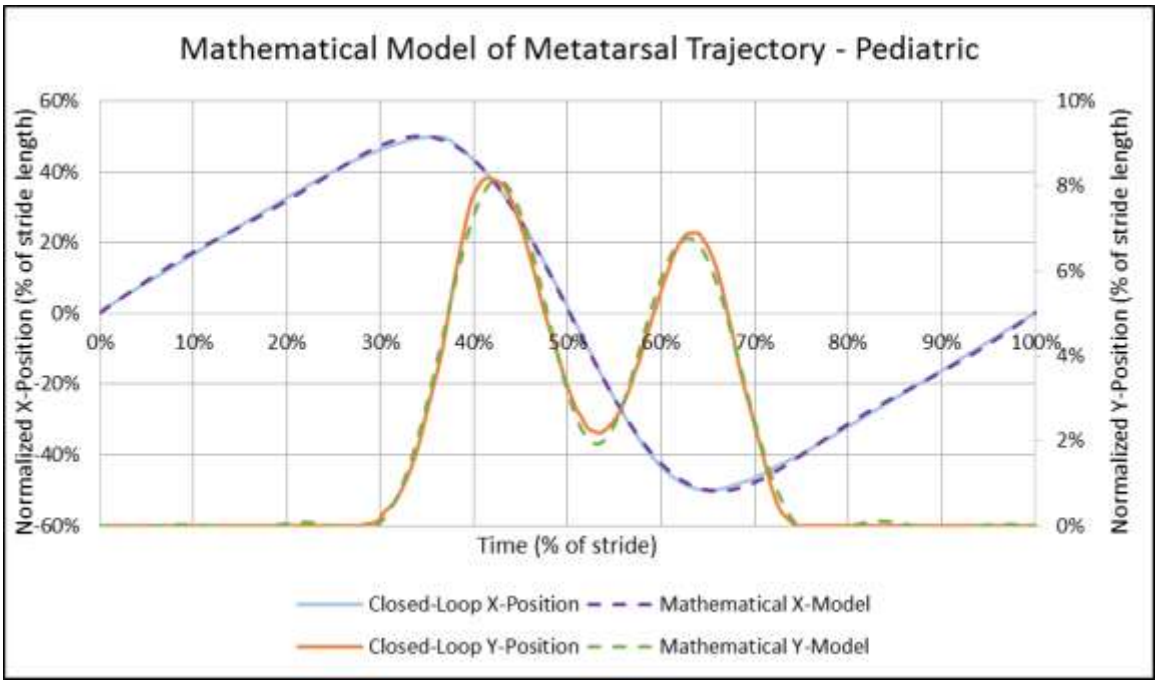

Pediatric Cartesian Metatarsal Parametrization Comparison (o_x=2,o_y=6)

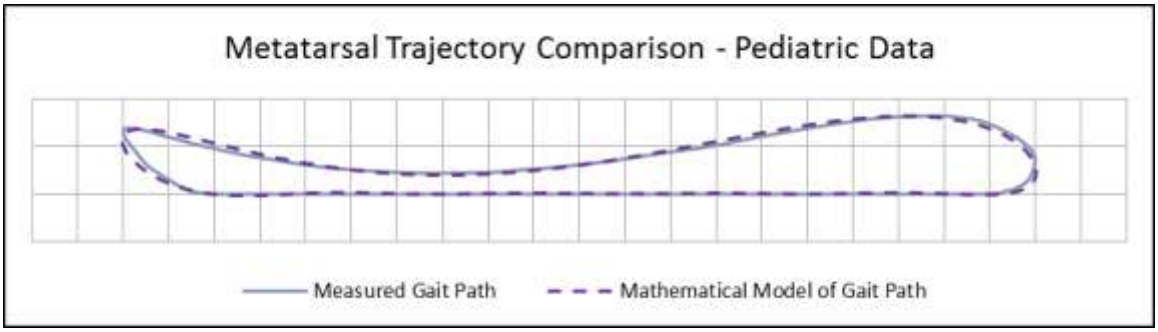

Pediatric Cartesian Metatarsal Trajectory Comparison (o_x=2,o_y=6)

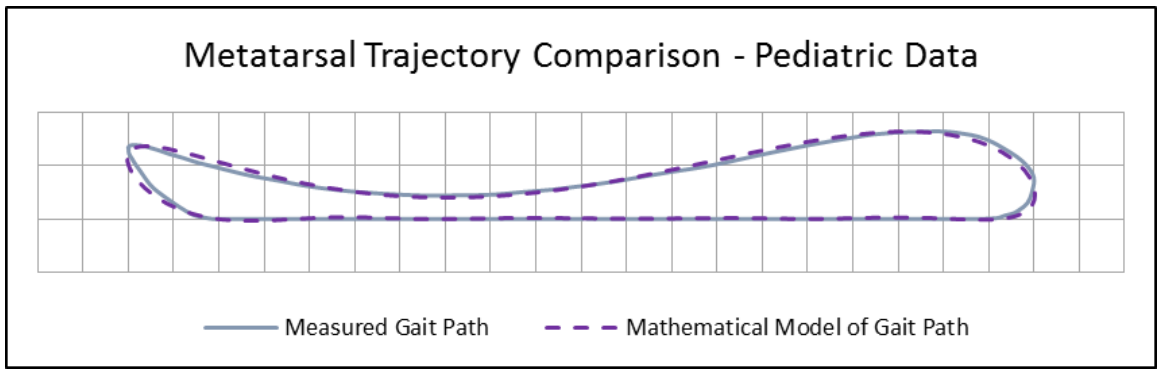

Pediatric Cartesian Metatarsal Trajectory Comparison (o_x=8,o_y=8)

Fourier Series Terms for Pediatric Metatarsal Trajectory

	Pediatric Am and Bn Constants					
	X-Coordinate		R^2	Y-Coordinate		R^2
m,n	a	b		a	b	
0	0.00390			0.01885		
1	-0.00149	0.44097	0.90534	-0.02920	-0.00245	0.61266
2	0.00345	-0.13606	0.99158	0.01023	0.00021	0.68802
3	-0.00359	0.04140	0.99963	0.00597	0.00571	0.73625
4	0.00255	-0.00695	0.99988	-0.01120	-0.00981	0.89382
5	-0.00104	-0.00201	0.99990	0.00750	0.00845	0.98476
6	0.00094	0.00363	0.99997	-0.00211	-0.00345	0.99644
7	-0.00053	-0.00120	0.99998	-0.00040	-0.00069	0.99690
8	0.00069	-0.00027	0.99998	0.00041	0.00173	0.99914

Author's Metatarsal Data

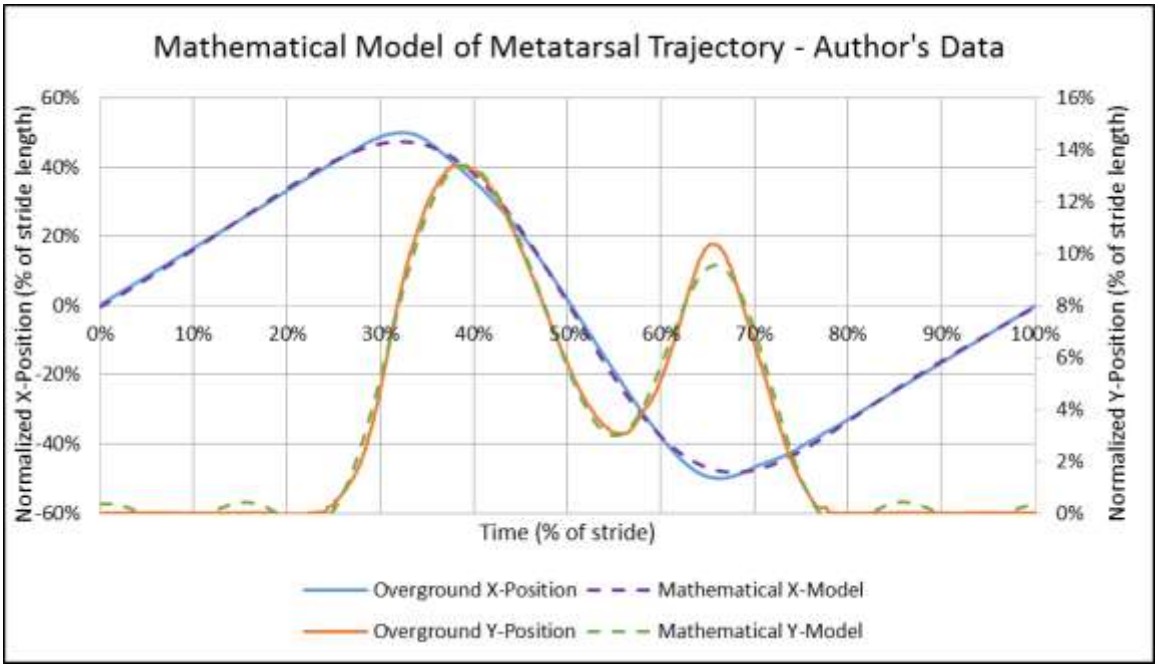

Author's Cartesian Metatarsal Parametrization Comparison (o_x=2,o_y=6)

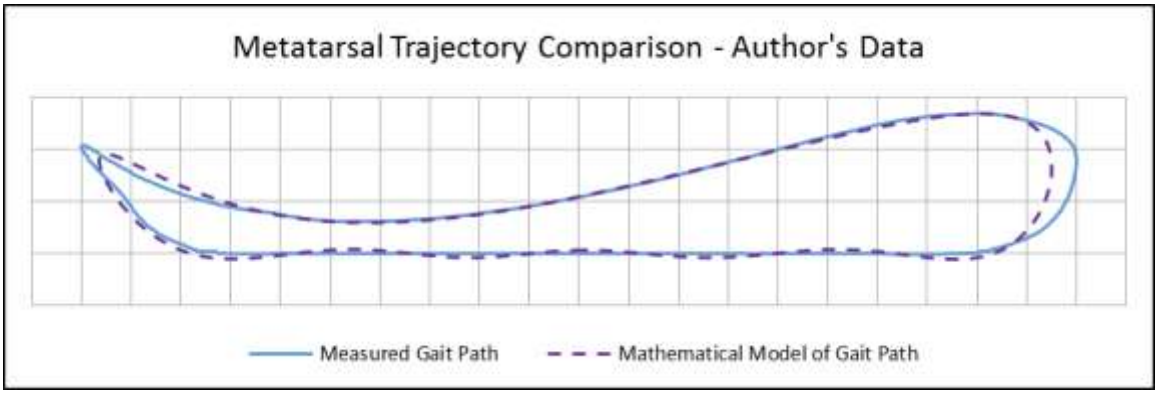

Author's Cartesian Metatarsal Trajectory Comparison (o_x=2,o_y=6)

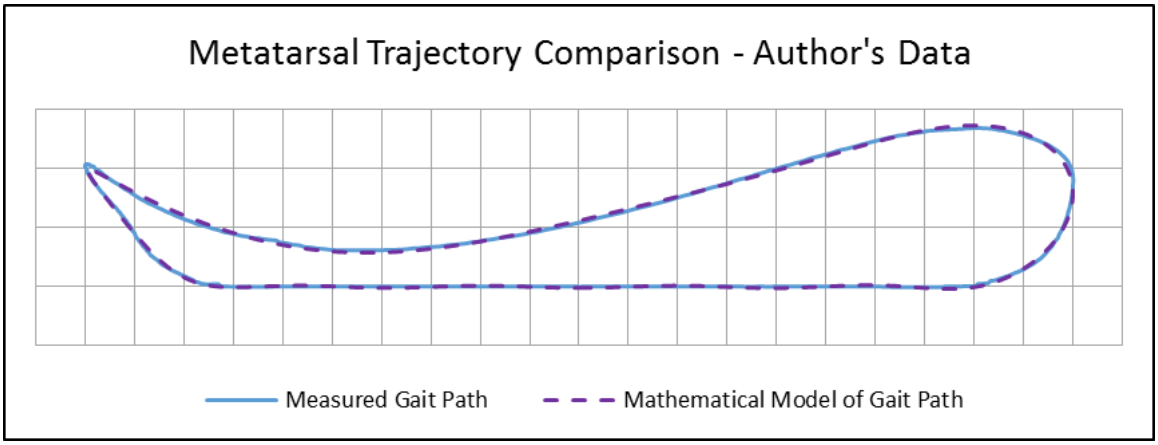

Author's Cartesian Metatarsal Trajectory Comparison (o_x=8,o_y=8)

Fourier Series Terms for Author's Metatarsal Trajectory

	Author's Am and Bn Constants					
	X-Coordinate		R^2	Y-Coordinate		R^2
m,n	a	b		a	b	
0	0.00128			0.03628		
1	-0.00084	0.43503	0.93211	-0.04992	0.00587	0.63050
2	0.00102	-0.11515	0.99742	0.00469	-0.01255	0.67530
3	-0.00414	0.01565	0.99871	0.02245	0.01583	0.86325
4	0.00684	0.00999	0.99943	-0.01789	-0.01199	0.97894
5	-0.00545	-0.00753	0.99986	0.00113	0.00427	0.98382
6	0.00132	0.00134	0.99988	0.00661	0.00076	0.99485
7	0.00190	0.00246	0.99992	-0.00372	-0.00128	0.99872
8	-0.00240	-0.00226	0.99998	-0.00055	0.00037	0.99883

Winter's Metatarsal Data

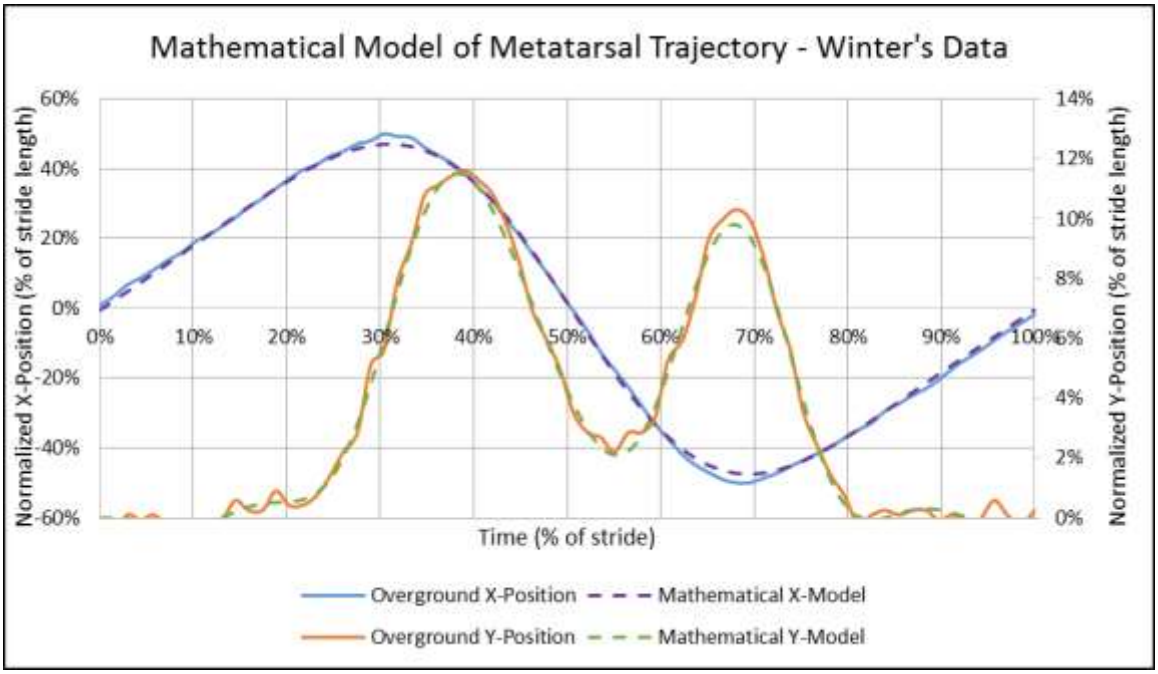

Winter's Cartesian Metatarsal Parametrization Comparison (o_x=2,o_y=6)

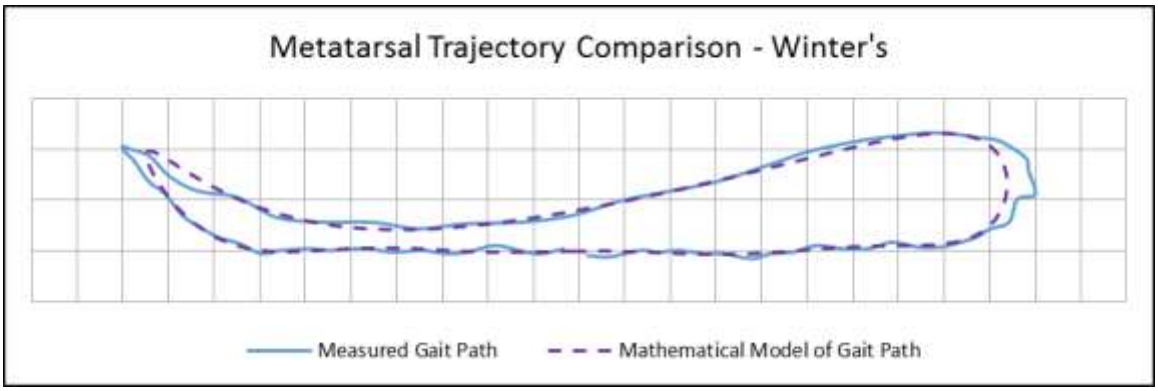

Winter's Cartesian Metatarsal Trajectory Comparison (o_x=2,o_y=6)

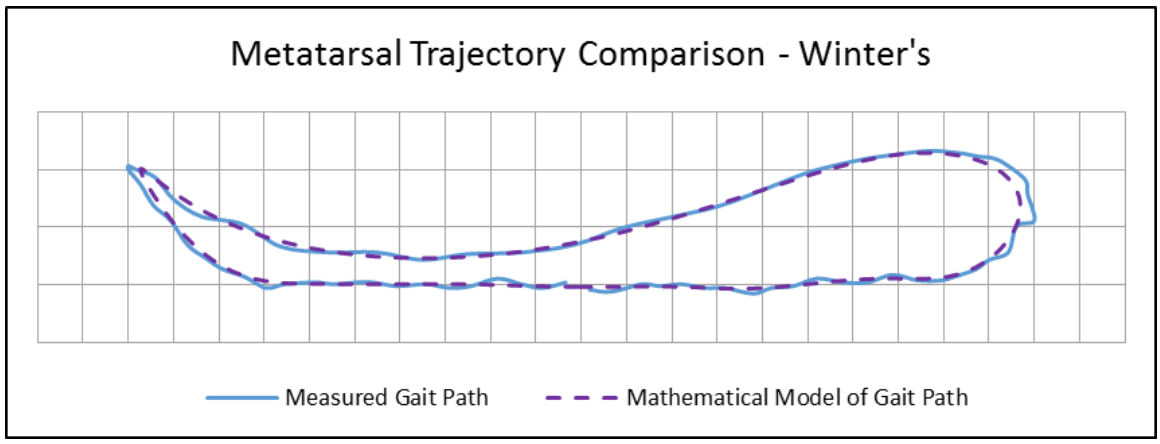

Winter's Cartesian Metatarsal Trajectory Comparison (o_x=8,o_y=8)

Fourier Series Terms for Winter's Metatarsal Trajectory

	Winter's Am and Bn Constants					
	X-Coordinate		R^2	Y-Coordinate		R^2
m,n	a	b		a	b	
0	0.00055			0.03505		
1	-0.00711	0.44439	0.95824	-0.04216	0.00115	0.58105
2	0.00426	-0.09081	0.99836	-0.00722	-0.01001	0.62845
3	-0.00304	0.00772	0.99870	0.02340	0.01643	0.89298
4	0.00425	0.01054	0.99932	-0.01039	-0.01303	0.98326
5	0.00080	-0.00195	0.99935	-0.00266	0.00141	0.98595
6	-0.00015	0.00074	0.99936	0.00366	0.00317	0.99409
7	0.00044	0.00292	0.99940	0.00057	-0.00081	0.99442
8	-0.00233	0.00074	0.99940	-0.00171	-0.00003	0.99524

Average Metatarsal Data

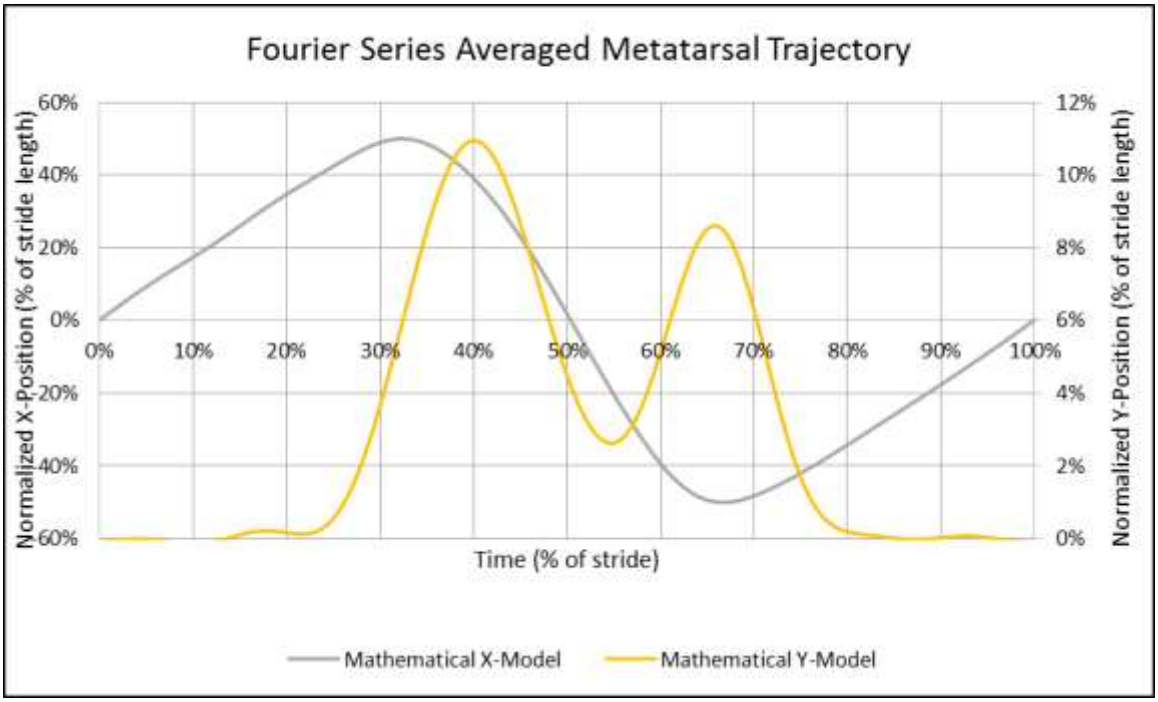

Average Winter's Cartesian Metatarsal Parametrization Comparison (o_x=8,o_y=8)

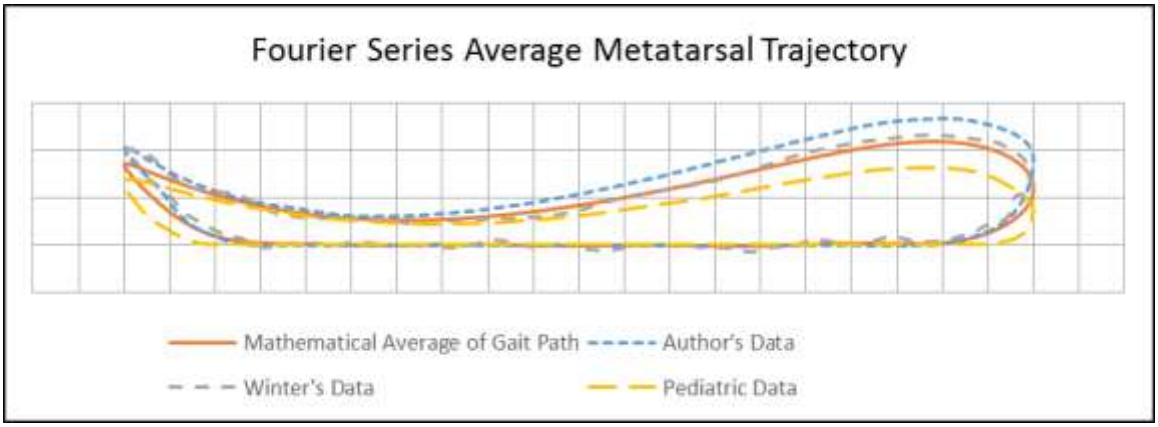

Average Cartesian Metatarsal Trajectory Comparison (o_x=8,o_y=8)

Fourier Series Terms for Average Metatarsal Trajectory

	Average Metatarsal Am and Bn Constants				
	X-Coordinate			Y-Coordinate	
m,n	a	b		a	b
0	0.001952			0.030684	
1	-0.00321	0.449314		-0.04127	0.001555
2	0.002967	-0.11639		0.00262	-0.0076
3	-0.00367	0.022039		0.017633	0.01292
4	0.004643	0.004623		-0.01344	-0.01185
5	-0.00193	-0.00391		0.002033	0.004808
6	0.000715	0.001944		0.002778	0.000164
7	0.000618	0.001426		-0.00121	-0.00095
8	-0.00138	-0.00061		-0.00063	0.000702

Pediatric Heel Data

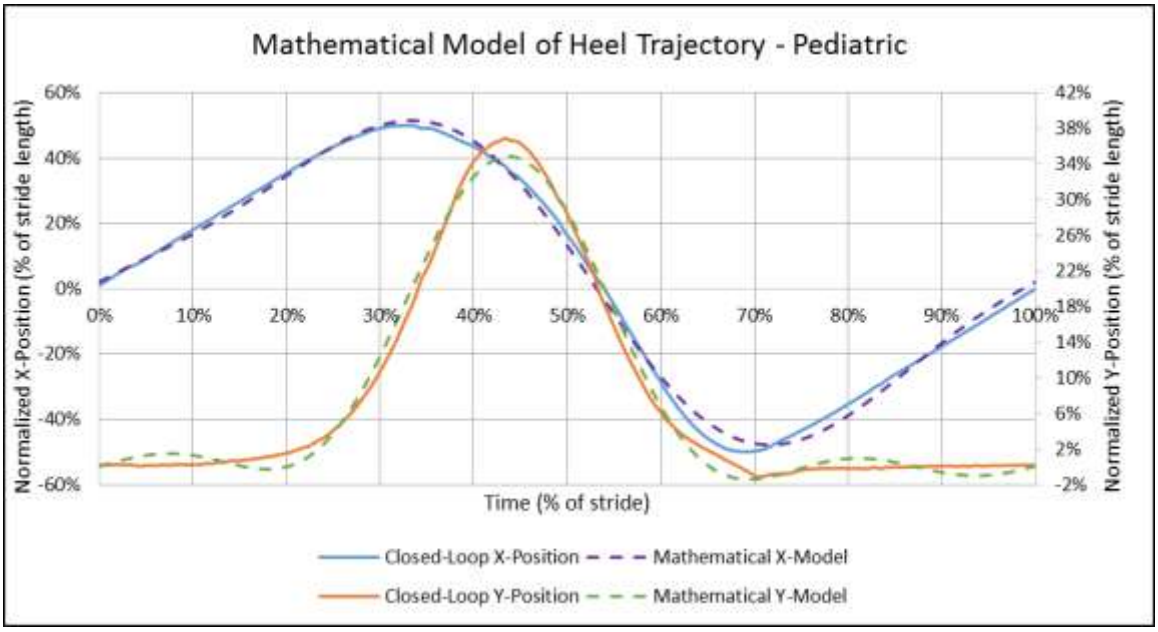

Pediatric Cartesian Heel Parametrization Comparison (o_x=2,o_y=3)

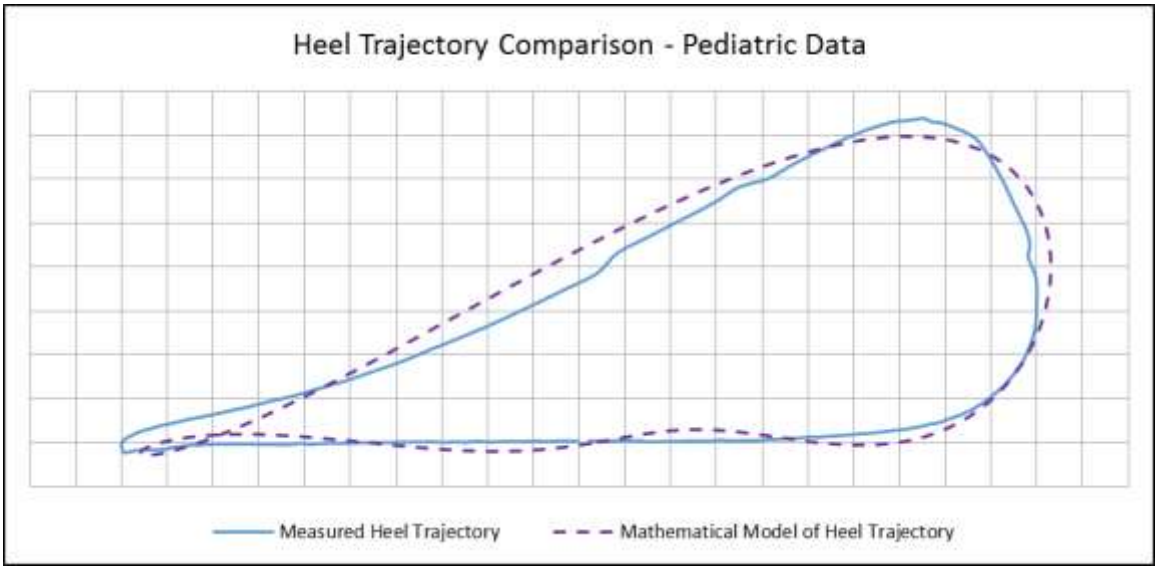

Pediatric Cartesian Heel Trajectory Comparison (o_x=2,o_y=3)

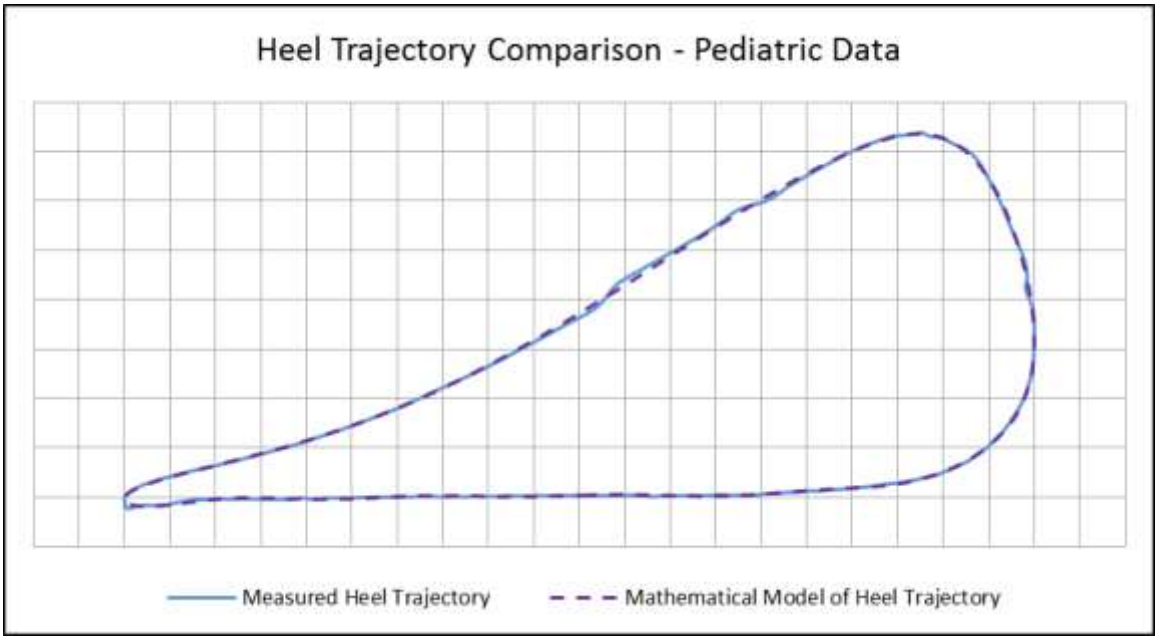

Pediatric Cartesian Heel Trajectory Comparison (o_x=8,o_y=8)

Fourier Series Terms for Pediatric Heel Trajectory

	Pediatric Heel Am and Bn Constants					
	X-Coordinate		R^2	Y-Coordinate		R^2
m,n	a	b		a	b	
0	0.03199			0.08048		
1	-0.05539	0.44963	0.93842	-0.12603	0.05731	0.66035
2	0.04444	-0.10243	0.99543	0.06275	-0.06301	0.93283
3	-0.02571	0.00799	0.99877	-0.01672	0.03768	0.99133
4	0.01083	0.01075	0.99983	-0.00109	-0.01481	0.99891
5	-0.00097	-0.00432	0.99992	0.00314	0.00372	0.99972
6	-0.00104	0.00059	0.99993	-0.00049	-0.00065	0.99975
7	0.00167	0.00230	0.99996	-0.00076	-0.00069	0.99978
8	-0.00012	-0.00061	0.99929	0.00074	0.00165	0.99990

Author's Heel Data

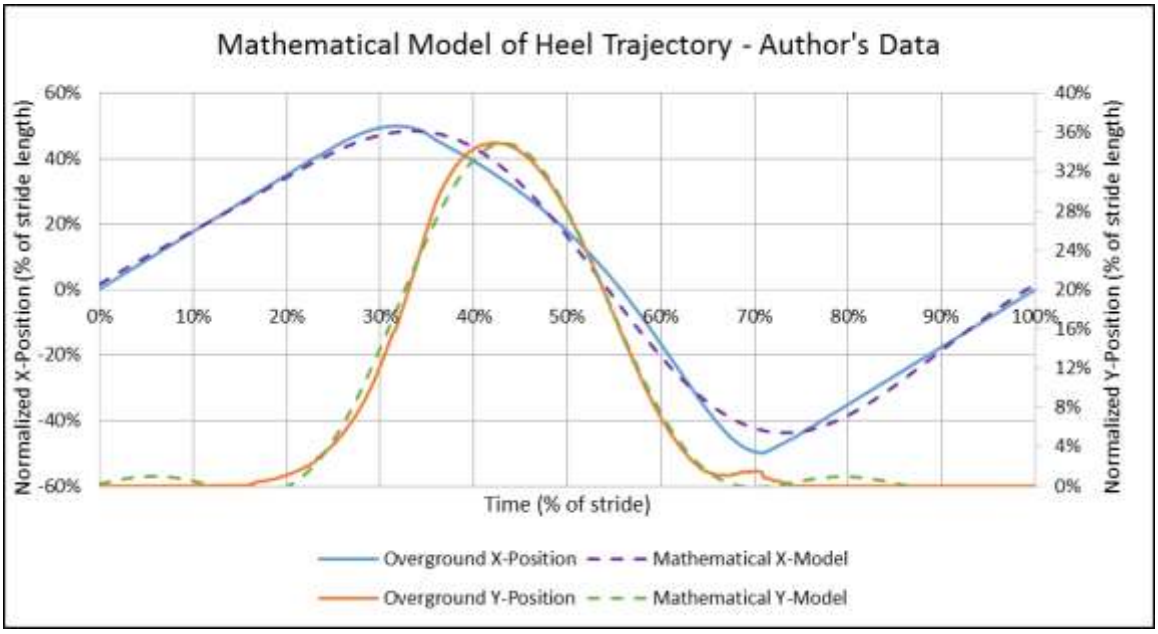

Author's Cartesian Heel Parametrization Comparison (o_x=2,o_y=3)

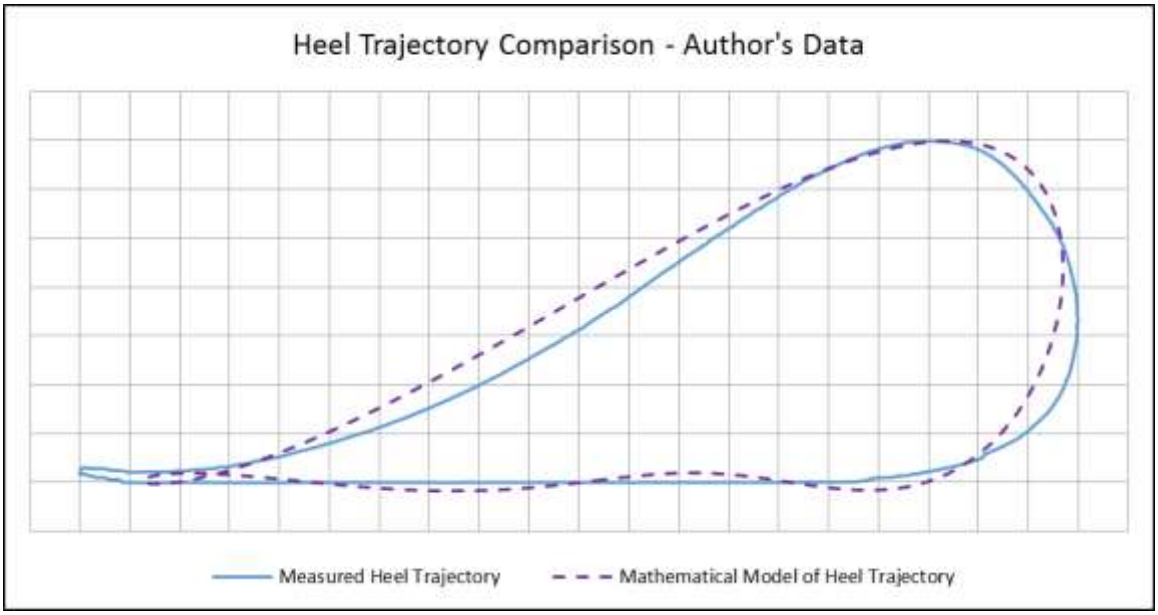

Author's Cartesian Heel Trajectory Comparison (o_x=2,o_y=3)

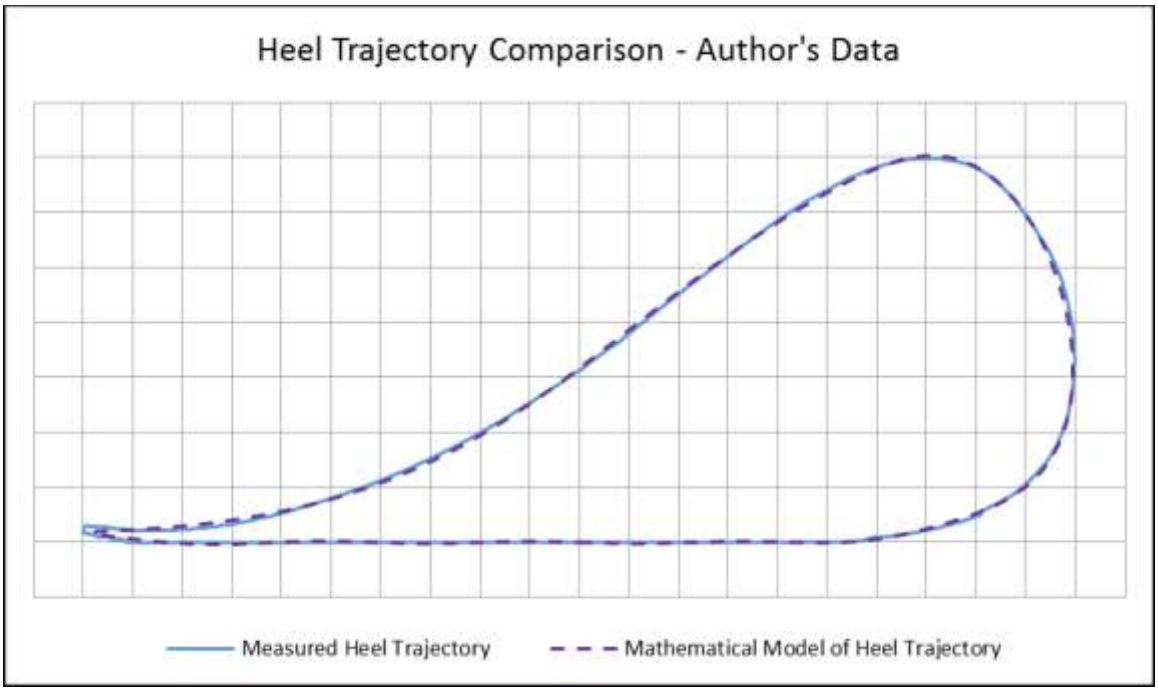

Author's Cartesian Heel Trajectory Comparison (o_x=8,o_y=8)

Fourier Series Terms for Author's Heel Trajectory

	Author's Heel Am and Bn Constants					
	X-Coordinate		R^2	Y-Coordinate		R^2
m,n	a	b		a	b	
0	0.04155			0.08345		
1	-0.07263	0.42644	0.95394	-0.13008	0.05684	0.69004
2	0.04821	-0.07173	0.99203	0.05770	-0.06485	0.94807
3	-0.01952	-0.02139	0.99630	-0.00929	0.03592	0.99518
4	0.00062	0.02492	0.99947	-0.00341	-0.00831	0.99794
5	0.00446	-0.00457	0.99968	0.00138	-0.00376	0.99849
6	-0.00159	-0.00556	0.99985	0.00104	0.00534	0.99950
7	-0.00139	0.00425	0.99995	-0.00125	-0.00235	0.99975
8	0.00096	0.00045	0.99996	0.00061	-0.00081	0.99978

Winter's Heel Data

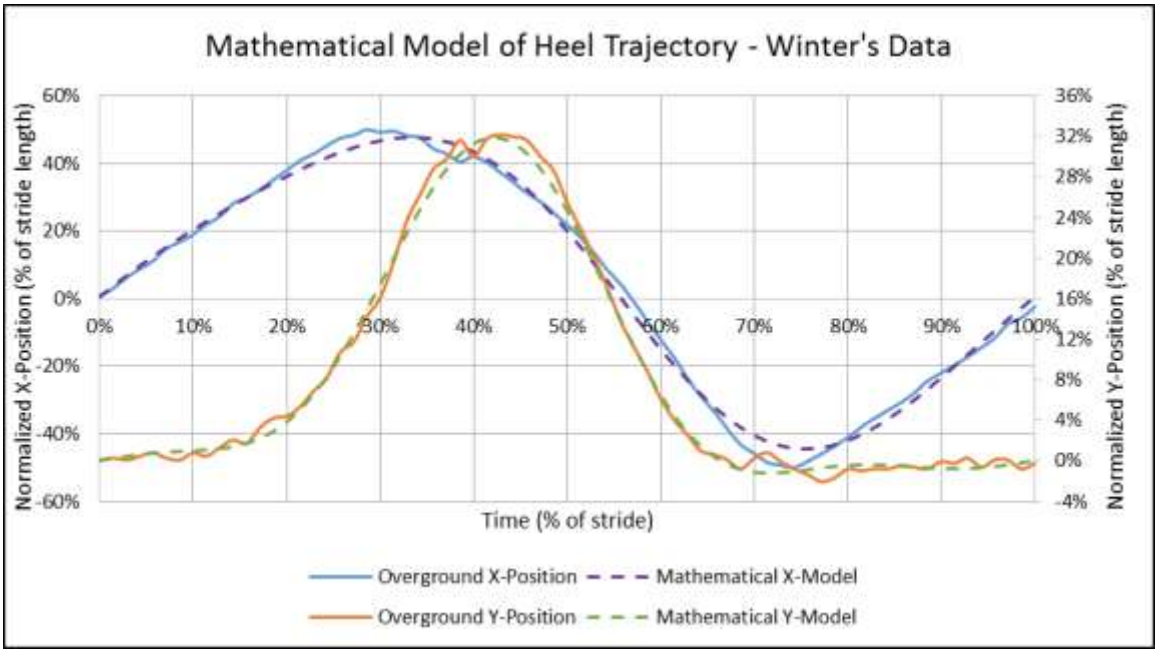

Winter's Cartesian Heel Parametrization Comparison (o_x=2,o_y=3)

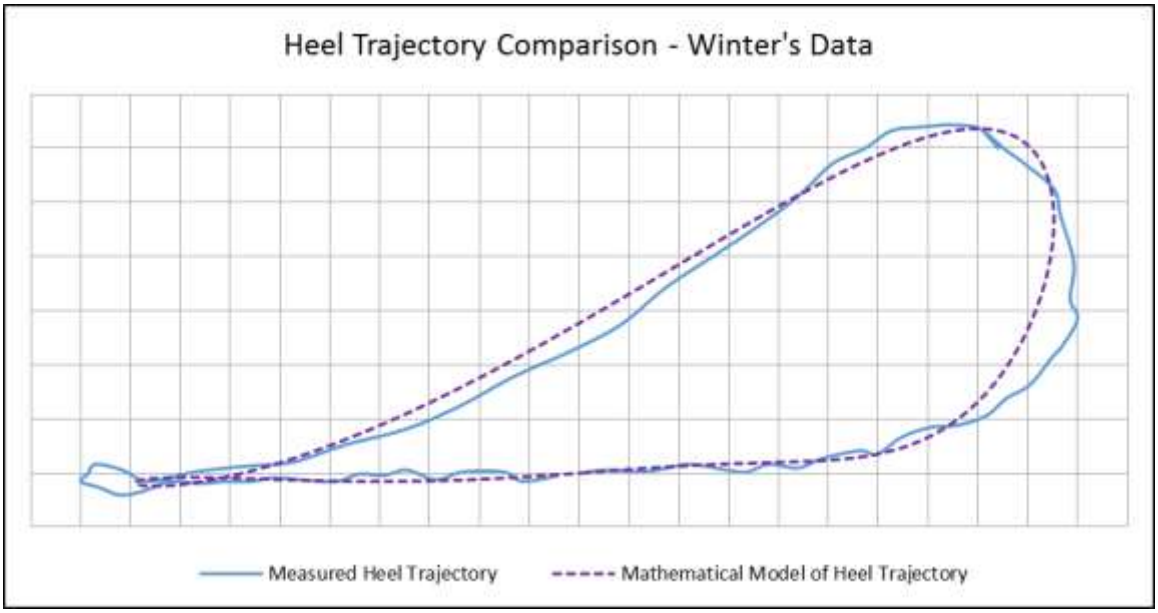

Winter's Cartesian Heel Trajectory Comparison (o_x=2,o_y=3)

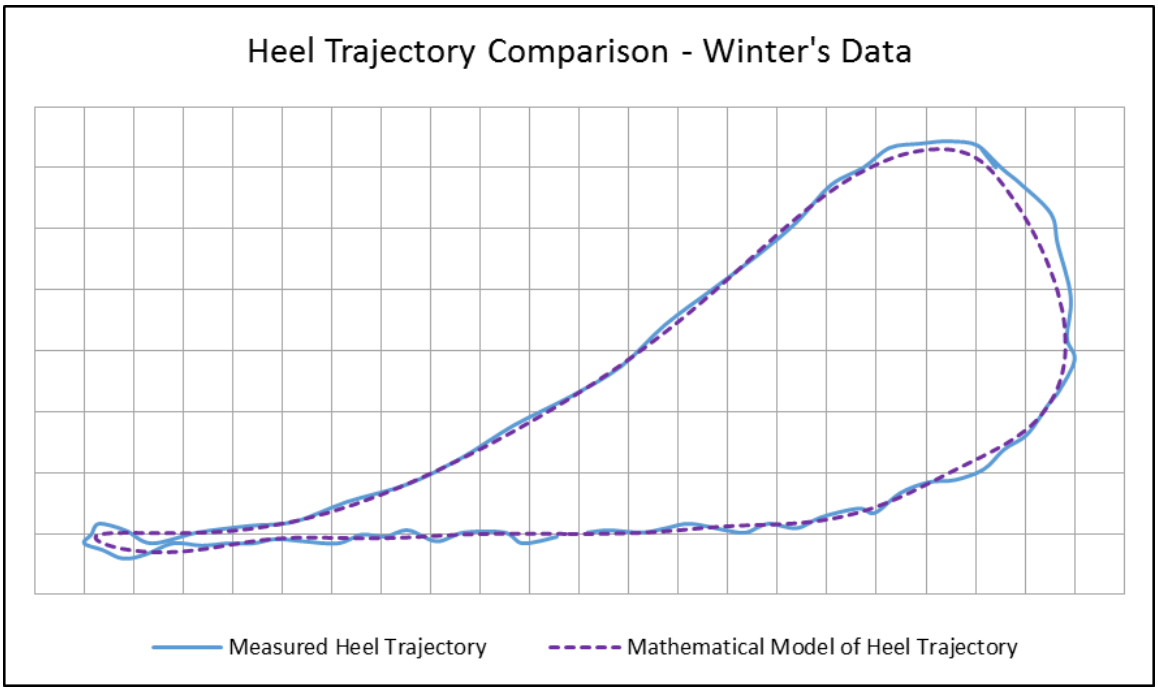

Winter's Cartesian Heel Trajectory Comparison (o_x=8,o_y=8)

Fourier Series Terms for Winter's Heel Trajectory

	Winter's Heel Am and Bn Constants					
	X-Coordinate		R^2	Y-Coordinate		R^2
m,n	a	b		a	b	
0	0.04585			0.08267		
1	-0.09804	0.43456	0.97056	-0.11803	0.07442	0.76376
2	0.05621	-0.03823	0.99338	0.04113	-0.06036	0.97265
3	-0.01561	-0.02489	0.99760	-0.00529	0.02355	0.99539
4	0.00001	0.01581	0.99883	0.00030	-0.00487	0.99629
5	0.00261	0.00827	0.99916	-0.00209	-0.00223	0.99671
6	0.00047	-0.00379	0.99920	0.00229	0.00312	0.99738
7	0.00108	0.00113	0.99921	-0.00074	0.00145	0.99749
8	-0.00248	0.00424	0.99927	-0.00063	-0.00302	0.99786

Average Heel Data

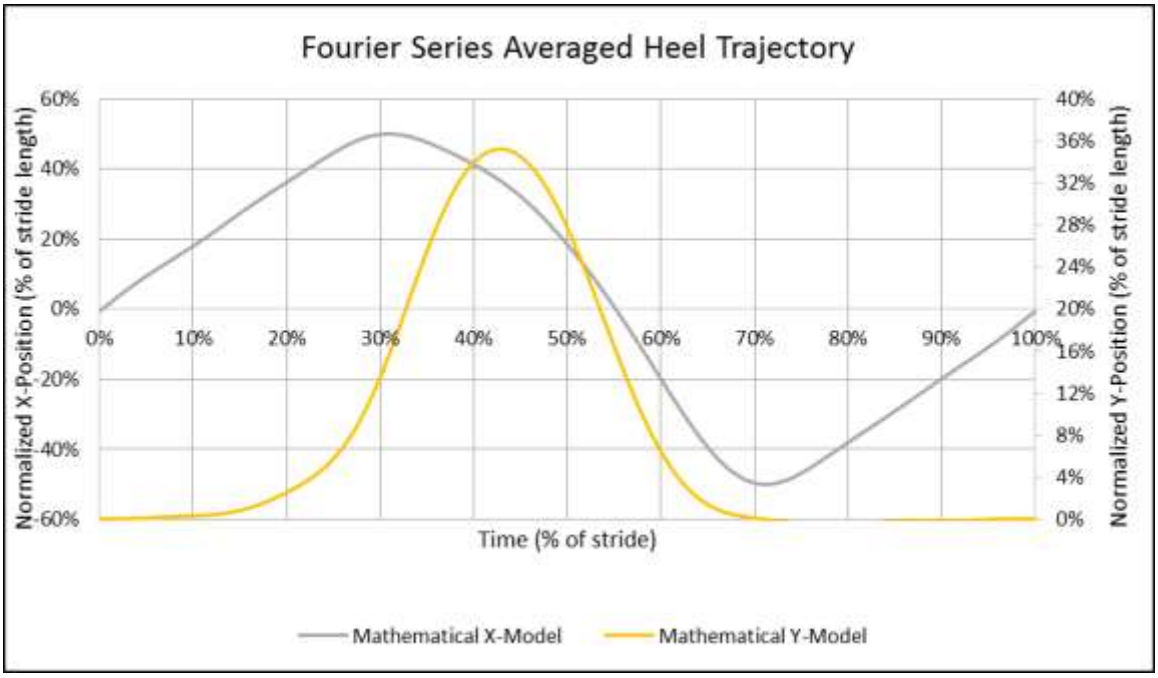

Average Cartesian Heel Parametrization Comparison (o_x=8,o_y=8)

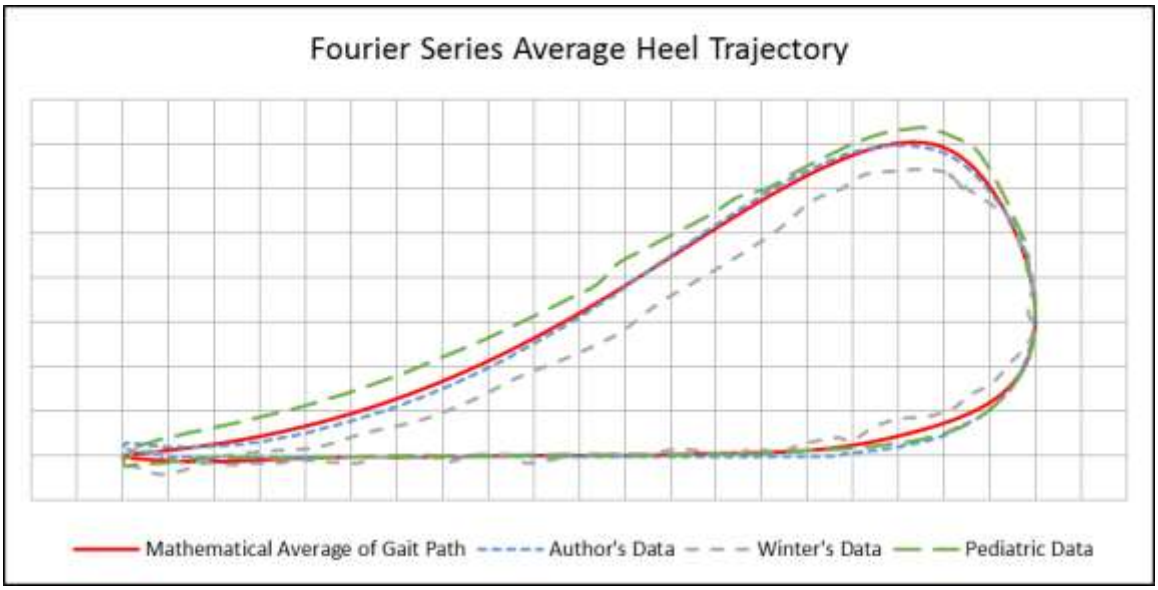

Average Cartesian Heel Trajectory Comparison (o_x=8,o_y=8)

Fourier Series Terms for Average Heel Trajectory

	Average Heel Am and Bn Constants				
	X-Coordinate			Y-Coordinate	
m,n	a	b		a	b
0	0.040722			0.084108	
1	-0.0771	0.447013		-0.12761	0.064313
2	0.050769	-0.07244		0.055108	-0.06419
3	-0.02075	-0.01306		-0.01068	0.033135
4	0.003907	0.017561		-0.00143	-0.00955
5	0.002082	-0.00021		0.000826	-0.00077
6	-0.00074	-0.00299		0.000967	0.002664
7	0.000463	0.00262		-0.00094	-0.00054
8	-0.00056	0.00139		0.000245	-0.00074

Pediatric Foot Angle Data

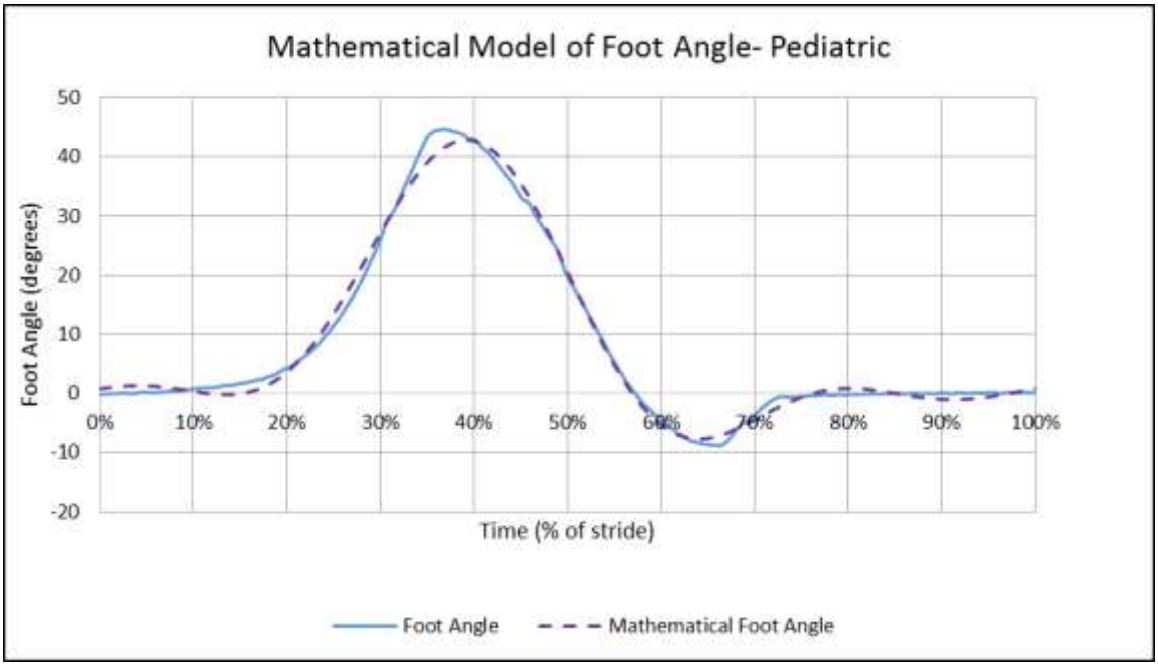

Pediatric Foot Angle Comparison (o_x=3)

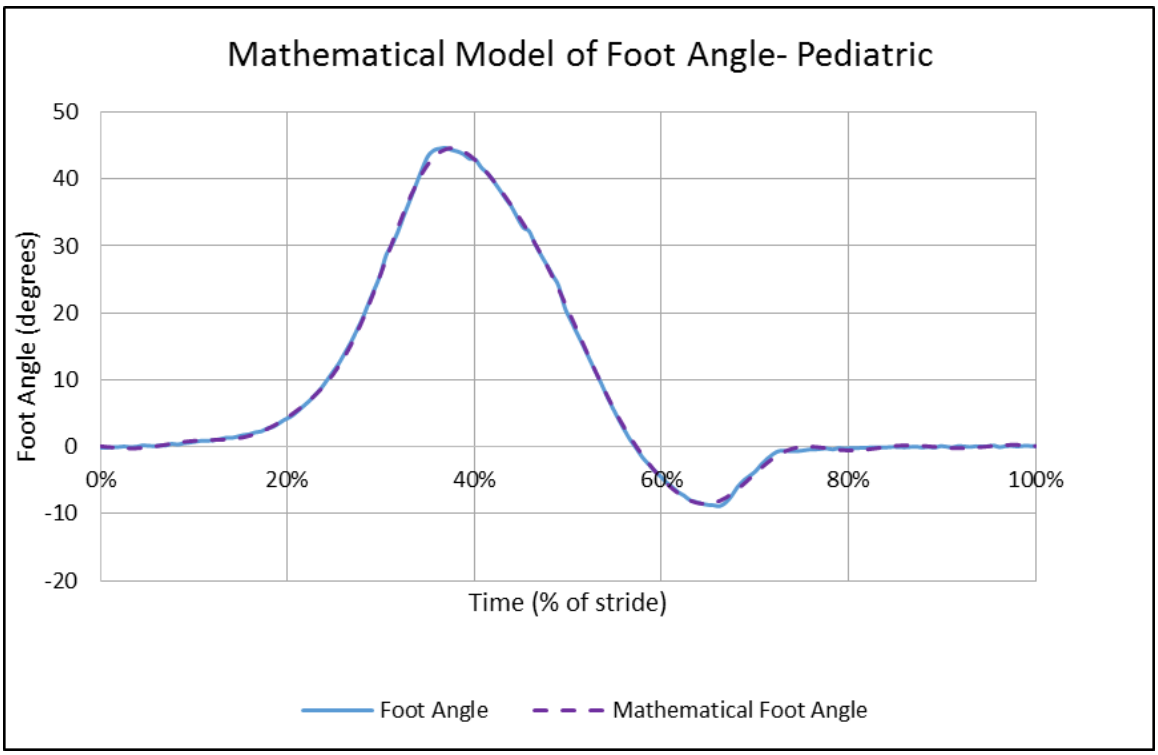

Pediatric Foot Angle Comparison (o_x=8)

Fourier Series Terms for Pediatric Foot Angle

Pediatric Am and Bn Constants			
	X-Coordinate		R^2
m,n	a	b	
0	8.545291		
1	-11.2107	12.39033	0.59644
2	2.078406	-12.3024	0.92820
3	1.381781	5.348146	0.99319
4	-0.82889	-0.16663	0.99472
5	-0.12025	-1.25694	0.99812
6	0.232149	0.552856	0.99889
7	-0.16688	0.205267	0.99903
8	0.179615	-0.48264	0.99960

Author's Foot Angle Data

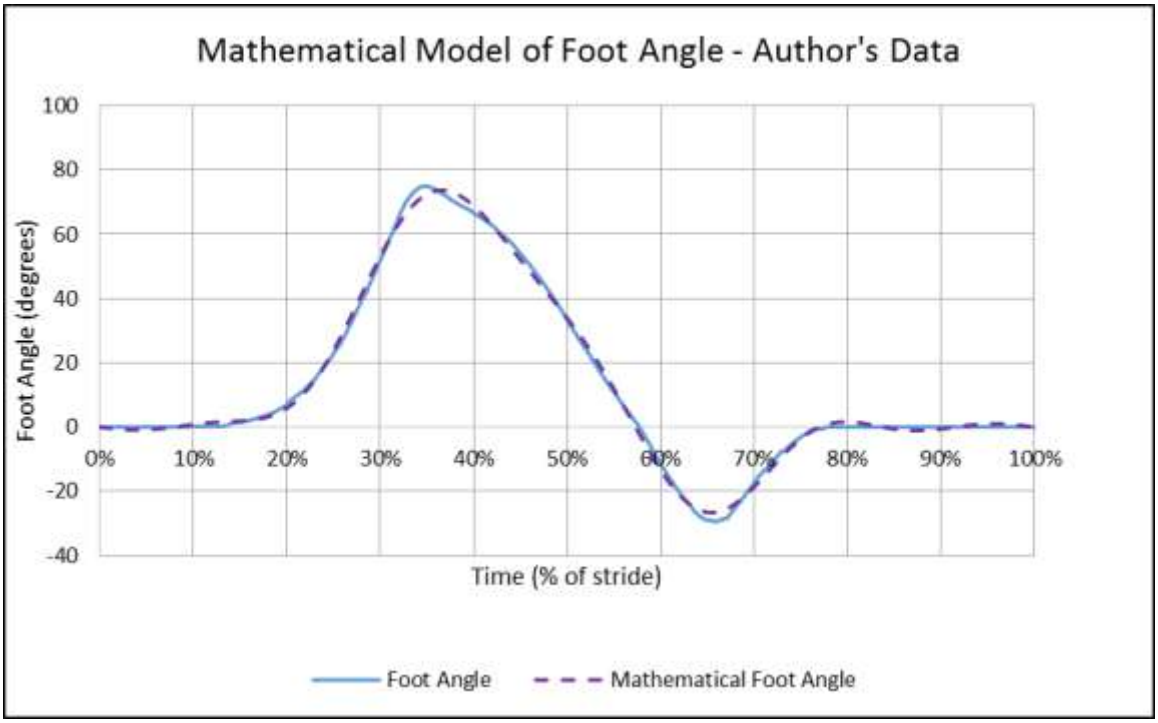

Author's Foot Angle Comparison (o_x=5)

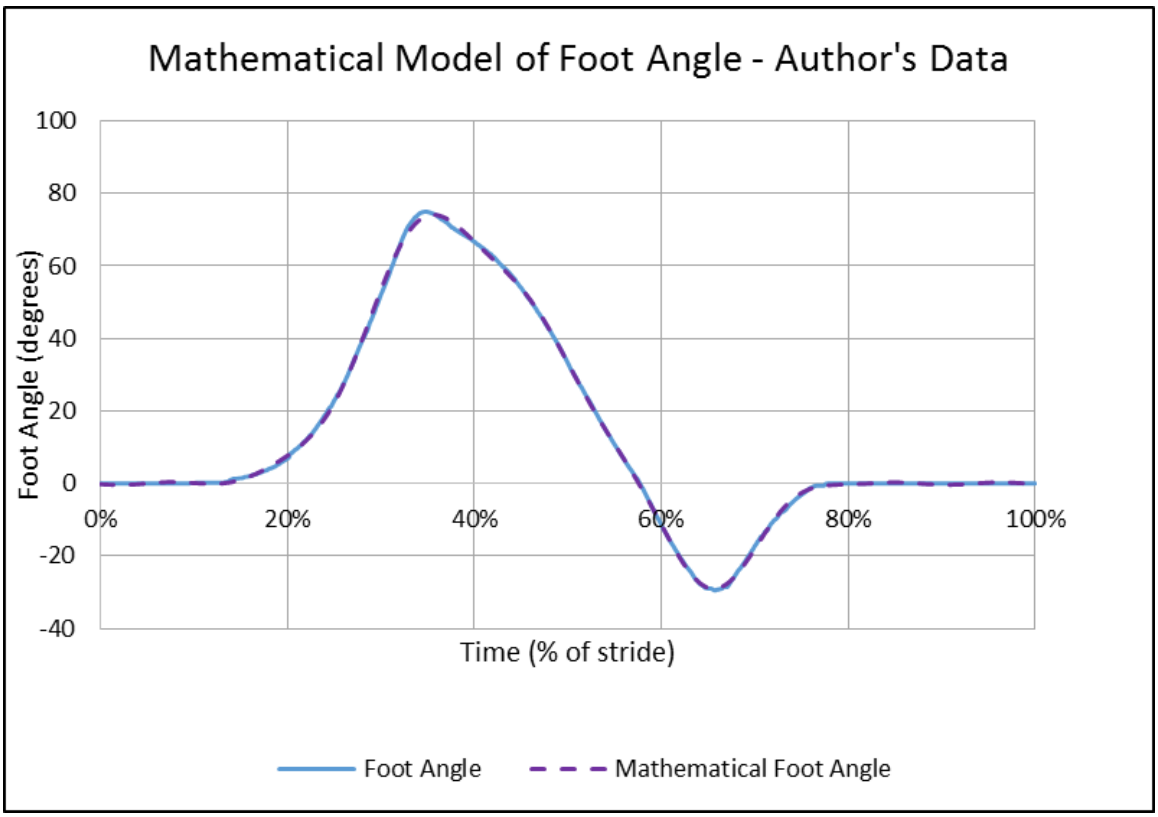

Author's Foot Angle Comparison (o_x=8)

Fourier Series Terms for Author's Foot Angle

Author's Am and Bn Constants			
	Foot Angle		R^2
m,n	a	b	
0	13.13296		
1	-17.4539	24.31764	0.58540
2	3.485944	-23.3338	0.94892
3	0.975032	6.980353	0.98136
4	0.351219	3.360969	0.98881
5	-0.54635	-3.57697	0.99736
6	-0.05078	0.392631	0.99747
7	0.236929	1.383102	0.99875
8	-0.29699	-1.1244	0.99964

Winter's Foot Angle Data

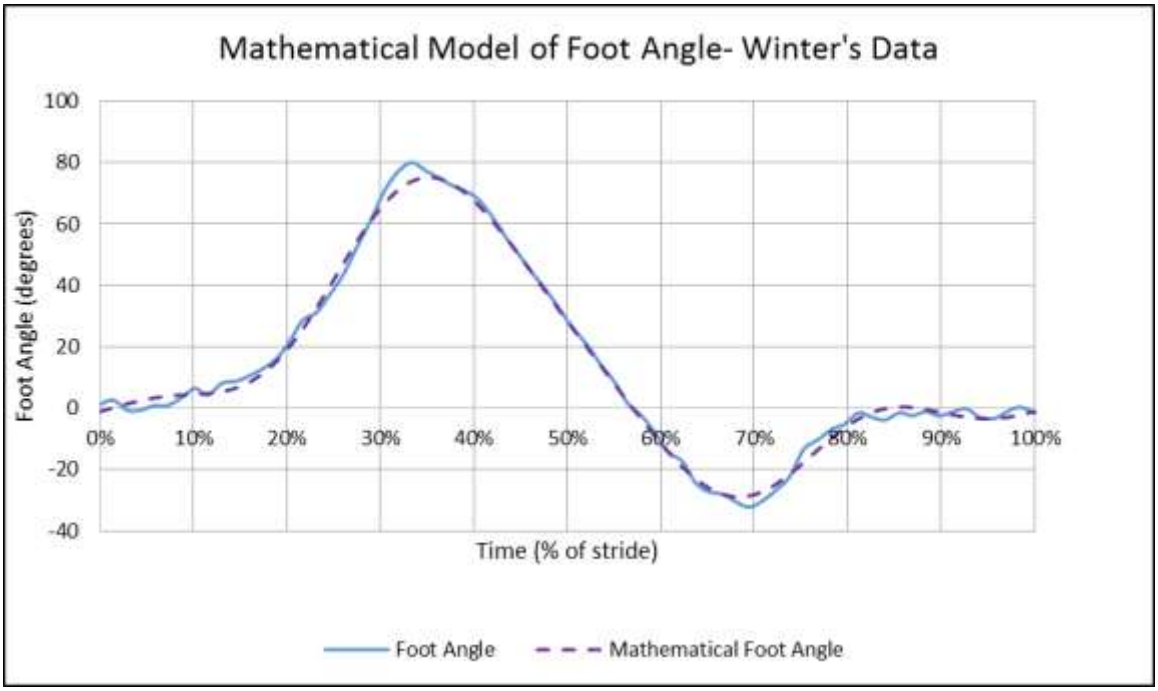

Winter's Foot Angle Comparison (o_x=4)

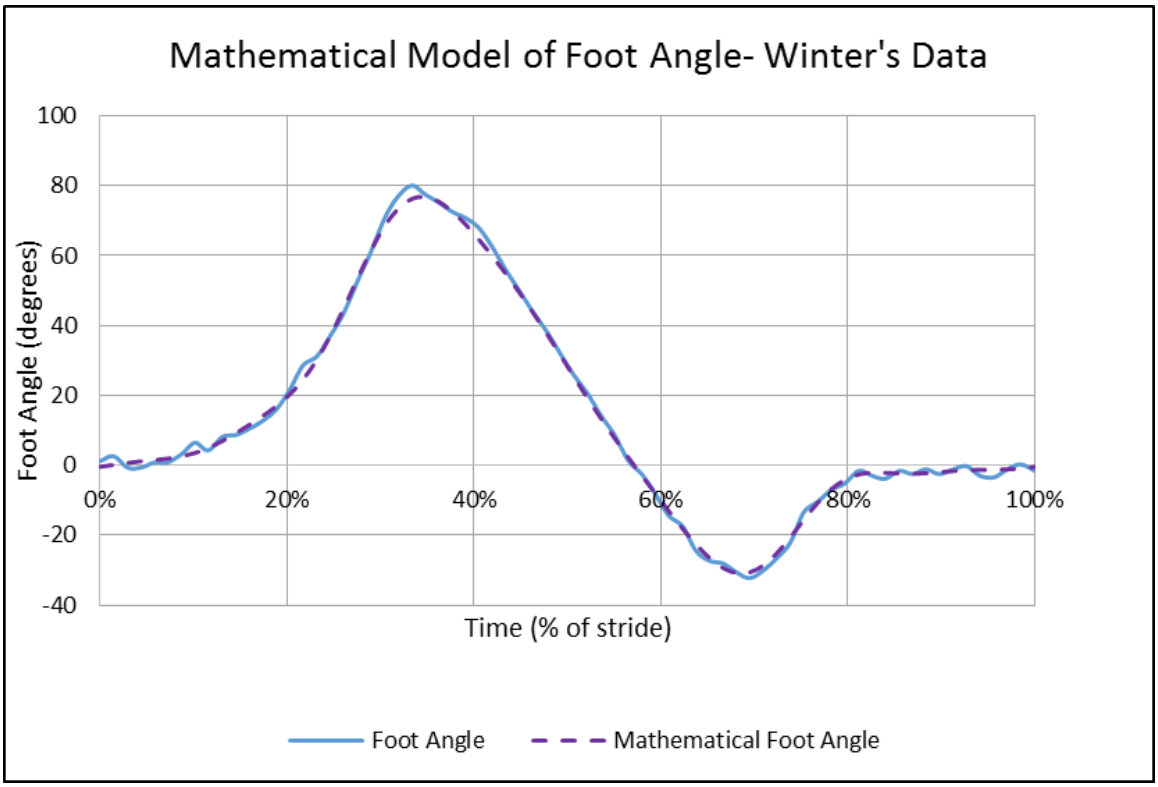

Winter's Foot Angle Comparison (o_x=8)

Fourier Series Terms for Winter's Foot Angle

Winter's Am and Bn Constants			
	Foot Angle		R^2
m,n	a	b	
0	13.73055		
1	-15.8727	32.37969	0.71515
2	0.936005	-21.9507	0.97963
3	1.223366	2.272873	0.98331
4	-0.99845	4.46098	0.99486
5	0.542386	-1.58599	0.99651
6	0.469622	-1.12671	0.99721
7	-0.28759	0.792762	0.99759
8	-0.21619	0.214468	0.99761

Average Foot Angle Data

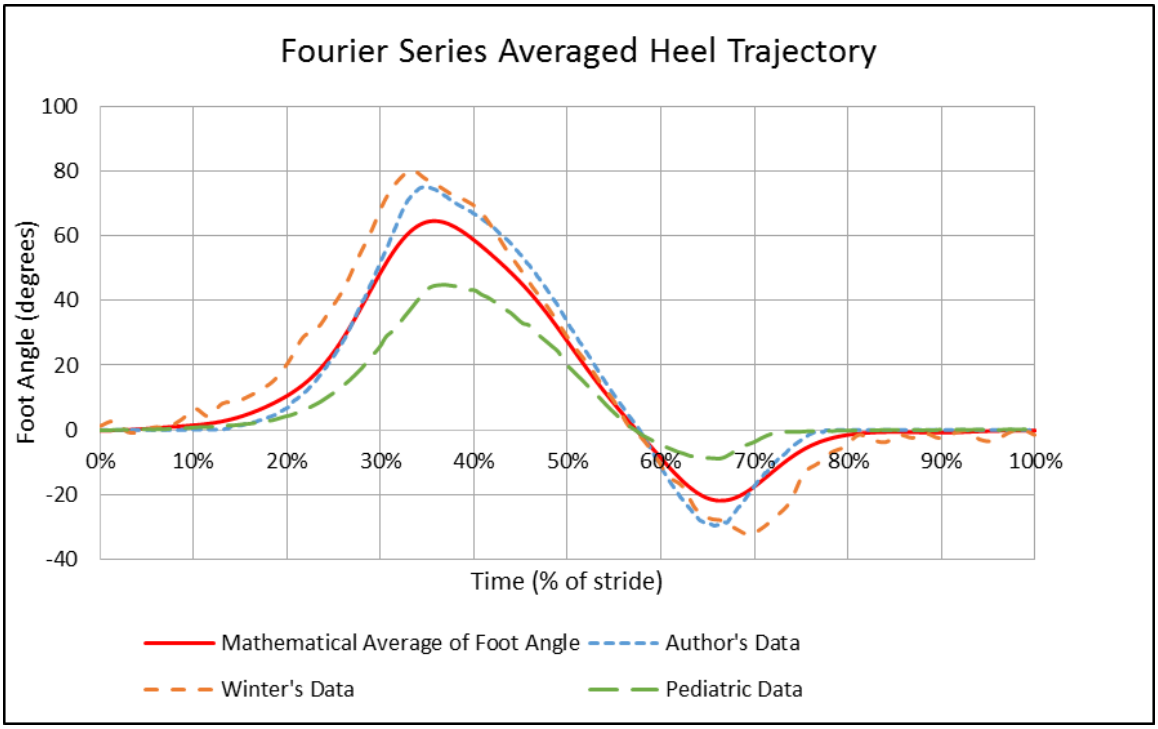

Average Foot Angle Comparison (o_x=8)

Fourier Series Terms for Average Foot Angle

Average Foot Angle Am and Bn Constants		
	X-Coordinate	
m,n	a	b
0	11.80293	
1	-14.8457	23.02922
2	2.166785	-19.1956
3	1.193393	4.867124
4	-0.49204	2.551773
5	-0.0414	-2.13996
6	0.216997	-0.06041
7	-0.07251	0.79371
8	-0.11119	-0.46419

APPENDIX B – PART DIAGRAMS OF PEDIATRIC ICARE CRANK

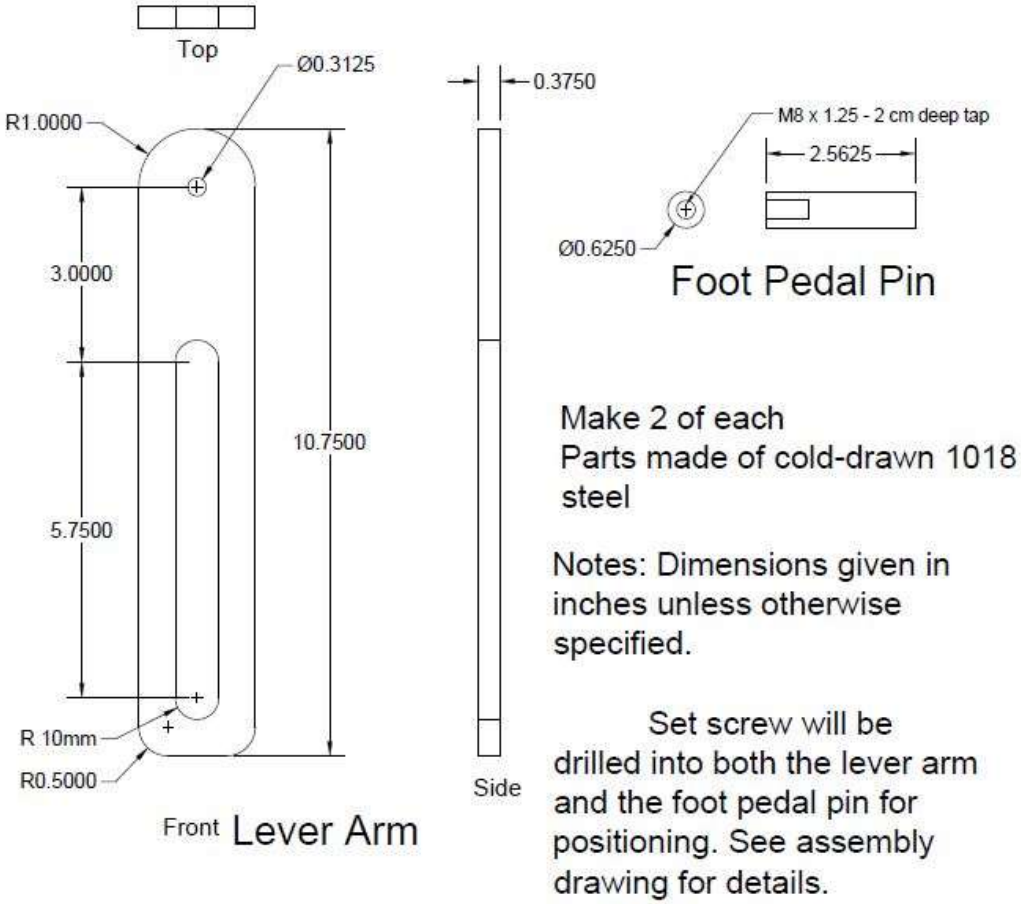

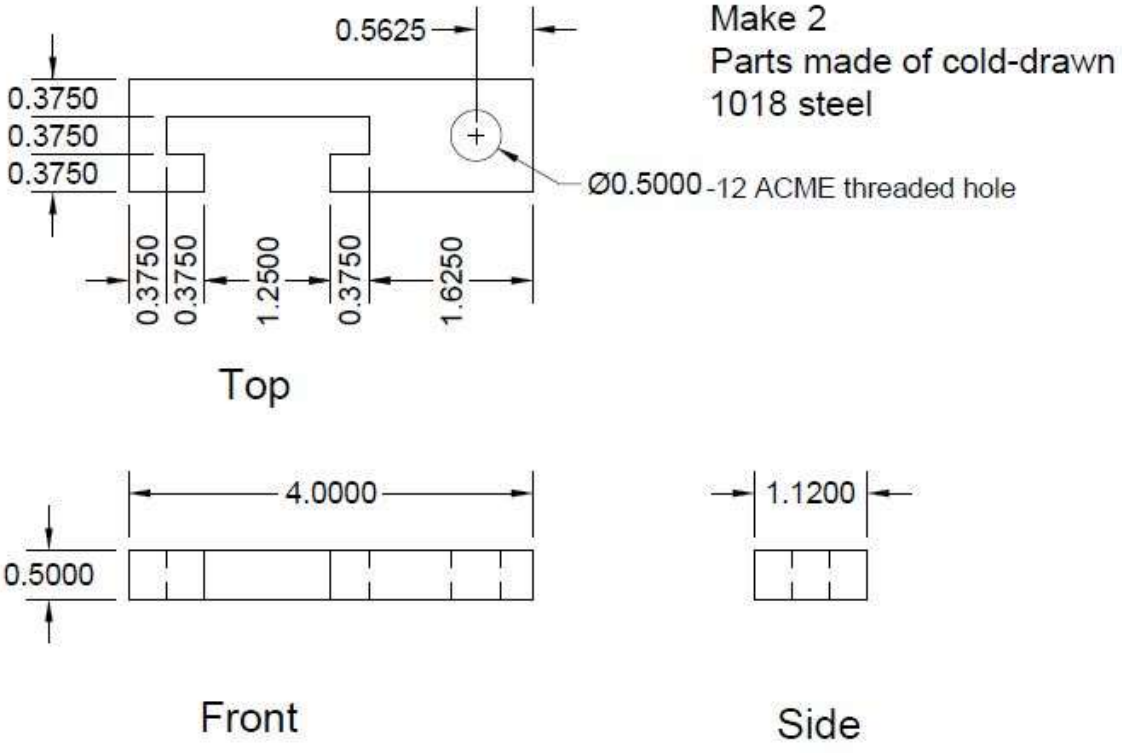

Fixed Bracket

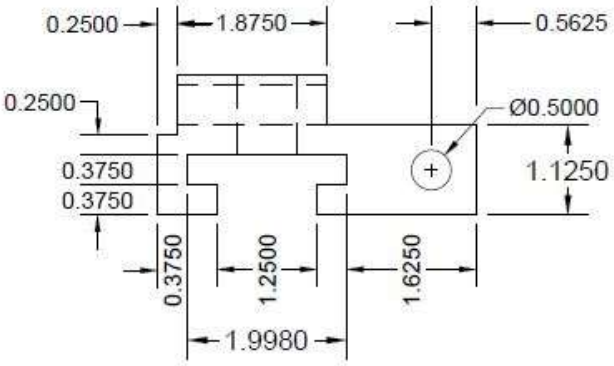

Top

Note: Dimensions given in inches unless otherwise specified

Make 2
Parts made of cold-drawn 1018 steel

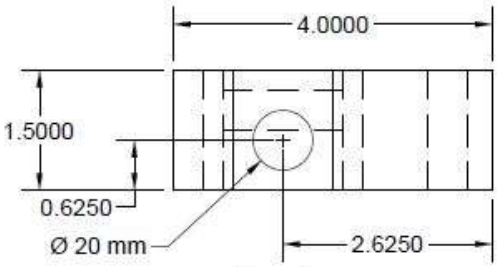

Front

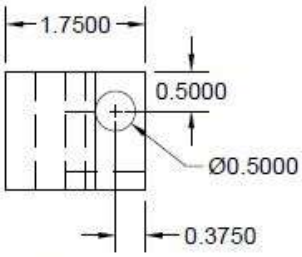

Side

Motor Bracket

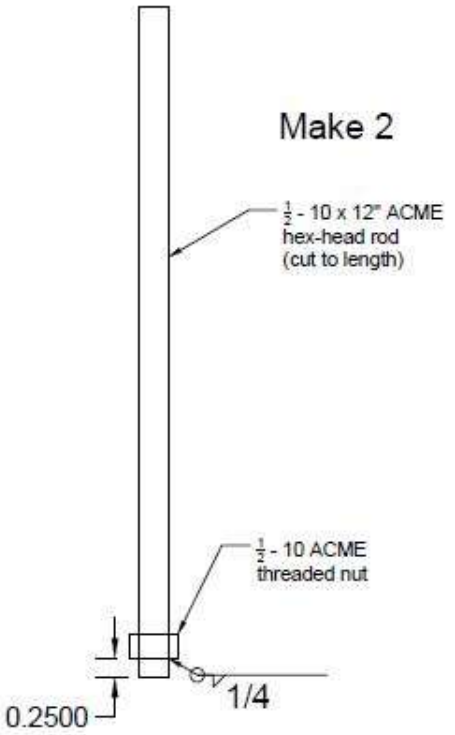

Adjustment Screw

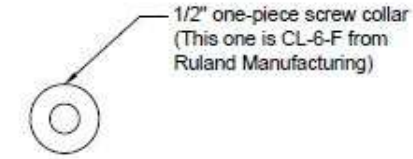

Collar

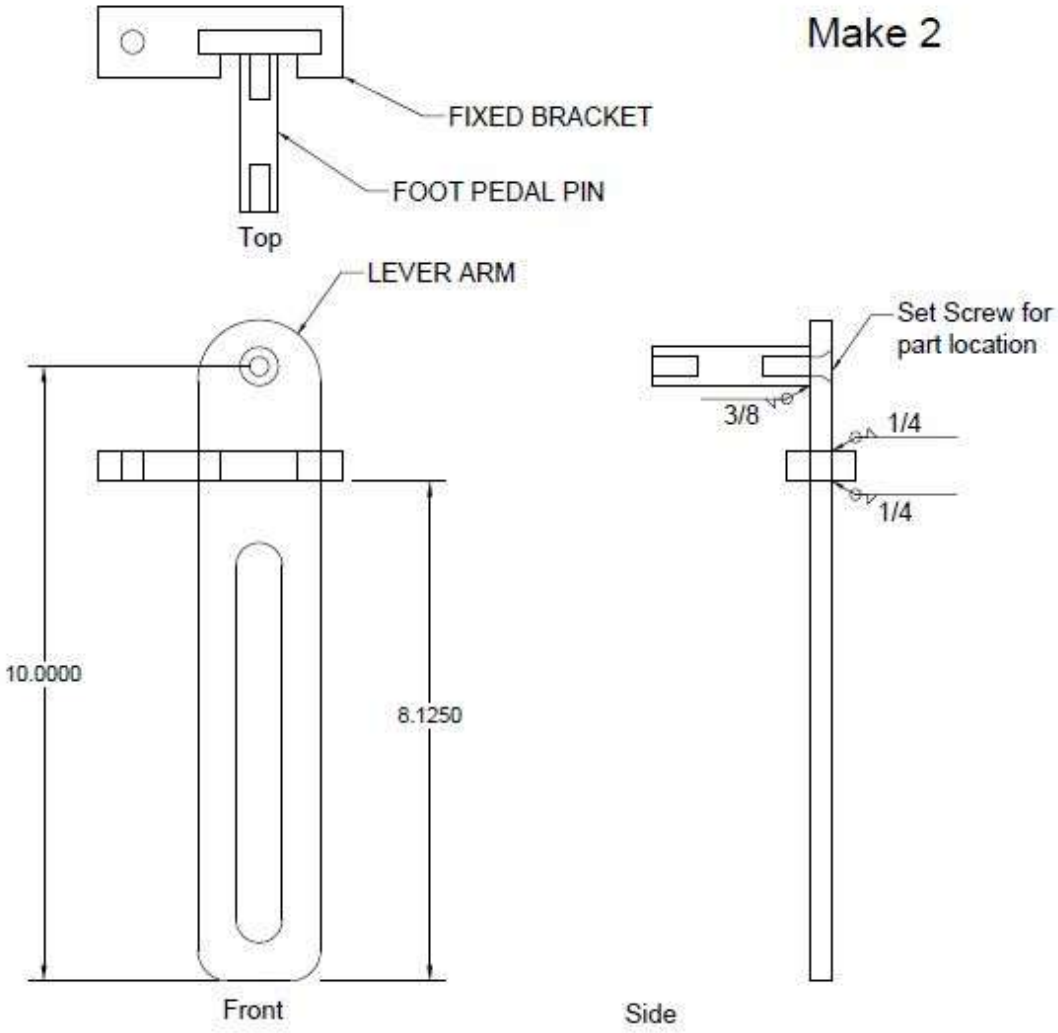

Lever Arm Assembly

APPENDIX C NONLINEAR OPTIMIZATION OF ROCKER ANGULAR POSITION USING MATLAB

```
% The period is normalized to 1 second.
%  The data begins with the foot positioned at centerline of stride.

%%%%%%%%%%%%%%%%%%%%%%%%%%%%%%%%%%%%%%%%%%%%%%%%%%%%%%%%%%%%%%%%%%%%%%%%%%%%%%%
%%%%
%%%%%%%%%%%%%%%%%%%%%%%%%%%%%%%%%%%%%%%%%%%%%%%%%%%%%%%%%%%%%%%%%%%%%%%%%%%%%%%
%%%%
% Set time and constant values for Fourier series

% Fourier Am and Bn constants
Am = [-0.016352666; -0.374850467; -0.114519546; -0.001371391; -
0.006903369; -0.006738177; -0.000660878; -0.003511986; -0.002300941];
Bn = [-0.239342072; 0.057472015; 0.026786152; -0.002042114;
0.004048092; 0.002331935; -0.000816269; 0.001939239];

%Number of data points
N = 201;

% Set time values
t = zeros(N,1);
for j = 1:N
    t(j,1) = (j-1)/(N-1);
end

% Fourier-Determined Angular Curve
FourierM = [Am(1)*ones(N,1) + Am(2)*cos(2*pi*t) + Bn(1)*sin(2*pi*t) +
Am(3)*cos(2*pi*2*t) + Bn(2)*sin(2*pi*2*t) + Am(4)*cos(3*pi*2*t) +
Bn(3)*sin(3*pi*2*t) + Am(5)*cos(4*pi*2*t) + Bn(4)*sin(4*pi*2*t) +
Am(6)*cos(5*pi*2*t) + Bn(5)*sin(5*pi*2*t) + Am(7)*cos(6*pi*2*t) +
Bn(6)*sin(6*pi*2*t) + Am(8)*cos(7*pi*2*t) + Bn(7)*sin(7*pi*2*t) +
Am(9)*cos(8*pi*2*t) + Bn(8)*sin(8*pi*2*t)];
FourierM = FourierM + ones(N,1)*0.5; %Adjusts the lowest Fourier series
point to 0

%%%%%%%%%%%%%%%%%%%%%%%%%%%%%%%%%%%%%%%%%%%%%%%%%%%%%%%%%%%%%%%%%%%%%%%%%%%%%%%
%%%%
%%%%%%%%%%%%%%%%%%%%%%%%%%%%%%%%%%%%%%%%%%%%%%%%%%%%%%%%%%%%%%%%%%%%%%%%%%%%%%%
%%%%
% Set initial values for independent parameters

% Link Lengths
L1 = 8.0;
L2 = 14.0;
L3 = 16.0;
L4 = 19.6977;

%Set Theta value
theta = zeros(N,1);
for m = 1:N;
    theta(m) = (m-1)/(N-1)*2*pi;
```

```
end

% Set constants for the Wolfe Conditions
C = 0.0001;

%Define vector dimensions
f = 0; fnew = 0; xnew = zeros(4,1);

A3 = zeros(N,1); dA3dx4 = zeros(N,1); dA3dx1 = zeros(N,1);

Psi = zeros(N,1); dPsidx1 = zeros(N,1); dPsidx4 = zeros(N,1);

phi = zeros(N,1); normphi = zeros(N,1); newphi = zeros(N,1); Jacobian =
zeros(N,4);

alpha0 = pi; % Initial value of alpha
rho = 0.6;   % Constant that alpha is multiplied by to test function
decrease
k = 0;       % Number of iterations
done = 0;    % Parameter that ends the program


x = [ L1; L2; L3; L4];
%%%%%%%%%%%%%%%%%%%%%%%%%%%%%%%%%%%%%%%%%%%%%%%%%%%%%%%%%%%%%%%%%%%%%%%%%%%%
%%%%
%%%%%%%%%%%%%%%%%%%%%%%%%%%%%%%%%%%%%%%%%%%%%%%%%%%%%%%%%%%%%%%%%%%%%%%%%%%%
%%%%
while done == 0
    %%% Determine the constants R1, R2, and R3
    R1 = x(4) / x(3);
    R2 = x(4) / x(1);
    R3 = (x(1)^2 + x(3)^2 + x(4)^2 - x(2)^2) / (2 * x(1) * x(3));

    dR3dx1 = 1/(2*x(3)) + (x(3)^2 + x(4)^2 - x(2)^2)/(2*x(1) * x(3));
    dR3dx2 = -1 * x(2) / (x(1) * x(3));
    dR3dx3 = 1/(2*x(1)) + (x(1)^2 + x(4)^2 - x(2)^2)/(2*x(1) * x(3));
    dR3dx4 = x(4) / (x(1) * x(3));

    for m=1:N

    %%%Calculate derivatives and function values

        %A3
        A3(m) = ((cos(theta(m)) + R2)^2 + sin(theta(m))^2)^(1/2);
        dA3dx4(m) = 2 * (cos(theta(m)) + R2) / (x(1) * ((cos(theta(m))
+ R2)^2 + sin(theta(m))^2)^(1/2));
        dA3dx1(m) = -2 * x(4) * (cos(theta(m)) + R2) / (x(1)^2 *
((cos(theta(m)) + R2)^2 + sin(theta(m))^2)^(1/2));

        %Psi
        Psi(m) = atan(-1 * sin(theta(m)) / (cos(theta(m)) + R2));
        dPsidx4(m) = 1 / (x(1) * (1 - (sin(theta(m)) / (cos(theta(m)) +
R2))^2));
```

```
        dPsidx1(m) = -x(4) / (x(1)^2 * (1 - (sin(theta(m)) /
(cos(theta(m)) + R2))^2));

        %Phi
        phi(m) = acos((R1 * cos(theta(m)) + R3) / A3(m)) - Psi(m);
        if cos(phi(m)-theta(m)) + R2 * cos(phi(m)) - (R1 *
cos(theta(m)) + R3) > 1*10^-8
            phi(m) = phi(m);
        else
            phi(m) = -phi(m);
        end

        % Calculate the Jacobian for determining steepest descent
        Jacobian(m,1) = -1 / (1-((R1 * cos(theta(m)) + R3) /
A3(m))^2)^(-1/2) * (dR3dx1 / A3(m) -
(R1*cos(theta(m))+R3)/(A3(m)^2)*dA3dx1(m)) - dPsidx1(m);
        Jacobian(m,2) = -1 / (1-((R1 * cos(theta(m)) + R3) /
A3(m))^2)^(-1/2) * (dR3dx2 / A3(m));
        Jacobian(m,3) = -1 / (1-((R1 * cos(theta(m)) + R3) /
A3(m))^2)^(-1/2) * (dR3dx3 / A3(m) - x(4)/x(3)^2 *
cos(theta(m))/A3(m));
        Jacobian(m,4) = -1 / (1-((R1 * cos(theta(m)) + R3) /
A3(m))^2)^(-1/2) * (dR3dx4 / A3(m) - x(4)/x(3)^2 * cos(theta(m))/A3(m)
- (R1*cos(theta(m))+R3)/(A3(m)^2)*dA3dx4(m)) - dPsidx4(m);
    end

    %The rocker angle in the comparison data starts at the minimum
value at
    %t = 0 seconds. In order to compare these two functions, we have to
    %change the projected rocker angle to match this.
    f = 0;

    [offsetAng,I] = min(phi);
    for m = 1:N;
        if m+I > N
            normphi(m) = phi(m+I-N)-offsetAng;
        else
            normphi(m) = phi(m+I)-offsetAng;
        end

    % Define function values
        f = f + (normphi(m) - FourierM(m))^2;
    end

    NormValues = normphi; %For plotting purposes

    %The gradient is the Jacobian multiplied by the function values.
    grad = transpose(Jacobian) * (normphi - FourierM);

   %Define the descent vector p
    p = -0.1 * grad;            %For Steepest Descent

    xnew = x+p;
    if xnew(1) < 6
        xnew = xnew * 6/xnew(1);
```

```
    end

    %Impose Grashof Conditions
    Grashof = 0;
    while Grashof == 0
    if xnew(2) + xnew(4) > xnew(1) + xnew(3)
        if xnew(3) + xnew(4) > xnew(1) + xnew(2)
            if xnew(2) + xnew(3) > xnew(1) + xnew(4)
                Grashof = 1;
            else
                p = p * 1.1;
                p(1) = p(1)/1.1;
            end
        else
            p = p * 1.1;
            p(1) = p(1)/1.1;
        end
    else
        p = p * 1.1;
        p(1) = p(1)/1.1;
    end
    xnew = x + p;
    end


    ready = 0;
    alpha = alpha0;

while ready == 0
            %R values
            R1 = xnew(4) / xnew(3);
            R2 = xnew(4) / xnew(1);
            R3 = (xnew(1)^2 + xnew(3)^2 + xnew(4)^2 - xnew(2)^2) / (2 *
xnew(1) * xnew(3));

        for m=1:N;

        A3(m) = ((cos(theta(m)) + R2)^2 + sin(theta(m))^2)^(1/2);

        Psi(m) = atan(-1 * sin(theta(m)) / (cos(theta(m)) + R2));

        newphi(m) = acos((R1 * cos(theta(m)) + R3) / A3(m)) - Psi(m);

        end
        if imag(newphi)==0
            fnew = 0;
            phi = newphi;
        [offsetAng,I] = min(phi);
        for m = 1:N;
            if m+I > N
                normphi(m) = phi(m+I-N)-offsetAng;
            else
                normphi(m) = phi(m+I)-offsetAng;

            % Define function values
```

```
            fnew = fnew + (normphi(m) - FourierM(2))^2;
            end
        end

        %Test to see if new r value meets the Wolfe criteria
        %%%if fnew > f + C * alpha *transpose(grad) * p;
        if fnew > f
            alpha = rho * alpha;
            xnew = x + alpha * p;
        else
            ready = 1;
            display(fnew)
        end
        else
            xnew = x;
        end
        if alpha < 1 * 10^8
            p = p * 1.1;
            p(1) = p(1)/1.1;
        end
        end

if imag(fnew) == 0
    f = fnew;
    xnew = x + p;
    x = xnew;
else
    return
end
if x(1) < 6
    x(1) = 6;
end
end
display(x)
```